



Wrocław University  
of Science and Technology

Faculty of Mechanical and Power Engineering  
Department of Energy Conversion Engineering  
Scientific discipline: **Environmental engineering, mining and energy**

## DOCTORAL THESIS

### **CFD modelling of the gasification process of solid fuels**

Keywords: CFD, coal gasification, entrained flow reactor

Jakub Mularski, BEng, MSc

under the supervision of

**Norbert Modliński, BEng, PhD, DSc, Assoc. Prof.**

at the Department of Energy Conversion Engineering

Wrocław, 2021

This work was supported by the Polish National Science Center as part of Preludium 15 under the project designated with the number 2018/29/N/ST8/00799.

Some of the calculations have been carried out using resources provided by Wroclaw Center for Networking and Supercomputing, grant No. 492.

## **Acknowledgements**

Thanks to my family, for your support, your love and encouragement in every moment. I would not have done it without you.

A special gratefulness to Professor Halina Pawlak-Kruczek and Professor Norbert Modliński for your guidance, your instructions and your patience with me.

A sincere thanks to Professor Krzysztof Czajka, Łukasz Niedźwiecki, and Krystian Krochmalny for your suggestions and assistance.

## Publications, conferences and activity

### Publications:

- **J. Mularski**, N. Modliński, Entrained flow coal gasification process simulation with the emphasis on empirical char conversion models optimization procedure, *Energies* **2021**, vol. 14, p. 1-20. *MNiSW pts: 140, IF (2019): 2.702*
- **J. Mularski**, N. Modliński, Impact of chemistry-turbulence interaction modeling approach on the CFD simulations of entrained flow coal gasification, *Energies* **2020**, vol. 13, p. 1-25. *MNiSW pts: 140, IF (2019): 2.702*
- **J. Mularski**, N. Modliński, Entrained flow coal gasification process simulation with the emphasis on empirical devolatilization models optimization procedure, *Applied Thermal Engineering* **2020**, vol. 175, p. 1-14. *MNiSW pts: 140, IF (2019): 4.725*
- **J. Mularski**, H. Pawlak-Kruczek, N. Modliński, A review of recent studies of the CFD modelling of coal gasification in entrained flow gasifiers, covering devolatilization, gas-phase reactions, surface reactions, models and kinetics, *Fuel* **2020**, vol. 271, p. 1-36. *MNiSW pts: 140, IF (2019): 5.578*
- **J. Mularski**, A. Arora, M. A. Saeed, Ł. Niedźwiecki, Impact of turbulence models on the air flow in a confined rectangular space, *Engineering Science & Technology* **2021**, vol. 2, p. 46-53.
- A. Arora, H. Pawlak-Kruczek, M. J. Baranowski, M. K. Dębowski, K. K. Krochmalny, Ł. Niedźwiecki, **J. Mularski**, Examination of combustion processes of hard coal and predried lignite blends, *Pollution Research* **2019**, vol. 38, p. 145-151. *MNiSW pts: 20*
- H. Pawlak-Kruczek, M. J. Czerep, **J. Mularski**, K. K. Krochmalny, Ł. Niedźwiecki, M. J. Baranowski, M. J. Ostrycharczyk, M. Wnukowski, Innowacyjne termiczne przekształcanie osadów ściekowych cz. 2, *Wodociągi, Kanalizacja* **2019**, vol. 1, p. 24-26
- H. Pawlak-Kruczek, M. J. Czerep, **J. Mularski**, K. K. Krochmalny, Ł. Niedźwiecki, M. J. Baranowski, M. J. Ostrycharczyk, M. Wnukowski, Innowacyjne termiczne przekształcanie osadów ściekowych cz. 1, *Wodociągi, Kanalizacja* **2018**, vol. 12, p. 33-34
- **J. Mularski**, H. Pawlak-Kruczek, N. Modliński, Comparison of eddy dissipation concept and finite-rate/eddy dissipation models in case of coal gasification in a two-stage entrained flow gasifier and their relation to the experimental results, *Rynek Energii* **2018**, vol. 4, p. 97-106. *MNiSW pts: 11*
- **J. Mularski**, H. Pawlak-Kruczek, N. Modliński, Comparison of a discrete coal gasification global model in an entrained flow gasifier with the GRI-Mech 1.2 mechanism, *Archivum Combustionis* **2017**, vol. 37, p. 139-154. *MNiSW pts: 12*

*MNiSW points: 603*

*Impact Factor: 15.707*

### **International Conferences:**

- **J. Mularski**, N. Modliński, Wpływ modelowania fazy gazowej na symulacje CFD zgazowania węgla, Międzynarodowa Druga edycja XII Konferencji Młodych Energetyków, Wrocław 9-11 grudnia 2020, s. 44-45.
- **J. Mularski**, N. Modliński, An optimization procedure of two devolatilization models: (one-step SFOR and two-step Kobayashi) basing on the advanced network FG-DVC model with CFD implementation, XXIV International Symposium on Combustion Processes, Wrocław 23-25 September 2019, p. 56-57
- **J. Mularski**, H. Pawlak-Kruczek, N. Modliński, The effect of gas-phase on CFD coal gasification modelling in entrained flow reactor, XXIV International Symposium on Combustion Processes, Wrocław 23-25 September 2019, p. 58-59
- K. K. Krochmalny, M. B. Tkaczuk-Serafin, W. Sebestowicz, **J. Mularski**, H. Pawlak-Kruczek, Ł. Niedzwiecki, Coal co-firing with torrefied biomass residues in a drop tube, XXIV International Symposium on Combustion Processes, Wrocław 23-25 September 2019, p. 86-87
- **J. Mularski**, N. Modliński, H. Pawlak-Kruczek, Ł. Niedzwiecki, Comparison of Eddy dissipation concept and Laminar Finite-Rate/Eddy dissipation models in case of coal gasification in a two-stage entrained flow gasifier and their relation to the experimental results, Joint meeting of the Polish and Scandinavian-Nordic Sections of the Combustion Institute, Kraków 6-7 September 2018, p. 187-188
- H. Pawlak-Kruczek, M. J. Czerep, **J. Mularski**, K. K. Krochmalny, Ł. Niedzwiecki, Innowacyjna, wielostopniowa instalacja do termicznego przekształcania osadów ściekowych, Międzynarodowa konferencja, Poznań-Berlin 25-27 września 2018, p. 132-146
- **J. Mularski**, H. Pawlak-Kruczek, N. Modliński, Comparison of a discrete coal gasification global model in an entrained flow gasifier with the GRI-Mech 1.2 mechanism, XXIII International Symposium on Combustion Processes, Rynia 3-6 September 2017, p. 50-51.

### **National Conferences:**

- **J. Mularski**, Optymalizacja modeli empirycznych odgazowania węgla na podstawie zaawansowanego modelu sieciowego FG-DVC i jej wpływ na procesy zgazowania i pirolizy, XII Konferencja Młodych Energetyków, Wrocław 22-24 czerwca 2020, s. 21-22.
- **J. Mularski**, Modelowanie CFD procesu zgazowania węgla, XI Konferencja Młodych Energetyków, Złotniki Lubańskie 31 stycznia – 2 luty 2019, s. 21-22

### **Member of the Conferences Organizing Committee:**

- XXIV International Symposium on Combustion Processes 2019
- Druga edycja XII Konferencji Młodzi w Energetyce 2020
- ECOS 2019 32nd International Conference on Efficiency, Cost, Optimization, Simulation and Environmental Impact of Energy Systems

### **Reviewer in the following journals:**

Energy and Fuels (IF: 3.421), Journal of the Taiwan Institute of Chemical Engineers (IF: 4.794), International Journal of Mining Science and Technology (IF: 3.903), Fuel (IF: 5.578), Energy Conversion and Management (IF: 8.208), Fluids (CiteScore: 1.8). *Verified reviews: 7*

### **Nomination for the award „Naukowiec Przyszłości 2021”**

# Streszczenie

**Wprowadzenie:** Ponad 80% światowej energii pochodzi z paliw kopalnych. Węgiel jest jednym z głównych źródeł energii pozyskiwanej z paliw kopalnych, podczas gdy spalanie węgla jest kluczowym sposobem konwersji tej energii. Niestety, proces ten znacząco wpływa na środowisko naturalne, klimat i ludzkie zdrowie. W rezultacie, konkretne kroki są podejmowane w celu promowania i rozwijania skutecznych technologii, które zmniejszą negatywny wpływ na naszą planetę. Węgiel, pomimo jego malejącego zużycia w wielu krajach, nadal będzie kluczowym źródłem energii przez wiele nadchodzących lat. Na skutek tego rozwijane są non-stop technologie oparte na węglu z minimalnym wpływem na środowisko. Zgazowanie strumieniowe jest jedną obiecujących technologii opartych na węglu z wysoką sprawnością i małą szkodliwością dla środowiska. Głównym produktem zgazowania jest gaz syntezowy, który może zostać wykorzystany w wielu gałęziach przemysłu, jak i w produkcji energii elektrycznej (np. w silnikach wewnętrznego spalania, ogniwach paliwowych, turbinach gazowych). Gaz syntezowy może być także zamieniony w produkty mające zastosowanie w innych dziedzinach (etanol, diesel). Jednakże, proces zgazowania nie jest dokładnie poznany na poziomie fundamentalnym i wiele modeli opisujących ten proces nie dają wysoce dokładnych wyników. Zgazowanie strumieniowe różni się od konwencjonalnego spalania pyłowego i wiele kwestii nie zostało gruntownie zbadanych.

**Cele:** Przegląd literaturowy pozwoli na gruntowne poznanie stosowanych modeli procesów odgazowania, fazy gazowej oraz konwersji koksu, będących głównymi pod-procesami zgazowania. Głównym celem pracy jest opracowanie i zastosowanie procedur optymalizacyjnych powszechnie stosowanych modeli w celu poprawy skuteczności/dokładności symulacji numerycznych wykorzystujących komputerową mechanikę płynów (CFD) całego procesu zgazowania.

**Metodologia badań:** Przegląd literaturowy pozwolił zebrać najważniejsze informacje dotyczące stosowanych modeli, ich założeń i uproszczeń oraz parametrów kinetycznych.

W przypadku odgazowania, główny nacisk został położony na dwa modele globalne (model jednokrokowy oraz model dwóch konkurujących reakcji). Na podstawie przeglądu literaturowego stwierdzono, że większość badań zawierała parametry kinetyczne wzięte z dostępnej literatury, nieoptymalizowane dla konkretnego badanego przypadku. Biorąc pod uwagę fakt, że parametry te są ściśle powiązane z paliwem, parametrami pracy reaktora, nieskalibrowane wartości mogą znacząco wpłynąć na wyniki symulacji. W związku z tym, postanowiłem skupić się na tym aspekcie rozpatrując różne metody optymalizacji, które w efekcie pozwolą otrzymać unikatowe, skalibrowane parametry kinetyczne pasujące tylko do warunków pracy konkretnego reaktora.

Badania nad fazą gazową poświęcone były mechanizmom reakcji oraz wpływowi interakcji kinetyka-turbulencja na proces zgazowania. Na podstawie przeglądu literaturowego stwierdziłem, że znaczna część publikacji wykorzystywała modele i mechanizmy w fazie gazowej identyczne jak w przypadku spalania pyłowego. Jednakże, biorąc pod uwagę parametry pracy, warunki, procesy te znacznie się różnią. Ponadto, nie znaleziono literatury, w której analizowano by wpływ poszczególnych mechanizmów i modeli fazy gazowej na cały

proces zgazowania. Na tej podstawie, jednym z głównych celów pracy były badania w tym zakresie.

W przypadku reakcji powierzchniowych, skupiono się tutaj, podobnie jak w przypadku odgazowania, na procedurze optymalizacji pozwalającej wyznaczyć unikatowe parametry kinetyczne modelu globalnego (kinetyczno-dyfuzyjnego) bazując na zaawansowanym modelu „carbon burnout kinetics” (CBK) [1–4]. Zoptymalizowane parametry kinetyczne ściśle odpowiadają rozpatrywanym warunkom pracy.

**Główne wyniki:** Odgazowanie – Zoptymalizowane parametry kinetyczne zależą od parametrów pracy (szybkość nagrzewania) oraz własności paliwa (analiza techniczna i analiza elementarna). Otrzymane zależności zostały otrzymane dzięki zaawansowanym modelom sieciowym, które jako wartość zadaną wymagają podania szybkości nagrzewu, oraz informacji z analizy technicznej i elementarnej. Bezpośrednie wykorzystanie zaawansowanych modeli sieciowych w ramach symulacji CFD mogłoby wpłynąć na czas symulacji znacznie zwiększając nakłady obliczeniowe. W związku z tym, wykorzystanie takiej procedury optymalizacyjnej pozwoli zwiększyć dokładność symulacji nie zwiększając przy tym nakładów obliczeniowych. Ponadto, wykorzystanie metod eksperymentalnych może być dużym wyzwaniem, zwłaszcza w przypadku reaktorów na dużą skalę. Przegląd literaturowy wykazał, że stosowano już procedury optymalizacyjne parametrów kinetycznych modeli odgazowania. Jednakże, dotyczyły one jedynie średniej szybkości nagrzewu. Jednym z elementów nowości jest analiza chwilowej szybkości nagrzewu jako parametru wejściowego. Ta rozszerzona analiza została przeprowadzona dla zgazowania strumieniowego węgla oraz dla odgazowania węgla w atmosferze inertej (pirolizie). Ponadto, badania skupiły się także na dwóch zaawansowanych modelach sieciowych (CPD [5–7], FG-DVC [8]) w odniesieniu do ilości przewidywanych gazów pirolitycznych wyraźnie wykazując niedoskonałości modelu FG-DVC. Procedura optymalizacyjna ma charakter iteracyjny i jej zastosowanie pozwoliło zwiększyć dokładność obliczeń i dla zgazowania i dla pirolizy, wnioskuje na podstawie wyników eksperymentalnych.

Faza gazowa – badania dotyczyły dwóch reaktorów idealnych (reaktor typu plug-flow oraz reaktor idealnego wymieszania) oraz trzech reaktorów rzeczywistych w ramach analizy CFD. Główny nacisk położyłem na analizę rozkładu temperatury oraz skład gazu syntezowego w każdym reaktorze. Danymi referencyjnymi były wyniki eksperymentalne oraz dwa zaawansowane modele GRI-Mech [9] i CRECK [10]. Modele te, bazujące na reakcjach rodnikowych, pozwoliły otrzymać dokładne wyniki dla szerokiego zakresu warunków pracy. Dwa z trzech badanych reaktorów wykorzystywały ciśnienia wyższe niż te zwalidowane dla mechanizmu GRI-Mech. W tym celu przeprowadzone zostały dodatkowe badania dla mechanizmu GRI-Mech poza zakresem optymalizacyjnym w celu oceny dokładności wyników tego mechanizmu. Badania te pozwoliły ustalić zasadność stosowania GRI-Mecha dla wyższych ciśnień. Analiza reaktorów idealnych plug-flow i idealnego wymieszania pozwoliła wyznaczyć mechanizm globalny dający najbardziej zbliżone wyniki do mechanizmów zaawansowanych GRI-Mech oraz CRECK w warunkach zgazowania. Pokazany został także istotny wpływ interakcji kinetyka-turbulencja na skład gazu. Dodatkową uwagę poświęcono reakcji konwersji CO z H<sub>2</sub>O, która okazała się być kluczową reakcją w fazie gazowej.

Konwersja koksu – zoptymalizowane parametry kinetyczne do modelu kinetyczno-

dyfuzyjnego są otrzymane na podstawie zaawansowanego modelu „carbon burnout kinetics” (CBK) dla oksydacji (CBK/E) [11] i zgazowania (CBK/G) [12], który określa szybkość reakcji powierzchniowych oksydacji i zgazowania, uwzględniając takie aspekty jak ewolucja wewnętrznej powierzchni węgla, dyfuzja w porach, termiczne wyżarzanie, inhibicja przez popiół. Na skutek zastosowanej procedury, skalibrowane parametry kinetyczne zastosowane w modelu globalnym dokładnie oddają przebieg szybkości reakcji modelu zaawansowanego. Analiza CFD została przeprowadzona w celu oszacowania, czy optymalizacja parametrów kinetycznych zwiększa dokładność obliczeń w odniesieniu do wyników eksperymentalnych. Badania pokazały, że zastosowanie procedury pozwoliło uzyskać dokładniejsze wyniki składu gazu oraz stopnia konwersji koksu. Ponadto pokazano, że zastosowane parametry kinetyczne miały znaczący wpływ na formowanie się gazu w obszarze zarówno zgazowania jak i płomienia. Porównując wpływ każdego z badanych w tej rozprawie doktorskiej podprocesów zgazowania ustaliłem, że faza konwersji koksu i towarzyszące jej reakcje powierzchniowe wywierają największy wpływ na proces zgazowania. Niemniej jednak każdy z podprocesów jest istotny, jeśli zależy nam na rzetelnych i wiarygodnych symulacjach strumieniowego zgazowania węgla.

**Układ pracy:** Rozprawa doktorska składa się z 7 rozdziałów. Rozdział 1 - wprowadzenie dotyczy uzasadnienia naukowego problemu, który postanowiłem zgłębić. Rozdział 2 dotyczy przeglądu literaturowego w kontekście modelowania procesów odgazowania, fazy gazowej oraz reakcji powierzchniowych będących kluczowymi pod-procesami w całym zgazowaniu. W podrozdziale 2.1 przedstawiony jest także cel i zakres rozprawy doktorskiej. Rozdział 3 przedstawia dokładny opis zastosowanego modelu CFD, który pozwolił zasymulować proces zgazowania strumieniowego węgla. Rozdział 4 przedstawia procedurę optymalizacyjną odgazowania, zastosowaną w celu poprawy dokładności symulacji CFD. Rozdział 5 dotyczy badań nad fazą gazową gdzie analizowane były modele, które najdokładniej odwzorowują proces zgazowania. Rozdział 6 opisuje procedurę optymalizacyjną konwersji koksu, zastosowaną również w celu poprawy dokładności symulacji. Rozdział 7 przedstawia wnioski.



# Abstract

**Introduction:** More than 80% of the world's energy comes from fossil fuels. Coal is one of the main sources of fossil fuel energy, whereas coal combustion is a key way of energy conversion. Unfortunately, this ongoing process tremendously impacts the natural environment, climate, and human health. As a result, specific measures are taken to promote and develop efficient technologies which can mitigate the negative impact on our planet. Coal, despite its gradually decreasing consumption in many countries, will continue to be a meaningful energy source for many years to come. This results in continuous research in environmentally benign coal-based technologies. Entrained flow coal gasification is one of the promising coal-technologies with high efficiency and low environmental impact. The gasification main product – syngas, can be utilized in many branches of industry and electricity production (e.g., in internal combustion engines, fuel cells, and gas turbines). It also can be converted into other chemical products of commercial interest (diesel, ethanol fuels). However, the process is still not fully understood on a fundamental level and many models that describe specific gasification sub-phenomena still lack high accuracy. Many aspects in gasification differ from conventional pulverized coal combustion and many issues have not yet been thoroughly investigated.

**Objectives:** This work aims to investigate thoroughly the most commonly applied modeling techniques of devolatilization, gas phase, and char conversion which are the key sub-processes of entrained flow coal gasification, and to propose optimization techniques and most optimum modeling approaches for these sub-processes that improve the accuracy of the CFD modeling of entrained flow coal gasification. These optimized models will be validated for a wide range of operating conditions.

**Research methodology:** The extensive literature review allowed me to gather the most important information regarding the formulas of the utilized models and applied kinetic parameters, their benefits, and drawbacks, made assumptions and simplifications.

As regards devolatilization, the emphasis was laid on two global models (single-step first-order approach, competing two-step reaction approach). The literature review indicated that the majority of researchers incorporated literature kinetic parameters for these models. Considering the fact that kinetic parameters are only valid for the conditions for which they were determined, such a simplification can cause huge inaccuracies. Therefore, I have focused on incorporating an optimization technique that would consider unique kinetic parameters for the specific conditions.

As regards the gas phase, the literature review indicated that the majority of authors utilized global combustion mechanisms and turbulence-chemistry interaction approaches the same as in coal combustion studies. However, these processes differ substantially. On top of that, no study was found that would thoroughly investigate and compare the gas phase models strictly in gasification conditions which would help to assess their accuracy in such conditions. On this basis, I have decided to study these aspects thoroughly.

In the char conversion process the main focus, similarly to devolatilization, was laid on the optimization techniques of the global empirical model (kinetic/diffusion model) based on the advanced carbon burnout kinetic (CBK) approach [1–4]. This procedure will also allow me

to obtain optimized kinetic parameters corresponding to the investigated coal and operating conditions.

**Main results:** Devolatilization - The optimized kinetic parameters depend on operating conditions (heating rate) and fuel properties (proximate and ultimate analysis). Such an outcome was possible thanks to the complex devolatilization models which require heating rate as input and data from proximate and ultimate analyses. Direct utilization of complex network approaches within CFD can substantially raise the computational effort, therefore such an optimization procedure is an optimum choice of raising the accuracy without increasing the computational burden. Moreover, the use of experimental techniques could be very challenging, or even inviable, especially in the case of large-scale reactors. The literature review indicated that similar approaches of gaining kinetic parameters have already been undertaken, but only for a constant heating rate. The novelty of this dissertation consists in employing the instantaneous heating rate as input data. This extended analysis was performed for both entrained flow coal gasification and for coal devolatilization in an inert atmosphere (coal pyrolysis). Moreover, the research considered the comparison of two detailed devolatilization models (CPD [5–7] and FG-DVC [8]) with respect to the volatile yield prediction, providing clear drawbacks of the latter. The entire optimization procedure has an iterative character and its utilization allowed to increase the accuracy of simulations with regard to the experimental data for both coal gasification and coal pyrolysis on the basis of the error analysis.

Gas phase - The investigation considered two ideal reactors (plug flow reactor and a perfectly stirred reactor) and three actual gasifiers, as part of the CFD analysis. I laid emphasis on the temperature distribution and main syngas components distribution in each reactor. The reference data that I compared the numerical results with were the experimental results and two detailed mechanisms – GRI-Mech [9] and CRECK [10]. These detailed mechanisms allowed me to obtain accurate results for a wide range of operating conditions. However, the two reactors that I examined considered pressures higher than the ones for which GRI-Mech was validated. On this basis, I have also decided to carry out additional simulations to see what would be the performance of GRI-Mech outside of its validation/optimization range. The results confirmed the utility of GRI-Mech for higher pressures. The analysis of the plug-flow reactor and the perfectly stirred reactor allowed me to determine the most accurate global reaction mechanism with regard to GRI-Mech and CRECK in gasification conditions. A substantial influence of the turbulence-chemistry interaction on the gas composition was pronounced. Specific attention was also paid to the impact of the water-gas shift reaction which was found to be the key gas-phase reaction.

Char conversion – the optimized kinetic parameters for the kinetic/diffusion global model are obtained based on the advanced carbon burnout kinetic model for oxidation (CBK/E) [11] and gasification (CBK/G) [12], which determines the oxidation and gasification surface reaction rates taking into account such aspects as intrinsic surface area evolution, pore diffusion, thermal annealing, and ash inhibition. Thanks to the procedure, the optimized parameters accurately matched the prediction of the advanced approach. A CFD analysis was performed in order to estimate, whether the optimized global model provided more accurate results than the model with literature kinetic parameters, based on the experimental measurements. It turned

out that, similarly to devolatilization, the optimization method for char conversion managed to increase the agreement of the syngas composition and char conversion degree with experimental data. Additionally, it was emphasized that the applied kinetic parameters had a very strong impact on the gas formation in the reforming zone and the flame zone. After the comparison of each of the gasification main sub-processes, I determined that the char conversion phase and accompanying its surface reactions have the greatest impact on the gasification process. Nevertheless, each of the subprocesses is of crucial importance, when one considers effective and credible simulations of entrained flow coal gasification.

**Work layout:** The work consists of 7 chapters. Introduction aims to present and justify the scientific problem which I decided to investigate. Chapter 2 considers the review of literature on devolatilization modeling, gas-phase modeling, and char conversion modeling which are the key phases in entrained flow coal gasification. In sub-chapter 2.1 the main objectives and scope of the thesis are summarized. Chapter 3 regards the CFD model description that was used to model the entire entrained flow coal gasification processes for various cases. Chapter 4 discusses the optimization procedure of devolatilization that was applied to improve the accuracy of CFD simulations of entrained flow coal gasification. Chapter 5 presents the utilized gas-phase modeling techniques with the aim of assessing which are most suitable for reproducing the entrained flow gasification process. Chapter 6 discusses the optimization procedure of char conversion which was employed to improve the accuracy of CFD simulation of entrained flow coal gasification. Chapter 7 considers conclusions.

## Acronyms

BYU – Brigham Young University

BT – Biagini and Tognotti model

C2SM – Competing two-step reaction model

CBK – Carbon burnout kinetic model

CBK/E – Carbon burnout kinetic model for oxidation

CBK/G – Carbon burnout kinetic model for gasification

CCS – Carbon capture and storage

CFD – Computational fluid dynamics

CPD – Chemical percolation devolatilization model

DAE – Distributed activation energy models

Daf – Dry-ash-free

DME – Dimethyl ether

DNS – Direct numerical simulation

DOM – Discrete ordinate method

DTF – Drop tube furnace

F-R/EDM – Laminar finite-rate/eddy dissipation model

EDC – Eddy dissipation concept

FG-DVC – Functional-group, depolymerization, vaporization and cross-linking model

HRSG – Heat recovery steam generator

H-Zone – Homogeneous zone  
IGCC – Integrated gasification combined cycle  
JL – Jones and Lindstedt mechanism  
LES – Large eddy simulation  
LGRE – Laboratoire de Gestion des Risques et Environnement  
LH – Langmuir-Hinshelwood kinetics  
LHV – Lower heating value  
MFF – Moving flame front model  
MHI – Mitsubishi Heavy Industries  
MILD – Moderate and/or intense low oxygen dilution  
PCC – Pulverized coal combustion  
PFR – Plug flow reactor  
PM – Particulate matter  
PSI – Particle-source-in-cell method  
PSR – Perfectly stirred reactor  
RANS – Reynolds averaged Navier-Stokes equations  
RPM – Random pore model  
RTE – Radiative transport equation  
SC – Supercritical  
SCM – Shrinking core model  
SFOR – Single-step first-order reaction model  
SIMPLE – Semi-implicit method for pressure linked equations  
SNOR – Single n-th order reaction model  
SST – Shear stress transport model  
TCI – Turbulence-chemistry interaction  
TDM – Tabulated devolatilization model  
TGA – Thermogravimetric analysis  
TH – Taiheiyo coal  
USC – Ultra-supercritical  
WD – Westbrook and Dryer mechanism  
WGS- Water-gas shift reaction  
WSGG – Weighted-sum of gray gas model

# Table of Contents

Acknowledgements .....	ii
Publications, conferences and activity .....	iii
Streszczenie .....	v
Abstract .....	viii
Acronyms .....	x
Table of Contents .....	xii
List of figures .....	xv
List of tables .....	xx
1. Introduction.....	1
1.1 Coal gasification and its applications .....	1
1.2 Energy background.....	2
1.3 Methods for CO <sub>2</sub> mitigation from coal-fired plants .....	3
1.4 Coal gasification .....	6
1.5 Types of gasifiers.....	7
1.6 Computational fluid dynamics (CFD) - introduction .....	10
2. Literature review on CFD modeling of entrained flow coal gasification .....	11
2.1 Introduction – aims and objectives of Thesis .....	11
2.2 Devolatilization .....	12
2.2.1 Global approaches.....	12
2.2.2 Detailed mechanisms .....	15
2.2.3 Performance of global approaches and detailed mechanisms.....	17
2.2.4 Kinetic parameters of global devolatilization models.....	21
2.2.5 Summary of devolatilization stage.....	24
2.3 Gas-phase modeling .....	25
2.3.1 Global kinetic mechanisms .....	26
2.3.2 Detailed kinetic mechanisms .....	28
2.3.3 Water-gas shift reaction .....	28
2.3.4 Turbulence-chemistry interaction models (TCI) .....	31
2.3.5 Gas phase kinetic parameters .....	35
2.3.6 Summary of gas phase stage .....	39

2.4	Char conversion modeling.....	39
2.4.1	Global mechanisms .....	40
2.4.2	Detailed mechanisms .....	56
2.4.3	Double-film model.....	58
2.4.4	Char conversion kinetic parameters.....	59
2.4.5	Summary of char conversion stage .....	64
3.	CFD model description .....	66
3.1	Background and introduction .....	66
3.2	Key sub-models .....	68
3.2.1	Gas phase .....	69
3.2.2	Discrete phase .....	72
3.2.3	Coupling between gas and discrete phase.....	73
3.2.4	Radiation .....	75
4.	Optimization procedure of devolatilization .....	77
4.1	Introduction .....	77
4.2	Optimization procedure .....	78
4.3	Optimization of kinetic parameters .....	79
4.3.1	Kinetic approximations – Linear approximation .....	81
4.3.2	Kinetic approximations – Second Linear approximation .....	81
4.3.3	Kinetic approximations – exponential approximation.....	83
4.3.4	Minimization of the objective function.....	84
4.3.5	Comparison of the approximation methods.....	86
4.4	Optimization of volatile composition .....	87
4.5	Coal gasification simulation – brief model setup .....	89
4.6	Coal pyrolysis simulation – brief model setup .....	91
4.7	Results and discussion .....	93
4.7.1	Coal gasification results .....	93
4.7.2	Coal pyrolysis results.....	99
4.7.3	Constant heating rate vs instantaneous heating rate .....	102
4.7.4	Model quality estimation .....	103
4.7.5	Conclusions.....	106
5.	Gas phase modeling .....	107
5.1	Introduction .....	107

5.2	Mathematical model – brief setup .....	108
5.2.1	Plug flow reactor study .....	109
5.2.2	Ideal perfectly stirred reactor study .....	111
5.2.3	CFD study .....	112
5.3	Results and discussion .....	116
5.3.1	Plug flow results .....	116
5.3.2	Perfectly stirred reactor results .....	118
5.3.3	CFD results .....	119
5.4	Conclusions .....	130
6.	Optimization procedure of char conversion.....	131
6.1	Introduction .....	131
6.2	Optimization procedure .....	131
6.3	Optimization of kinetic parameters .....	132
6.4	Coal gasification simulation – brief model setup .....	133
6.5	Results and discussion .....	134
6.5.1	Optimization procedure - results.....	135
6.5.2	CFD results .....	140
6.5.3	CFD results – GRI-Mech vs Global reaction approach .....	150
6.5.4	Conclusions.....	157
7.	General conclusions and future work.....	157
7.1	Conclusions .....	157
7.2	Future work.....	158
	References .....	158

## List of figures

Figure 1.1. Gasification and related technologies [13].	1
Figure 1.2. Projected global energy consumption from 1990 to 2040 by energy source [18].	3
Figure 1.3. Forecast of CO <sub>2</sub> emissions worldwide from 2018 to 2050 [19].	3
Figure 1.4. IGCC block flow diagram [28].	5
Figure 1.5. Updraft fixed-bed reactor [29].	7
Figure 1.6. Downdraft fixed-bed reactor [29].	8
Figure 1.7. Fluidized-bed reactor [30].	8
Figure 1.8. Entrained-flow reactors [30].	9
Figure 2.1. Ultimate volatile yield vs heating rate for 1-step (SFOR), Yamamoto model, BT (Biagini and Tognotti), Schroeder model (1-step DAE), and complex chemical percolation devolatilization (CPD) model [31].	18
Figure 2.2. Ultimate volatile yield vs heating rate for 2-step (Kobayashi) model, Yamamoto model (2-step*), Fletcher approach (2-step DAE), and complex chemical percolation devolatilization (CPD) model [31].	18
Figure 2.3. Mass-weighted temperature and major species for different devolatilization models [31].	19
Figure 2.4. Final yield composition of Utah coal predicted by FG-DVC, CPD and FLASHCHAIN [77].	20
Figure 2.5. R-factor for Utah bituminous coal for CPD, FG-DVC and FLASHCHAIN as function of heating rate [31].	20
Figure 2.6. MHI gasifier [128].	23
Figure 2.7. Conoco-Philips E-gas gasifier [129].	24
Figure 2.8. Comparison of syngas outlet composition with experimental data , original Jones' rates and calibrated Jones' rates [31].	31
Figure 2.9. Potential rate-limiting steps in char conversion process [31].	39
Figure 2.10. Arrhenius plot of char conversion dominant regimes in entrained flow gasification [31].	40
Figure 2.11. Single film model [31].	41
Figure 2.12. Char conversion rate for the intrinsic sub-model (upper part) and for the surface-based approach (lower part) [31].	54
Figure 2.13. Models for active sites by H <sub>2</sub> O and CO <sub>2</sub> gasification [31].	55
Figure 2.14. Mechanistic features of CBK/E [202].	56
Figure 2.15. Double film model [31].	58
Figure 3.1. Block scheme representing particular components of the CFD model and their interactions.	67
Figure 3.2. Schematic of turbulent structures in turbulent flows [213].	67
Figure 3.3. Centerline mean axial velocity for a) swirling flow b) non-swirling flow [219,220].	71
Figure 4.1. Optimization procedure of global devolatilization models [224].	79
Figure 4.2. Objective function visualization of the SFOR model (A - 1/s, E - J/mol). Black line depicts the compensation effect [224].	80



Figure 4.3. Linear approximation of FG-DVC yield data with respect to the inverse temperature (1/K). .....	81
Figure 4.4. Second linear approximation of the FG-DVC data with respect to the inverse temperature (1/K). .....	83
Figure 4.5. Exponential approximation of the reaction rate constant (1/s) obtained from FG-DVC data with respect to temperature (K).....	84
Figure 4.6. Calibration of the SFOR model - Volatile yield for three randomly taken heating rates (2000, 3500, 5000 K/s) (Continuous lines – FGDVC yields, dashed lines – SFOR yields). .....	85
Figure 4.7. Calibration of the Kobayashi model - Volatile yield for three randomly taken heating rates (2000, 3500, 5000 K/s) (Continuous lines – FGDVC yields, dashed lines – Kobayashi yields).....	85
Figure 4.8. Approximation curves of reaction rate coefficient (1/s) for aforementioned methods with respect to temperature (C). .....	86
Figure 4.9. Volatile yield curves (% wt) with respect to time, obtained by different approximation methods [224]. .....	87
Figure 4.10. Devolatilization modelling approach [224]. .....	88
Figure 4.11. BYU gasifier geometry with axisymmetric mesh [210]. .....	91
Figure 4.12. Drop tube furnace (DTF) geometry at LGRE with axisymmetric mesh [133]....	92
Figure 4.13. CO, H <sub>2</sub> , CO <sub>2</sub> and H <sub>2</sub> O mole fraction distribution along the centerline for consecutive iterations and for the CPD model [224]. .....	94
Figure 4.14. Temperature distribution along the centerline for consecutive iterations and for CPD [224]. .....	94
Figure 4.15. Temperature contour inside the BYU reactor. (Left: CPD model, Middle: C2SM with non-optimized kinetic parameters, Right: C2SM with optimized parameters) [224]. ....	95
Figure 4.16. CO, H <sub>2</sub> , CO <sub>2</sub> and H <sub>2</sub> O mole fraction distribution along the axial distance x = 0.13 m for consecutive iterations and for the CPD model [224]. .....	95
Figure 4.17. CO, H <sub>2</sub> , CO <sub>2</sub> and H <sub>2</sub> O mole fraction distribution along the axial distance x = 0.20 m for consecutive iterations and for the CPD model. ....	96
Figure 4.18. CO, H <sub>2</sub> , CO <sub>2</sub> and H <sub>2</sub> O mole fraction distribution along the axial distance x = 0.28 m for consecutive iterations and for the CPD model [224]. .....	96
Figure 4.19. CO, H <sub>2</sub> , CO <sub>2</sub> and H <sub>2</sub> O mole fraction distribution along the axial distance x = 0.34 m for consecutive iterations and for the CPD model. ....	97
Figure 4.20. CO, H <sub>2</sub> , CO <sub>2</sub> and H <sub>2</sub> O mole fraction distribution along the axial distance x = 0.51 m for consecutive iterations and for the CPD model. ....	97
Figure 4.21. CO, H <sub>2</sub> , CO <sub>2</sub> and H <sub>2</sub> O mole fraction distribution along the axial distance x = 0.81 m for consecutive iterations and for the CPD model. ....	98
Figure 4.22. CO, H <sub>2</sub> , CO <sub>2</sub> and H <sub>2</sub> O mole fraction distribution along the axial distance x = 1.12 m for consecutive iterations and for the CPD model [224]. .....	98
Figure 4.23. Seven radial traverses: x = 0.13 m, x = 0.20 m, x = 0.28 m, x = 0.34 m, x = 0.51 m, x = 0.81 m, x = 1.12 m. ....	99
Figure 4.24. Volatile yield of the Calenturitas coal for the SFOR, C2SM, CPD models (dry-ash-free), Wall temperature: 1473, 1673 K [224]. .....	100

Figure 4.25. Volatile yield of the Calenturitas coal for the SFOR, C2SM, CPD models (dry-ash-free), Wall temperature: 1073, 1173 K [224]. .....	101
Figure 4.26. Volatile yield of the Calenturitas coal for the wall temperature: 1073K. Left: FG-DVC and CPD models with the final volatile yield taken from FG-DVC. Right: CPD model with the final volatile yield taken from the experiment [224]......	102
Figure 4.27. Volatile yield of the Calenturitas coal as a function of time for the devolatilization-time-averaged heating rate and for the instantaneous heating rate. Wall temperatures: 1073K, 1173K, 1473K, 1673K [224]. .....	102
Figure 4.28. Particle temperature of the Calenturitas coal as a function of devolatilization time for different wall temperatures. ....	103
Figure 5.1. Sketch map of plug flow reactor [241]. .....	110
Figure 5.2. Sketch map of perfectly stirred reactor [241]. .....	111
Figure 5.3. MHI reactor geometry with mesh [87]. .....	113
Figure 5.4. Conoco-Philips E-gas reactor geometry with mesh [81,96]......	114
Figure 5.5. Temperature distribution and O <sub>2</sub> , CO and H <sub>2</sub> mole fraction distributions in PFR for each mechanism (Table 5.2) [241]. .....	117
Figure 5.6. CO <sub>2</sub> , H <sub>2</sub> O and C(s) mole fraction distributions in PFR for each mechanism (Table 5.2) [241]......	117
Figure 5.7. CO, H <sub>2</sub> , Temperature and CO <sub>2</sub> mole fraction distributions in PFR for GRI-Mech and CRECK [241]. .....	118
Figure 5.8. CO, H <sub>2</sub> , CO <sub>2</sub> , H <sub>2</sub> O and C(s) mole fraction distributions in PSR for global and detailed mechanisms [241]......	119
Figure 5.9. CO, H <sub>2</sub> , CO <sub>2</sub> and H <sub>2</sub> O mole fraction distributions along centerline for three gas-phase modeling approaches – BYU reactor [241]. .....	120
Figure 5.10. Map of radial traverses in BYU reactor. ....	121
Figure 5.11. CO, H <sub>2</sub> , CO <sub>2</sub> and H <sub>2</sub> O mole fraction distributions along axial distance x = 0.13 m for three gas-phase modeling approaches – BYU reactor [241]. .....	121
Figure 5.12. CO, H <sub>2</sub> , CO <sub>2</sub> and H <sub>2</sub> O mole fraction distributions along axial distance x = 0.20 m for three gas-phase modeling approaches – BYU reactor. ....	122
Figure 5.13. CO, H <sub>2</sub> , CO <sub>2</sub> and H <sub>2</sub> O mole fraction distributions along axial distance x = 0.28 m for three gas-phase modeling approaches – BYU reactor [241]. .....	122
Figure 5.14. CO, H <sub>2</sub> , CO <sub>2</sub> and H <sub>2</sub> O mole fraction distributions along axial distance x = 0.34 m for three gas-phase modeling approaches – BYU reactor. ....	123
Figure 5.15. CO, H <sub>2</sub> , CO <sub>2</sub> and H <sub>2</sub> O mole fraction distributions along axial distance x = 0.51 m for three gas-phase modeling approaches – BYU reactor. ....	123
Figure 5.16. CO, H <sub>2</sub> , CO <sub>2</sub> and H <sub>2</sub> O mole fraction distributions along axial distance x = 0.81 m for three gas-phase modeling approaches – BYU reactor. ....	124
Figure 5.17. CO, H <sub>2</sub> , CO <sub>2</sub> and H <sub>2</sub> O mole fraction distributions along axial distance x = 1.12 m for three gas-phase modeling approaches – BYU reactor [241]. .....	124
Figure 5.18. CO, H <sub>2</sub> , CO <sub>2</sub> and H <sub>2</sub> O mole fraction distributions along axial distance x = 1.73 m for three gas-phase modeling approaches – BYU reactor. ....	125
Figure 5.19. CO, H <sub>2</sub> , CO <sub>2</sub> and H <sub>2</sub> O mole fraction distributions along centerline for three gas-phase modeling approaches – MHI reactor [241]. .....	126

Figure 5.20. Temperature distribution along centerline for three gas-phase modeling approaches – MHI reactor [241].	127
Figure 5.21. CO, H <sub>2</sub> , CO <sub>2</sub> and H <sub>2</sub> O mole fraction distributions along centerline for three gas-phase modeling approaches – E-gas reactor [241].	128
Figure 5.22. Temperature distribution along centerline for three gas-phase modeling approaches – E-gas reactor [241].	128
Figure 5.23. BYU reactor and E-gas reactor outlet syngas composition [241].	130
Figure 6.1. Optimization procedure of char conversion models [245].	132
Figure 6.2. Reaction rates of CBK/E and kinetic-diffusion model with lit. parameters no. 1 [245].	135
Figure 6.3. Reaction rate of CBK/E and optimized kinetic-diffusion model [245].	136
Figure 6.4. Location of the coals in the van Krevelen diagram. The plot also reports coal database used for CBK/G validation [12].	137
Figure 6.5. Char conversion of the Illinois coal as a function of the residence time in a drop tube furnace. Gas temp - 1727K, Composition: 21% CO <sub>2</sub> , 79% N <sub>2</sub> [245].	137
Figure 6.6. Reaction rates of CBK/G and kinetic-diffusion model with literature-taken parameters [245].	138
Figure 6.7. Reaction rate of CBK/G and modified reaction rate of the kinetic-diffusion model [245].	139
Figure 6.8. Comparison of oxidation reaction rates for global model with literature parameters [245].	139
Figure 6.9. Comparison of gasification reaction rates for global model with literature parameters [245].	140
Figure 6.10. CO, H <sub>2</sub> , CO <sub>2</sub> and H <sub>2</sub> O mole fraction distribution along the centerline for five different sets of kinetic parameters [245].	140
Figure 6.11. Particle tracks of volatiles mass fraction for the optimized kinetic-diffusion model during devolatilization of 50 particles for 6 representative diameters a) 1 μm, b) 17 μm, c) mean - 36 μm, d) 51 μm, e) 77 μm, f) 85 μm [245].	142
Figure 6.12. Temperature distribution along the centerline for five different sets of kinetic parameters [245].	142
Figure 6.13. CO, H <sub>2</sub> , CO <sub>2</sub> and H <sub>2</sub> O mole fraction distribution along the radial traverse x=0.13m for five different sets of kinetic parameters [245].	144
Figure 6.14. CO, H <sub>2</sub> , CO <sub>2</sub> and H <sub>2</sub> O mole fraction distribution along the radial traverse x=0.20m for five different sets of kinetic parameters [245].	145
Figure 6.15. CO, H <sub>2</sub> , CO <sub>2</sub> and H <sub>2</sub> O mole fraction distribution along the radial traverse x=0.28m for five different sets of kinetic parameters [245].	146
Figure 6.16. CO, H <sub>2</sub> , CO <sub>2</sub> and H <sub>2</sub> O mole fraction distribution along the radial traverse x=0.34m for five different sets of kinetic parameters [245].	146
Figure 6.17. CO, H <sub>2</sub> , CO <sub>2</sub> and H <sub>2</sub> O mole fraction distribution along the radial traverse x=0.51m for five different sets of kinetic parameters [245].	147
Figure 6.18. CO, H <sub>2</sub> , CO <sub>2</sub> and H <sub>2</sub> O mole fraction distribution along the radial traverse x=0.81m for five different sets of kinetic parameters [245].	148
Figure 6.19. CO, H <sub>2</sub> , CO <sub>2</sub> and H <sub>2</sub> O mole fraction distribution along the radial traverse x=1.12m for five different sets of kinetic parameters [245].	148

Figure 6.20. CO, H <sub>2</sub> , CO <sub>2</sub> and H <sub>2</sub> O mole fraction distribution along the radial traverse x=1.73m for five different sets of kinetic parameters [245].	149
Figure 6.21. CFD results – contour plot of temperature with axial and radial distances [245].	149
Figure 6.22. Contours for the optimized kinetic parameters: a) temperature (K), b) CO mole fraction, c) H <sub>2</sub> mole fraction, d) CO <sub>2</sub> mole fraction [245].	149
Figure 6.23. Contours for the optimized kinetic parameters: a) H <sub>2</sub> O mole fraction, b) O <sub>2</sub> mole fraction, c) devolatilization rate (kmol/m <sup>3</sup> s) [245].	150
Figure 6.24. CO, H <sub>2</sub> , CO <sub>2</sub> and H <sub>2</sub> O mole fraction distribution along the centerline for modified kinetic parameters for global approach with F-R/EDM and for GRI-Mech with EDC.	151
Figure 6.25. CO, H <sub>2</sub> , CO <sub>2</sub> and H <sub>2</sub> O mole fraction distribution along the radial traverse x=0.13m for modified kinetic parameters for global approach with F-R/EDM and for GRI-Mech with EDC.	152
Figure 6.26. CO, H <sub>2</sub> , CO <sub>2</sub> and H <sub>2</sub> O mole fraction distribution along the radial traverse x=0.20m for modified kinetic parameters for global approach with F-R/EDM and for GRI-Mech with EDC.	152
Figure 6.27. CO, H <sub>2</sub> , CO <sub>2</sub> and H <sub>2</sub> O mole fraction distribution along the radial traverse x=0.28m for modified kinetic parameters for global approach with F-R/EDM and for GRI-Mech with EDC.	153
Figure 6.28. CO, H <sub>2</sub> , CO <sub>2</sub> and H <sub>2</sub> O mole fraction distribution along the radial traverse x=0.34m for modified kinetic parameters for global approach with F-R/EDM and for GRI-Mech with EDC.	153
Figure 6.29. CO, H <sub>2</sub> , CO <sub>2</sub> and H <sub>2</sub> O mole fraction distribution along the radial traverse x=0.51m for modified kinetic parameters for global approach with F-R/EDM and for GRI-Mech with EDC.	154
Figure 6.30. CO, H <sub>2</sub> , CO <sub>2</sub> and H <sub>2</sub> O mole fraction distribution along the radial traverse x=0.81m for modified kinetic parameters for global approach with F-R/EDM and for GRI-Mech with EDC.	154
Figure 6.31. CO, H <sub>2</sub> , CO <sub>2</sub> and H <sub>2</sub> O mole fraction distribution along the radial traverse x=1.12m for modified kinetic parameters for global approach with F-R/EDM and for GRI-Mech with EDC.	155
Figure 6.32. Contours for the optimized kinetic parameters for GRI-Mech with EDC: a) temperature (K), b) CO mole fraction, c) H <sub>2</sub> mole fraction, d) CO <sub>2</sub> mole fraction.	156

## List of tables

Table 1.1. Main characteristics of gasification reactors.....	9
Table 2.1. List of the mostly studied entrained flow reactors [31]. .....	21
Table 2.2. Devolatilization kinetic parameters for global models with reactor numbers from Table 2.1 [31]. .....	22
Table 2.3. Westbrook and Dryer global mechanism kinetic data (units in cm, s, cal, kmol) [106][137]. .....	26
Table 2.4. Jones and Lindstedt global mechanism kinetic data (units in cm, s, cal, kmol) [105]. .....	27
Table 2.5. Mechanism based on water-gas shift equilibrium.....	28
Table 2.6. Mechanism based on the work of Glassman et al. [139]. .....	28
Table 2.7. WGS reaction rate parameters used in [142]. .....	29
Table 2.8. CFD simulated syngas composition for two reaction rates reported in literature [142]. .....	30
Table 2.9. CFD simulated syngas composition using two calibrated reaction rates [142]. .....	30
Table 2.10. Gas-phase reactions with kinetic parameters [31]. .....	35
Table 2.11. Tar reactions with kinetic parameters [31]. .....	37
Table 2.12. Benfell's shape representation system [83,180,184]. .....	50
Table 2.13. Calculation of Thiele modulus and effectiveness factor based on char morphology [83,180]. .....	51
Table 2.14. Char conversion kinetic parameters for global models [31]. .....	59
Table 4.1. Coefficients of determination [224]. .....	86
Table 4.2. Coal analysis [133,210] and FG-DVC output data for two examined coals [224].	88
Table 4.3. Kinetic parameters for gas-phase and surface reactions [224]. .....	90
Table 4.4. Boundary conditions for the BYU reactor [210]. .....	91
Table 4.5. Boundary conditions for the LGRE gasifier [133]. .....	92
Table 4.6. Error analysis of volatile yield for wall temperature of 1073K, 1173K, 1473K and 1673K – Devolatilization in an inert atmosphere – C2SM (Figure 4.24,Figure 4.25). .....	104
Table 4.7. Error analysis of volatile yield for wall temperature of 1073K, 1173K, 1473K and 1673K – Devolatilization in an inert atmosphere – SFOR (Figure 4.24,Figure 4.25). .....	104
Table 4.8. Error analysis of CO, H <sub>2</sub> , CO <sub>2</sub> and H <sub>2</sub> O concentration along the centerline of the BYU reactor – gasification (Figure 4.13). .....	104
Table 4.9. Error analysis of CO, H <sub>2</sub> , CO <sub>2</sub> and H <sub>2</sub> O concentration along radial traverse x=0.13 of the BYU reactor – gasification (Figure 4.16). .....	105
Table 4.10. Error analysis of CO, H <sub>2</sub> , CO <sub>2</sub> and H <sub>2</sub> O concentration along radial traverse x=0.28 of the BYU reactor – gasification (Figure 4.18). .....	105
Table 4.11. Error analysis of CO, H <sub>2</sub> , CO <sub>2</sub> and H <sub>2</sub> O concentration along radial traverse x=1.12 of the BYU reactor – gasification (Figure 4.22). .....	105
Table 4.12. Error analysis of volatile yield for wall temperature of 1073K – Devolatilization in an inert atmosphere – CPD and FG-DVC (Figure 4.26). .....	105

Table 4.13. Error analysis of volatile yield for wall temperature of 1073K, 1173K, 1473K, 1673K – Devolatilization in an inert atmosphere – the constant heating rate and the instantaneous heating rate (Figure 4.27). .....	106
Table 5.1. Summary of applied models [241]. .....	108
Table 5.2. Investigated global reaction mechanisms [241]. .....	109
Table 5.3. Input parameters for PFR [241]. .....	110
Table 5.4. Input parameters for PSR [241]. .....	111
Table 5.5. Proximate and ultimate analyses of coals for three reactors. ....	114
Table 5.6. Mass flow rates of coal and gas with molar composition for BYU reactor. ....	114
Table 5.7. Mass flow rates of coal and gas for MHI reactor. ....	115
Table 5.8. Mass flow rates of coal and oxidant for E-gas reactor. ....	115
Table 5.9. Kinetic parameters for surface reactions and gas-phase reactions (global reaction approach). .....	115
Table 5.10. Kinetic parameters of WGS reaction [241]. .....	129
Table 6.1. Summary of applied models [245]. .....	134
Table 6.2. Surface reactions kinetic parameters [245]. .....	134
Table 6.3. Char conversion degree for surface reaction model with different kinetic parameters [245]. .....	143
Table 6.4. Error analysis of CO, H <sub>2</sub> , CO <sub>2</sub> and H <sub>2</sub> O concentration along the centerline - Figure 6.10 [245]. .....	143
Table 6.5. Char conversion degree for optimized char conversion parameters for GRI-Mech with EDC and for global approach with F-R/EDM. ....	157

# 1. Introduction

## 1.1 Coal gasification and its applications

Gasification is considered to be a high-potential technology, considering, especially, the application of its main product - syngas. The general relationship between gasification and this application is presented in Figure 1.1.

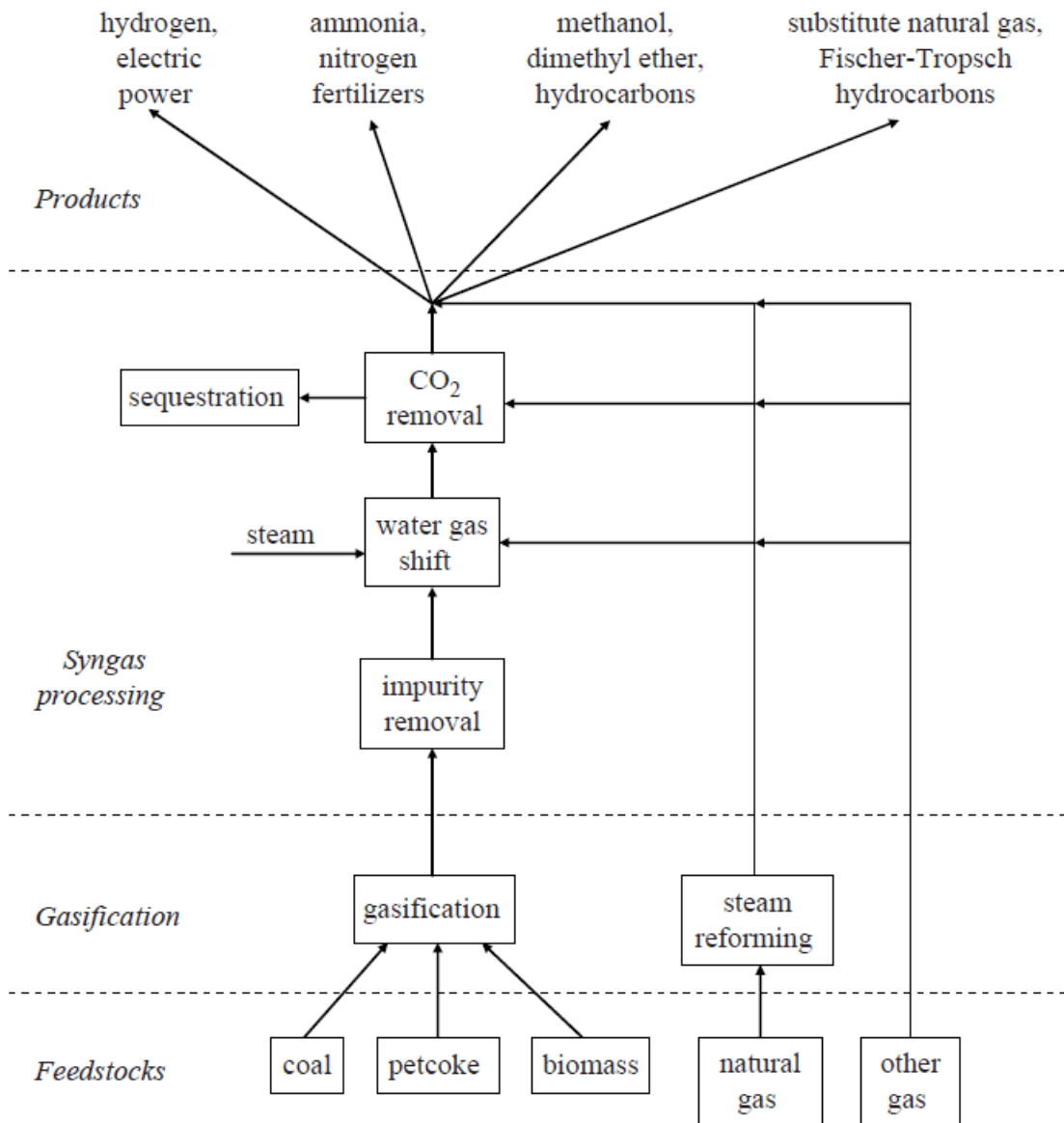


Figure 1.1. Gasification and related technologies [13].

Syngas is generally obtained either through gasification or through steam reforming of natural gas. As regards gasification, it begins with a proper feedstock, such as coal or biomass. In the current dissertation, the main focus will be laid on coal. Syngas which is primarily a mixture of CO and H<sub>2</sub> can be further used, for instance, in hydrogen production for electric

power, where hydrogen can be burned in a gas turbine. This results in the production of electric power from coal with minimal greenhouse emissions. Hydrogen is also a potential transportation fuel. The most common approach is to produce electric power from hydrogen in a fuel cell and use that power in an electric motor afterward. The main obstacle regards hydrogen storage. Syngas can be also utilized in ammonia production for e.g. nitrogen fertilizers which are, by far, the largest volume synthetic nitrogen chemicals. It can also be utilized in Fischer-Tropsch synthesis for e.g. synthetic natural gas production or in methanol production. Methanol is a significant commodity chemical obtained from syngas. It is also an intermediate used to make a wide range of products, such as dimethyl ether (DME). DME can be applied as a fuel or converted to hydrocarbons, including gasoline or olefins for polymer production.

There are two major aspects that induce current interest in coal gasification. The first one concerns the belief that conventional petroleum supplies are diminishing, while the demand for transportation fuels continuously rises. The second aspect regards global warming. Gasification offers a relatively cost-effective means of utilizing coal while minimizing greenhouse gas emissions [13].

## **1.2 Energy background**

Easy access to energy is a key pillar for economic development, human well-being, and poverty reduction. In 2015, 80% of the world's energy came from fossil fuel sources [14]. Coal is one of the main sources of fossil fuel energy. From 1990 to 2018, China increased its consumption from 1 billion tons to 4.64 billion tons [15]. In 2018, coal accounted for 60% percent of China's energy use and 23% of the U.S energy use. Overall, it made up 27% of all energy used worldwide and accounted for 38% of electricity generation [16]. Figure 1.2 depicts the increasing trend of global energy consumption up to 2040. Despite the invigorated push to renewable sources of energy by all major countries in recent years as their developing and exploitation would enhance the world's energy security, conserve the reserves of fossil fuels for future generations and, most importantly, reduce pollution, coal will nevertheless continue to be a meaningful energy source in the 21<sup>st</sup> century. However, traditional methods of coal utilization have been firmly criticized for their low efficiency and high-pollution tendencies. Coal raises special concerns because it leaves the largest environmental footprint due to the fact that it releases more CO<sub>2</sub> per unit of energy than any other energy source. Coal-fired power plants were the single largest contributor to the growth in emissions observed in 2018 [17]. As a result, coal-fired electricity generation made up 30% of global CO<sub>2</sub> emissions [17]. Figure 1.3 presents the forecast of CO<sub>2</sub> emissions worldwide up to 2050. One may also observe an increasing trend in emissions. It is obvious that specific measures have to be taken in order to mitigate global warming due to CO<sub>2</sub> emissions through the development of environmentally benign technologies.



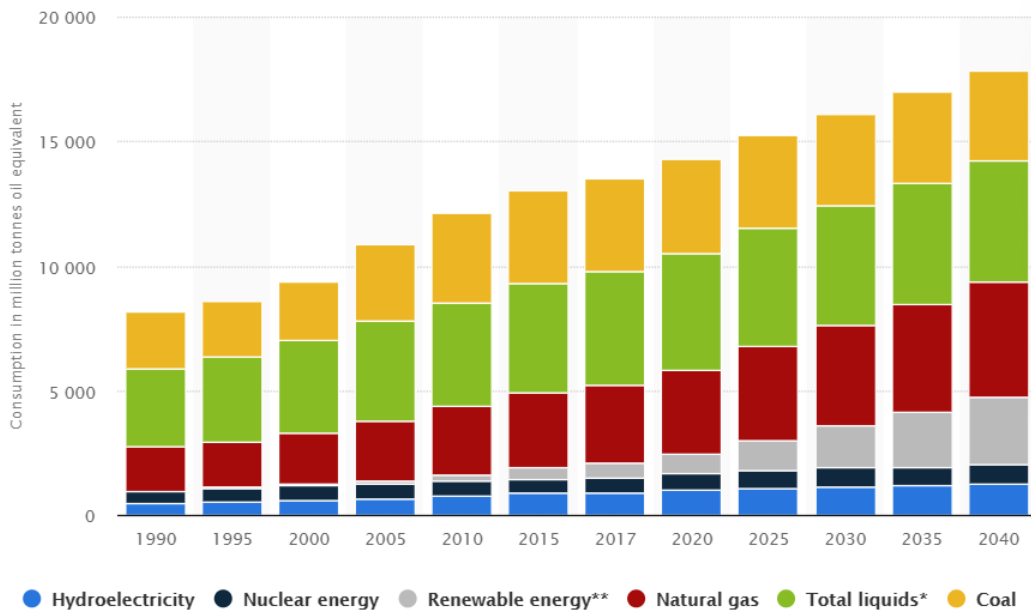


Figure 1.2. Projected global energy consumption from 1990 to 2040 by energy source [18].

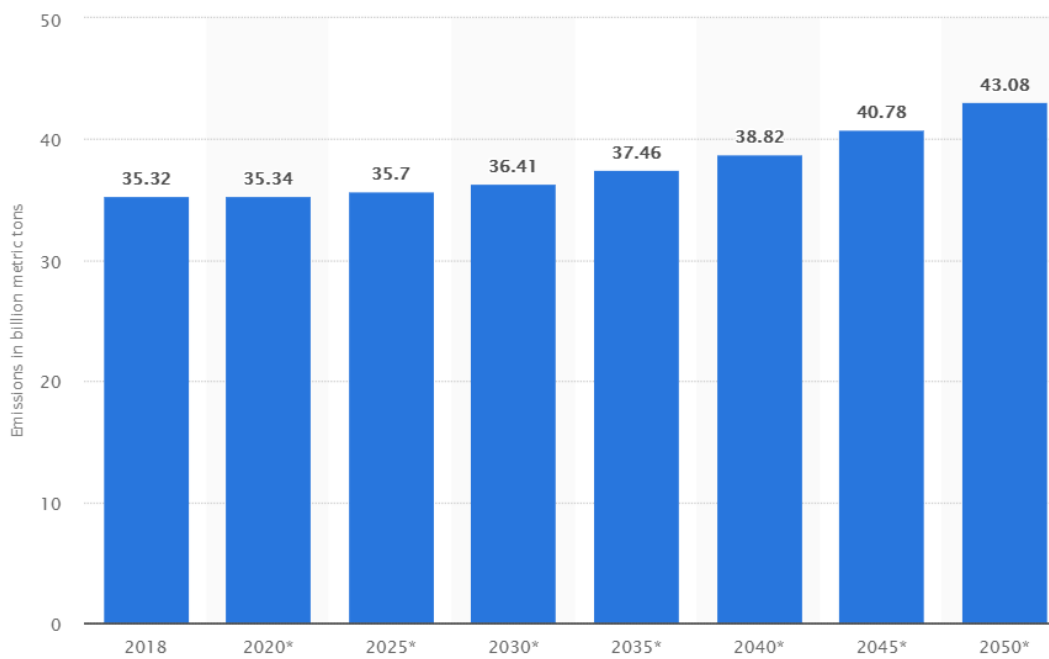


Figure 1.3. Forecast of CO<sub>2</sub> emissions worldwide from 2018 to 2050 [19].

### 1.3 Methods for CO<sub>2</sub> mitigation from coal-fired plants

As it was mentioned, coal-fired power plants have the greatest impact on the worldwide emissions of CO<sub>2</sub>. There are several ways of tackling the emission problems.

- Improving the efficiency of coal-fired power plants
- Employing carbon capture and sequestration methods

By improving the efficiency of existing power plants, one has to design the operation of such a plant at higher temperatures and pressures in order to obtain supercritical (SC) parameters or ultra-supercritical (USC) parameters. The increase in efficiency arises from a higher amount of electricity obtained with the same CO<sub>2</sub> emission. However, the operating parameters are restricted by the availability of proper materials capable of withstanding them. Currently, the most efficient USC technology in the world allows delivering efficiency up to 47.5% with the operating parameters of 27.5 MPa and 893K, considerably higher than the global average efficiency of 34% [20].

Carbon capture and storage (CCS) is a technology that can capture up to 90% of CO<sub>2</sub> emissions produced in power plants or industrial processes [21]. CCS comprises three key stages: capturing CO<sub>2</sub>, transporting CO<sub>2</sub>, and storing CO<sub>2</sub> underground in deep saline aquifer formations or in depleted oil and gas fields. Transportation is usually by pipelines or by ships. Millions of tons of CO<sub>2</sub> is transported annually by road tankers, pipelines, and ships. Storage takes place in a scrupulously selected geological rock formations that is usually located several kilometers below the surface. Carbon capture methods allow CO<sub>2</sub> separation from the gases produced during the process. They can be categorized in the following way:

- Post-combustion capture: CO<sub>2</sub> can be captured from the flue gas of a combustion process by absorbing it into a specific solvent. In the next step, CO<sub>2</sub> is liberated from the solvent and compressed for transportation and storage.
- Oxy-fuel combustion capture: In this method, oxygen is separated from the air prior to combustion. This oxygen-rich and nitrogen-free environment result in the flue gas consisting mainly of CO<sub>2</sub> and H<sub>2</sub>O. This ensures a more simple way of extracting the CO<sub>2</sub> from the flue gas.
- Pre-combustion capture: In this method, coal is not combusted completely within the reactor, but it is converted into a mixture of CO<sub>2</sub> and H<sub>2</sub> through one of such processes as reforming or gasification.

Integrated gasification combined cycle (IGCC) with carbon capture and sequestration is an attractive application of pre-combustion capture method. It employs gasification to generate electric power from coal with minimal greenhouse gas emissions. It has more environmental advantages over conventional subcritical pulverized combustion (PC) plants because of higher plant efficiency and higher control efficiencies for environmental emissions. For instance, for an IGCC plant with CO<sub>2</sub> capture, the emissions of NO<sub>x</sub>, particulate matter (PM), and mercury were about 70%, 55%, 50%, respectively, of the corresponding emissions from a supercritical pulverized combustion plant on the energy basis [22]. In comparison with combustion, gasification operates at higher pressure, which makes the syngas volume much smaller than the flue gas. On this basis, pollutants are more concentrated in the flow of syngas and can be more easily and efficiently removed. A typical IGCC plant consists of the following components:

- an oxygen plant: it is a plant where oxygen is separated from the air. Current technologies apply cryogenic air separation methods or membrane-based plants. In the case of an oxygen-blown reactor, air separation unit carries both oxygen and nitrogen to the gas turbine for NO<sub>x</sub> control. Some power plants incorporate air instead of oxygen

as the gasification medium. Unfortunately, air-based plants are less amenable to high levels of CO<sub>2</sub> capture than oxygen-based plants.

- a gasification plant: a conversion of carbon-based fuels into synthesis gas (syngas) takes place.
- a syngas gas clean-up system. Before entering the gas turbine syngas undergoes a cleaning process where particulate matter, ammonia, chlorides, and other gases containing e.g. sulfur are removed.
- a combined cycle power plant. The gasifier feeds syngas to the combustion chamber in the gas turbine system where it is burnt. The combustion process produces a hot gas product that expands and propels the gas turbine and the generator producing electrical power. Sensible heat from the exhaust gas and from syngas coolers is further used in a steam cycle in the Heat Recovery Steam Generator (HRSG). Produced steam propels the steam turbine and the generator producing electricity – Figure 1.4.

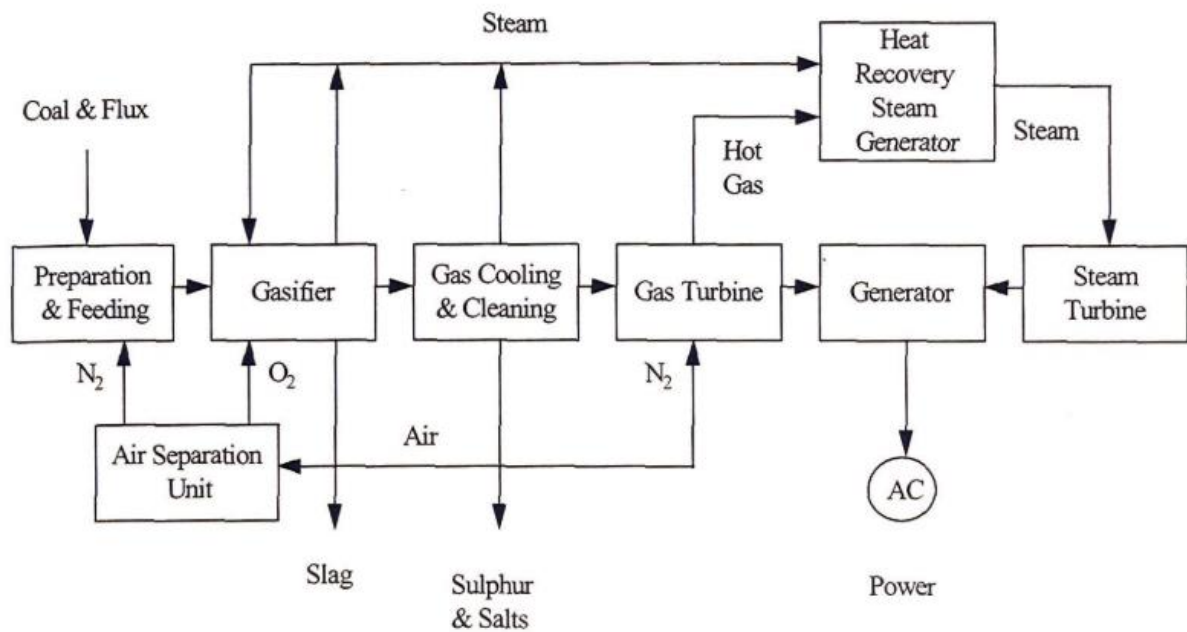


Figure 1.4. IGCC block flow diagram [28].

Based on the given overview related to the current and future world's energy consumption data and the contribution of particular energy sources, keeping in mind that coal will continue to be a key energy source and its entire exclusion is impossible, it is crucial to implement efficient and environmentally benign coal-based technologies. Coal gasification, considering its huge potential in the combustible gas product which can be utilized in many branches of industry and in electricity production (e.g., in internal combustion engines, fuel cells, and gas turbines) with efficient CCS capabilities, or that it can be converted into other chemical products of commercial interest, it will be the main focus of the present dissertation and will be further discussed in detail.

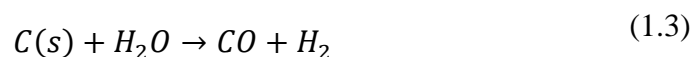
## 1.4 Coal gasification

Gasification can be described as the thermochemical conversion of a carbon-based solid fuel within different mediums, such as air, O<sub>2</sub>, H<sub>2</sub>O, CO<sub>2</sub>, and H<sub>2</sub>. It is a process consisting of many overlapping reactions in the gas and solid phases which depend on the process parameters, such as temperature, pressure, or fuel properties. The final product is a synthesis gas which consists mostly of CO and H<sub>2</sub>. It is an efficient method of raising the quality and value of the fuel. Gasification has the following key stages:

- **Drying:** moisture is released from the fuel and vaporized. In general, it is a complex, pressure-dependent [23] and multiphase process that combines three coexisting phases: liquid water, vapor, and the porous solid, through which water and vapor move to the surface.
- **Devolatilization:** it is the thermal decomposition of the organic material in an oxygen-deprived environment at elevated temperatures (600-900K) [24,25]. Light gases and tars evolve from the particle surfaces as jets or bubbles. Volatiles are also likely to be reinstated to the solid phase – polymerization. This phenomenon is usually accounted for by means of secondary reactions. During devolatilization, particles are heated at a rate of approximately 10<sup>4</sup> to 10<sup>5</sup> K/s up to 1700K [24]. Their shape and size are not maintained as it swells and possibly fragments. The operating pressure has also a substantial effect on the rate of release of volatiles. The acting forces hinder the transport of matter out of the particle. Devolatilization rates are the highest in entrained flow reactors due to very high operating temperatures, ultra-fine pulverization and the extremely turbulent flow. In the literature, the term “devolatilization” is often used interchangeably with “pyrolysis”. However, to be precise, pyrolysis means devolatilization in an inert atmosphere [26].
- **Partial oxidation:** the volatile products and some of the char react in an exothermic reaction with O<sub>2</sub> to form CO<sub>2</sub>, H<sub>2</sub>O, and CO, thus providing heat for the endothermic gasification reactions – an autothermal process. The amount of oxidant that should be provided to support the gasification process ranges from 25 to 40 percent. Among the gas-phase reactions, the water-gas shift reaction contributes to the balance between major gas species CO and H<sub>2</sub> – Eq. (1.1).



- **Gasification/reduction:** the remaining char (carbonized residue) reacts with CO<sub>2</sub>, H<sub>2</sub>O to produce a gas that contains mainly CO, H<sub>2</sub> - Eq. (1.2), and Eq. (1.3). Gasification reactions are strictly endothermic.



The great interest in this process can be easily explained by looking at its thermodynamics. During the incomplete oxidation of carbon to CO, only 28% of the coal's heating value is released as thermal energy. Therefore, the major part remains as chemically bonded energy in the gas phase. If the released heat from the partial oxidation could be applied

to supply endothermic reactions – Eqs. (1.2), (1.3), then 73-89% of coal’s heating value could be conserved in the gas phase [27].

In general, gasification is not a new technology because it was already used in the past in Europe and the USA to produce “town gas” for cooking and lighting. However, its usage was substantially diminished when natural gas and oil appeared. Gasification was also applied for the production of liquid fuels during world wars when there was a lack of petroleum. The last twenty years have seen the start of a renaissance of gasification technology. Electricity generation has emerged as a large new market for the development of gasification because of enhancing the environmental acceptability of coal but also of increasing the overall efficiency of the conversion into electricity.

## 1.5 Types of gasifiers

Although there are many types of gasifiers, different in operating characteristics and design, there are three main types into which most of the commercially available reactors fall:

- Fixed-bed gasifiers (also known as moving-bed reactors)
- Fluidized-bed gasifiers
- Entrained-flow gasifiers

Fixed-bed reactors are fed with fuel in the form of large coal particles. It can be provided at the top of the refractory-lined reactor and moves slowly toward the bottom. The gasification agent (air/oxygen, steam) is introduced at the bottom and moves upward counter-currently (an updraft reactor) –Figure 1.5.

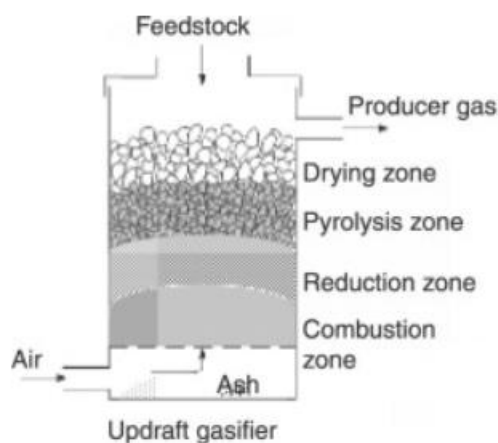


Figure 1.5. Updraft fixed-bed reactor [29].

Reactions that take place within the reactor occur in different areas. In the “drying” area coal is heated and dried. At the same time, the product gas is cooled before it leaves the gasifier. In the next step, coal is further heated and devolatilized as it enters the “carbonization” area. In the “gasification” zone, the devolatilized coal undergoes gasification reactions with  $H_2O$  and  $CO_2$ . Near the bottom of the reactor, there is a “combustion” zone with the highest temperatures where oxygen/air reacts with the remaining carbonized residue. The updraft reactor can handle feedstocks with a more diverse inner composition. Moreover, they have high energy efficiency

and there is no need for additional cooling before cleaning the gas. However, the produced syngas is rich in tars. As opposed to updraft reactors, downdraft gasifiers or co-current gasifiers - Figure 1.6 are the most common type of reactors. The oxidant is passed downwards and the syngas leaves from the bottom of the gasifier. With respect to the updraft reactor, in the downdraft gasifier, the reduction zone is below the combustion zone. The main advantage of this design is low tar content in the produced gas. The position of the combustion zone is thus a key factor in the design of fixed-bed reactors.

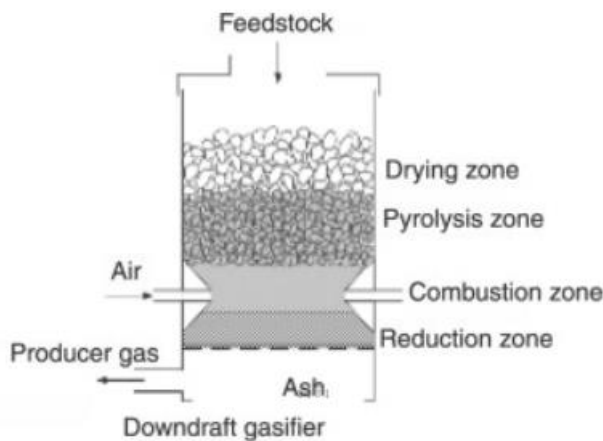


Figure 1.6. Downdraft fixed-bed reactor [29].

Fluidized-bed reactors –Figure 1.7 suspend fuel particles in an oxygen-rich environment so the resulting bed within the reactor acts as a fluid. To ensure a constant fluidization/suspension, small coal particles (<6 mm) are usually used. Coal is provided at the side of the reactor, while oxidant and steam are provided near the reactor bottom with such velocity that enables to fully suspend/fluidize the bed of the reactor. The constant mixing allows maintaining a constant temperature inside the reactor. The moderate operating temperatures allow to achieve an acceptable carbon conversion (90-95%) and to decompose most of the tars and other high-molecular-weight hydrocarbons. The operating reactor temperature is lower than the ash fusion temperature which avoids clinker formation or the de-fluidization of the reactor bed. It signifies that these reactors are best suited for low-rank coals and biomass.

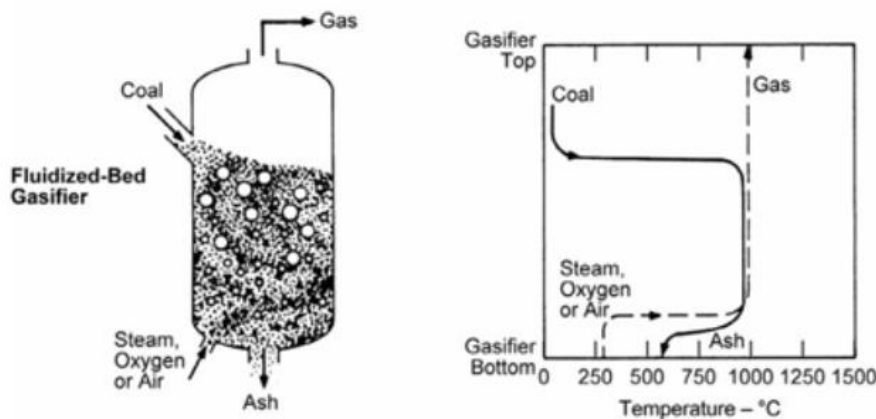


Figure 1.7. Fluidized-bed reactor [30].

Entrained-flow reactors –Figure 1.8 are fed with finely pulverized coal, oxidant, and or steam co-currently. This ensures an oxidant and steam surrounding which entrains fine coal particles as they flow through the reactor. These reactors operate at high and uniform temperatures and extremely turbulent flow. Very high conversion rates are achieved (98-99.5%). At such high temperatures, tars and other liquids produced during the process are easily decomposed to CO, H<sub>2</sub>, and other light hydrocarbons e.g. CH<sub>4</sub>. Entrained-flow gasifiers are capable of handling practically any coal feedstock and produce a clean, tar-free gas. It is achieved with the penalty of high O<sub>2</sub> consumption. This reactor is considered to be an environmentally most benign design [30]. The produced syngas contains mostly CO, H<sub>2</sub>, CO<sub>2</sub> with trace amounts of other contaminants that can be easily removed downstream of the gasifier.

Table 1.1. Main characteristics of gasification reactors.

Gasifier design	Feed size (mm)	Temperature (°C)	Residence time (s)	Ash character	Ash fusion temperature	Carbon conversion
Fixed bed	5-80	600-1400	high	dry ash or slagging	low or high	high
Fluidized bed	<6	850-1100	medium	agglomerating or dry ash	high	moderate
Entrained-flow	<0.1	>1300	low	slagging	low	high

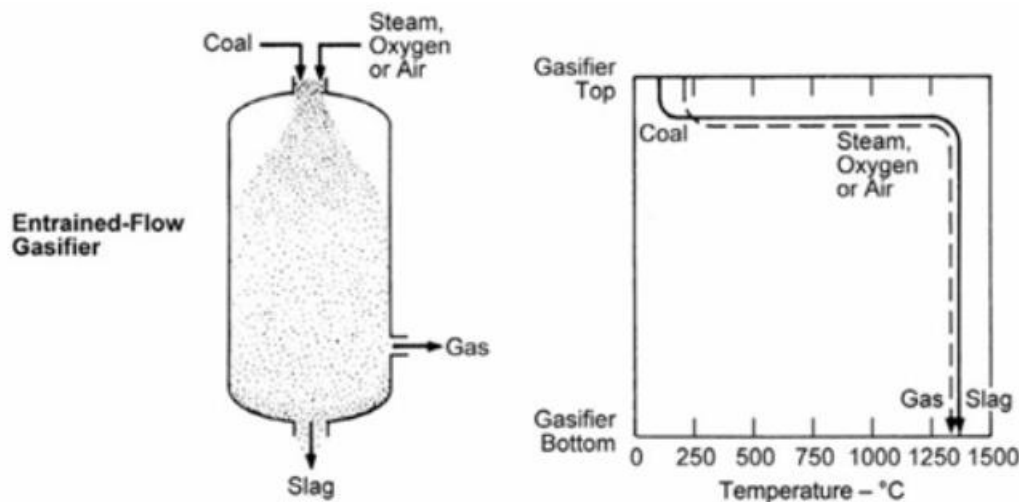


Figure 1.8. Entrained-flow reactors [30].

Table 1.1 presents the summary of the operating parameters of the three reactors. With respect to the fixed-bed reactor and a fluidized bed reactor, an entrained-flow gasifier has relatively the highest requirements for stable and efficient operation. However, the resulting benefits and the lowest environmental impact make it nowadays the most widely used reactor, especially in IGCC. On this basis, it has been decided that entrained flow reactors will be the main focus of this dissertation.

## 1.6 Computational fluid dynamics (CFD) - introduction

CFD is a branch of fluid mechanics that incorporates data structures and numerical analysis to investigate and solve issues related to fluid flows in accordance with its physical, chemical, and thermal properties. To virtually generate an accurate solution for a particular phenomenon, all fluid flow properties have to be considered simultaneously. A mathematical model can vary depending on the content of the problem such as heat transfer, mass transfer, phase change, chemical reaction, the influence of electromagnetism, acoustics, etc. CFD tool is considered to be a key element in generating sustainable product development. It gives an insight into flow patterns that are difficult, expensive, or impossible to investigate using traditional (experimental methods). Of course, one may not replace experiments completely with a CFD analysis, but the overall cost and the level of experimentation can be substantially reduced. On top of that, one has to keep in mind that the results of the CFD simulation are not 100% reliable. The input data may involve too much guessing or imprecision. The utilized mathematical model may be inadequate for the given phenomena. The reliability is far greater for laminar, single-phase flows, and chemically inert systems than for turbulent, multi-phase and chemically reactive flows. Simplifying assumptions are often made in order to make the problem tractable (e.g., steady-state, incompressible, inviscid, 2-D). Moreover, the obtained results can be too much dependent on the available computing power. Nevertheless, the potential and application of CFD are overwhelming. It is applied to a wide range of research and engineering problems in many fields, including aerodynamics, weather simulation, environmental engineering, industrial system design, fluid flows, combustion analysis. The methodology in CFD modeling is practically universal:

- Pre-processing:
  - The geometry and physical bounds are defined.
  - The volume occupied by the fluid is divided into the finite number of cells - discretization. The obtained mesh can be structured or unstructured containing tetrahedral, hexahedral, prismatic, polyhedral, or pyramidal elements.
  - The physical model is defined: (equations of fluid motion, enthalpy, radiation, species conservation). The physics of any fluid motion is governed by three fundamental principles. Mass balance equation, Newton's second law of dynamics and energy balance equation. Since Newton's law of dynamics is expressed in three spatial coordinates (x, y, z) there are overall five governing differential equations which are known as the Navier-Stokes equations. They will be discussed in detail in Chapter 3.
  - Boundary conditions are set. In the case of transient problems, the initial conditions are also specified.
- Processing:
  - The simulation is started and the specified equations are solved in an iterative way in a steady-state or transient mode.
- Post-processing:
  - Post-processor is utilized to analyze and visualize the obtained results. They can be reviewed in two ways: graphically or alphanumerically. Vector plots,



contours, iso-surfaces, flowlines, or animations are a graphical visualization. Integral values, drag, lift, torque calculations, minima, maxima, averages, comparison with experimental data are an alphanumeric visualization.

Important variables in CFD:

Pressure and fluid velocities are always calculated in conjunction. Pressure can be utilized to calculate forces on objects, e.g. for the prediction of drag on a vehicle. Velocities can be visualized to show structures of the flow. Based on the flow field, one may derive other variables, such as vorticity and shear. Shear stresses may be related to erosion of surfaces. Vorticity describes the rotation of fluid elements. In mixing processes, the deformation of fluid elements is of key importance. In the case of turbulent flows, eddy dissipation rate and turbulent kinetic energy are vital for such processes as mass transfer or heat transfer in boundary layers. As regards the non-isothermal flows, the temperature field is of crucial importance. It governs evaporation, combustion, and other processes.

Based on the given overview regarding CFD, its overwhelming potential, and predictive capabilities, it has been decided that CFD will be the main tool to investigate entrained flow coal gasification in the current dissertation.

## **2. Literature review on CFD modeling of entrained flow coal gasification**

### **2.1 Introduction – aims and objectives of Thesis**

The aspects covered in this thesis are directly related to the aims and objectives of the project Preludium 15 (2018/29/N/ST8/00799), financed by the Polish National Science Center, which I am the manager of.

The aim of this literature review, which is based on the article of Mularski et al. [31], is:

[31] Mularski J, Pawlak-Kruczek H, Modlinski N. A review of recent studies of the CFD modelling of coal gasification in entrained flow gasifiers, covering devolatilization, gas-phase reactions, surface reactions, models and kinetics. *Fuel* 2020;271:1–36. <https://doi.org/10.1016/j.fuel.2020.117620>. *MNiSW (2019-2021): 140 pts, IF (2019): 5.578*

- to thoroughly discuss the most widely applied modeling techniques for devolatilization, gas phase, and char conversion which are the most important sub-phenomena in entrained flow coal gasification,
- to summarize the most widely applied kinetic parameters for devolatilization, gas phase, and char conversion,
- to clarify the benefits and drawbacks related to the applied modeling techniques for these three stages,
- to indicate which aspects require further investigation.

The main objective of the current dissertation is:

- to investigate the most commonly used modeling approaches of devolatilization, gas phase, and char conversion and to propose optimization techniques that will allow obtaining unique kinetic parameters valid only for the examined conditions and which will improve the accuracy of CFD simulations.

## 2.2 Devolatilization

Since coal devolatilization is one of the most crucial processes in gasification, an accurate description of it is very important. Flame ignition, its structure, lift-off, and stabilization are substantially associated with the rate of volatile matter release from coal to the gas phase and the final volatile yield. The process has already been studied [32] and many models have been developed. Several detailed reviews (1982-1994) of the models are available [5,33–36]. This chapter considers only the most widely used recent approaches, which were applied by researchers since the year 2000. Both global models and detailed mechanisms are briefly summarized in sub-chapters 2.2.1 and 2.2.2, respectively. Their performance in entrained flow coal gasification is discussed in sub-chapter 2.2.3.

### 2.2.1 Global approaches

Global devolatilization kinetic mechanisms can be divided into three main types: one-step models, two-step models, and distributed activation energy models. The number of steps is related to the number of pathways that the reaction can follow.

The empirical devolatilization models most widely used are: the single-step first-order reaction model (SFOR), already studied over the years [37–40], the competing two-step (C2SM) model [39], also expressed as the Kobayashi model, and the distributed activation energy (DAEM) model [41]. Despite the fact that there are various modifications of SFOR, C2SM, and DAEM [6,42–49], which increase the reliability of these approaches, but also their complexity, most of the authors actually apply the basic models.

SFOR is a single-step first-order reaction equation that calculates the devolatilization rate as follows:

$$\frac{dV}{dt} = A \cdot \exp\left(-\frac{E}{RT}\right) (V_{\infty} - V) \quad (2.1)$$

where:

- $V_{\infty}$  and  $V$  are the final and instantaneous volatile yield, respectively
- $A$  - the pre-exponential factor (the unit depends on the reaction order)
- $E$  - activation energy (J/mol)
- $R$  - the universal gas constant (J/mol/K)
- $T$  - temperature (K).

Yamamoto et al. (2011) [46] presented a modified one-step kinetic mechanism that increases the capabilities of the basic SFOR model. The modification is based on the additional parameter for the pre-exponential factor in the rate law.

$$\frac{d(C)}{dt} = -F \cdot A \cdot \exp\left(-\frac{E}{RT}\right) \cdot C \quad (2.2)$$

where:

C – unreacted coal

F- a modification factor which depends on the extent of the devolatilization process.

$$F = \exp\left(\sum_{i=0}^5 c_i [X_{coal}]^i\right) \quad (2.3)$$

where:

$c_i$  stands for the polynomial fitting coefficients tuned to match the results obtained from the experiment or from the complex model.

$X_{coal}$  - the overall conversion of the unreacted coal defined as  $X_{coal} = 1 - C$ .

If high accuracy is required, the number of matching coefficients  $c_i$  can be increased.

Biagini and Tognotti (2014) [47] proposed a different modified one-step kinetic approach. It was validated against a database for 20 coals. The modification was based on the correlation of the final volatile yield with temperature.

$$V_{\infty} = 1 - \exp\left(-DI \cdot \frac{T}{T_{st}}\right) \quad (2.4)$$

where:

DI – a coal specific index

$T_{st}$  - the reference temperature (K).

Tremel and Spliethoff (2013) [50] proposed a final volatile yield relation dependent on temperature and pressure, assuming that there is a linear decrease in volatiles concentration within the solid fuel with regard to temperature.

$$V_{\infty} = \theta \cdot P \cdot Y_{V,P_{set},T_{set}} \quad (2.5)$$

where:

$$\theta = \frac{1}{Y_{V,T_{set}}} \left( Y_{v,T_{set}} + (Y_{v,T_{max}} - Y_{v,T_{set}}) \cdot (1 - \exp(-\vartheta(T - T_{set}))) \right) \quad (2.6)$$

$$P = \frac{1}{Y_{v,p_{set}}} Y_{v,p_{set}} \left( \frac{p}{p_{set}} \right) \cdot \frac{1}{\rho} \quad (2.7)$$

$Y_{V,T_{set},P_{set}}$  – the volatile yield at the reference temperature and pressure

$Y_{v,T_{max}}$  – the max. temperature at which the max. volatile yield is achieved

$\vartheta, \rho$  – parameters yielded by the least squares fitting procedure.

Schroeder (2016) [48] proposed a modification to the Biagini and Tognotti (2014) [47] one-step model, which incorporates sequential distributed activation energy, to obtain correct volatile yields at different heating rates and temperatures.

$$\frac{dV}{dt} = A \cdot \exp\left(-\frac{E_0 - \sigma_a Z}{RT}\right) (V_\infty - V) \quad (2.8)$$

$$V_\infty = \frac{a}{2} \left( 1 - \tanh\left( (b + c \cdot a) \frac{T_{ignite} - T}{T} + (d + e \cdot a) \right) \right) \quad (2.9)$$

where:

a, b, c, d, e and  $T_{ignite}$  represent the ultimate yield curve. The coefficients are determined through the regression of either CPD or experimental data.

$E_0$  - the mean activation energy

$\sigma_a$  - the standard deviation.

The C2SM model is based on two competing reactions producing char and volatiles from coal. It considers the relationship between the volatile yield and the heating rate.



where:

$Y_1$  and  $Y_2$  – volatile yields at low and high temperature, respectively

$k_1$  and  $k_2$  – reaction rates defined in the form of Arrhenius law at low and high temperatures, respectively.

Coals characterized by a higher volatile yield will have higher  $Y_1$  and  $Y_2$  values. The first reaction has lower activation energy and a lower pre-exponential factor than the second reaction, whereby it occurs at low temperatures. The second (much faster) reaction occurs at high temperatures, whereby  $Y_2$  is always larger than  $Y_1$ . Usually,  $Y_1$  is set close to the volatile yield from proximate analysis, whereas  $Y_2$  is equal to 1.

The rate function is expressed as follows:

$$\frac{dV}{dt} = \left( Y_1 A_1 \exp\left(-\frac{E_1}{RT_1}\right) + Y_2 A_2 \exp\left(-\frac{E_2}{RT_2}\right) \right) \cdot C \quad (2.12)$$

where: C – char yield.

The third widely applied approach is the DAEM model which is a modified one-step model. The idea of this approach is that aliphatic bridges broken during devolatilization have a set of bond-breaking energies. At each time or temperature, all reaction pathways are likely. The process consists of “n” series of simultaneous first-order reactions. The subscript “i” denotes one specific reaction in the process.

$$\frac{dV_i}{dt} = k_i \cdot (V_i^\infty - V_i) \quad (2.13)$$

$$k_i = A_i \exp\left(-\frac{E_i}{RT}\right) \quad (2.14)$$

For a large number of reactions, continuous distribution  $f(E)$  of activation energies is assumed with identical pre-exponential factors. The function  $f(E)$  is unknown and is usually expressed as a Gaussian distribution [51–53].

$$f(E) = \frac{1}{\sigma\sqrt{2\pi}} \exp\left(-\frac{(E - E_0)^2}{2\sigma^2}\right) \quad (2.15)$$

A detailed description of the DAEM model, including its history, can be found in the work by Cai et al. [54].

As regards the modifications of the two-step approaches, Yamamoto et al. [46] proposed a corrective function for the two-step model, similarly as in the one-step approach. The final form of the equation is as follows:

$$\frac{dV}{dt} = \left( F_1 Y_1 A_1 \exp\left(-\frac{E_1}{RT_1}\right) + F_2 Y_2 A_2 \exp\left(-\frac{E_2}{RT_2}\right) \right) \cdot C \quad (2.16)$$

where:  $F_i$  is defined in the same way as in the one-step model.

Fletcher et al. [6] proposed a two-step model using sequentially distributed activation energies to reduce the number of fitting polynomial coefficients which are necessary for the Yamamoto model.

$$\frac{dV}{dt} = \left( Y_1 A_1 \exp\left(-\frac{E_1 + \sigma_{E1} Z}{RT_1}\right) + Y_2 A_2 \exp\left(-\frac{E_2 + \sigma_{E2} Z}{RT_2}\right) \right) \cdot C \quad (2.17)$$

The performance of the approaches presented in this section is discussed further in sub-chapter 2.2.3.

## 2.2.2 Detailed mechanisms

Detailed mechanisms are much more complex in nature because they consider the evolution of volatile matter, using the network models. The functional group depolymerization, vaporization and cross-linking (FG-DVC) model [8], the chemical percolation devolatilization (CPD) model [5–7] and the FLASHCHAIN model [55–57]. These algorithms cover network modelling, coal structure characterization, depolymerization reactions, cross-linking reactions, and non-condensable gas, tar, and char formation. However, these approaches differ in their way of modeling. The FG-DVC model incorporates a two-parameter Bethe lattice. FLASHCHAIN uses a straight-chain model without three-dimensional cross-linking to approximate the impact of a macromolecular network. The CPD model uses percolation theory with a three-dimensional Beth lattice to approximate a coal network. Coordination numbers and fractions of intact bridges are obtained from  $^{13}\text{C}$  NMR data. Coal structure is defined in a

similar way in all the three models with aromatic nuclei, peripheral groups, and labile bridges, non-labile or charred. NMR and ultimate analysis with experiments are required to obtain such parameters as the molecular weight of monomers, aromatic nuclei, or bridges. The FG-DVC model treats bridges as ethylene bridges, whereas FLASHCHAIN and CPD model them phenomenologically as splitting into two peripheral groups. Depolymerizing reactions are modelled differently by the three models. The DVC model presumes simple ethylene bridge scission, while CPD and FLASHCHAIN apply a competitive formula to model the reactions. Cross-linking is modeled in the FG-DVC by CO<sub>2</sub> and CH<sub>4</sub> formation, in the FLASHCHAIN by recombination reactions and in the CPD as a cross-linking mechanism. Tar is modeled in a similar way in all three models – as an equilibrium flash distillation process. The FG-DVC model consists of two sub-models. The FG component describes specific functional groups which decompose to form light gas species, whereas the DVC component considers macromolecular network depolymerization by combining bridge breaking with cross-linking and tar formation. In other words, the FG model determines the evolution of gases with the functional and elemental group compositions of tar and char. The DVC model determines both the yield and molecular weight distribution of char and tar.

The main features of the FG-DVC model are as follows:

- the thermal decomposition of the specific functional groups in the coal feedstock leads to light-gas species formation,
- the thermal decomposition of the macromolecular network induces tar and metaplast creation. This decomposition is controlled by bridge breaking,
- metaplast distribution is affected by the network coordination number,
- cross-linking controls the network re-solidification. It takes place with the formation of CH<sub>4</sub> and CO<sub>2</sub>. Hence in high-rank coals bridge breaking occurs before cross-linking, whereby the coal becomes fluid. In the case of low-rank coals, the reverse occurs, whereby the coal is thermosetting,
- the evolution of tar is restrained by mass transport. During the transport, the low-molecular-weight tar evaporates which leads to the release of tar molecules at a rate proportional to the light-gas evolution and to the tar vapor pressure.

The CPD model describes the devolatilization of coal by applying percolation lattice statistics in order to predict the evolution of tar precursors. The theory has been adjusted to predict mass and yield distributions of tar and the generation of light gases. The model assumes that during the devolatilization process the labile bonds between the aromatic clusters in the coal structure lattice are cleaved, which results in two main classes of fragments. One fragment is characterized by high vapor pressure and a low molecular weight and is released as light-gases from the coal. The second fragment comprises tar with low vapor pressure and a high molecular weight, which tends to remain in the particle for most of the time during typical pyrolysis. At the same time reattachment with the coal lattice (cross-linking) can take place. Residual lattice and high molecular weight compounds are metaplasts. The model has in short the following features:

- input parameters which depend on the type of the coal and its composition are obtained from NMR data,

- percolation lattice statistics provide the arrangement of tar molecular structures,
- the weighted averages of light-gas species release reaction parameters are taken from the FG-DVC model,
- the cross-linking mechanism takes into consideration the reattachment of the metaplast in the char matrix.

The CPD model has been shown to agree with the devolatilization data for a wide range of coals, temperatures, pressures, and heating rates [6,58,67–71,59–66]. Recently, Fletcher [72] carried out a state-of-the-art comprehensive review that considers 30 years of research using the CPD model.

The FLASHCHAIN model consists of the distributed-energy array chain model (Dischain) and the distributed-energy array model (Disarray) combined with the flash distillation analogy (Flashtwo). In the FLASHCHAIN model:

- coal is treated as a linear chain distribution composed of aromatic clusters interrelated with char links and labile bridges,
- bond scission mechanisms, the spontaneous charring of bridges, the bimolecular formation of char, and the elimination of peripheral groups are proposed,
- chain statistics describe the size distribution of large fragments of the reactants,
- tar formation is obtained from the metaplast by applying the flash distillation analogy,
- volatile species are released through a convective flow, neglecting any mass transfer resistances.

### **2.2.3 Performance of global approaches and detailed mechanisms**

The final volatile yield and composition, with the rate of volatile matter release, are the key aspects that need to be accurately estimated in order to effectively describe devolatilization. The literature has already confirmed [39,60,73] that the volatile yield obtained during devolatilization depends on the coal type and the heating rate. A higher heating rate always induces a higher volatile yield. In the global SFOR model, it is constant, which decreases the accuracy of the approach. Richards et al. [74] compared the different versions of the simple global kinetic models presented in sub-chapter 2.2.1 with regard to the advanced CPD model – Figure 2.1, and concluded, that an accurate devolatilization model should satisfy two conditions: devolatilization temperature should increase with the increasing heating rate and the final volatile yield should increase with rising temperature. Since each of the global models accurately copes with one specific heating rate, some of them fail when dealing with multiple heating rates. All of the examined global one-step mechanisms: SFOR, the Yamamoto model, the Biagini and Tognotti (BT) model, and the Schroeder approach failed to predict the ultimate volatile yield and devolatilization rates for different heating rates. Although the optimized BT model predicts much better the yield than the literature version proposed by Biagini and Tognotti, it does not follow the direction of the yield trend so well.

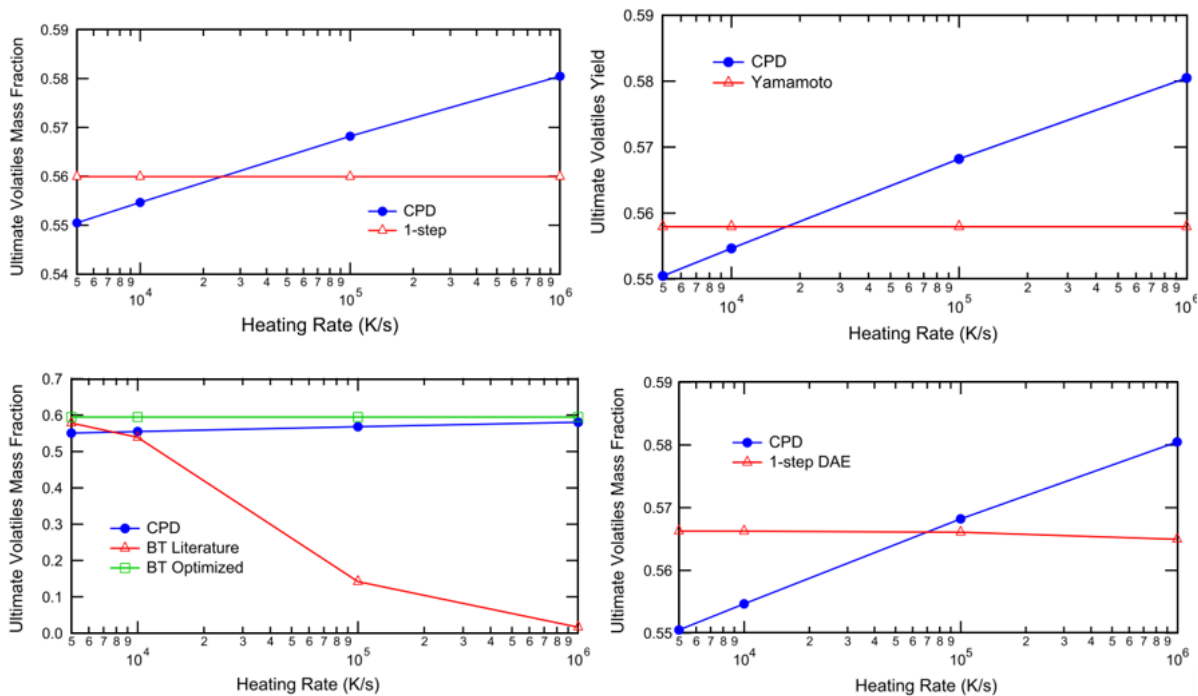


Figure 2.1. Ultimate volatile yield vs heating rate for 1-step (SFOR), Yamamoto model, BT (Biagini and Tognotti), Schroeder model (1-step DAE), and complex chemical percolation devolatilization (CPD) model [31].

Figure 2.2 shows the prediction of the ultimate volatile yield versus the heating rate by the two-step approaches. The two-step models showed the expected trend and were able to predict the ultimate volatile yield with a much smaller margin of error than the one-step models.

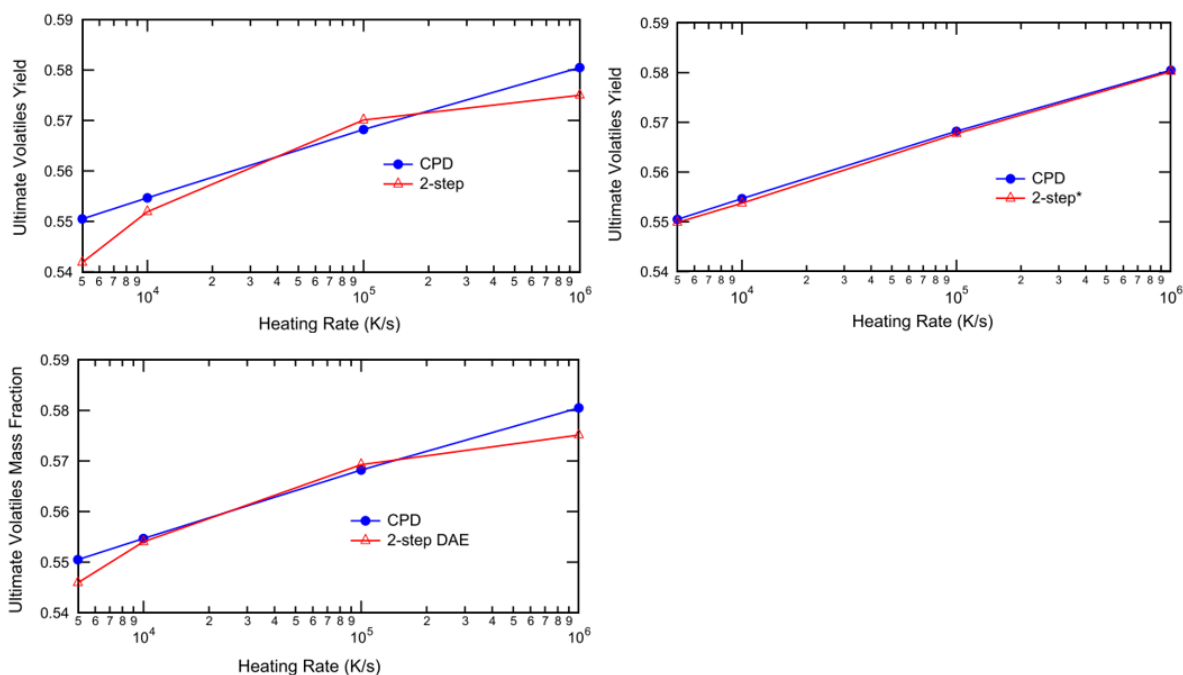


Figure 2.2. Ultimate volatile yield vs heating rate for 2-step (Kobayashi) model, Yamamoto model (2-step\*), Fletcher approach (2-step DAE), and complex chemical percolation devolatilization (CPD) model [31].



Silaen and Wang [75] compared the effect of devolatilization models on gasification performance in a two-stage gasifier. Among the four pyrolysis models taken into account, the Kobayashi model [39] produced the slowest pyrolysis rate. The CPD model [5] and the single rate model [37] yielded moderate results. The constant rate approach [76] performed faster than the rest. Figure 2.3 shows the results for gas temperature and major species concentration. It appears from the figure that the constant rate model is the least accurate approach, whereas the closest agreement can be seen between the Kobayashi/C2SM model and the CPD model.

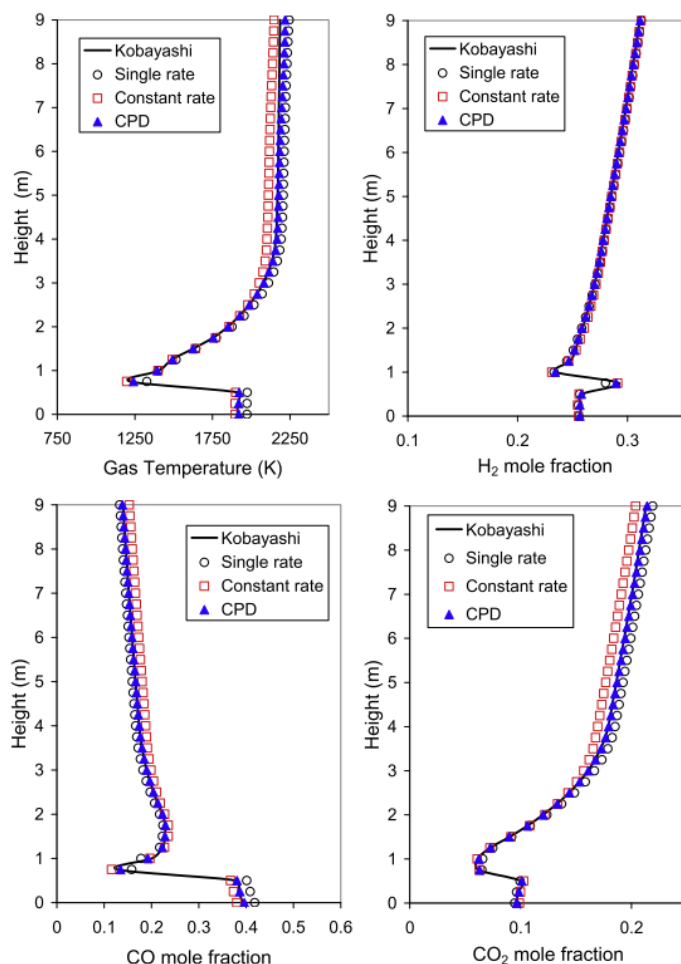


Figure 2.3. Mass-weighted temperature and major species for different devolatilization models [31].

Vascellari et al. [77] compared the performance of the detailed devolatilization models – FG-DVC, CPD, FLASHCHAIN. It turned out that as regards the final yield composition, non-negligible differences can be observed, especially for tar, while similar contents of light gases are found –Figure 2.4. On the other hand, the R-factor of the Utah bituminous coal as a function of the heating rate for CPD, FG-DVC, and FLASHCHAIN (Figure 2.5) was also calculated. The R-factor is defined as a ratio of the ultimate volatile yield to the value obtained from proximate analysis (not to be confused with the Q-factor which additionally takes into account the volatiles remaining in the char [78]). One can notice large variations between the advanced network models, especially, for FG-DVC and FLASHCHAIN. Figure 2.5 can be an explanation of the results from Figure 2.4 where FG-DVC predicted the lowest volatiles content

and consequently, the highest char content, whereas FLASHCHAIN predicted the highest volatiles content and the lowest char content.

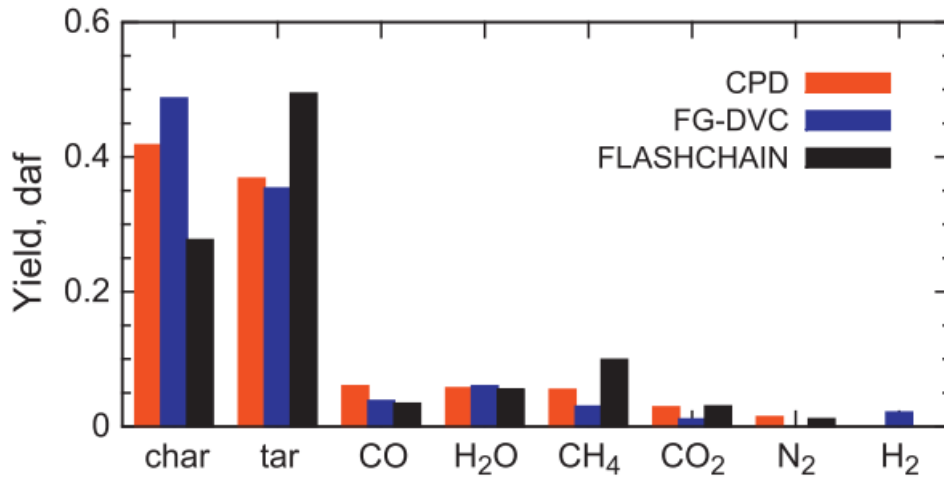


Figure 2.4. Final yield composition of Utah coal predicted by FG-DVC, CPD and FLASHCHAIN [77].

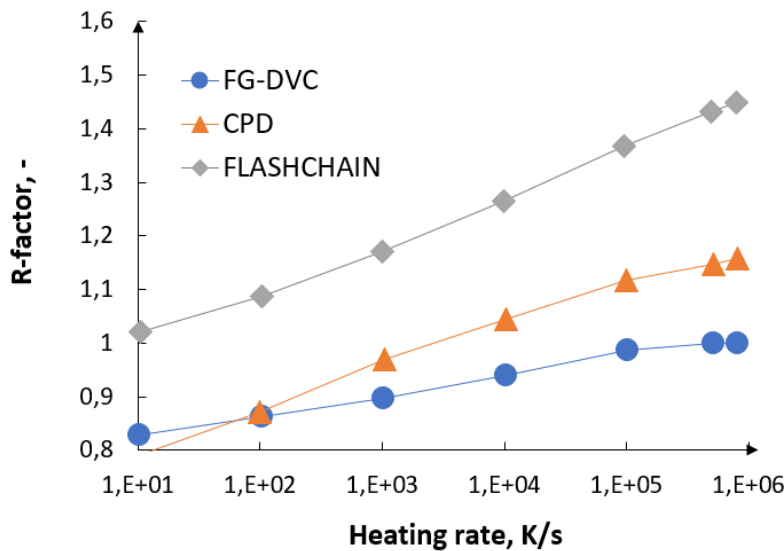


Figure 2.5. R-factor for Utah bituminous coal for CPD, FG-DVC and FLASHCHAIN as function of heating rate [31].

The second important aspect in devolatilization modeling is the description of the volatile composition. In most of the studies, it was assumed that volatiles is produced as a single compound, referred to as “volatiles”, undergoing an instantaneous reaction that breaks it up into products. The products tend to consist of tar, light hydrocarbons, H<sub>2</sub>O, CO, CO<sub>2</sub>, H<sub>2</sub>, and N<sub>2</sub>. The rate of release of the products is controlled by the devolatilization model. In some studies, tar and light hydrocarbons were simplified to be mainly CH<sub>4</sub> [79–85], while in other studies they were considered as the CH<sub>x</sub> molecule [86–89]. In [90–92] the combination of CH<sub>4</sub> and C<sub>2</sub>H<sub>2</sub> was used, whereas in [75,93] the combination of CH<sub>4</sub> and C<sub>6</sub>H<sub>6</sub> was adopted. Some works [77,94–99] considered a C<sub>x</sub>H<sub>y</sub>O<sub>z</sub> molecule. X,y,z coefficients were obtained either from proximate and ultimate analysis or from detailed approaches such as FG-DVC or CPD. Halama

et al. [100,101] used a  $C_xH_yO_zN_a$  molecule, whereas Chen et al. [102–104] adopted a  $C_xH_yO_zN_aS_p$  molecule. In most of the cases, the examined molecule was assumed to kinetically behave like  $CH_4$ . The assumption of  $CH_4$  reaction kinetics is valid because the rates of the reaction of many hydrocarbons with  $O_2$  and  $H_2O$  do not vary significantly from each other [105,106].

## 2.2.4 Kinetic parameters of global devolatilization models

Another important observation regarding global devolatilization models considers kinetic parameters. Unfortunately, kinetic parameters which are utilized within global devolatilization models are valid only for the specific conditions for which they were determined. One way of evaluating these parameters is by experimental techniques. However, in many cases, this can be challenging, particularly in the case of large-scale reactors. On the other hand, direct implementation of advanced phenomenological network models, like FG-DVC, CPD, or FLASHCHAIN, which do not require these parameters and which depend on the fuel type and the operating conditions, into CFD, can substantially raise the computational effort, especially, when simulations with large eddy simulation (LES) techniques with huge mesh refinements on a 3D domain are investigated. Table 2.1 presents the list of the most widely studied entrained flow reactors that were found in the literature review, while Table 2.2 shows the list of the most widely applied kinetic parameters for SFOR and C2SM.

Table 2.1. List of the mostly studied entrained flow reactors [31].

No.	Reference reactor parameters with the list of papers studying a specific reactor:
1	MHI two-stage dry-feed upflow gasifier 200 t/d [86,87,89,102–104,107] Pressure: 2.7 MPa Oxidant: Air Equivalence ratio: 2.5
2	CRIEPI two-stage dry-feed upflow gasifier 2 t/d [80,91] Pressure: 2.0 MPa Oxidant: Air Equivalence ratio: 2.0
3	E-Gas two-stage slurry-feed upflow gasifier 2550 t/d [81,85,93,107–111] Pressure: 2.84 MPa Oxidant: Oxygen Equivalence ratio: 2.27
4	Generic two-stage slurry-feed upflow gasifier 3000 t/d [75,92,112,113] Pressure: 2.8 MPa Oxidant: Oxygen Equivalence ratio: 2.0 The shape is based on the MHI two-stage air blown 200 t/d gasifier

5	Two-stage upflow gasifier 1t/h	
	Slurry-feed [82] Pressure: 2.4 MPa Oxidant: Oxygen Equivalence ratio: 2.0	Dry-feed [114] Oxidant: Oxygen O/C ratio: 0.7,0.8,0.9
6	Shell one-stage downflow gasifier 3000 t/d Pressure: 4.2 MPa Oxidant: Oxygen, steam Equivalence ratio: 2.51, various	
	[98] Pressure: 4.2 MPa Oxidant: Oxygen, steam O/C ratio: 0.8	[115] Pressure: 4.2 MPa Oxidant: Oxygen, steam Equivalence ratio: 2.51
7	KIER one-stage downflow gasifier [116,117] Pressure: 2.5 MPa Oxidant: Oxygen/Air Equivalence ratio: various	
8	BYU one-stage downflow gasifier 1t/d [77,87,88,94,95] Pressure: 0.1 MPa Oxidant: Oxygen, steam	
9	PiTER one-stage downflow gasifier [50,100,101,118,119] Pressure: 0.5, 2.5 MPa Temperature: 1500, 1800, 1900 K Oxidant: N <sub>2</sub> , O <sub>2</sub> , H <sub>2</sub> , CO <sub>2</sub> , H <sub>2</sub> O, O/C ratio: 1	

Table 2.2. Devolatilization kinetic parameters for global models with reactor numbers from Table 2.1 [31].

Single-step first-order reaction model (SFOR)	
$A = 2.1 \cdot 10^6$ $E = 2.1 \cdot 10^7$	Used by: [88] Reactor: 8
$A = 4.92 \cdot 10^5$ $E = 7.4 \cdot 10^7$	Used by: [75] Reactor: 4 Used by: [120]
$A = 293$ $E = 5.1 \cdot 10^7$	[50,118,119] Reactor: 9 Where $V_{total} = f(p, T)$ Pressure up to 5.0 MPa
$A = 2.1 \cdot 10^5$ $E = 3.28 \cdot 10^7$	Used by: [121,122]
$A = 10^5$ $E = 5 \cdot 10^7$	Used by: [123]

Competing two-step reaction model (Kobayashi)	
$A_1 = 2 \cdot 10^5$ $A_2 = 1.3 \cdot 10^7$ $E_1 = 1.046 \cdot 10^8$ $E_2 = 1.674 \cdot 10^8$ $a_1 = 0.3$ $a_2 = 1$	Parameters taken from Kobayashi: [124] Used by: [98] Reactor: 6 [110][85][96][108][109] Reactor: 3 [84] [101] Reactor: 9, $a_1 = 0.558$ [114] Reactor: 5 [125] [115] Reactor: 6 [107]
$A_1 = 3.7 \cdot 10^5$ $A_2 = 1.5 \cdot 10^{13}$ $E_1 = 7.5 \cdot 10^7$ $E_2 = 2.5 \cdot 10^8$ $a_1 = 0.565$ $a_2 = 0.565$	Parameters taken from Ubhayakar et al. [73] Used by: [93] Reactor: 3 [102–104][126,127] Reactor: 1

Judging by Table 2.1 and Table 2.2, one can notice that the same sets of global kinetic parameters for both SFOR and C2SM tend to be repeated in devolatilization modeling for different reactors. But these reactors differ in their operating conditions, coal properties, stoichiometry, and gasifying agents. For instance, Figure 2.6 and Figure 2.7 present two of the most widely studied gasifiers.

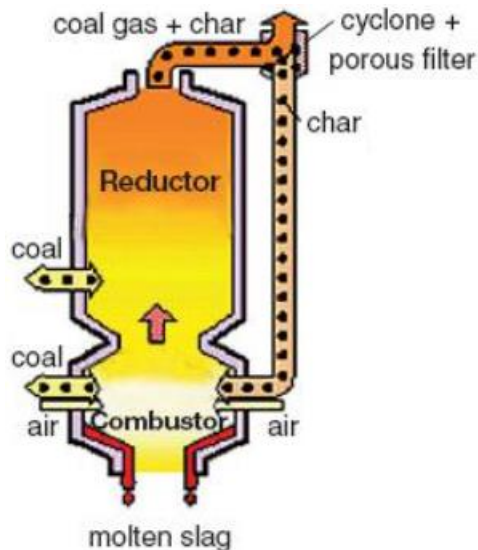


Figure 2.6. MHI gasifier [128].

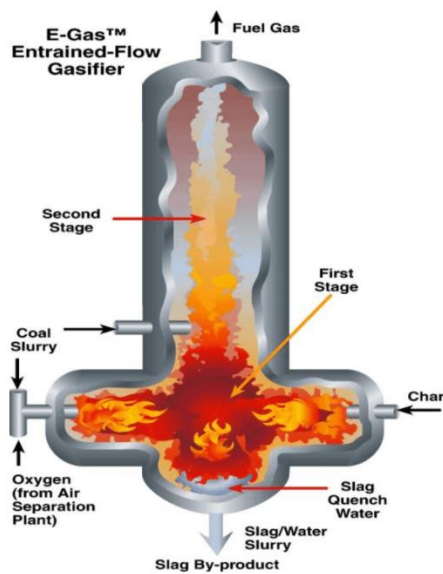


Figure 2.7. Conoco-Philips E-gas gasifier [129].

Mitsubishi Heavy Industries (MHI) reactor and a Conoco-Philips E-gas reactor, respectively. The MHI reactor is a 200 tons/day, two-stage, air-blown, and pressurized entrained-flow gasifier with a swirling flow. It has three stages of dry-feed injectors. Two of them are located in the combustion region and the third one is in the reductor. Coal with air is injected in the 1<sup>st</sup> stage. Recycled char is injected through the second-stage injectors in the combustion region. The third-stage injectors are supplied with coal and air. On the other hand, the E-gas reactor is a 2400 tons/day, two-stage, oxygen-blown, and pressurized entrained flow gasifier. It has two stages of feed injectors. One of them is located in the combustor region and the second one in the throat. Coal-water slurry, oxygen, and a small amount of nitrogen are injected in the 1<sup>st</sup> stage, whereas in the 2<sup>nd</sup> stage only coal-water slurry is injected. This results in entirely different operating conditions and consequently, in an inaccurate description of the devolatilization stage because the applied kinetic parameters are invalid for the given conditions.

### 2.2.5 Summary of devolatilization stage

This sub-chapter discussed the most widely applied simplified devolatilization models, complex devolatilization approaches, volatile yield formulation methods, kinetic parameters, and the comparison of global and detailed mechanisms on the basis of the volatile yield, syngas composition, and R-factor. Based on the literature review, it was found that the single-step SFOR model and the competing two-step C2SM/Kobayashi model were the most widely utilized global approaches. SFOR was incorporated by [50,75,130,131,81,88,118–123]. C2SM was applied by [77,83,101–104,107–110,114,115,84,116,117,125–127,132–135,85,93–96,98,99]. As regards the accuracy, SFOR performed accurately for one heating rate but failed to predict rates and yields correctly for multiple heating rates. The reason lies in the constant term  $V_{total}$  which is independent of the varying conditions. On the other hand, C2SM performed better for multiple heating rates with a much smaller margin of error than SFOR. As for the examined advanced phenomenological approaches, FG-DVC, CPD, and FLASHCHAIN

predicted the yields differently with respect to the heating rate. Tar prediction by FLASHCHAIN was substantially greater than by CPD or FG-DVC. Another aspect considers the amount of volatile matter released during devolatilization. One should note that the amount of volatile matter determined during proximate analysis should not be higher than the volatile yield estimated for higher heating rates. This phenomenon could be observed for FG-DVC and CPD, where the R-factor was lower than 1. On the basis of the accurately predicted volatile yield in devolatilization, apart from having correct flame characteristics, one can correctly estimate the overall carbon conversion in a gasification reactor since the carbon conversion is characterized by the repartition of fast devolatilization reactions and slow gasification reactions [99]. As regards the kinetic parameters, it was found that for most of the gasification studies no attention was paid to the kinetic parameters. For instance, in the case of the C2SM approach, the same set of global kinetic parameters ( $A_1 = 2 \cdot 10^5$ ,  $A_2 = 1.3 \cdot 10^7$ ,  $E_1 = 1.046 \cdot 10^8$ ,  $E_2 = 1.674 \cdot 10^8$ ,  $\alpha_1 = 0.3$ ,  $\alpha_2 = 1$ ) was repeated for different reactors [85,96,98,107,108,110,114,115,125]. But these reactors differ in their operating conditions, coal properties, stoichiometry, and gasifying agents. On the basis of the reviewed literature and the drawn conclusions, one of the objectives of the current dissertation was to propose an optimization procedure that utilized specific kinetic parameters within global devolatilization models valid only for the examined conditions. These parameters can be obtained by means of advanced phenomenological approaches, like FG-DVC, CPD, or FLASHCHAIN. Thanks to this method, the accuracy of the global approaches increased. The process of obtaining these parameters will be discussed in detail in Chapter 4.

### 2.3 Gas-phase modeling

As in devolatilization modeling, there are two main approaches to CFD modeling of gas-phase reaction rates. The first approach is a global mechanism where reaction rates are derived empirically based on experimental results. They are usually described by the Arrhenius equation. For the gas-phase reactions, the relation is defined in the following way:

$$k = AT^n \exp\left(-\frac{E_a}{RT}\right) [Fuel]^a [Oxidizer]^b [3^{rd}]^c \quad (2.18)$$

where:

A – the pre-exponential factor (the unit depends on the reaction order)

n – a temperature exponent

T – temperature (K)

$E_a$  – activation energy (J/kmol, cal/mol)

R – the universal gas constant (J/kmol\*K)

a, b, c – concentration exponents

[3<sup>rd</sup>] – the molar concentration of the third species (neither a reactant nor a product).

In the global approach, Eq. (2.18) represents the average of the numerous individual reaction rates for the usually occurring elementary reactions. Using results from experimental measurements or detailed mechanisms one can estimate A, n,  $E_a$ , a and b constants. Concentration exponents a, and b are not linked to the stoichiometric coefficients but are determined either based on an experiment or detailed mechanisms. Temperature exponent n

describes an additional dependence of the reaction rate on temperature. Usually, for modest temperature ranges the dependence can be applied into a single exponential term (with  $n=0$ ) where most of the elementary reactions follow the Arrhenius behavior. However, for the conditions encountered in combustion or gasification, a non-Arrhenius behavior can be exposed [136], which requires the additional constant  $n$ .

One of the main benefits of the global mechanism is its relatively simple form due to which computational power and simulation time can be conserved. However, the main disadvantages are the narrow operating conditions within which the reaction rate was obtained. As a result, such kinetic data can be applied only to concrete gasification conditions similar to the ones prevailing in the experiment.

The second approach is a detailed mechanism. It is based on the knowledge regarding the elementary steps involved in the reaction and the latter's energy connections. In most cases, such a mechanism contains a significant amount of reactions and rates, whereby a software package, such as the Chemkin software, is needed for external calculations. This approach ensures the right pathway and prediction of the reaction, but it can be computationally very expensive when utilized in CFD and it can be problematic when trying to achieve convergence.

### 2.3.1 Global kinetic mechanisms

A literature review indicates that there are two major global gas-phase modeling approaches that have been extensively used, namely the two-step Westbrook and Dryer (WD) mechanism [106] and the four-step Jones and Lindstedt (JL) mechanism developed for several hydrocarbon fuels [105]. Other global approaches are in fact based on these two.

The Westbrook and Dryer (WD) mechanism includes two reactions Eq. (2.19) and Eq. (2.20), where the second reaction is reversible.



The reaction rate parameters are presented in Table 2.3:

Table 2.3. Westbrook and Dryer global mechanism kinetic data (units in cm, s, cal, kmol) [106][137].

Mechanism	Reactions	A	n	E <sub>a</sub>	Order
Eq. (2.19)	$CH_4 + 1.5O_2 \rightarrow CO + 2H_2O$	$1.59 \cdot 10^{13}$	0	47.8	$[CH_4]^{0.7}[O_2]^{0.8}$
Eq. (2.20)	$CO + 0.5O_2 \rightarrow CO_2$	$3.98 \cdot 10^{14}$	0	40.7	$[CO][O_2]^{0.25}[H_2O]^{0.5}$
Eq. (2.20) - rev	$CO_2 \rightarrow CO + 0.5O_2$	$5.0 \cdot 10^8$	0	40.7	$[CO_2]$

Westbrook and Dryer [106] developed the simplified reaction mechanism by using a numerical laminar flame model. The parameters of the reaction rates were changed to get the most accurate agreement between the calculated and experimentally determined flame speed values for various fuel and air mixture proportions. The impact of different reaction rate parameters on the properties of the laminar flame was investigated and a final procedure for determining the best values was developed [106]. As opposed to other simplified reaction rates not mentioned in this study, these rates, as Westbrook and Dryer stated, “correctly reproduce



experimental flame speeds over a wide range of equivalence ratios and pressures". They stressed, however, that for each set of reaction parameters the pre-exponential factor should be treated as an initial estimate if they are to be used in other numerical models, and finally calibrated on the basis of the computed and experimental data for the specific operating conditions. The activation energy and concentration exponents should be valid for other models.

The second global mechanism is the Jones and Lindstedt (JL) mechanism. Jones and Lindstedt validated the model empirically by using experimental data for premixed propane and methane flames along with diffusion flame data for the methane-air flame. The mechanism performed well for both fuel-lean and moderately fuel-rich stoichiometries. The JL mechanism includes two competing fuel breakdown reactions, of which Eq. (2.21) dominates under fuel-lean conditions, while Eq. (2.22) dominates under fuel-rich conditions. Eq. (2.23) and Eq. (2.24) are the two reversible reactions that control the rate of CO and H<sub>2</sub>.



Accounting only for CH<sub>4</sub>, the 1<sup>st</sup> reaction and the 2<sup>nd</sup> reaction have the respective forms:



The reaction rate parameters are presented in Table 2.4

Table 2.4. Jones and Lindstedt global mechanism kinetic data (units in cm, s, cal, kmol) [105].

Mechanism	Reactions	A	n	E <sub>a</sub>	order
Eq. (2.25)	$CH_4 + 0.5O_2 \rightarrow CO + 2H_2$	$7.82 \cdot 10^{13}$	0	30	$[CH_4]^{0.5}[O_2]^{1.25}$
Eq. (2.26)	$CH_4 + H_2O \rightarrow CO + 3H_2$	$0.30 \cdot 10^{12}$	0	30	$[CH_4][H_2O]$
Eq. (2.23)a	$H_2 + 0.5O_2 \leftrightarrow H_2O$	$4.45 \cdot 10^{18}$	-1	40	$[H_2]^{0.5}[O_2]^{2.25}[H_2O]^{-1}$
Eq. (2.23)b	$H_2 + 0.5O_2 \leftrightarrow H_2O$	$1.21 \cdot 10^{18}$	-1	40	$[H_2]^{0.25}[O_2]^{1.5}$
Eq. (2.24)	$CO + H_2O \leftrightarrow CO_2 + H_2$	$2.75 \cdot 10^{12}$	0	20	$[CO][H_2O]$

The reverse rate parameters of reactions Eq. (2.23) and Eq. (2.24) are calculated using the equilibrium constant. As opposed to the Jones and Lindstedt mechanism, in the Westbrook and Dryer mechanism, the rate constants for reactions Eq. (2.19) and Eq. (2.20) come from the work by Dryer and Glassman [137]. The constants were determined during the high-temperature oxidation of CO and CH<sub>4</sub> under fuel-lean conditions ( $\lambda > 2$ ) in a turbulent flow [138]. Consequently, the direct use of this approach in coal gasification with standard kinetic parameters may lead to inaccurate results.

Table 2.5 presents the mechanism based on the equilibrium of the water-gas shift

reaction. With regard to the Westbrook and Dryer mechanism, this approach considers also the oxidation reaction of H<sub>2</sub>.

Table 2.5. Mechanism based on water-gas shift equilibrium.

Reactions	A (s-m-kmol)	n	E <sub>a</sub> (J/kmol)
$CH_4 + 1.5O_2 \rightarrow CO + 2H_2O$	$7.82 \cdot 10^9$	0.5	$1.6736 \cdot 10^8$
$CO + 0.5O_2 \rightarrow CO_2$	$5.42 \cdot 10^9$	0	$1.2552 \cdot 10^8$
$H_2 + 0.5O_2 \rightarrow H_2O$	$1 \cdot 10^7$	0	$8.368 \cdot 10^6$

Table 2.6 also describes the mechanism similar to the Westbrook and Dryer approach but additionally takes into account incomplete oxidation of CH<sub>4</sub> [139].

Table 2.6. Mechanism based on the work of Glassman et al. [139].

Reactions	A (s-m-kmol)	n	E <sub>a</sub> (J/kmol)
$CH_4 + 1.5O_2 \rightarrow CO + 2H_2O$	$2.33 \cdot 10^{11}$	0.5	$1.6736 \cdot 10^8$
$CH_4 + 0.5O_2 \rightarrow CO + 2H_2$	$3.8 \cdot 10^7$	0	$5.5463 \cdot 10^7$
$CO + 0.5O_2 \rightarrow CO_2$	$1.3 \cdot 10^{11}$	0	$1.2552 \cdot 10^8$

### 2.3.2 Detailed kinetic mechanisms

GRI-Mech [9] is an optimized detailed kinetic mechanism designed to model not only natural gas and air mixture combustion but also flame propagation. All the reaction rate constants were obtained empirically. The mechanism consists of radical reactions. NO formation and reburn chemistry are also included. The conditions for which GRI-Mech was optimized are approximately 1000 to 2500 K, 10 Torr to 10 atm, and the equivalence ratio of 0.1-5 for premixed systems [9,61]. In fact, this is the main detailed mechanism incorporated in the latest works on the CFD modeling of the gasification process in entrained flow gasifiers [77,94,95,99,140].

CRECK [10] – the detailed kinetic mechanism that is provided by the CRECK modeling group at Politecnico de Milano. It is a C1-C3 mechanism, where the fuel is CH<sub>4</sub>. The mechanism is a radical reaction approach which consists of 114 species and 1999 reactions. Due to its complexity, no CFD study was found that directly investigated this approach in entrained flow coal gasification.

### 2.3.3 Water-gas shift reaction

The water-gas shift (WGS) reaction – Eq. (2.24) is a reaction traditionally used for H<sub>2</sub> production from synthesis gas, which can be further used to produce ammonia in the fertilizer industry, in petroleum refineries, and also as a fuel for power generation. The use of gasification for power generation has also greatly increased the use of water-gas shift reactors [141]. The water-gas shift reaction is one of the major reactions in the industrial-scale gasification process.

It is a moderately exothermic reversible reaction where the standard enthalpy of formation is equal to:  $\Delta H_{298}^0 = -41.09 \text{ kJ/mol}$ . The main characteristics of this reaction are as follows [141]:

- the equilibrium constant decreases as the temperature increases, whereby the reaction exhibits decreasing conversion with increasing temperature,
- the reaction is thermodynamically favored at low temperatures and kinetically favored at high temperatures,
- since there is no change in the volume from reactants to products the reaction is pressure-independent.

According to some authors [92,100,101], WGSR plays a key role in the accurate prediction of the syngas composition at the reactor outlet. This reaction and its kinetic parameters had already been mentioned in the Jones and Lindstedt global mechanism [105], but many authors were forced to modify these parameters [75,80,82,86,87,90,91,93,142] because the Jones' rate had been obtained under catalytic conditions and it was too fast for gasification conditions. It is obvious that employing any of the published reaction rates, which may not work in other temperature or pressure conditions than the laboratory conditions, can simply lead to misleading results.

Lu et al. [142] calibrated the WGS reaction rate on the basis of experimental data obtained from the quench section of an actual gasifier and compared it to three rates taken from Jones and Lindstedt [105] and from Sato et al. [143], presented in Table 2.7.

Table 2.7. WGS reaction rate parameters used in [142].

Sources of the WGS rate	Catalyst	$k = AT^n \exp\left(-\frac{E}{RT}\right) n = 0$
Jones and Lindstedt [105]	Yes	$A = 2.75 \cdot 10^{10} \text{ s}^{-1}, E = 83.8 \frac{\text{kJ}}{\text{mol}}$
Sato et al. [143]	No	$A = 10^{5.58 \pm 1.38} \text{ s}^{-1}, E = 11.6 \frac{\text{kJ}}{\text{mol}}$

Table 2.8 presents the syngas composition results obtained by Lu et al. [142] from the experiment and numerical simulations, using two reaction rates reported in the literature. For water quench simulations, the reaction rates presented by Bustamante et al. [144,145] were used. The results turned out to be very similar to Jones' rate. Table 2.9 shows the calibrated WGS reaction rates.

Table 2.8. CFD simulated syngas composition for two reaction rates reported in literature [142].

Primary injection		Exit mole fraction	
Syngas	Experimental data	Jones and Lindstedt [105]	Sato et al. [143]
		$A = 2.75 \cdot 10^{10} \text{ s}^{-1}$	$A = 10^{5.58 \pm 1.38} \text{ s}^{-1}$
		$E = 83.8 \frac{\text{kJ}}{\text{mol}}$	$E = 11.6 \frac{\text{kJ}}{\text{mol}}$
H <sub>2</sub>	0.36	0.50	0.49
CO <sub>2</sub>	0.29	0.46	0.45
CO	0.34	0.03	0.05
CH <sub>4</sub>	0.01	0.01	0.01
CO conversion (%)	-	88	80

Table 2.9. CFD simulated syngas composition using two calibrated reaction rates [142].

Primary injection		Exit mole fraction	
Syngas	Experimental data	Jones and Lindstedt [105]	Sato et al. [143]
		$A = 2.75 \cdot 10^3 \text{ s}^{-1}$	$A = 10^{-1} \text{ s}^{-1}$
		$E = 83.8 \frac{\text{kJ}}{\text{mol}}$	$E = 11.6 \frac{\text{kJ}}{\text{mol}}$
H <sub>2</sub>	0.36	0.36	0.34
CO <sub>2</sub>	0.29	0.28	0.29
CO	0.34	0.38	0.36
CH <sub>4</sub>	0.01	0.01	0.01
CO conversion (%)	-	88	80

Therefore, it was ultimately concluded that the WGS reaction rate significantly affected the CFD results. Due to the different operating conditions, none of the adopted reaction rates worked well in the simulation of the water quench process.

The same procedure was applied by Lu et al. [91] to the CRIEPI gasifier. The results presented in Figure 2.8 prove that the outcome is consistent with the outcome obtained in Part 1 [142] when only the water quench process was simulated in the ITIR gasifier. For these particular operating conditions the calibrated reaction rates best matching the experimental data are:

modified Jones' rate:  $A = 2.75, E = 8.38 \cdot 10^4 \text{ J/mol}$ ,

modified Sato's rate:  $A = 10^{-3}, E = 1.16 \cdot 10^5 \text{ J/mol}$ .

With regard to the original rate values, only the pre-exponential factor was modified.

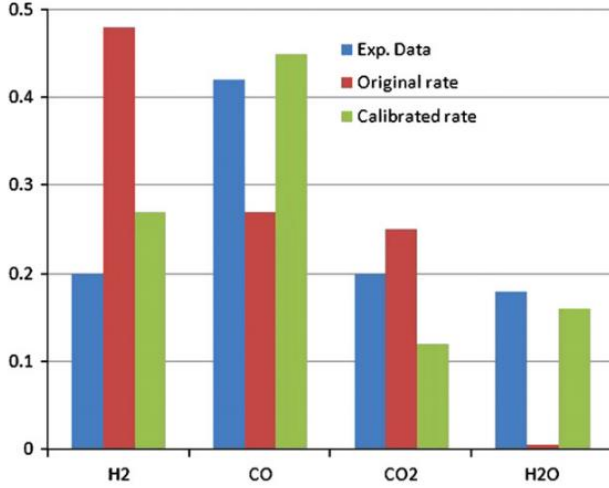


Figure 2.8. Comparison of syngas outlet composition with experimental data , original Jones ' rates and calibrated Jones ' rates [31].

### 2.3.4 Turbulence-chemistry interaction models (TCI)

The interaction between chemical reactions and the flow which is turbulent in nature has a major effect on the gasification process. Turbulence itself is currently not fully understood on the fundamental level. The turbulence-kinetics interaction needs to be modeled since the chemical source term  $R_i$  is non-linear (Arrhenius law) and cannot be easily calculated from Reynolds Averaged Navier-Stokes equation transported quantities. In non-premixed reacting turbulent flows the local time-dependent mixing, chemical reaction of the species, and heat transfer away from the reaction determine the processes taking place in the gas phase during gasification.

$$\nabla \cdot (\bar{\rho} \tilde{u} \tilde{Y}_i) = -\nabla \cdot \bar{J}_i - \nabla \cdot (\bar{\rho} \widetilde{u'' Y_i''}) + \bar{R}_i + \bar{S}_i \quad (2.27)$$

where:

$\bar{\rho}$  – average density

$\tilde{u}$  – average velocity

$\tilde{Y}_i$  – average mass fraction of species i

$\bar{J}_i$  – laminar diffusion flux of species i

$\bar{\rho} \widetilde{u'' Y_i''}$  - turbulent diffusion flux of species i

$\bar{R}_i$  – chemical source term due to homogeneous reactions

$\bar{S}_i$  – chemical source term due to heterogeneous reactions

Eq. 2.27 is the form of species transport equation obtained after Reynolds decomposition of the instantaneous Navier-Stokes equations. It must be mentioned that the detailed description of the applied models, made assumptions, and general information concerning equations will be provided in Chapter 3 – Model description.

As already discussed, the main issue with turbulent combustion modeling considers the determination of the mean chemical source term due to homogeneous reactions  $R_i$ . Because of the non-linearity, the source term cannot be easily expressed as a function of the mean mass

fractions of fuel, oxidizer, the mean density, or the mean temperature.

According to Veynante and Verisch [146], the reaction rate  $R_i$  modeling is either based on a purely statistical view, geometrical view of turbulent flames or mixing analysis and turbulent time scales.

- One-point statistics: this approach considers a probability density (PDF) function of species and enthalpy.
- Geometrical analysis: this approach identifies the flame front as a geometrical surface which is usually combined with flamelet assumptions, where flame elements are considered to be a laminar flame.
- Turbulent mixing: this approach considers turbulent mixing to be a key element in controlling the chemical reaction rate.

Unfortunately, there is scarce information regarding the application of flamelet models or PDF function in gasification processes. Some latest results with PDF [147,148] and flamelet modeling [149] for coal combustion processes have been recently published. Therefore, in the current dissertation, only the third interpretation will be discussed in detail as it is most commonly applied on the basis of the literature review [31].

In most conventional pulverized coal combustion (PCC) simulations, the most simple approach is to assume infinitely fast chemistry which originates from the observation that most species produced during combustion rapidly reach chemical equilibrium at high temperatures. According to the third interpretation, the mixing process of large eddies with the time scale  $k/\varepsilon$  controls the rate at which chemical reactions proceed [150]. No kinetic information is needed. However, the above assumption can no longer be applied for coal gasification where there is an extended reacting flow region with lower temperatures and the chemical reaction rates and the turbulent mixing rates are comparable due to the usually low Damköhler number (The Damköhler number defines the quotient between the flow and the chemical time scales – in other words, a large Damköhler number signifies a “fast chemistry”). Therefore, models applicable to combustion can be inaccurate for such processes as gasification. Owing to its simplicity, one of the TCI models which was most frequently applied to the gasification process is the combined finite-rate/eddy dissipation model [151]. In this approach, the reaction rates of both the finite-rate model and the eddy dissipation model are calculated and the slower rate is chosen as the dominant one. The description of both models is presented below.

In the *finite-rate model*, the reaction rates of the reversible reaction and the irreversible reaction are determined from the Arrhenius expression, neglecting the effects of turbulence. The model yields good results for laminar flames, but it can be imprecise for turbulent flows. Nevertheless, this model can be applied to supersonic flames where the chemistry is slow and the turbulent character of the flow can be neglected.

For the reversible reaction, the molar rate of creation/destruction of species  $i$  in reaction  $r$  is given by:

$$R_{i,r} = \Gamma(v''_{i,r} - v'_{i,r}) \left( k_{f,r} \prod_{j=1}^N [C_{j,r}]^{\eta'_{j,r}} - k_{b,r} \prod_{j=1}^N [C_{j,r}]^{v''_{j,r}} \right) \quad (2.28)$$

where:

$\Gamma$  – the net effect of third bodies

$C_{j,r}$  – the molar concentration of species  $j$  in reaction  $r$  (kgmol/m<sup>3</sup>)

$\eta'_{j,r}$  – the rate exponent for reactant species  $j$  in reaction  $r$

$v'_{i,r}$  – a stoichiometric coefficient of the reactant species

$v''_{j,r}$  – a stoichiometric coefficient of the product species

$k_{b,r}$  – the backward rate constant

$k_{f,r}$  – the forward rate constant.

The forward rate constant for reaction  $r$  ( $k_{f,r}$ ) is defined by the Arrhenius expression

$$k = AT^n \exp\left(-\frac{E_a}{RT}\right) [Fuel]^a [Oxidizer]^b \quad (2.29)$$

where:

$A$  – the pre-exponential factor (the unit depends on the reaction order)

$n$  – the temperature exponent

$T$  – temperature (K)

$E_a$  – activation energy (J/kmol, cal/mol)

$R$  – the universal gas constant (J/mol/K)

$a, b$  – concentration exponents.

The *eddy dissipation model* is a concept originally introduced by Spalding (1971) as the *eddy break-up model* [152] and later generalized by Magnussen and Hjertager (1976) [151] as the eddy dissipation model. This model is based on the turbulent mixing rate. The assumption is that chemical reactions occur much faster than turbulence. The turbulent mixing rate is related to the timescale (eddy lifetime)  $\frac{\varepsilon}{k}$  of turbulent eddies which are present in the flow. This can be a good assumption for many combustors since most fuels burn rapidly [153]. The crucial adjusting parameters in this approach are Magnussen's empirical constants  $A$  and  $B$  (default:  $A = 4.0$ ,  $B = 0.5$ ) for the reactant and the product, respectively. Their modification can significantly change the results [150].

The net rate of production of species  $i$  due to reaction  $r$  is given by the shorter of the two expressions:

$$R_{i,r} = v'_{i,r} M_{w,i} A \rho \frac{\varepsilon}{k} \min\left(\frac{Y_R}{v'_{R,r} M_{w,R}}\right) \quad (2.30)$$

$$R_{i,r} = v'_{i,r} M_{w,i} A B \rho \frac{\varepsilon \sum_P Y_P}{k \sum_j v''_{j,r} M_{w,j}} \quad (2.31)$$

where:

$v'_{i,r}$  - the stoichiometric coefficient of the reactant species

$M_{w,i}$  - the molecular weight of species  $i$

$A$  - an empirical constant equal to 4.0

$B$  - an empirical constant equal to 0.5

$Y_R$  - the mass fraction of particular reactant  $R$

$Y_p$  - the mass fraction of particular product P  
 $\frac{\varepsilon}{k}$  – a large eddy mixing time scale.

The combined *finite-rate/eddy dissipation model* (F-R/EDM) is a trivial method of distinguishing between kinetical and mixing rates in the gasification process where both can be the rate-limiting step. However, there is no direct interaction between kinetics and turbulence in this approach. Owing to its simplicity, robustness and stability, it was one of the most frequently used turbulence-chemistry interaction modeling approaches [75,79,90–93,98,107–111,80,114–117,120,125,132,142,154,81,82,84–87,89]. Unfortunately, this approach has a serious disadvantage when considering multi-step reaction mechanisms. The reason is that each reaction has its own Arrhenius rate. In the EDM model, every reaction has the same mixing rate. The model cannot predict kinetically controlled species such as radicals. It also cannot handle reversible reactions. Consequently, in order to minimize the probability of an error, this approach should be used only for one-step or two-step global reactions.

The *eddy dissipation concept* [155] is an extension of the eddy-dissipation model for the case of multistep chemical kinetics and includes chemical mechanisms in turbulent flows. It can be used for a large variety of both diffusion-controlled and premixed combustion problems both when turbulent mixing is faster than chemical reaction kinetics and when turbulent fluctuations are dominant. The main assumption of this model is that combustion occurs in the regions of the flow where the dissipation of turbulence kinetic energy takes place. It is a cascade model of energy dissipation from larger to smaller scales. The smallest scales are defined as fine structures and can be described as perfectly stirred reactors. The control volume is conceptually divided into fine structures and the surroundings [156].

The length fraction of the fine-scale is as follows:

$$\xi^* = \frac{L^*}{L'} = C_\xi \left( \frac{\nu \varepsilon}{k^2} \right)^{\frac{1}{4}} \quad (2.32)$$

where:

$C_\xi$  - a volume fraction constant,

$L^*$  - the length scale of the fine structure,

$L'$  - the length scale from the first cascade level

$\nu$  - kinematic viscosity ( $m^2/s$ )

$\varepsilon$  - the turbulence dissipation rate ( $m^2/s^3$ ),

$k$  – turbulence kinetic energy ( $m^2/s^2$ ).

The time-scale [s] for such a reaction is

$$\tau^* = C_\tau \left( \frac{\nu}{\varepsilon} \right)^{\frac{1}{2}} \quad (2.33)$$

The source term for mean species i is defined as:

$$R_i = \frac{\rho(\xi^*)^2}{\tau^*[1 - (\xi^*)^3]} (Y_i^* - Y_i) \quad (2.34)$$



where:

$Y_i^*$  - the mass fraction on small scales of species  $i$  after reaction time  $\tau^*$ .

The mass fraction in small scales of species  $i$  is calculated from the Arrhenius law. Therefore, Eq. 2.34 because a non-linear equation where the solution is obtained through iterative methods. As a result, in comparison with the EDM model, the EDC model needs a relatively long calculation time for integrating the chemistry [26]. On the other hand, it is more reliable than EDM which involves empirical constants  $A$  and  $B$  having no physical meaning.

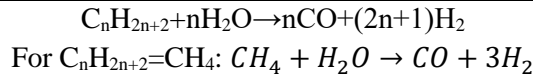
### 2.3.5 Gas phase kinetic parameters

This sub-chapter considers the most widely investigated gas-phase reactions with kinetic parameters for the global approach – Table 2.10 and Table 2.11. One may notice that similarly to devolatilization, kinetic parameters for the particular gas-phase reactions also kept repeating for different reactors with different operating conditions.

Table 2.10. Gas-phase reactions with kinetic parameters [31].

$CO + 0.5O_2 \rightarrow CO_2$	
The Westbrook and Dryer: (1981)	
Reactors: 1,2,3,4,5,6,8,9	
Number of works, that applied The WD mechanism:	
Used by: [75,80,98,101,107–111,114,115,120,82,125,84,86,87,90–93]	
$k = AT^n \exp\left(-\frac{E_a}{RT}\right), n = 0$	
$A = 2.2 \cdot 10^{12} s^{-1}, E = 1.67 \cdot 10^8 J/kmol$	
Siminski et al (1972) [157]: Reactors: 7	
Number of works, that applied kinetics based on [157]	
Used by: [116,117]	
$k = -AP^{0.3}T_g M_v(C_v)^{0.5}C_0 \exp\left(-\frac{12200}{T_g}\right)$	
$CO + H_2O \leftrightarrow CO_2 + H_2$	
<u>Forward rate:</u>	<u>Backward rate:</u>
Jones and Lindstedt:	Gururajan (1992):
Reactors: 2,3,5,8,9	Reactors: 2,5
$A = 2.75 \cdot 10^{10} s^{-1}$	$A = 2.65 \cdot 10^{-2}$
$E = 0.838 \cdot 10^8 J/kmol$	$E = 3.96 \cdot 10^3 J/kmol$
Used by:	Used by: [80,114,125]
[80,88,108,114,120,125,130,158][101]	Bustamente et al. (2004)
Modified Jones and Lindstedt:	Reactors: 3,6
$A = 2.75 \cdot 10^9 s^{-1}$	$A = 2.2 \cdot 10^7$
Reactors:1	$E = 1.9 \cdot 10^8 J/kmol$
Used by: [86,87]	Used by:
$A = 2.75 \cdot 10^2 s^{-1}$	[93,98,109,110,115]
Reactor: 3	
Used by: [75,92]	
$A = 2.75 s^{-1}$	

<p>Reactors: 2,5  Used by: [82,90,91,142]  Bustamante et al. (2005)  Reactors: 1,3,6  <math>A = 2.34 \cdot 10^{10}</math>  <math>E = 1.9 \cdot 10^8 \text{ J/kmol}</math>  Used by: [93,98,107,109,110,115]</p>	
<p>Equilibrium approach (Singh and Sharaf 1977):  Reactors: 1,3,4,7  <math>k_{eq} = \exp\left(-3.6893 + \frac{7234}{1.8T}\right)</math>  Used by: [84,102–104,107,113,116,117,159,160]</p>	
$H_2 + 0.5O_2 \rightarrow H_2O$	
<p><u>Forward reaction:</u>  Jones and Lindstedt:  Reactors: 1,2,3,5,6,8,9  <math>A = 6.8 \cdot 10^{15} \text{ s}^{-1}, E = 168 \text{ kJ/mol}</math>  Used by:  [80,82,109,110,114,115,125,84,86–88,90,91,98,101]  Modified Jones and Lindstedt:  <math>A = 8.8 \cdot 10^{12} \text{ s}^{-1}, E = 168 \text{ kJ/mol}</math>  Used by: [130]  Ansys Fluent default:[161]  Reactor:3  <math>A = 9.87 \cdot 10^8 \text{ s}^{-1}</math>  <math>E = 3.1 \cdot 10^7 \text{ J/kmol}</math>  Used by: [93,107]  Siminski et al (1972)  Reactor:7  Used by: [117][116]</p>	<p><u>Backward reaction:</u>  Ma, Zitney (2012)  Reactor: 3  <math>A = 2.5 \cdot 10^{10} \text{ s}^{-1}</math>  <math>E = 3.5 \cdot 10^8 \text{ J/kmol}</math>  Used by: [93]  Nakod (2013)  Reactor: 3  <math>A = 9.87 \cdot 10^8 \text{ s}^{-1}</math>  <math>E = 2.7 \cdot 10^8 \text{ J/kmol}</math>  Used by: [107]</p>
$C_nH_{2n+2} + 0.5nO_2 \rightarrow nCO + (n+1)H_2$	
<p>For <math>C_nH_{2n+2}=CH_4</math>: <math>CH_4 + 0.5O_2 \rightarrow CO + 2H_2</math>  Jones and Lindstedt:  Reactors: 1,3,6,9  <math>A = 4.4 \cdot 10^{11} \text{ s}^{-1}, E = 1.26 \cdot 10^8 \text{ J/kmol}</math>  Used by: [86,87,98,101,109,115]  Modified Jones and Lindstedt:  Reactors: 2  <math>A = 3 \cdot 10^8 \text{ s}^{-1}, E = 1.26 \cdot 10^8 \text{ J/kmol}</math>  Used by: [80,125]  Westbrook and Dryer (1984):  <math>k = 5.44 \cdot 10^{12} \exp\left(-\frac{24358}{T}\right) [CH_4]^{-0.3} [O_2]^{1.3}</math>  Used by: [84]  Siminski et al (1972)  Reactors: 7  Used by: [117][116]</p>	



Forward rate:	Backward rate:
Jones and Lindstedt:	Benyon, PhD [28]:
Reactors: 1, 9	Reactors: 2,3,5,6
$A = 3 \cdot 10^8 s^{-1}$	$A = 5.12 \cdot 10^{-14} s^{-1}$
$E = 1.26 \cdot 10^8 J/kmol$	$E = 2.73 \cdot 10^4 J/kmol$
Used by: [84,86,87,101]	Used by:
Modified Jones and Lindstedt:	[80,82,90,91,98,109,115,131]
Reactors: 2, 5	
$A = 4.4 \cdot 10^{11} s^{-1}$	
$E = 1.26 \cdot 10^8 J/kmol$	
Used by: [80,82,90,91]	
Ma, Zitney (2012)	
Reactors: 3,6,	
$A = 8 \cdot 10^7$	
$E = 2.5 \cdot 10^8 J/kmol$	
Used by: [93,98,109,115]	
Hou and Hughes [162]:	
Reactors: 3	
$A = 5.9 \cdot 10^8 s^{-1}$	
$E = 2 \cdot 10^8$	
Used by: [107,110]	
Zahradnik et al. [163] :	
Reactors: 7	
$k = 312 \exp\left(-\frac{30000}{1.987T_g}\right)$	
Used by: [117]	

Table 2.11. Tar reactions with kinetic parameters [31].

$CH_x + 0.5O_2 \rightarrow CO + \frac{x}{2}H_2$
$CH_x + H_2O \rightarrow CO + \left(\frac{x}{2} + 1\right)H_2$
Tar is represented here as a $CH_x$ compound. This approach was incorporated by: [77,86,87,94,99–101,125]
Reactors: 1,8,9
The reaction rates are in fact assumed as for $CH_4$ (Jones and Lindstedt mechanism) because the rates with $O_2$ and $H_2O$ for many hydrocarbons, including $CH_4$ , do not vary considerably from one another. Used by: [105,106]
$C_2H_2 + O_2 \rightarrow CO + 2H_2$
Reactors: 2,4,5
Only eddy dissipation model: [82,90–92]
$C_6H_6 + 3O_2 \rightarrow 6CO + 3H_2$
Reactors: 3,4
Only eddy dissipation model: [75,108]

---

Petersen et al [164]:

Reactors: 3,6

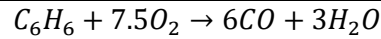
$$A = 1.58 \cdot 10^{15} \text{ m}^3/\text{kmol} \cdot \text{s}$$

$$E = 2 \cdot 10^8 \frac{\text{J}}{\text{kmol}}, n = 0, a = 1, b = 1, c = 0$$

$$k = AT^n \exp\left(-\frac{E}{RT}\right) [F]^a [O]^b [3^{rd}]^c$$

Used by: [98,109,115]

---



Parameters taken from: Fluent default [161]:

Reactors: 3

$$A = 1.125 \cdot 10^9 \text{ s}^{-1}$$

$$E = 1.256 \cdot 10^8 \frac{\text{J}}{\text{kmol}}, a = 0.1, b = 1.85$$

Used by: [93]

Parameters taken from: Turns SR. [165]:

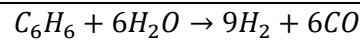
Reactors: 3,6

$$A = 2 \cdot 10^8, E = 1.255 \cdot 10^8 \text{ J/kmol}$$

$$a = -0.1, b = 1.85$$

Used by: [98,109,115]

---



Parameters taken from: Ma and Zitney [93]:

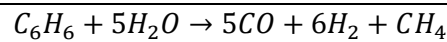
Reactors: 3

$$A = 8 \cdot 10^8, E = 2.5 \cdot 10^8 \text{ J/kmol}$$

$$a = 0.5, b = 1$$

Used by: [93]

---



Parameters taken from: Virks et al. [166]:

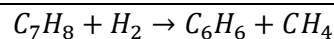
Reactors: 3,6

$$A = 4.4 \cdot 10^8, E = 2.2 \cdot 10^8 \text{ J/kmol}$$

$$a = 1, b = 1$$

Used by: [98,109,115]

---



Parameters taken from: Jess et al. [167]:

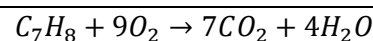
Reactors: 3,6

$$A = 1.04 \cdot 10^{12}, E = 2.47 \cdot 10^8$$

$$a = 1, b = 0.5$$

Used by: [98,109,115]

---



Parameters taken from: Turns SR. [165]:

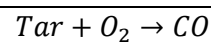
Reactors: 3,6

$$A = 1.6 \cdot 10^8, E = 1.255 \cdot 10^8 \text{ J/kmol}$$

$$a = -0.1, b = 1.85$$

Used by: [98,109,115]

---



Nakod [107]:

Reactor: 3

---

---

Species “Tar” is a pseudo gas phase species. It comprises left over carbon from volatile matter, if any.

$$A = 1e + 15, E = 1e + 08$$

$$a = 1, b = 0.5$$


---

### 2.3.6 Summary of gas phase stage

Sub-chapter 2.3 presented the most widely applied global combustion reaction mechanisms, detailed combustion mechanisms, kinetic parameters, the impact of the water-gas shift reaction, and the most widely applied turbulence-chemistry interaction approaches. Based on the literature review, no publication was found that thoroughly investigated the impact of gas-phase modeling stage on entrained flow coal gasification. Without such information, it is unclear how the incorporated combustion-based reaction mechanisms or turbulence-chemistry interaction approaches will perform in gasification conditions. As a result, one of the goals of this dissertation is to investigate these uncertain aspects. Different global reaction mechanisms and turbulence-chemistry interaction approaches strictly in gasification conditions will be examined and the aim will be to determine which approach is most suitable for reproducing the entrained flow gasification process. The detailed CRECK mechanism will be investigated and compared to GRI-Mech. The importance of the water-gas shift reaction will be further investigated. The results from the analysis will be discussed in detail in Chapter 5.

### 2.4 Char conversion modeling

In comparison with all the gasification steps, the char conversion process is the coal gasification rate-limiting step which determines the residence time in the gasifier. For the gas-solid reaction to take place, the following steps are required (Figure 2.9): the diffusion of the reactant gases from the bulk to the external surface, diffusion into the particle pores, adsorption, the chemical reaction, and desorption, and re-diffusion to the bulk. Usually one of the steps is considerably slower than the rest and it becomes the rate-limiting step that controls the overall gas-solid reaction rate. When it comes to entrained flow gasifiers and their typical operating conditions (regime II), the pore diffusion step is the most dominant factor constricting the overall reaction rate (Figure 2.10). In regime II the activation energy ( $E_a$ ) is equal to half of the true activation energy ( $E_t$ ):  $E_a = 0.5E_t$ , while the reaction order ( $n$ ) and the true reaction order ( $m$ ) are related in the following way:  $n = \frac{m+1}{2}$ .

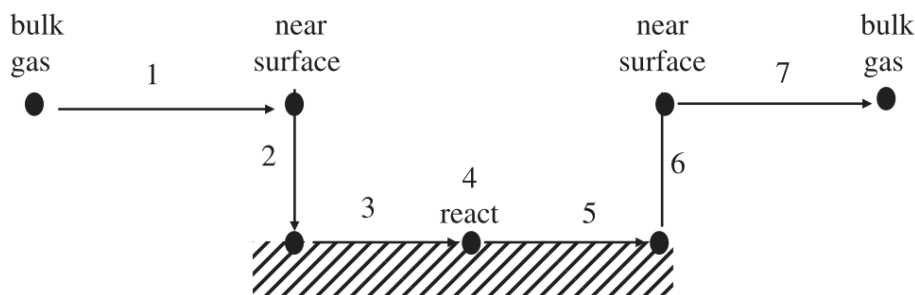


Figure 2.9. Potential rate-limiting steps in char conversion process [31].

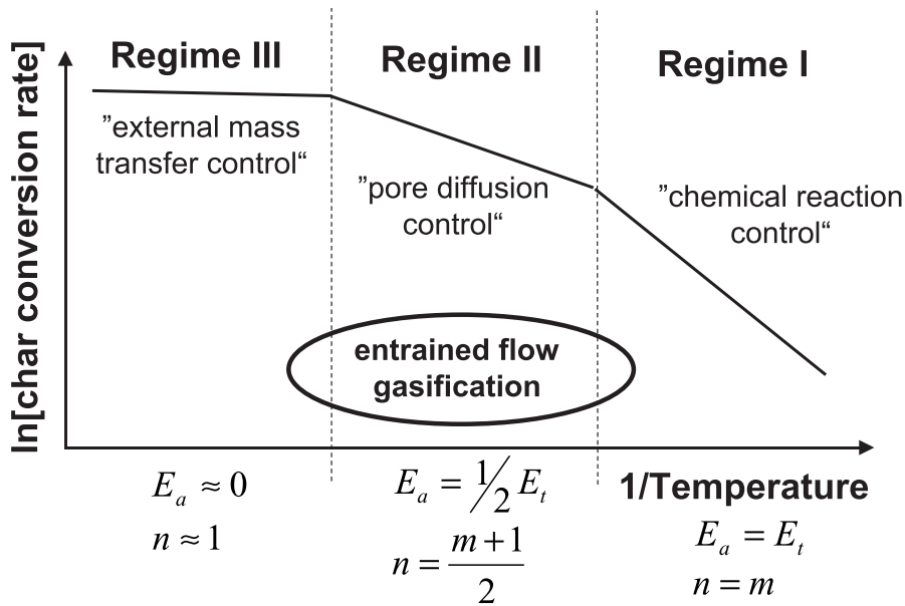


Figure 2.10. Arrhenius plot of char conversion dominant regimes in entrained flow gasification [31].

External mass transfer control (regime III) leads to carbon consumption on the external particle surface. The models developed by Smith [168], Baum and Street [76], or the shrinking core model [159] are usually applied there where bulk diffusion can be perceived by considering the competition between chemical kinetics and film diffusion. In regime II pore diffusion controls the species transport to the particle internal surface area. A significant concentration gradient is established within the char particle as the gas is consumed before it can fully penetrate all particle pores. The effectiveness factor is usually used. Regime I is dominated by chemical reaction control. It occurs mostly in the oxygen-depleted regions with lower temperatures. In this regime, the gas concentration throughout the particle is the same as in the bulk gas. The Arrhenius and the Langmuir-Hinshelwood kinetics are generally used.

### 2.4.1 Global mechanisms

In this section the surface reaction rate modeling approaches most widely used in coal gasification will be presented, from the basic ones which incorporate the Arrhenius kinetics with film diffusion effects to more advanced which include the effect of gas partial pressures on reaction rates, intrinsic surface area evolution, ash inhibition, CO or H<sub>2</sub> inhibition, thermal annealing and pore closing. A review of the main sub-grid models for char combustion has already been carried out by Edge et al. [169].

Most of the studies incorporated single-film models characterized by the sole consideration of heterogeneous reactions at the particle. Homogeneous reactions in the boundary layer are not taken into account (Figure 2.11).

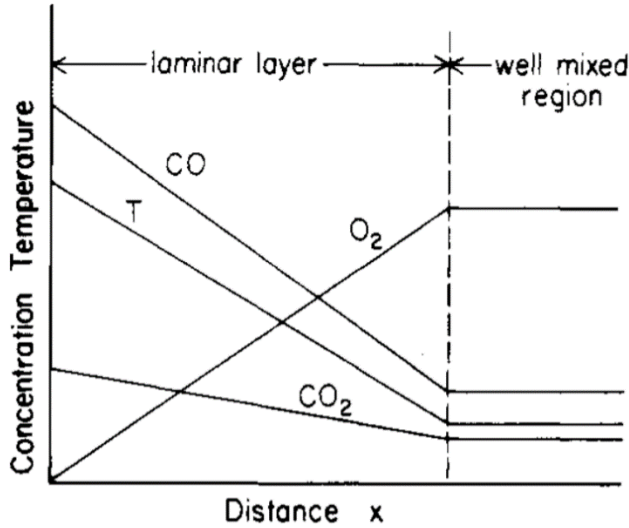


Figure 2.11. Single film model [31].

The *kinetics/diffusion fixed-core model* uses the Field [170] and the Baum and Street [76] model. The surface of the reaction is assumed to be within a fixed radius coinciding with the original particle surface area. The rate is determined either by the kinetics or the diffusion rate. It is defined as follows:

$$\frac{dm_p}{dt} = \frac{A_p p_{ox}}{\frac{1}{D_0} + \frac{1}{R_{kin}}} \quad (2.35)$$

where:

- $p_{ox}$  – the partial pressure of the oxidant
- $D_0$  – the diffusion rate coefficient ( $m^2/s$ )
- $R_{kin}$  – the kinetic rate (units vary)
- $A_p$  – the particle surface area ( $m^2$ ).

The main assumption of the *kinetics/diffusion fixed-core model* is that heterogeneous reactions take place on the external particle surface. The char characteristics remain constant during the process. This model does not take into account particle swelling, char porosity, internal reactions, or internal oxygen diffusion. Another disadvantage is the inability to capture the transition between the combustion regimes due to the poor definition of surface area variation. In the mathematical formulation of the Baum and Street model, only the  $C+O_2$  reactions were considered. The gasification reactions with  $CO_2$  and  $H_2O$  were neglected.

The *diffusion-limited approach* assumes that the reaction rate is determined solely by the diffusion of the gaseous oxidant to the particle surface.

$$\frac{dm_p}{dt} = Sh\pi d_p D_M \frac{Y_{ox} T_{\infty} \rho}{S_b \frac{(T_p + T_{\infty})}{2}} = 2\pi d_p D_M \frac{Y_{ox} T_{\infty} \rho}{S_b \frac{(T_p + T_{\infty})}{2}} \quad (2.36)$$

The equation is derived from the Baum and Street model [76] with the kinetic contribution ignored.

where:

$D_M$  – the diffusion rate coefficient for the oxidant in the bulk gas ( $m^2/s$ )

$Y_{ox}$  – the mass fraction of the oxidant in the gas

$S_b$  – the stoichiometric coefficient ( $kg_{ox}/kg_C$ )

$Sh$  – the Sherwood number.

The Sherwood number is equal to two. It assumes that the gas and the particles move at almost the same velocity ( $Re \approx 0 \rightarrow Sh \approx 2$ ) where stagnant atmosphere can be postulated.

$$Sh = 2 + 0.6Re^{0.5}Sc^{0.33} \quad (2.37)$$

As with the kinetics/diffusion fixed-core model, the diffusion-limited approach considers unchanged particle diameter. It is also based on the char external area. Carbon consumption on the external particle surface occurs in regime III conditions, where the particle diameter should decrease and the density ought to remain unchanged. In the diffusion-limited model the diameter is constant and the density decreases which is inconsistent with regime III conditions. Particle size and density are the two known properties to affect the reaction rate.

The *shrinking core (SCM) model* developed by Wen and Chaung [159] is an extended and more accurate version of the kinetics/diffusion fixed-core model. Apart from the Arrhenius kinetics and diffusion effects, the model includes the reduction in the particle radius as conversion proceeds. The effect of diffusion through the surrounding ash layer is taken into account. Carbon consumption occurs only on the outer surface of the particle where its diameter decreases over time.

$$\frac{dm_p}{dt} = \frac{A_p p_{ox}}{\frac{1}{D_0} + \frac{1}{R_{kin} \cdot \left(\frac{r_p}{R_p}\right)^2} + \frac{1}{D_{ash}} \left(\frac{R_p}{r_p} - 1\right)} \quad (2.38)$$

where:

$D_{ash}$  - an ash diffusion constant dependent on the diffusion rate and the ash voidage layer

$r_p$  and  $R_p$  are the instantaneous radius and the original radius of the char-ash particle, respectively.

The SCM model is considered to be the best fit at very high reaction rates, where the mass transfer to and from the exterior of the particle is the rate-limiting step [171].

The most frequently applied approach, available in the CFD software ANSYS Fluent as the *multiple surface reaction model*, is based on the implicit relation - Eq. (2.40), discussed in detail by Smith [168]. With regard to the kinetics/diffusion fixed core model (Baum and Street [76] and Field [170]), which considers only the C-O<sub>2</sub> reaction, Smith [168] generalized his approach for multispecies surface reactions which were represented by C-O<sub>2</sub>, C-CO<sub>2</sub>, and C-H<sub>2</sub>O reactions.

The reaction rate of species  $j$  undergoing reaction  $r$  is defined as follows:

$$\bar{R}_{j,r} = A_p \eta_r Y_j R_{j,r} \quad (2.39)$$

where:



$\bar{R}_{j,r}$  - the rate of particle surface species depletion (kg/s)

$A_p$  - the particle surface area,  $A_p = \pi d_p^2$  (m<sup>2</sup>)

$Y_j$  - the mass fraction of surface species j in the particle

$\eta_r$  – the effectiveness factor (the default value: 1)

$R_{j,r}$  - the rate of particle surface species reaction per unit area ( $\frac{kg}{m^2s}$ )

The rate of particle surface species reaction per unit area is defined in the iterative way:

$$R_{j,r} = R_{kin,r} \left( p_n - \frac{R_{j,r}}{D_{0,r}} \right)^{N_r} \quad (2.40)$$

where:

$p_n$  - the bulk partial pressure of the gas phase species (Pa)

$D_{0,r}$  - the diffusion rate coefficient for reaction r

$R_{kin,r}$  - the kinetic rate of reaction r (units vary)

$N_r$  - the apparent order of reaction r.

The diffusion rate coefficient for reaction r is given by:

$$D_{0,r} = C_{1,r} \frac{\left[ \frac{T_p + T_\infty}{2} \right]^{0.75}}{d_p} \quad (2.41)$$

where  $C_{1,r}$  – an overall mass diffusion-limited constant (the default value:  $5 \cdot 10^{-12} \text{ sK}^{-0.75}$ )

The overall mass diffusion-limited constant ( $C_{1,r}$ ) depends on a heterogeneous reaction [150]. In the CFD software ANSYS Fluent this parameter can be defined for the specific heterogeneous reaction, but only as a constant value. As a result, Eq. (2.41) does not accurately account for each gasifying agent.

Chen et al. [150] characterized the overall mass-diffusion limited constant in the following way:

$$C_{1,r} = \frac{v_r M_c \bar{M}}{M_r R T_0^{1.75}} Sh \cdot D_{r,0} \cdot \frac{P_0}{P} \quad (2.42)$$

where:

Sh – the Sherwood number

$v_r$  – the stoichiometric coefficient for reaction r

$\bar{M}$  – the average molecular weight of the gas mixture in the boundary layer (kg/kmol)

$M_c, M_r$  – the molecular weight of char and specific gas components, respectively (kg/kmol)

$P_0, T_0$  – the reference pressure (Pa) and temperature (K).

The kinetic rate of reaction r in the multiple surface reaction model is defined as:

$$R_{kin,r} = A_r T_p^{\beta_r} \exp\left(-\frac{E_r}{RT_p}\right) \quad (2.43)$$

In this approach, the solution is obtained using an iterative procedure, except when the reaction order is equal to 0 or 1. When the reaction order is equal to one, the char consumption rate takes the following form:

$$\bar{R}_{j,r} = \frac{A_p \eta_r Y_j p_n}{\frac{1}{D_0} + \frac{1}{R_{kin}}} \quad (2.44)$$

One may observe that the form of the multiple surface reaction approach presented in Eq. (49) resembles the kinetics/diffusion fixed-core model - Eq. (2.35). However, with regard to the latter, the former considers two additional parameters that affect the reaction rate:

- the carbon mass fraction in the particle ( $Y_j$ ). The higher its conversion degree, the slower the reaction rate,
- the effectiveness factor. It is related to the surface area [161] and is defined as a constant value. It appeared from the review that each of the researchers who incorporated this approach assumed  $\eta$  to be equal to one. Nonetheless, the effectiveness factor that accounts for the intrinsic effects should not be constant during char conversion.

However, based on Eq. (2.39), one may conclude that the multiple surface reaction model should not be considered as the intrinsic-based approach [168]. The reasons are as follows:

- in the multiple surface reaction model, the surface area that participates in the reaction is the external surface area  $A_p$  ( $\pi d_p^2$ ). In general, the effectiveness factor was developed to predict the fraction of the surface area involved in regime II. Since the loss of the effective surface area that participates in the reaction is due to pore diffusion resistance, this area should be related to the intrinsic surface area, not to the external surface area,
- according to the multiple surface reaction model when  $\eta=1$ , the entire external surface area is considered. However, the heterogeneous reactions that take place only on the outer surface of the particle indicate regime III conditions, where  $\eta \approx 0$ . Therefore, based on the characteristic features of the effectiveness factor mentioned above, unless a more precise description of the effectiveness factor for the multiple surface reaction approach is provided, it should be rather perceived as the correction parameter that accounts for the impact of other phenomena, e.g. the nonporous fraction of the external particle surface. As a result, the multiple surface reaction approach in the current form should also be considered as the surface-based kinetics/diffusion model.

The *intrinsic-based models* take into account pore diffusion phenomena [168,172]. It is important because the surface area of char and pores and their diffusion effects have a major impact on the overall char burnout. The commonly applied approach is based on the  $n^{\text{th}}$  order equation with the effectiveness factor  $\eta$ . The reaction rate is determined in the following way:

$$R_i = \eta_i A_g k_i P_{s,i}^n \quad (2.45)$$

where:

$P_{s,i}$  – the partial pressure of reactant gas  $i$  on the particle surface (Pa) ( $i = O_2, CO_2, H_2O, H_2$ )

$A_g$  – the specific internal surface area of char ( $m^2/kg$ )

$k_i$  – intrinsic reactivity expressed in the Arrhenius form

$n$  – the reaction order.

Effectiveness factor  $\eta$  [172,173] is a ratio of the actual char conversion rate to the rate as if there was no pore diffusion effect.

$$\eta = \frac{R_{obs}}{R_{sl}} \quad (2.46)$$

where:

$R_{obs}$  – the observed reaction rate

$R_{sl}$  – the surface limited reaction which would be observed with no mass transfer restriction.

As the surface reaction rate increases, the mass transfer rate reduces the overall reaction rate, causing the effectiveness factor to be less than one. Hence, in regime I (Figure 2.10) the effectiveness factor is equal to 1, which indicates that all pores are penetrated with the oxidant and that the reaction takes place in the particle interior. Particle size is almost constant, whereas particle density decreases. In regime II the effectiveness factor is in the range of (0,1), where both particle size and density gradually decrease. In regime III  $\eta$  is very close to zero and the reaction takes place at the outer surface of the particle, where particle size decreases and density remains constant [174]. Effectiveness factor is a function of Thiele modulus  $\Phi$  and for the spherical particle for gasifying agent  $i$  it is expressed as follows [173]:

$$\eta_i = \frac{1}{\phi_i} \left( \frac{1}{\tanh(3\phi_i)} - \frac{1}{3\phi_i} \right) \quad (2.47)$$

The Thiele modulus describes the ratio of the surface reaction rate to the rate of diffusion into particle pores [172]:

$$\phi_i = \frac{d_p}{6} \sqrt{\frac{(n_i + 1)k_i A_g \rho_p R T_p v_i P_{s,i}^{n-1}}{2D_{eff,i} M_c}} \quad (2.48)$$

where:

$v_i$  – the stoichiometric coefficient of each gasifying agent for each mole of carbon consumed

$\rho_p$  – particle density ( $kg/m^3$ )

$M_c$  – the molecular weight of carbon ( $kg/kmol$ )

$A_g$  – the specific internal surface area of the particle ( $m^2/kg$ )

$k_i$  – intrinsic reactivity

$T_p$  – particle temperature (K)

$D_{eff}$  – effective diffusivity ( $m^2/s$ ).

Effective diffusivity is expressed as follows:

$$D_{eff,i} = \frac{\theta}{\tau} \left( \frac{1}{D_{KN,i}} + \frac{1}{D_{0,i}} \right)^{-1} \quad (2.49)$$

where:

$D_{KN}$  – the Knudsen diffusion coefficient (m<sup>2</sup>/s)

$D_0$  – the molecular diffusion coefficient (m<sup>2</sup>/s)

$\theta$  – particle porosity

$\tau$  – the tortuosity of the pores.

The molecular diffusion coefficient  $D_0$  has already been characterized for the multiple surface reaction model - Eq. (2.41). However, as it was emphasized, this simplified relation does not accurately account for each gasifying agent that participates in the reaction.

Jeong et al. [109,115] defined the molecular diffusion coefficient with the empirical correlation:

$$D_{0,i} = \frac{T^{1.75} \left( \frac{1}{M_i} + \frac{1}{M_{CO}} \right)^{1/2}}{P \left( (V_i)^{1/3} + (V_{CO})^{1/3} \right)^2} \cdot 10^{-7} \quad (2.50)$$

where:

$P$  – total pressure (atm)

$V_r$  – binary diffusion volume for the gas component  $i$  (O<sub>2</sub>, CO<sub>2</sub>, H<sub>2</sub>O) (cm<sup>3</sup>)

The Knudsen diffusion coefficient is given as follows:

$$D_{KN} = \frac{1}{3} \bar{d}_{pore} \sqrt{\frac{8RT_p}{\pi \cdot M_i}} \quad (2.51)$$

where:

$\bar{d}_{pore}$  – the mean pore diameter (m).

The rate of diffusion is affected by pore size. Char consists of macropores with pore diameters greater than 50 nm, mesopores with pore diameters between 2 and 50 nm, and micropores with diameters between 0.4 and 2 nm [171]. When the diameter of pores is large in comparison with the mean free path of gas molecules, bulk diffusion is the dominant mechanism. Otherwise, the mechanism changes to slower Knudsen diffusion.

According to the kinetic theory of gases, the mean free path can be estimated as:

$$s_{mean} = \frac{2.33 \cdot 10^{-20} T}{\xi^2 p_{torr}} \quad (2.52)$$

where:

$s_{mean}$  – the mean free path (cm)

$\xi$  – molecular diameter (cm)

$P_{\text{torr}}$  – pressure (torr)

T- temperature (K).

On the other hand, some studies [99] express effective diffusivity by neglecting the influence of micro-porosity.

$$D_{eff,i} = \theta D_{0,i} \frac{f_{\theta}}{\tau} \quad (2.53)$$

where  $f_{\theta}$  is the fraction of the total porosity in feeder pores.

This approach was also introduced into the advanced CBK model [11,12]. The main advantage of this approach is that all the parameters apart from  $f_{\theta}/\tau$  are known. This unknown  $f_{\theta}/\tau$  factor can be expressed in an empirical way and can also include other effects, e.g. micro-porosity.

In order to accurately determine the intrinsic reaction rate - Eqs. (2.45), (2.48), partial pressures of the reactants on the particle surface are required. Eq. (2.54) allows evaluating the partial pressure of the reactants ( $P_{s,i}$ ) including the effect of Stefan flow [94,99].

$$\left(1 - \gamma_i \frac{P_{s,i}}{P_t}\right) = \left(1 - \gamma_i \frac{P_{\infty,i}}{P_t}\right) \exp\left(\frac{q_i \gamma_i}{k_{d,i} P_t}\right) \quad (2.54)$$

where:

$q_i$  – mass flux of i per external particle surface unit

$P_t$  – gas total pressure

$P_{\infty,i}$  – partial pressures of the species i in the bulk phase

$k_{d,i}$  – the transport coefficient,  $k_{d,i} = \frac{Sh D_i M_i}{R_{gas} T_{mean} d_p}$

$\gamma_i$  – molar ratio between the total flux and the flux of the i-species.

One of the drawbacks of the intrinsic-based sub-models is their poor modeling of the influence of particle velocity and heat transfer coefficients on the combustion/gasification rate [26]. Furthermore, the  $n^{\text{th}}$  order power-law approach does not directly include the effect of product, saturation, or competitive inhibition. It is a simplification compared to Langmuir-Hinshelwood kinetics and should not be used for a wide range of operating conditions. Moreover, the form of the intrinsic-based model - Eq. (2.45) is characterized by the inability to predict the carbon consumption rate correctly when the effectiveness factor is close to zero (regime III). In such conditions, the external surface area must be included when the reaction is taking place at the outer surface of the particle and not its internal surface area. In [101,172,175], the specific surface area of char  $A_g$  consists of internal part  $A_{g,in}$  and external part  $A_{g,ex}$ . As a result, the relation for the char reaction rate is expressed as follows:

$$R_i = (\eta_i A_{g,in} + A_{g,ex}) k_i P_{s,i}^n \quad (2.55)$$

When the effectiveness factor approaches zero,  $A_{g,ex} \gg \eta_i A_{g,in}$  and the  $R_i \rightarrow A_{g,ex} k_i P_{s,i}^n$ .

With regard to the critical discussion concerning the multiple surface reaction model, one may observe that the effectiveness factor, in this particular case, strictly correlates with the

internal surface area, whereas the external surface area is independent of it.

The *random pore (RPM) model* developed by Bhatia and Perlmutter [176] describes the evolution of the internal surface area during char conversion. Eqs. (2.56) and (2.57) show the mass- and volume-based forms of the RPM model:

$$A_g = A_{g,0} \sqrt{1 - \psi \ln(1 - x)} \quad (2.56)$$

$$A_v = A_{v,0} (1 - x) \sqrt{1 - \psi \ln(1 - x)} \quad (2.57)$$

where  $A_v = \rho_p A_g$

Eq. (2.56), expressed in ( $\text{m}^2/\text{g}$ ) and Eq. (2.57), expressed in ( $\text{m}^2/\text{m}^3$ ), relate the surface area to sample mass and volume, respectively. Considering the reaction rate to be a function of char mass, Eq. (2.56) should be applied. Kleinhans et al. [174] noticed that Eq. (2.57) is very often misused in the literature to fit experimental data ( $\text{m}^2/\text{g}$  instead of  $\text{m}^2/\text{m}^3$ ). Despite the fact that the fit works well, it is physically incorrect.

where:

$x$  – the conversion ratio

$\psi$  – a structure parameter for depending on the coal type, determined by a least-squares fit

$A_{g,0}, A_{v,0}$  – the mass- and volume-based initial specific surface area.

In the RPM model, the pore surface area increases. During the gasification process, pores begin to merge and the walls dividing them start disappearing which leads to surface area loss.

As opposed to the SCM model which was a mass transfer limiting mechanism where porosity was assumed to be constant and particle diameter changed during the process, the RPM model states that the surface reaction is a rate-limited mechanism where the particle diameter is constant and porosity is not. This approach assumes cylindrical pores of different sizes within the solid phase. It is one of the models most commonly used to describe the specific surface area. However, the model assumptions (the constant particle diameter and the neglect of the influence of mineral matter) indicate that it cannot take into account all the effects necessary to comprehensively describe particle surface area evolution at high temperatures. The constant diameter assumption can be valid only in regime I [101]. The RPM model predicts an increase in mass-specific surface area during the later stages of char conversion. However, the literature on the subject suggests that as regards the ash melting temperatures the trend is opposite [50,177,178].

Kumar et al. [86] examined the direct influence of the kinetics/diffusion fixed-core model, the shrinking core model, and the random pore model in terms of coal conversion under high-pressure conditions in a two-stage entrained flow gasification reactor. Only the random pore model with the Langmuir-Hinshelwood kinetics managed to reproduce the results, considering major gas species estimation and final coal conversion, with a relatively high agreement. The shrinking core model performed better than the kinetics/diffusion fixed-core approach.

Halama and Spliethoff [101,179] used the  $n^{\text{th}}$  order effectiveness factor approach to

model the entrained flow gasification of coal and applied state-of-the-art methods taking into account pore closing (important above the ash fusion temperature – ash melting) and diameter evolution, which the random pore model does not include. Pore closing is implemented through a time- and temperature-dependent factor which reduces the total length and void volume of the pore system on the basis of devolatilization experiments. Diameter evolution depends on the char conversion and temperature exponent which is dependent on the reaction regime. The change in particle diameter with respect to the conversion rate is expressed in terms of the power-law approach – Eqs. (2.58) and (2.59).

$$d_{p,j} = (\Omega_j)^{\beta_j} \cdot d_{p,j-1} \quad (2.58)$$

$$\Omega_j = 1 + \left( \left( \frac{d_{p,min}}{d_{p,j-1}} \right)^3 - 1 \right) \cdot \left( 1 - \frac{m_{c,p,j}}{m_{c,p,j-1}} \right) \quad (2.59)$$

$$\beta_j = \frac{1}{3} \cdot (1 - \bar{\eta}_j) \quad (2.60)$$

The regime-dependent exponent was modeled assuming a linear relationship between  $\beta_j$  and reaction-rate-weighted mean effectiveness factor  $\bar{\eta}_j$ .

where:

$\Omega_j$  – the char conversion over time step j

$d_{p,j}$  – the particle diameter over time step j

$\beta_j$  – the regime-dependent exponent over time step j

$d_{p,min}$  – the ash fusion diameter

$\bar{\eta}_j$  – the reaction-rate-weighted mean effectiveness factor over time step j

$m_{c,p,j}$  – the particle carbon mass over time step j.

The decrease in the total length of the pore system is presented in Eq. (2.61)

$$L_{pore} = L_{pore,init} \cdot \frac{1 - PO}{1 - PO_{init}} \cdot \frac{V_p - V_{ash}}{V_{p,init} - V_{ash}} \cdot F_{pc} \quad (2.61)$$

where:

$PO$  – the porosity of the carbon matrix  $PO = \frac{V_{void}}{V_{void} + V_c}$

$F_{pc}$  – the pore closing factor

$V_{void}$  – the void volume.

The following assumptions are made in this model:

- cylindrical pores (carbon matrix) and ash are uniformly distributed,
- internal surface area  $S_{in}$  depends on the mean pore diameter and pore system total length  $L_{pore}$ ,
- pore intersections lead to a reduction in  $L_{pore}$ ,

- pore closing and the decreasing diameter cause a reduction in  $L_{pore}$  and void volume  $V_{void}$ ,
- the procedure considers each particle in the system.

The authors did not include such phenomena as fragmentation or ash layer inhibition due to high fuel density, low swelling propensity, and low ash content. The inhibition effects due to CO or H<sub>2</sub> or saturation effects were also neglected.

Some studies have shown the importance of including particular char morphologies when estimating char-CO<sub>2</sub> conversion rates at high temperatures and pressures (1670K, 2MPa) [180,181]. The studies have demonstrated that the assumption of coal particles as porous spheres can be incorrect when particles represent Group I or Group II (Table 2.12 and Table 2.13) with high internal voidage. Mostly Group III of chars, characterized by low swelling propensity and high density, can be assumed to represent porous spherical particles. Due to the fact that the reacting char particle usually represents a combination of each group, it is necessary to account for each group since the groups are characterized by different properties in terms of restricting gas diffusion. For example, gas restriction in Group I and Group II is effected only by the outer wall, whereas in Group III it takes place along the particle radius, extending to the center. The overall effectiveness factor can be calculated by taking into consideration the impact of each of the morphological groups in the char sample.

$$\eta_{sum} = (Group\ I)\eta_{flat\ plate\ L_1} + (Group\ II)\eta_{flat\ plate\ L_2} + (Group\ III)\eta_{sphere} \quad (2.62)$$

Group I and II type particles are also more likely to experience fragmentation, as the thin particle wall becomes thinner and eventually falls apart [182]. Kajitani et al. [183] noticed a decrease in particle size in either CO<sub>2</sub> or H<sub>2</sub>O. The size was constant until 50% of the conversion and decreased between 50-70% of the latter. This change was attributed to fragmentation.

The effect of char morphology groups, taking into account the modified effectiveness factor – Eq. (2.62), has been lately examined by Hla et al. [83] for four different coals. The study was based on Hodge’s work [180]. The model was able to show differences in the gasification behavior for the examined coals, validating the presented approach.

Table 2.12. Benfell’s shape representation system [83,180,184].




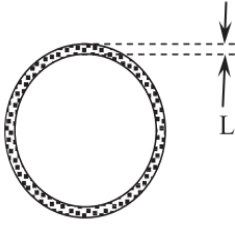
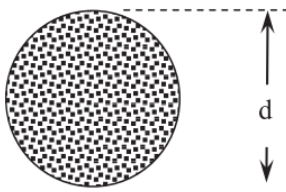
Char groups	Group I	Group II	Group III
Two-dimensional representation			
Porosity (%)	>60	40-60	<40
Average wall thickness (μm)	<5	>5	>5
Shape	Spherical	Sub-spherical	Angular
Swelling ratio	>1.3	<1.0	<0.9
Residual mass ratio	0.1-0.5	0.1-0.5	1.0



Table 2.13. Calculation of Thiele modulus and effectiveness factor based on char morphology [83,180].

Morphology	Group I and II	Group III
Geometry	Flat plate	Sphere
Shape factor	Wall thickness (L)	Particle size (d)
		
Thiele modulus	$\phi = \frac{L}{2} \sqrt{\frac{(n+1)k_i A_t m_{c,p} R T_p \nu P_s^n \sigma_a}{2M_c \cdot D_{eff} \cdot p_s}}$	$\phi = \frac{d_p}{6} \sqrt{\frac{(n+1)k_i A_t m_{c,p} R T_p \nu P_s^n \sigma_a}{2M_c \cdot D_{eff} \cdot p_s}}$
Effectiveness factor	$\eta_{flat} = \frac{\tanh \phi}{\phi}$	$\eta_{sphere} = \frac{1}{\phi} \left( \frac{1}{\tanh(3\phi)} - \frac{1}{3\phi} \right)$

The single  $n^{\text{th}}$  order reaction (SNOR) model, proposed by Liu and Niksa [12], includes such effects as CO and H<sub>2</sub> inhibition and structural evolution. The rates of the reaction of char with CO<sub>2</sub>, H<sub>2</sub>O, H<sub>2</sub>, and O<sub>2</sub> are respectively expressed as follows:

$$R_{C-CO_2} = \theta_g(X) \cdot \frac{k_{s,CO_2} \cdot P_{s,CO_2}^{n_{s,CO_2}}}{1 + K_{CO} P_{s,CO_2}} \quad (2.63)$$

$$R_{C-H_2O} = \theta_g(X) \cdot \frac{k_{s,H_2O} \cdot P_{s,H_2O}^{n_{s,H_2O}}}{1 + K_{H_2} P_{s,H_2O}} \quad (2.64)$$

$$R_{C-H_2} = \theta_g(X) \cdot k_{s,H_2} \cdot P_{s,H_2}^{n_{s,H_2}} \quad (2.65)$$

$$R_{C-O_2} = \theta_o(X) \cdot k_{s,O_2} \cdot P_{s,O_2}^{n_{s,O_2}} \quad (2.66)$$

where:

$P_{s,CO_2}, P_{s,H_2O}, P_{s,H_2}, P_{s,O_2}$  – the partial pressures defined on the particle surface

$k_{s,CO_2}, k_{s,H_2O}, k_{s,H_2}, k_{s,O_2}$  – the reaction rates

$n_{s,CO_2}, n_{s,H_2O}, n_{s,H_2}, n_{s,O_2}$  – the reaction order

$K_{CO}, K_{H_2}$  – the rate constants accounting for the inhibition due to CO and H<sub>2</sub>

$\theta_g(X), \theta_o(X)$  – an empirical factor which takes into account thermal annealing, random pore evolution and changes in particle density.

This model assumes the inhibition effect due to CO and H<sub>2</sub>. This effect was observed and described in [185–188]. However, no final consensus was reached as to whether there is any other inhibitor that could noticeably affect the reaction.

Huang et al. [189] did not confirm that C-H<sub>2</sub>O and C-CO<sub>2</sub> share the active sites, which

would lead to another inhibition factor due to char reactions. On the basis of their experimental results, Everson et al. [190] concluded that the idea of separate active sites is acceptable, whereas Roberts et al. [191] found that the reaction rate of C-H<sub>2</sub>O is reduced when CO<sub>2</sub> is present.

The above expressions do not take into account the intrinsic chemistry, transport, pore evolution, and deactivation, which means that they cannot work well in a wide range of operating conditions. This global approach was supposed to closely mimic the predictions of the advanced CBK/G model through the calibration procedure, which is its main disadvantage.

The empirical factors which take into account thermal annealing, random pore evolution, or density changes are expressed in the form of polynomial decay which is a function of the char conversion extent and regression coefficients. The density change was calculated as follows:

$$\rho_c = \rho_{c,0}(1 - X)^{\alpha_n}, X = 1 - \frac{m_c}{m_{c,0}} \quad (2.67)$$

where  $\alpha_n$  is an empirical model parameter.

However, it can be noticed that this model does not include the simultaneous change in particle density and particle diameter. During the char oxidation process, the diffusion-controlled regime governs char conversion, whereby the particle diameter changes instead of density [172,192]. Considering these arguments, further improvements of the intrinsic-based models are desirable in order to avoid the many unphysical empirical parameters, which in fact only make the direct use of such models more difficult due to the necessity of proper calibration.

Thermal annealing is taken into account by Tremel and Spliethoff (2013) [50]. The main assumption is that the loss of active sites is responsible for char deactivation. The concentration of active sites decreases with increasing temperature. The measure of this decrease is the pre-exponential factor. During the experiment, the authors observed that thermal annealing did not have a major impact on the activation energy of the intrinsic char conversion, but it had an effect on the pre-exponential factor [118].

$$\frac{A_F}{A_D} = \exp\left(\omega \cdot \left(1 - \frac{T}{T_{max}}\right)\right) \quad (2.68)$$

where:

$T_{max}$  – the maximum temperature at which the lowest reactivity occurs

$A_F, A_D$  – the pre-exponential factor for current properties and highly deactivated char

$\omega$  – an adjustable parameter.

Two different active sites on the surface of char are assumed. One type of active sites is produced during pyrolysis and their character is reactive. During thermal annealing, these sites become deactivated sites with lower reactivity. A thermal annealing model was already used by Cai et al. [193], but it incorporated two adjustable parameters. Salatino et al. [194] used a two-site assumption model with a non-linear kinetic equation with three adjustable parameters. Tremel's model incorporates one adjustable parameter.

The total reaction rate is defined as:

$$r_{total} = r_{Fresh} + r_{Deact} = \left(1 + f(A_{max} - 1) \cdot A_D \cdot \exp\left(-\frac{E}{RT}\right) p^n\right) \quad (2.69)$$

where:

$A_{max}$  – the ratio of pre-exponential factors  $A_F$  and  $A_D$ .

$f$  – fresh sites (obtained from first order Arrhenius equation).

Schulze et al. [195] developed a novel intrinsic-based sub-model for spherical char particles moving in a hot gas environment consisting of  $CO_2$  and  $H_2O$ . The distinguishing feature of this approach is that it accounts for the transport of chemical species between the surface and the particle center. It is an alternative to the effectiveness factor approach to describe the internal species transport.

The mass of the char particle changes due to heterogeneous reactions at the surface and inside particle pores - Eq. (2.70).

$$\frac{dm_p}{dt} = V_p \frac{d\rho_p}{dt} + \rho_p \frac{dV_p}{dt} \quad (2.70)$$

The first term on the right side of Eq. (2.70) considers the change in particle density due to carbon conversion. The second term characterizes the decrease in particle size due to heterogeneous reactions that occur on the particle surface. The volumetric-based and surface-based carbon mass flows have the following form:

$$\dot{m}_c^V = V_p \frac{d\rho_p}{dt} = V_p S''' M_c \left( k_{R1} \left( \frac{\rho_{g,p} Y_{CO_2,p}}{M_{CO_2}} \right)^{n_{R1}} + k_{R2} \left( \frac{\rho_{g,p} Y_{H_2O,p}}{M_{H_2O}} \right)^{n_{R2}} \right) \quad (2.71)$$

$$\dot{m}_c^S = \rho_p \frac{dV_p}{dt} = A_p M_c \left( k_{R1} \left( \frac{\rho_{g,s} Y_{CO_2,s}}{M_{CO_2}} \right)^{n_{R1}} + k_{R2} \left( \frac{\rho_{g,s} Y_{H_2O,s}}{M_{H_2O}} \right)^{n_{R2}} \right) \quad (2.72)$$

where:

$k_{R1}$  and  $k_{R2}$  are the reaction constants for the gasification reaction of char with  $CO_2$  and  $H_2O$ , respectively

$\rho_{g,p}$  – the density of the gas inside pores

$S'''$  - the development of surface area (the random pore model).

This model takes into consideration the simultaneous change of particle size and apparent density with coal conversion, the thermal annealing taken from Tremel and Spliethoff [50], and the volumetric and surficial Stefan flow. In the surface-based model, heterogeneous reactions take place at the outer particle surface. Mass transport into the particle is not considered. The intrinsic sub-model accounts for pore diffusion. The results showed that the rates predicted by the intrinsic- and surface-based approaches differed locally by up to 30%. The surface-based model predicted higher char conversion rates (Figure 2.12). Consequently, a lower outlet temperature was predicted due to the endothermic character of the heterogeneous char conversion reactions.

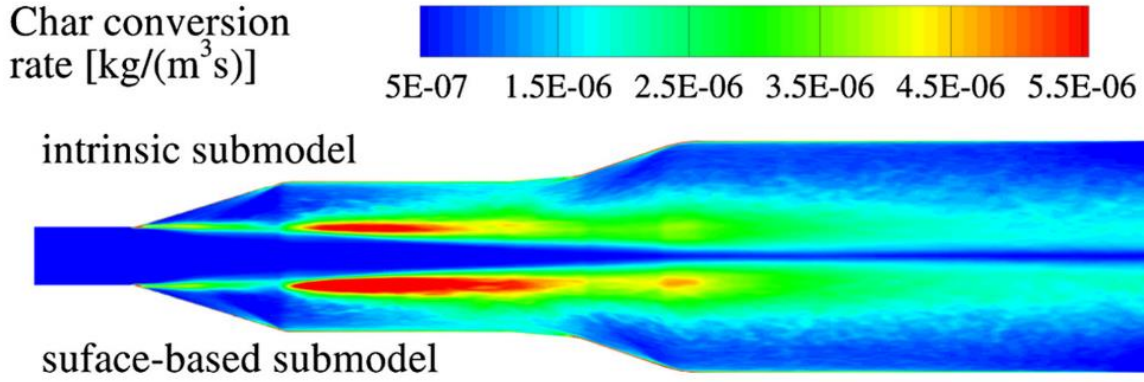


Figure 2.12. Char conversion rate for the intrinsic sub-model (upper part) and for the surface-based approach (lower part) [31].

The Stefan flow was found to have a major effect by Richter et al. [95]. It was shown that for exothermic reactions, due to the high reaction rates, the Stefan flow significantly increased the boundary layer around the particle. This layer influenced the heat transfer from the particle surface and the transport of reactants and products to or from the particle. During oxidation, the Stefan flow played a crucial role in char conversion.

The effect of gas partial pressures on surface reaction rates was modeled by Roberts and Harris [196] who applied the Langmuir-Hinshelwood (LH) equations based on the adsorption-desorption mechanism. The generally accepted  $n^{\text{th}}$  order Arrhenius equation can be inaccurate for high-pressure kinetic rate modeling. In fact, the LH equations represent much better the char- $\text{CO}_2$  and char- $\text{H}_2\text{O}$  surface reactions than the Arrhenius rate expressions [12,187,188,196–199]. The reactions commonly used for  $\text{CO}_2$  and  $\text{H}_2\text{O}$  gasification are presented in sub-chapter 2.4.2 - Detailed mechanisms. The kinetic expressions are as follows:

$$R_{\text{CO}_2} = \frac{k_1 P_{\text{CO}_2}}{1 + k_2 P_{\text{CO}_2} + k_3 P_{\text{CO}}} \quad (2.73)$$

$$R_{\text{H}_2\text{O}} = \frac{k_4 P_{\text{H}_2\text{O}}}{1 + k_5 P_{\text{H}_2} + k_6 P_{\text{H}_2\text{O}}} \quad (2.74)$$

where:

$k_1$ - $k_6$  – Arrhenius rate constants

$P_{\text{CO}_2}$ ,  $P_{\text{H}_2\text{O}}$ ,  $P_{\text{H}_2}$ ,  $P_{\text{CO}}$  – partial pressures.

The main difficulty connected with the LH equations is that the active site concentration is usually unknown. Hence very often it is assumed to be constant for different pressures, temperatures, and different char conversion levels, which simply leads to inaccurate results.

During char conversion, when both  $\text{CO}_2$  and  $\text{H}_2\text{O}$  are present, there is competition for active sites on the particle surface. At atmospheric pressures, separate active sites for  $\text{H}_2\text{O}$  and  $\text{CO}_2$  are assumed (model 1 in Figure 2.13) [189,190,200], whereas at high pressures the overall reaction rate will not be the sum of the rates for the two gasifying agents since  $\text{CO}_2$  inhibits the  $\text{H}_2\text{O}$  rate (model 2 in Figure 2.13). The relation for model 2 is defined as:

$$R_{CO_2+H_2O} = R_{CO_2} + R_{H_2O} \left( 1 - \frac{k_3 p_{CO_2}}{1 + k_3 p_{CO_2}} \right) \quad (2.75)$$

The main idea underlying the above equation is that both CO<sub>2</sub> and H<sub>2</sub>O compete for the same active sites. H<sub>2</sub>O adsorption is blocked by the already absorbed CO<sub>2</sub>, which reduces the steam rate.

Umemoto et al. (2013) [201] proposed a model in which CO<sub>2</sub> and H<sub>2</sub>O partially share active sites - Figure 2.13.

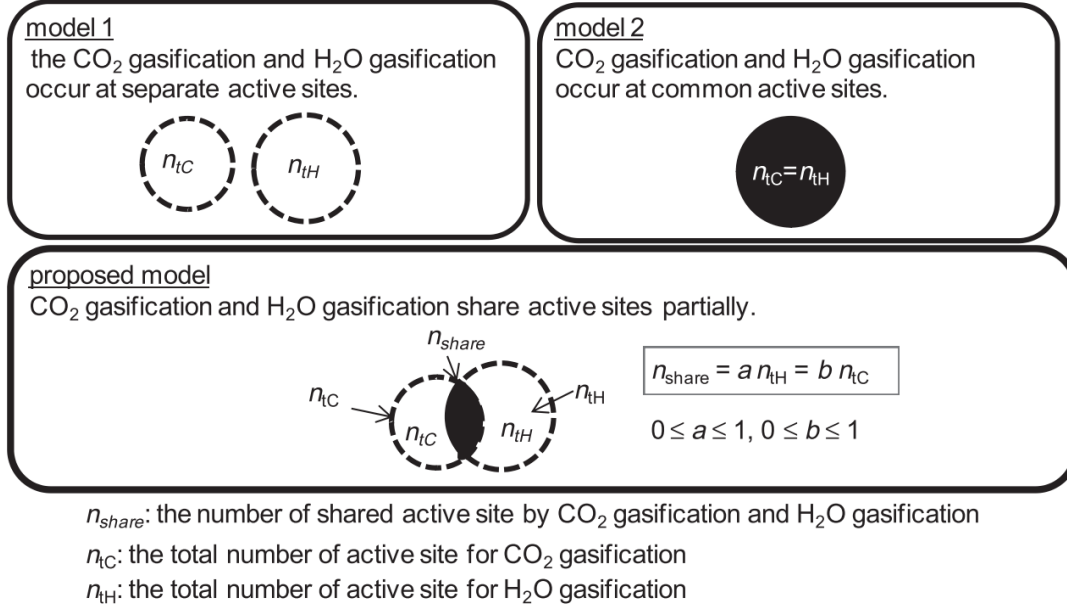


Figure 2.13. Models for active sites by H<sub>2</sub>O and CO<sub>2</sub> gasification [31].

The gasification rate in the proposed model, which incorporates the L-H kinetics and the random pore model, is defined as:

$$r = \frac{k_{11} P_{CO_2} (1-x) \sqrt{1 - \psi_1 \ln(1-x)}}{1 + k_{12} P_{CO_2} + k_{13} P_{CO} + \frac{a}{c} k_{22} P_{H_2O} + \frac{a}{c} k_{23} P_{H_2}} + \frac{k_{21} P_{H_2O} (1-x) \sqrt{1 - \psi_2 \ln(1-x)}}{1 + bck_{12} P_{CO_2} + bck_{13} P_{CO} + k_{22} P_{H_2O} + k_{23} P_{H_2}} \quad (2.76)$$

where:

$$a = \frac{n_{share}}{n_{tH}}, b = \frac{n_{share}}{n_{tC}} \quad (2.77)$$

$n_{share}$  – the total number of shared active sites for CO<sub>2</sub> and H<sub>2</sub>O gasification

$n_{tH}, n_{tC}$  – the total number of active sites for H<sub>2</sub>O and CO<sub>2</sub>, respectively.

The proposed model describes the gasification behavior more accurately than conventional models.

## 2.4.2 Detailed mechanisms

One of the most advanced char conversion models available is the carbon burnout kinetics model (CBK) [1–4] with the latest modifications for oxidation (CBK/E) [11] and for gasification (CBK/G) [12]. These models incorporate the eight-step Langmuir-Hinshelwood kinetic approach: Eqs. (2.78) – Eq. (2.85) with random pore model intrinsic surface area evolution, single film, and pore diffusion, based on an effectiveness factor defined by a Thiele analysis, a thermal annealing, and ash inhibition. Together, these mechanisms contribute to a significant reduction in char conversion rates during the later stages of combustion/gasification, in accord with observations of very long reaction times for conversion of the remaining amount of the char mass - Figure 2.14. As a detailed devolatilization model, the CBK model accurately describes the char conversion process over a wide range of operating conditions, including Zone I, Zone II, and Zone III and their transitional regimes. This approach predicts the rate of oxidation/gasification, char particle temperature, particle diameter, and density during conversion, by providing the gas temperature, the radiative exchange temperature, and the partial pressures for the gasification agents.

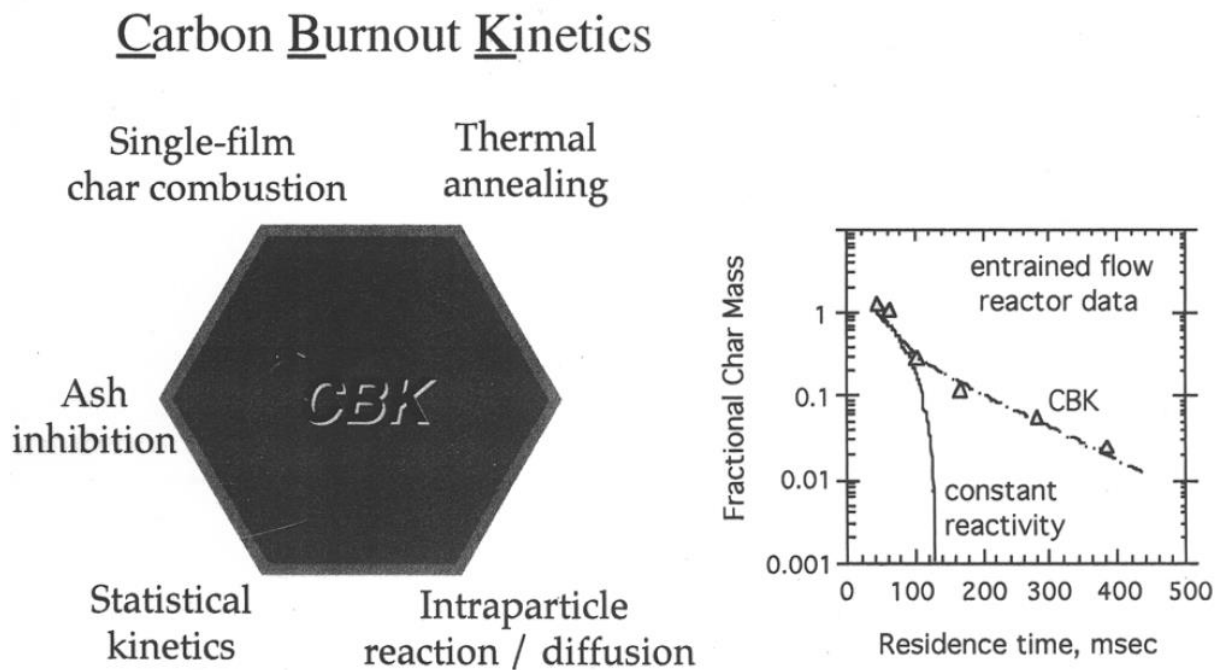


Figure 2.14. Mechanistic features of CBK/E [202].

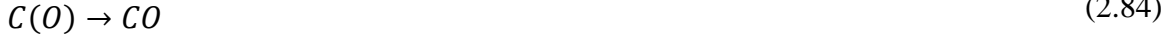
The combined oxidation/gasification model CBK/E and CBK/G is based on the following reactions [202]:

Combustion:





Gasification:



where C(O) is the oxide complex on the carbon surface.

The overall steady-state oxidation rate for the reactions (2.78) - (2.80) and the gasification rate (2.81) - (2.85) are expressed as follows:

$$r_{c-o_2} = \frac{k_8 k_9 P_{O_2}^2 + k_8 k_{10} P_{O_2}}{k_8 P_{O_2} + \frac{k_{10}}{2}} \quad (2.86)$$

$$r_{c-gas} = (k_{14} + k_{12})\theta + k_{15} P_{H_2} \quad (2.87)$$

$$r_{total} = r_{c-o_2} + r_{c-gas} \quad (2.88)$$

$$r_{o_2} = \frac{-\left(\frac{k_8 k_{10} P_{O_2}}{2} + k_8 k_9 P_{O_2}^2\right)}{k_8 P_{O_2} + \frac{k_3}{2}} \quad (2.89)$$

$$r_{H_2O} = -\frac{k_{14} k_{13} P_{H_2O}}{k_{14} + \gamma k_{11} P_{CO_2} + \gamma k'_{11} P_{CO} + k_{13} P_{H_2O} + k'_{13} P_{H_2}} \quad (2.90)$$

$$r_{CO_2} = -\frac{k_{14} k_{11} P_{CO_2}}{k_{14} + \gamma k_{11} P_{CO_2} + \gamma k'_{11} P_{CO} + k_{13} P_{H_2O} + k'_{13} P_{H_2} + \frac{k_9 k_8 P_{O_2}^2}{k_8 P_{O_2} + \frac{k_{10}}{2}}} \quad (2.91)$$

$$r_{CO} = \frac{k_8 k_{10} P_{O_2}}{k_8 P_{O_2} + \frac{k_{10}}{2}} + 2R_{CO_2} + R_{H_2O} \quad (2.92)$$

$$r_{H_2} = R_{H_2O} - 2k_{15} P_{H_2} \quad (2.93)$$

$$r_{CH_4} = k_{15} P_{H_2} \quad (2.94)$$

where:

$$\theta = \frac{k_{11}P_{CO_2} + k_{13}P_{H_2O}}{k_{14} + \gamma k_{11}P_{CO_2} + k_{13}P_{H_2O} + k'_{13}P_{H_2}} \quad (2.95)$$

$k_8$ - $k_{15}$  – Arrhenius rate constants

$P_{CO_2}$ ,  $P_{H_2O}$ ,  $P_{H_2}$ ,  $P_{CO}$  – partial pressures

$\gamma$  – the ratio of desorption rates.

For a detailed description of the model refer to [11,12,202].

### 2.4.3 Double-film model

As it was mentioned at the beginning of this section, most of the models, including the detailed CBK model, are single-film models which do not take into account the combustion of volatiles or CO, produced close to the particle during char conversion. This can lead to an inaccurate prediction of particle temperature and consequently, carbon consumption. Double-film models, on the other hand, assume that volatiles or CO rapidly combust in the flame sheet within the laminar layer (Figure 2.15), which is much closer to reality. However, the direct implementation of such an approach into CFD would require the solution of a system of coupled partial differential equations for each tracked particle.

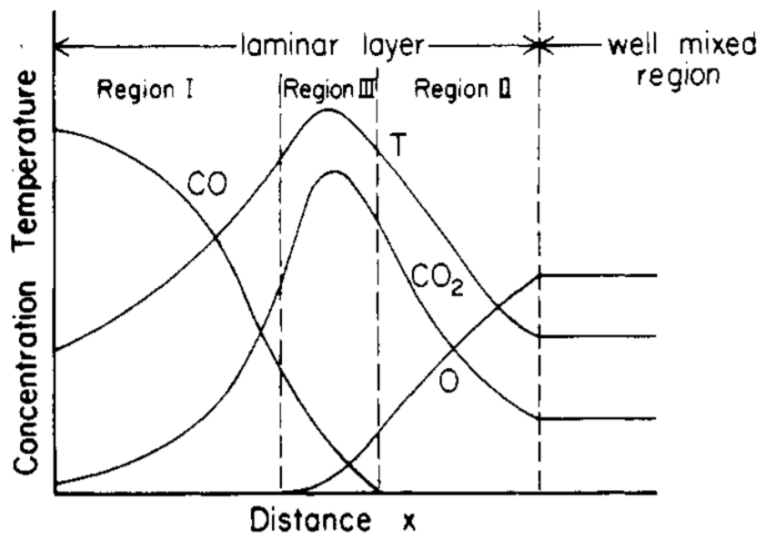


Figure 2.15. Double film model [31].

Zhang et al. [203] proposed a moving flame front model (MFF) of char consumption, which reduces the set of governing equations introduced into CFD without a significant increase in computational effort. The flame sheet location, where the combustion of CO takes place within the laminar layer, can be estimated through explicit functions of the various diffusion and kinetic rates involved. The approach is based on the following assumptions:

- the reaction:  $C + CO_2 \rightarrow 2CO$  is neglected since in the presence of oxygen partial combustion of C occurs at a much faster rate than the Boudouard reaction,
- the location of the flame sheet varies depending on the bulk species mole fraction and the instantaneous particle parameters.



The model has the following form:

$$\frac{dm_p}{dt} = \frac{1}{\frac{1}{R_{d,i} \left(1 + \frac{d_p}{2b}\right)} + \frac{1}{R_{s,i}}} \quad (2.96)$$

Eq. (2.96) is a modified version of Eq. (2.97) which represents the basic kinetics/diffusion single-film model approach.

$$\frac{dm_p}{dt} = \frac{1}{\frac{1}{R_{d,i}} + \frac{1}{R_{s,i}}} \quad (2.97)$$

where:

b- the flame front location.

The MFF model is used only in regions where O<sub>2</sub> is available, where combustion reactions dominate. When endothermic gasification reactions prevail the approach switches back to the basic single-film model where no oxygen is available to produce a CO-O<sub>2</sub> flame around the particles.

Kumar et al. [87] compared the two approaches for both one-stage and two-stage entrained flow gasifiers. The results were found to be identical for one-stage reactors. In the case of two-stage reactors, in the combustor region, the CO concentration was higher and the CO<sub>2</sub> concentration was lower for the MFF model than for the single-film approach.

Lately, the MFF model was extended to account for the CO<sub>2</sub> reaction [204]. For homogeneous reactions, a finite-rate reaction rate was considered [205].

A different approach was developed by Schulze et al. [206]. The approach incorporates the so-called homogeneous reaction layer (H-Zone) next to the particle. The H-Zone single-film approach assumes that the layer temperature is equal to the particle temperature. The layer thickness and consequently, the energy obtained from homogeneous reactions, is a function of the Reynolds number, the particle diameter, and the air composition. The distinguishing feature of this approach is the coupling of the CO oxidation reaction with the gasification reactions for the calculation of the particle temperature and the carbon conversion rate. The main drawback is that the layer thickness is an input parameter that depends on the particle velocity and the ambient conditions.

#### 2.4.4 Char conversion kinetic parameters

This sub-chapter provides the most widely applied kinetic parameters in char conversion models that were applied by researchers to model the entrained flow gasification process.

Table 2.14. Char conversion kinetic parameters for global models [31].

<b>Iterative procedure of Smith [168] – Multiple surface reaction model</b>	
$R. 1 \rightarrow C + 0.5O_2 \rightarrow CO$	
$k = T(A + BT)$	Taken from Field [170]

$A = -0.067 \text{ m/s K}$ $B = 5.25 \cdot 10^{-5} \text{ m/s K}^2$	Used by: [75] Reactor: 4
$k = AT^n \exp\left(-\frac{E}{RT}\right)$ $A = 0.052$ $E = 6.1 \cdot 10^7$ $n = 0$	Taken from Chen et al. [104] Reactors: 1, 2, 3, 4, 5 Used by: [82,90,120,125–127,91,92,96,102–104,108,114]
$A = 300$ $E = 1.3 \cdot 10^8$ Rate exponent: $O_2 = 0.65$	Taken from Wu et al. [122] Used by: [107]
$R. 2 \rightarrow C + CO_2 \rightarrow 2CO$	
$k = AT^n \exp\left(-\frac{E}{RT}\right)$ $A = 4.4 \text{ m/s K}$ $B = 1.62 \cdot 10^8 \text{ J/kmol}$ $n = 1.0$	Taken from Mayers [207] Used by: [75] Reactor: 4
$A = 0.0732$ $E = 1.125 \cdot 10^8$ $n = 0$	Taken from Chen et al. [104] Reactors: 1, 2, 3, 4, 5 Used by: [82,90,125–127,91,92,96,102–104,108,120]
$A = 246$ $E = 2.75 \cdot 10^8$ $n = 0$	Used by: [114]
$A = 2224$ $E = 2.2 \cdot 10^8$ Rate exponent: $CO_2 = 0.6$	Taken from Wu et al. [122] Used by: [107]
$R. 3 \rightarrow C + H_2O \rightarrow CO + H_2$	
$k = AT^n \exp\left(-\frac{E}{RT}\right)$ $A = 1.33 \text{ m/s K}$ $B = 1.47 \cdot 10^8 \text{ J/kmol}$ $n = 1.0$	Taken from Mayers [208] Used by: [75] Reactor: 4
$A = 0.0782$ $E = 1.15 \cdot 10^7$ $n = 0$	Taken from Chen et al. [104] Reactors: 1, 2, 3, 4, 5 Used by: [82,90,125–127,91,92,96,102–104,108,120]
$A = 426$ $E = 3.16 \cdot 10^8$ $n = 0$	Used by: [114]
$A = 42.5$ $E = 1.342 \cdot 10^8$ Rate exponent: $H_2O = 0.4$	Taken from Wu et al. [122] Used by: [107]
$R. 4 \rightarrow C + 2H_2 \rightarrow CH_4$	
$A = 1.62$ $E = 1.5 \cdot 10^8$	Taken from Wu et al. [122] Used by: [107]

<i>Rate exponent <math>H_2 = 1</math></i>	
$R. 5 \rightarrow C + O_2 \rightarrow CO_2$	
$A = 0.002$ $E = 7.9 \cdot 10^7$ $n = 0$	Used by: [114]
<b>Kinetics/diffusion fixed core model of Baum and Street [76]</b>	
$R. 1 \rightarrow C + 0.5O_2 \rightarrow CO$	
$k = T(A + BT)$ $A = -1.68 \cdot 10^{-2} \text{ m/s K}$ $B = 1.32 \cdot 10^{-5} \text{ m/s K}^2$	Taken from Field [170] Used by: [88] Reactor: 8 Kinetics/diffusion model was also used by Wu et al. [121,122]. His kinetic parameters have been already used above in the model of Smith.
$R. 2 \rightarrow C + CO_2 \rightarrow 2CO$	
$A = 8.3$ $E = 4.37 \cdot 10^7$ $n = 1$	Taken from Field [170] Used by: [88] Reactor: 8
$R. 3 \rightarrow C + H_2O \rightarrow CO + H_2$	
$A = 45.6$ $E = 4.37 \cdot 10^7$ $n = 1$	Taken from Field [170] Used by: [88] Reactor: 8
<b>Shrinking Core model of Wen and Chaung [159]</b>	
$R. 1 \rightarrow C + 0.5O_2 \rightarrow CO$	
$A = 87100$ $E = 1.494 \cdot 10^8$	Taken from Wen and Chaung[159] Used by: [81,85,93] Reactor: 3 [117]
$A = 8710$ $E = 17967$	Taken from Govin and Shah [209] Used by: [116]
$R. 2 \rightarrow C + CO_2 \rightarrow 2CO$	
$A = 2470$ $E = 1.751 \cdot 10^8$	Taken from Wen and Chaung[159] Used by: [81,85,93] Reactor: 3
$A = 4.40$ $E = 1.62 \cdot 10^8$	Taken from Brown and Smoot [210] Used by: [116] [86,87] Reactor: 1, 8
$R. 3 \rightarrow C + H_2O \rightarrow CO + H_2$	
$A = 2470$ $E = 1.751 \cdot 10^8$	Taken from Wen and Chaung[159] Used by: [81,85,93] Reactor: 3
$A = 1.33$ $E = 1.47 \cdot 10^8$	Taken from Brown and Smoot [210] Used by: [116] [86,87] Reactor: 1, 8
$R. 4 \rightarrow C + 2H_2 \rightarrow CH_4$	
$A = 1.2$	Taken from Wen and Chaung[159]

$E = 1.490 \cdot 10^8$	Used by: [81,85,93] Reactor: 3		
$A = 0.12$ $E = 17921$	Taken from Govin and Shah [209] Used by: [116][117]		
<b>The Intrinsic rate model</b>			
$R. 1 \rightarrow C + 0.5O_2 \rightarrow CO$			
	$R_i = \eta(A_t P_{Si}^n k_i)$ Coal CRC701 $A = 1.12 \cdot 10^3$ $E = 1.36 \cdot 10^8$ $n = 0.8$ Taken from:[211] Used by: [83][99]	$R_i = \eta(A_t P_{Si}^n k_i)$ Coal CRC702 $A = 1.12 \cdot 10^3$ $E = 1.36 \cdot 10^8$ $n = 0.8$ Taken from: [211] Used by: [83][99]	$R_i = \eta(A_t P_{Si}^n k_i)$ Coal CRC703 $A = 1.97 \cdot 10^5$ $E = 1.53 \cdot 10^8$ $n = 0.8$ Taken from: [211] Used by: [83][99]
$R_i = (\eta A_{t,in} + A_{t,ex})k_i$ $A = 0.024 \text{ kgm}^{-2} \text{ sPa}^n$ $E = 1.36 \cdot 10^8$ $n = 0.8$	Used by: [101][118] Reactor: 9		
$A = 5.06 \cdot 10^{-7} \text{ kgm}^{-2} \text{ sPa}^n$ $E = 9.87 \cdot 10^7$ $n = 0.81$	Used by: [100]		
$R_i = \eta(A_t P_{Si}^n k_i)$ $A = 1.36 \cdot 10^6 \text{ s}^{-1} \text{ MPa}^{-n}$ $E = 1.3 \cdot 10^8$ $n = 0.68$	Used by: [84]		
$\frac{dm_p}{dt} = \dot{m}_C^V + \dot{m}_C^S$ Kinetics of already mentioned [118]	Used by: [195]		
$R_i = \eta(A_t P_{Si}^n k_i)$ $A = 113 \text{ Pa}^{-n} \text{ s}^{-1}$ $E = 1.3 \cdot 10^8$ $n = 0.68$	Used by: [115,183]		
$R. 2 \rightarrow C + CO_2 \rightarrow 2CO$			
	$R_i = \eta(A_t P_{Si}^n k_i)$ Coal CRC701 A unit - $\text{gm}^{-2} \text{ s}^{-1} \text{ atm}^{-n}$ $A = 6.03 \cdot 10^7$ $E = 3.35 \cdot 10^8$ $n = 0.35$ Taken from:[180] Used by: [83][99]	$R_i = \eta(A_t P_{Si}^n k_i)$ Coal CRC702 $A = 1.46 \cdot 10^5$ $E = 2.78 \cdot 10^8$ $n = 0.32$ Taken from:[180] Used by: [83][99]	$R_i = \eta(A_t P_{Si}^n k_i)$ Coal CRC703 $A = 5.69 \cdot 10^3$ $E = 2.42 \cdot 10^8$ $n = 0.46$ Taken from:[180] Used by: [83][99]
$R_i = (\eta A_{t,in} + A_{t,ex})k_i$ $A = 0.022 \text{ kgm}^{-2} \text{ sPa}^n$ $E = 2.00 \cdot 10^8$	Used by: [101,118,119] Reactor: 9		

$n = 0.41$			
$A = 8.16 \cdot 10^{-3} \text{kgm}^{-2} \text{sPa}^n$ $E = 2.15 \cdot 10^8$ $n = 0.56$	Used by: [100] Reactor: 9		
$R_i = \eta(A_t P_{Si}^n k_i)$ $A = 3.78 \cdot 10^4 \text{s}^{-1} \text{MPa}^{-n}$ $E = 1.78 \cdot 10^8$ $n = 0.53$	Used by: [84]		
$\frac{dm_p}{dt} = \dot{m}_C^V + \dot{m}_C^S$ Kinetics of already mentioned [118]	Used by: [195]		
$R_i = \eta(A_t P_{Si}^n k_i)$ $A = 6.27 \cdot 10^5 \text{Pa}^{-n} \text{s}^{-1}$ $E = 2.83 \cdot 10^8$ $n = 0.54$	Used by: [115,183]		
$R. 3 \rightarrow C + H_2O \rightarrow CO + H_2$			
	$R_i = \eta(A_t P_{Si}^n k_i)$ Coal CRC701 $A = 1.81 \cdot 10^8$ $E = 3.35 \cdot 10^8$ $n = 0.35$ Taken from:[180] Used by: [83][99]	$R_i = \eta(A_t P_{Si}^n k_i)$ Coal CRC702 $A = 8.40 \cdot 10^4$ $E = 2.54 \cdot 10^8$ $n = 0.32$ Taken from:[180] Used by: [83][99]	$R_i = \eta(A_t P_{Si}^n k_i)$ Coal CRC703 $A = 2.41 \cdot 10^5$ $E = 2.63 \cdot 10^8$ $n = 0.46$ Taken from:[180] Used by: [83][99]
$R_i = (\eta A_{t,in} + A_{t,ex}) k_i$ $A = 0.423 \text{kgm}^{-2} \text{sPa}^n$ $E = 2.12 \cdot 10^8$ $n = 0.41$	Used by: [101,118,119] Reactor: 9		
$A = 2.68 \cdot 10^{-2} \text{kgm}^{-2} \text{sPa}^n$ $E = 1.83 \cdot 10^8$ $n = 0.35$	Used by: [100] Reactor: 9		
$R_i = \eta(A_t P_{Si}^n k_i)$ $A = 3.78 \cdot 10^4 \text{s}^{-1} \text{MPa}^{-n}$ $E = 2.26 \cdot 10^8$ $n = 0.60$	Used by: [84]		
$\frac{dm_p}{dt} = \dot{m}_C^V + \dot{m}_C^S$ Kinetics of already mentioned [118]	Used by: [195]		
$R_i = \eta(A_t P_{Si}^n k_i)$ $A = 4.18 \cdot 10^4 \text{Pa}^{-n} \text{s}^{-1}$ $E = 2.52 \cdot 10^8$ $n = 0.64$	Used by: [115,183]		
$R. 4 \rightarrow C + 2H_2 \rightarrow CH_4$	$R_i = \eta(A_t P_{Si}^n k_i)$ Coal CRC701	$R_i = \eta(A_t P_{Si}^n k_i)$ Coal CRC702	$R_i = \eta(A_t P_{Si}^n k_i)$ Coal CRC703

	$A = 2.58 \cdot 10^{-5}$ $E = 1.50 \cdot 10^8$ $n = 1.0$ Taken from:[180] Used by: [83]	$A = 2.58 \cdot 10^{-5}$ $E = 1.50 \cdot 10^8$ $n = 1.0$ Taken from:[180] Used by: [83]	$A = 2.58 \cdot 10^{-5}$ $E = 1.50 \cdot 10^8$ $n = 1.0$ Taken from:[180] Used by: [83]
$C + \frac{\psi + 1}{2} O_2 \rightarrow \psi CO_2 + (1 - \psi)CO$			
$A_c = 3 \cdot 10^8$ $E_c = 60kcal/mol$	$\frac{CO}{CO_2} = \frac{1 - \psi}{\psi} = A_c \exp\left(-\frac{E_c}{RT_p}\right)$ Taken from:[1] Used by: [94,95,99]		

## 2.4.5 Summary of char conversion stage

The aim of the literature review on char conversion was to thoroughly examine current modeling techniques since heterogeneous reactions were found to have the greatest impact on the overall gasification process and to propose which aspects require further investigation. The syngas yield was most sensitive to char-CO<sub>2</sub> and char-H<sub>2</sub>O reaction rates. The char-H<sub>2</sub> reaction was of minor importance and was mostly neglected. Unfortunately, because of the high level of complexity of the char conversion phenomena, the most-widely applied global models are incapable of yielding highly accurate results. The following simplifications have often been used:

- steady-state conditions, in which the average properties of particles are constant in a given position;
- the uniform temperature of coal particles along their radius;
- velocity inside particle pores is neglected;
- the particle diameter and density evolution is not included;
- deactivation or catalytic effects of minerals are neglected;
- particles are spherical in shape and have homogeneous chemical and physical properties;
- heterogeneous reactions are taken into account separately from homogeneous reactions;
- char consists of pure carbon when very high temperatures (>1000°C) are reached;
- char conversion reactions start only after the devolatilization process [76,170], but in general, there is an overlap between the two phenomena;
- kinetic parameters are not specified for the given case, but rather literature-taken.

Most of the reviewed studies included such approaches as the Baum and Street model, the multiple surface reaction approach, or the shrinking core model. Despite the fact that in some studies the outlet concentration or gas temperature of major species were in general agreement, these approaches failed to reproduce char conversion correctly with regard to experimental data. The random pore model managed to yield satisfactory results. However, this approach is based on a constant particle diameter, which can be assumed only in regime I. With

regard to the operating conditions in entrained flow gasifiers, the process is mostly pore-diffusion-controlled (regime II). The effectiveness factor is an approach accounting for the effects of diffusion and char morphology in high-temperature gasification. Wall thickness was shown to be a better parameter than particle size for chars exhibiting high-swelling propensity, low density, and high internal voidage particles. Langmuir-Hinshelwood kinetics, which describe surface saturation, were found to be much more accurate in modelling pressure-dependent kinetic rate expressions than the generally accepted  $n^{\text{th}}$  order equation. Moreover, they are a more mechanistic approach in comparison with power-law kinetics. For detailed analyses, advanced particle conversion models are required. The network CBK/E and CBK/G models as part of the NEA's PC Coal lab software were found to be the most ultramodern approaches in char conversion modeling. These models give consistent results for a wide range of operating conditions and fuels. However, due to the high level of complexity, the direct application of such models to CFD would considerably increase the computational effort. Therefore, similarly to devolatilization, an optimization procedure is proposed that incorporates simplified global models with calibrated kinetic parameters obtained on the basis of the ultramodern CBK/E and CBK/G models. The issue related to the application of literature parameters in char conversion modeling is also very common. Based on chapter 2.4.4, one can observe that the same set of kinetic parameters tend to be repeated for different reactors which have different operating conditions. For instance, for the char-H<sub>2</sub>O and char-CO<sub>2</sub> reactions,

the following pre-exponential factors and activation energies ( $A_{\text{H}_2\text{O}} = 0.0782$ ,  $E_{\text{H}_2\text{O}} = 1.15 \times 10^7$ ,  $A_{\text{CO}_2} = 0.0732$ ,  $E_{\text{CO}_2} = 1.125 \times 10^7$ ) were used by [82,90,125–127,91,92,96,102–104,108,120] for 5 different reactors (See Table 2.1). In the current research, detailed CBK/E and CBK/G approaches will be used independently of the CFD simulations and their results will serve as a basis to obtain unique kinetic parameters for global models. The literature review indicated that there are many widely used global empirical char conversion approaches varying in complexity and accuracy. The kinetic-diffusion model due to its simplicity and numerical stability is considered to be the most frequently used approach. Despite its obvious drawbacks in comparison with the detailed approaches, it provided reasonable results in terms of the gas composition. Although it inaccurately predicted char conversion. However, it must be emphasized that all of these results were obtained with literature-taken kinetic parameters. Therefore, in this dissertation, I will assess the utility of the global kinetic-diffusion model with uniquely specified kinetic parameters valid only for one specific condition. The analysis will regard the gas composition, temperature distribution, and char conversion. Additionally, I will investigate the level of error that can be obtained when applying different values of literature-taken kinetic parameters to emphasize their importance. The results from the analysis will be discussed in detail in Chapter 6.

## **3. CFD model description**

### **3.1 Background and introduction**

As it was described in Chapter 1.3, gasification is a very complex and intricate process. Therefore, in order to accurately describe it, a comprehensive CFD model needs to be developed – Figure 3.1. It should attempt to capture most of the physical, chemical, and thermal phenomena occurring in the particular reactor. Based on the fundamental laws of mass, momentum, energy, and species conservation equations, but also on empirical approaches, the physical, chemical and thermal variables, such as velocity, gas concentration, temperature, representing those key phenomena can be numerically solved with reasonable accuracy. Some of the most important properties and phenomena that have to be solved/described are as follows:

- particle and gas velocity and temperature
- particle dispersion
- turbulence
- drying
- devolatilization
- homogeneous reactions
- char conversion
- heat transfer



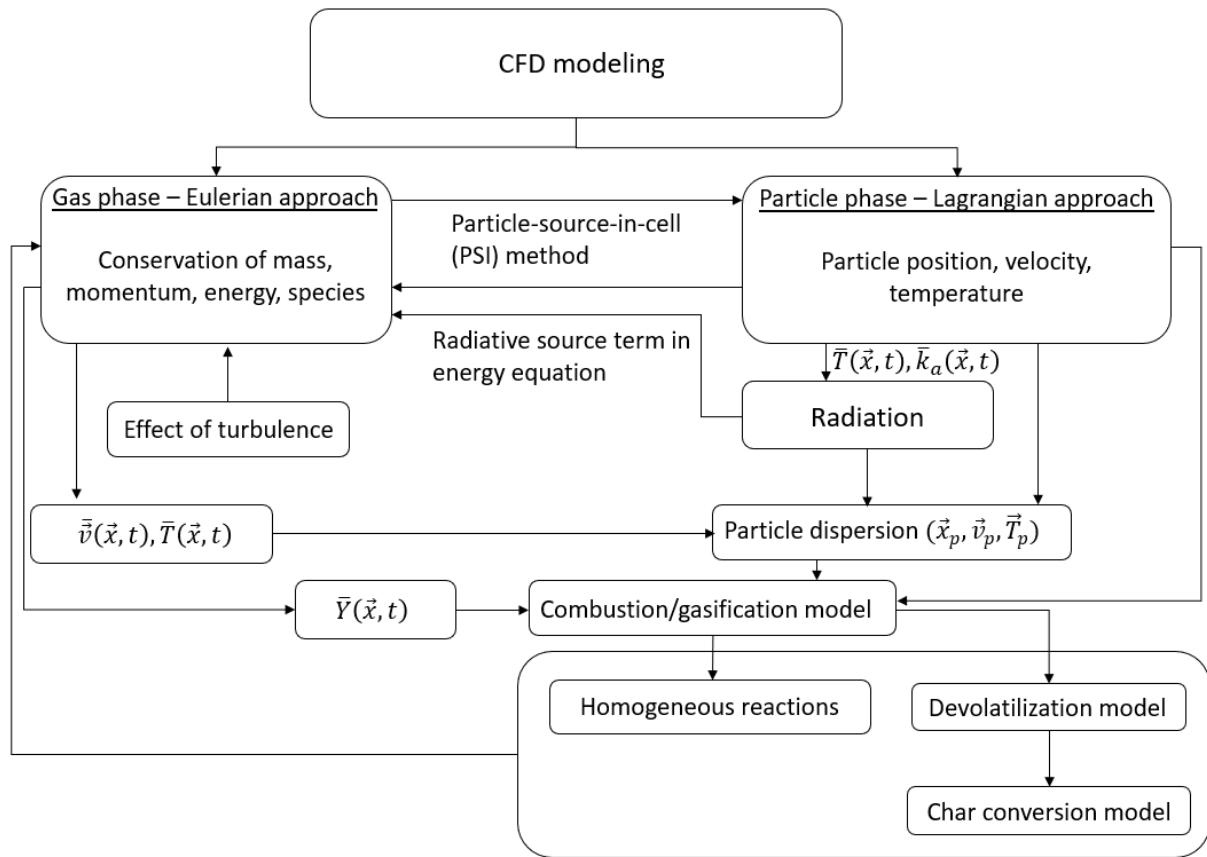


Figure 3.1. Block scheme representing particular components of the CFD model and their interactions.

In general, CFD simulations of the gasification process have been studied for many years. Coal gasification and combustion were already modeled over thirty years ago. Smoot's group at Brigham Young University developed a thorough three-dimensional CFD model called pulverized coal gasification and combustion (PCGC) and tested them on different coals [210,212]. Recently, due to the increase in computational power, there has been an increased interest in the CFD modeling of gasification.

The basis of the modeling lies in the turbulent aspect of the process. Nowadays, there are three main approaches to modeling turbulent combustion processes through CFD - Figure 3.2:

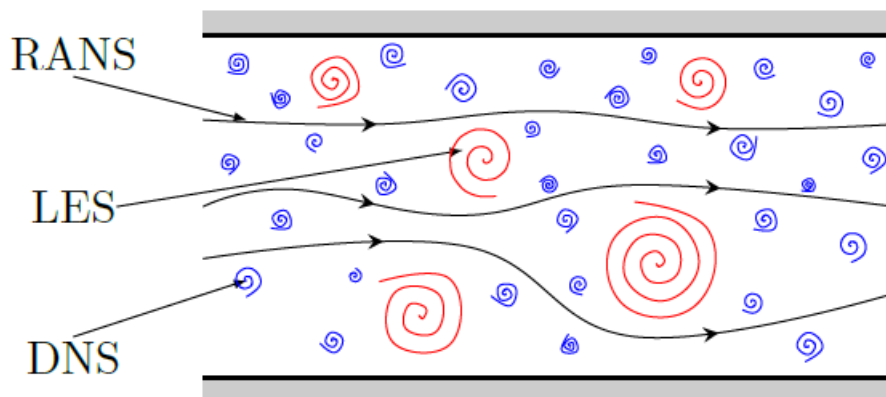


Figure 3.2. Schematic of turbulent structures in turbulent flows [213].

- Reynolds averaged Navier-Stokes equations (RANS), which solve the mean values of all quantities. Averaged balance equations are required to resolve averaged quantities. Hence, closure equations are needed, such as the turbulent model and turbulent combustion model which describe the flow dynamics, heat release, and species conversion. The discussion regarding the mean reaction source term in the species transport equation was already presented in sub-chapter 2.3.4.
- Large eddy simulation (LES). In this approach, only large turbulent scales are explicitly resolved, while the smaller ones are modeled through sub-grid closure rules. The closure terms that describe the sub-grid scale effects are required. In comparison with RANS, LES always requires a transient 3-D simulation with a much finer grid to capture fine scales, which substantially enlarges the computational effort.
- Direct numerical simulation (DNS). It is the most accurate and the most computationally expensive approach. It solves the full instantaneous Navier-Stokes equations directly without any closure models. All scales are fully resolved.

Based on the literature review, RANS is the most widely used modeling approach. It has the possibility to investigate simple 2-D cases, where the grid can be much more coarse than for LES or DNS. It depends only on the gradient of mean quantities. However, the accuracy is limited to the closure models [214].

Abani and Ghoniem [88] compared the performance of RANS and LES in the simulation of coal gasification in an entrained flow reactor. While LES provided more accurate results, being able to capture the unsteady flow structures, it also required a substantial amount of the computational cost and ultra-fine grid. On the other hand, RANS performed satisfactorily in terms of the mean gas composition prediction, temperature, and final conversion. On this basis, taking into account both computational effort requirement and accuracy of simulations, RANS application is reasonable and hence it is used in this dissertation. The general description of the incorporated approach with the key sub-models is presented in sub-chapter 3.2.

### **3.2 Key sub-models**

The mathematical model used here is based on the commercial CFD software Ansys Fluent 19.2 [215] which incorporates the finite-volume method. The gas phase is modeled assuming an Eulerian approach. Discrete phase trajectories are calculated using Lagrangian formulation and the coupling between the phases is introduced through particle sources of Eulerian gas-phase equations – Particle-source-in-cell method (PSI) [216]. The mass flow of coal parcels is represented by a number of trajectories that always represent a much larger number of actual particles. With respect to the Euler-Lagrangian formulation, there is also the Euler-Eulerian modeling approach. However, in the framework of Eulerian formalism, the particles are considered to behave as fluid. This method allows to model particle-particle stresses in dense flows by applying spatial gradients of particle volume fractions. Unfortunately, the continuum assumption in the Eulerian particle approach is not justified, as particles do not equilibrate with each other or with the local fluid while moving through the flow field. Moreover, Eulerian models are unable to account for the particle history because individual particles are not tracked. This aspect is essential in combustion/gasification modeling. On top of that, modeling

polydisperse particles becomes an issue because separate continuity and momentum equations have to be solved for each size and type.

### 3.2.1 Gas phase

The general steady-state conservation equations in the Eulerian frame of reference for mass, momentum, energy and for the species are as follows:

$$\frac{\partial}{\partial x_i}(\rho v_i) = S_{p,m} \quad (3.1)$$

$$\begin{aligned} \frac{\partial}{\partial x_i}(\rho v_i v_j) = \rho \bar{g}_j - \frac{\partial P}{\partial x_j} + \frac{\partial}{\partial x_i} \left( \mu \left( \frac{\partial v_i}{\partial x_j} + \frac{\partial v_j}{\partial x_i} - \frac{2}{3} \delta_{ij} \frac{\partial v_k}{\partial x_k} \right) - \rho \overline{v_i' v_j'} \right) \\ + S_{p,mom} \end{aligned} \quad (3.2)$$

$$\frac{\partial}{\partial x_i}(\rho c_p v_i T) = \frac{\partial}{\partial x_i} \left( \lambda \frac{\partial T}{\partial x_i} - \rho c_p \overline{v_i' T'} \right) + S_{rad} + S_h + S_{p,h} \quad (3.3)$$

$$\frac{\partial}{\partial x_i}(\rho v_i Y_j) = \frac{\partial}{\partial x_i} \left( \rho D_i \frac{\partial Y_j}{\partial x_i} - \rho \overline{v_i' Y_j'} \right) + R_j + S_{p,Y,j} \quad (3.4)$$

Where:

$S_{p,m}$  – mass source term from the discrete phase

$S_{p,mom}$  – momentum source term from the discrete phase

$v_i, v_j, v_k$  – velocity in the x, y and z directions (m/s)

T – temperature (K)

$c_p$  – specific heat (J/kg\*K)

$x_i, x_j, x_k$  – space coordinates in x, y and z

$S_{rad}$  – source term from radiation

$S_h$  - heat release due to volumetric reactions

$S_{p,h}$  - energy source term from the discrete phase – heterogeneous reactions

$D$  – mass diffusion coefficient

Y – local mass fraction of the species

$R_j$  – rate of creation/destruction of species from homogeneous reactions

$S_{p,Y,j}$  – rate of creation/destruction of species from heterogeneous reactions

From Eqs. (3.2)-(3.4),  $\rho \overline{v_i' v_j'}$ ,  $\rho c_p \overline{v_i' T'}$ ,  $\rho \overline{v_i' Y_j'}$  are the turbulent fluxes of momentum, energy and species.

Turbulent fluxes of energy and species are defined in the following way:

$$\rho c_p \overline{v_i' T'} = -c_p \frac{\mu_t}{Pr_t} \frac{\partial T}{\partial x_i} \quad (3.5)$$

$$\rho \overline{v_i' Y_j'} = -\frac{\mu_t}{Sc_t} \frac{\partial Y_j}{\partial x_i} \quad (3.6)$$

Where:

$Pr_t$  – turbulent Prandtl number

$Sc_t$  – turbulent Schmidt number

$\mu_t$  – turbulent eddy viscosity

The turbulent flux of momentum is modeled based on the hypothesis of Boussinesq. It introduces the concept of turbulent eddy viscosity  $\mu_t$ .

$$\overline{\rho v_i' v_j'} = -\mu_t \left( \frac{\partial v_i}{\partial x_j} + \frac{\partial v_j}{\partial x_i} - \frac{2}{3} \delta_{ij} \frac{\partial v_k}{\partial x_k} \right) + \frac{2}{3} \rho k \quad (3.7)$$

The turbulent eddy viscosity is defined as:

$$\mu_t = \rho C_\mu \frac{k^2}{\varepsilon} \quad (3.8)$$

Where  $k$  and  $\varepsilon$ , which are the turbulent kinetic energy and eddy dissipation rate, respectively, are modeled according to the realizable k- $\varepsilon$  approach – Eqs. (3.9) and (3.10).

$$\frac{\partial}{\partial x_i} (\rho k) + \frac{\partial}{\partial x_j} (\rho k v_j) = \frac{\partial}{\partial x_j} \left( \left( \mu + \frac{\mu_t}{\sigma_k} \right) \frac{\partial k}{\partial x_j} \right) + G_k + G_b - \rho \varepsilon - Y_M + S_k \quad (3.9)$$

$$\begin{aligned} \frac{\partial}{\partial x_i} (\rho \varepsilon) + \frac{\partial}{\partial x_j} (\rho \varepsilon v_j) \\ = \frac{\partial}{\partial x_j} \left( \left( \mu + \frac{\mu_t}{\sigma_\varepsilon} \right) \frac{\partial \varepsilon}{\partial x_j} \right) + \rho C_1 S_\varepsilon - \rho C_2 \frac{\varepsilon^2}{k + \sqrt{\nu \varepsilon}} + C_{1\varepsilon} \frac{\varepsilon}{k} C_{3\varepsilon} G_b + S_\varepsilon \end{aligned} \quad (3.10)$$

Where:

$G_k$  – generation of turbulent kinetic energy due to the mean velocity gradients

$G_b$  – generation of turbulent kinetic energy due to buoyancy

$Y_M$  – contribution of the fluctuating dilatation in compressible turbulence to the overall dissipation rate

$C_2, C_{1\varepsilon}$  – constants

$\sigma_k, \sigma_\varepsilon$  – turbulent Prandtl numbers

$S_k, S_\varepsilon$  – user-defined source terms

$C_1$  –relation which is defined as:  $\max \left( 0.43, \frac{\sqrt{2S_{ij}S_{ij}^k}}{\sqrt{2S_{ij}S_{ij}^k} + 5} \right)$

$S_{ij}$  – strain rate, which is present in the definition of  $C_1$  is defined as:  $\frac{1}{2} \left( \frac{\partial v_j}{\partial x_i} + \frac{\partial v_i}{\partial x_j} \right)$

The main difference between the standard k- $\varepsilon$  approach and the realizable k- $\varepsilon$  approach is the definition of the  $C_\mu$  present in Eq. (3.8). While in the former it is a constant value, in the latter it is defined through Eq. (3.8). The term “realizable” means that it satisfies certain mathematical constraints on the Reynolds stresses. The realizable k- $\varepsilon$  model has been extensively validated for a wide range of flows [204, 205], including rotating homogeneous shear flows, free flows with jets and mixing layers, separated flows and channel and boundary layer flows. For all of these cases, the performance of the realizable k- $\varepsilon$  approach was found to be substantially better than for the standard k- $\varepsilon$  model. A noteworthy is a fact that this model

resolves the anomaly related to the round jets and it also predicts the spreading rate for planar and axisymmetric jets.

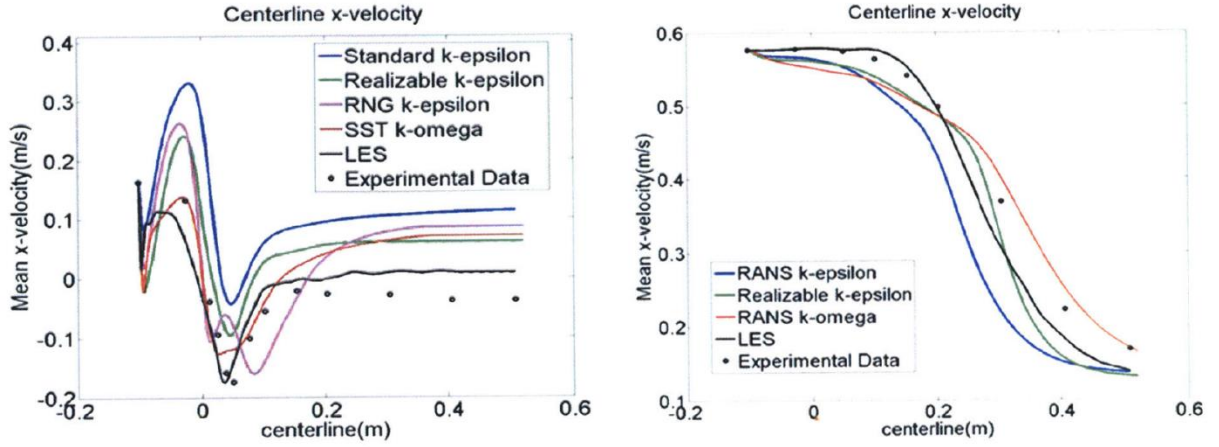


Figure 3.3. Centerline mean axial velocity for a) swirling flow b) non-swirling flow [219,220].

Recently, Kumar et al. [219,220] compared different turbulence models in swirling and non-swirling flow conditions - Figure 3.3. It turned out that while the LES method provided the most accurate results, the SST k- $\omega$  and realizable k- $\epsilon$  approach yielded reasonable results. The standard k- $\epsilon$  approach provided the worst accuracy among all turbulence models investigated.

Based on Eqs. (3.1)-(3.4) and Eqs. (3.9)-(3.10) significant commonalities can be observed between the equations. Using a general variable  $\phi$ , the conservative flow of all fluid equations can be written in the following way:

$$\frac{\partial}{\partial t}(\rho\phi) + \text{div}(\rho\phi v) = \text{div}(\Gamma \text{grad } \phi) + S_\phi \quad (3.11)$$

Where the sum of the rate of increase of  $\phi$  of fluid element and the net rate of flow of  $\phi$  out of fluid element (convection) is equal to the sum of the rate of increase of  $\phi$  due to diffusion and rate of increase of  $\phi$  due to other sources.

As it was mentioned, the model is developed and solved by means of ANSYS Fluent, which is a finite-volume-method software. The key step of the finite volume is to integrate the differential equation – Eq. (3.11) and to apply Gauss’s divergence theorem, which for a vector  $\mathbf{a}$  states:

$$\int_{CV} \text{div } \mathbf{a} dV = \int_A \mathbf{n} \cdot \mathbf{a} dA \quad (3.12)$$

This leads to the integral form of the general conservation equation:

$$\frac{\partial}{\partial t} \left( \int_{CV} \text{div } \mathbf{a} dV \right) + \int_A \mathbf{n} \cdot (\rho\phi v) dA = \int_A \mathbf{n} \cdot (\Gamma \text{grad } \phi) dA + \int_{CV} S_\phi dV \quad (3.13)$$

Eq. (3.13) is the actual form of the general conservation equation solved by finite-volume-method CFD software.

### 3.2.2 Discrete phase

As regards particle-phase conservation equations, the mass balance equation is as follows:

$$\frac{dm_p}{dt} = \frac{dm_{C-O_2}}{dt} + \frac{dm_{C-CO_2}}{dt} + \frac{dm_{C-H_2O}}{dt} + \frac{dm_{devol}}{dt} + \frac{dm_{evap}}{dt} \quad (3.14)$$

Where the change of mass of a particle is equal to the change of mass due to evaporation, devolatilization, and surface reactions.

The trajectories of the parcels were computed by integrating the momentum equation:

$$\frac{dv_p}{dt} = F_D + F_g \quad (3.15)$$

Where  $F_D$  and  $F_g$  are the drag and gravity forces per unit particle mass. The final form of the equation is as follows:

$$\frac{dv_p}{dt} = \frac{18\mu}{\rho_p d_p^2} \cdot \frac{C_D}{24} \cdot \frac{\rho d_p |\bar{v} + v'' - v_p|}{\mu} (\bar{v} + v'' - v_p) + \frac{g(\rho_p - \rho)}{\rho_p} \quad (3.16)$$

Where:

$v_p$  – particle velocity (m/s)

$\rho_p$  – particle density (kg/m<sup>3</sup>)

$C_D$  – dimensionless drag coefficient

$g$  – gravitational acceleration (m/s<sup>2</sup>)

$\rho$  – gas density (kg/m<sup>3</sup>)

$\mu$  – molecular viscosity (Pa\*s)

The track of particles is evaluated by the instantaneous velocity  $v$ , which is defined as the sum of the mean and of the fluctuating velocity:  $\bar{v} + v''$ . The fluctuating velocity is defined by the stochastic discrete random walk model.

$$v'' = \zeta \sqrt{\frac{2k}{3}} \quad (3.17)$$

Where  $\zeta$  is the normally distributed random number and  $k$  is the turbulent kinetic energy. This approach allows accounting for the effect of turbulent dispersion of particles. Each particle is stochastically tracked several times, while the exact number of tracking is case-specific. The random fluctuations are imposed on the velocity of the surrounding gas phase. The particle is considered to interact with fluid-phase eddies during its trajectory and the particle-eddy interaction time is taken to be smaller than the eddy-traverse time  $T_{cross}$  and the eddy lifetime  $T_e$ . Once the particle traverses from one eddy to another,  $v'$  is evaluated applying a different value of  $\zeta$ .  $T_e$  and  $T_{cross}$  are defined as:

$$T_e = C_L \frac{k}{\epsilon} \quad (3.18)$$

$$T_{cross} = \tau \ln \left( 1 - \left( \frac{L_e}{\tau |v - v_p|} \right) \right), L_e = C_L \frac{k^{1.5}}{\epsilon} \quad (3.19)$$

Where:

$C_L$  – time-scale modeling constant

$L_e$  – eddy length scale

$\tau$  – particle relaxation time which is defined as:  $\frac{\rho_p d_p^2}{18\mu}$

Based on the study by Kumar and Ghoniem [219], the time-scale modeling constant  $C_L$  was set from the default value of 0.15 to 0.6 in order to improve the prediction of turbulent diffusion of particles.

Heat transfer to the particle considers contributions from convection, radiation, and the heat consumed/released during e.g. surface reactions.

$$m_p c_p \frac{dT_p}{dt} = h_p A_0 (T - T_p) + \frac{\epsilon_p A_0}{4} (G - 4\sigma T_p^4) + Q_G \quad (3.20)$$

Where the heat from surface reactions  $Q_G$  is defined in the following way:

$$Q_G = \frac{dm_{C-O_2}}{dt} H_{C-O_2} + \frac{dm_{C-CO_2}}{dt} H_{C-CO_2} + \frac{dm_{C-H_2O}}{dt} H_{C-H_2O} \quad (3.21)$$

Where:

$H_{C-O_2}, H_{C-CO_2}, H_{C-H_2O}$  – heat from the surface reaction (J/kg)

$h_p$  – heat transfer coefficient between particle and gas (W/m<sup>2</sup>\*K)

$A_0$  – particle external surface area (m<sup>2</sup>)

### 3.2.3 Coupling between gas and discrete phase

Particle-source-in-cell method [216] is applied to evaluate the source terms that model the interactions between the gas and solid phases. These inter-phase terms are denoted by  $S_{p,m}$ ,  $S_{p,mom}$ ,  $S_{p,h}$  and  $S_{p,Y,j}$ .

The inter-phase mass source term is expressed as:

$$S_{p,m} = \frac{1}{V_{cell}} \sum_{i=1}^{N_p} \frac{dm_{p,i}}{dt} = \frac{1}{V_{cell}} \sum_{i=1}^{N_p} \left( \frac{dm_{p,i}}{dt} \right)^{Ev} + \left( \frac{dm_{p,i}}{dt} \right)^{Dev} + \left( \frac{dm_{p,i}}{dt} \right)^{Het} \quad (3.22)$$

Where:

$N_p$  – number of particles

The mass change between the cell exit and the cell entry appears in the continuity equation and as a source of chemical species:  $S_{p,Y,j}$ . The mass change is due to evaporation, devolatilization, and heterogeneous reactions.

The inter-phase momentum exchange source term is calculated simply by summing change in momentum of each particle passing through a control volume:

$$S_{p,mom} = \frac{1}{V_{cell}} \sum_{i=1}^{N_p} F_{D,i} \Delta m_{p,i} \quad (3.23)$$

The inter-phase energy exchange source term is defined as:

$$S_{p,h} = \frac{1}{V_{cell}} \left( \sum_{i=1}^{N_p} \frac{1}{\Delta t} \Delta m_{p,i} (-\Delta h_{evap} + \Delta h_{devot} + \Delta h_{het}) - \sum_{i=1}^{N_p} \frac{1}{\Delta t} \left( m_{p,i,out} \int_{T_{ref}}^{T_{p,out}} c_p dT - m_{p,i,in} \int_{T_{ref}}^{T_{p,in}} c_p dT \right) \right) \quad (3.24)$$

Where  $\Delta h_{evap}$ ,  $\Delta h_{devot}$  and  $\Delta h_{het}$  are the enthalpies of evaporation, devolatilization and heterogeneous reactions, respectively.

As regards *evaporation* of the coal particle, it is governed by the concentration difference between the surface and the bulk gas.

$$N_{molar} = v_c (C_s - C_\infty) \quad (3.25)$$

Where  $N_{molar}$  is the molar flux of vapor,  $v_c$  is the mass transfer coefficient,  $C_s$  is the vapor concentration at the surface of the droplet particle and the  $C_\infty$  is the vapor concentration in the bulk gas. The mass transfer coefficient can be obtained from empirical correlation by Marshall et al. [221]:

$$Sh = \frac{v_c d}{D} = 2.0 + 0.6 Re_d^{0.5} Sc^{0.33} \quad (3.26)$$

Where Sh is the Sherwood number, Sc is the Schmidt number, D is the diffusion coefficient of vapor, d is the particle (droplet) diameter. Vapor concentration at the droplet surface is obtained by assuming that the vapor partial pressure is equal to the saturated vapor pressure and the particle (droplet) temperature  $T_p$

$$C_s = \frac{p_{sat}(T_p)}{RT_p} \quad (3.27)$$

Vapor concentration in the bulk gas is expressed as:

$$C_\infty = X_i \frac{p}{RT_\infty} \quad (3.28)$$

Where  $X_i$  is the bulk mole fraction of species i

The vapor flux given by Eq. (3.25) is an inter-phase source of species in the gas phase species transport equation – Eq. (3.4).

$$\left( \frac{dm_p}{dt} \right)^{evap} = \sum_{i=1}^{N_p} N_i A_{p,i} M_{w,i} \quad (3.29)$$

The current dissertation utilizes two global *devolatilization* models that were mentioned in chapter 2.2.1. It is SFOR and C2SM.



As for the C2SM, mass loss due to devolatilization is defined as:

$$\left(\frac{dm_p}{dt}\right)^{devot} = \sum_{i=1}^{N_p} \left( (1 - f_{w,0})m_{p,0,i} - m_{a,i} \right) (k_{1,i}(\tau) + k_{2,i}(\tau)) \exp\left(-\int_0^\tau (k_{1,i}(T) + k_{2,i}(T))dT\right) \quad (3.30)$$

In the case of SFOR, mass loss is defined as:

$$\left(\frac{dm_p}{dt}\right)^{devot} = \sum_{i=1}^{N_p} -k_i (m_{p,i} - (1 - f_{v,0})(1 - f_{w,0})m_{p,0,i}) \quad (3.31)$$

Considering the source terms from chemical reactions -  $R_j$  - Eq. (3.4), it is defined twofold depending on the applied turbulence-chemistry interaction approach. This dissertation considers two approaches. The laminar finite-rate/eddy dissipation model (F-R/EDM) and the eddy dissipation concept (EDC). For the former one, the source term is defined based on Eqs. (2.27), (2.30) and (2.31). For the latter, it is defined based on Eq. (2.34).

As regards the char conversion modeling, the source term from heterogeneous reactions is defined, based on Eq. (2.39). Char conversion modeling is performed through the multiple surface reaction approach.

### 3.2.4 Radiation

In the current dissertation, two radiation models were employed. P-1 model [222] and the discrete ordinate method [223]. P-1 model assumes, that the radiation intensity  $I$  expands into an orthogonal series of spherical harmonics. The source term due to radiation in the energy equation is expressed as:

$$S_{rad} = (k_{a,g} + k_{a,p})G - 4 \left( k_{a,g}\sigma T^4 + \frac{E_p}{\pi} \right) \quad (3.32)$$

The first term represents local absorption and the second local emission. The influence of particulate effects is included. The  $k_{a,g}$  and the  $k_{a,p}$  terms consider absorption coefficient for gas and particles, respectively. Gas-phase radiative coefficients are modeled according to the Weighted-sum-of-the-gray-gases approach. Radiative coefficients of particles are expressed in terms of the control volume ( $V_{cell}$ ), particle emissivity  $\varepsilon_p$ , number of particles ( $N_p$ ) and particle external surface area ( $A_0$ ).

The equivalent particle absorption coefficient is expressed as:

$$k_{a,p} = \sum_{i=1}^{N_p} \varepsilon_{p,i} A_{0,i} \frac{1}{V_{cell}} \quad (3.33)$$

The equivalent emission of particles is expressed as:

$$E_p = \sum_{i=1}^{N_p} \varepsilon_{p,i} A_{0,i} \frac{\sigma T_{p,i}^4}{\pi V_{cell}} \quad (3.34)$$

Energy source in the energy equation due to homogeneous reaction for  $i$  species is expressed as:

$$S_{h,r} = - \sum_i \frac{h_i^0}{M_{w,i}} R_i \quad (3.35)$$

The P-1 model needs relatively little CPU demand and can easily be applied to different geometries. It is suitable for cases where the optical thickness is large. In an entrained flow gasifier, the optical thickness is thick owing to the presence of different gases, coal particles, ash. However, there are some limitations to this approach. First of all, all surfaces are assumed to diffuse. In such a case, the reflection of incident radiation at the surface becomes isotropic with regard to the solid angle. Second of all, gray radiation is assumed. Third of all, in the case of small optical thickness the model loses accuracy.

The discrete ordinate (DO) method solves the radiative transfer equation (RTE) for a finite number of discrete solid angles, each associated with a vector direction  $\vec{s}$  fixed in the global Cartesian system (x, y, z). The RTE equation is written as:

$$\nabla \cdot (I(\vec{r}, \vec{s})\vec{s}) + (a + \sigma_s)I(\vec{r}, \vec{s}) = an^2 \frac{\sigma T^4}{\pi} + \frac{\sigma_s}{4\pi} \int_0^{4\pi} I(\vec{r}, \vec{s}') \Phi(\vec{s} \cdot \vec{s}') d\Omega' \quad (3.36)$$

Where:

$\vec{r}$  – position vector

$\vec{s}$  – direction vector

$\vec{s}'$  – scattering direction vector

$a$  – absorption coefficient

$n$  – refractive index

$\sigma_s$  – scattering coefficient

$\sigma$  – Stefan-Boltzmann constant

$I$  – radiation intensity, which depends on position  $\vec{r}$  and direction  $\vec{s}$

$T$  – local temperature

$\Phi$  – phase function

$\Omega'$  - solid angle

DO model transforms the RTE equation into a transport equation for radiation intensity in three spatial coordinates (x, y, z). In this approach as many transport equations are solved as there are directions  $\vec{s}$ . It can be implemented in two versions: energy coupled or energy uncoupled. The uncoupled mode is of sequential nature and applies a conservative variant of the discrete ordinates model – the finite-volume scheme. The equations for the energy and radiation intensities are solved one by one, while in the energy coupled mode they are solved simultaneously. Usually, energy coupled mode is applied when the optical thickness is greater than 10. This can be encountered in glass-melting applications. Compared with the P-1 model, DO can fit for the entire range of optical thickness. The biggest disadvantage is that solving a case with a very fine angular discretization raises the computational effort.

## 4. Optimization procedure of devolatilization

The results from this chapter have been published in [224].

[224] J. Mularski, N. Modliński, Entrained flow coal gasification process simulation with the emphasis on empirical devolatilization models optimization procedure, *Appl Therm Eng* 2020;175:1–14. <https://doi.org/10.1016/j.applthermaleng.2020.115401>  
*MNiSW (2019-2021): 140 pts, IF (2019): 4.725*

### 4.1 Introduction

Recently, an innovative approach was suggested by Vascellari et al. [77], who presented an iterative optimization method for CFD simulations which estimated the kinetic parameters of global models based on phenomenological approaches. Thanks to this method, calibrated kinetic parameters of the global models were obtained, whereby the accuracy of the global approaches increased and the computational cost of the simulation was reduced. Reasonable agreement with experimental data was reported. In the present dissertation, the approach proposed in [77] is extended and further investigated. The novelty consists in:

- examining the impact of devolatilization on gasification simulation results through a comparison of stepwise-optimized models and non-optimized models;
- investigating the influence of the particles heating rate representation strategy on the optimization procedure accuracy; the constant devolatilization-time-averaged heating rate used in [77] and a detailed particle thermal history (the instantaneous heating rate) are compared.

The current investigation comprehensively examines the impact of different kinetic parameters on entrained flow coal gasification by visualizing the results from the non-optimized models and stepwise optimized models. The relative change obtained in these curves with regard to one another directly presents the effect of applying different kinetic parameters for global devolatilization models. As regards the heating rate representation strategy, two approaches are analyzed. The detailed network devolatilization models require heating rate as input data. The procedure applied in [77] utilized only a constant value in the investigation of entrained flow coal gasification process. In the current dissertation, I have also implemented a heating rate as a function of temperature as input data and examined it in both entrained flow coal gasification and coal pyrolysis. The coal pyrolysis study considered four different wall temperatures. Such a wide range of operating conditions will allow obtaining credible information regarding the accuracy of the implemented optimization procedure.

The process of optimizing kinetic parameters is performed through the minimization of the objective function. However, in this dissertation, I have additionally analyzed other numerical methods of approximation (the linear method, the exponential method, and the minimization of the objective function) and compared them focusing on their efficiency in volatile yield prediction referring to the coefficient of determination.

## 4.2 Optimization procedure

The optimization procedure introduces a link between complex network modeling and global empirical models commonly used with the CFD technique. Traditionally, global models utilize the kinetic data taken from the literature for some specific coal and type of reactor or extracted from complex network models for generally assumed operating conditions. The optimization procedure accounts for one more crucial parameter - particle thermal history, which makes the procedure a characteristic model reduction technique. The general idea of the iterative optimization procedure is presented in Figure 4.1. It consists of the following steps: initially, a CFD simulation is carried out with standard literature-taken kinetic parameters. The procedure utilizes a particle heating rate from the CFD, which is expressed in two ways. The first one considers the devolatilization-time-averaged heating rate, which is calculated as a ratio of the total change in temperature during the devolatilization process to its time of duration (the constant heating rate). The second one considers detailed particle thermal history (the instantaneous heating rate). In the next step, based on the proximate and ultimate analysis of the examined coal, the detailed FG-DVC devolatilization model predicts the rate of production and high-temperature yields of char, tar, volatiles, and their composition during the devolatilization for the just calculated particle heating rate. The particle thermal history, which is the time-temperature relation, after being incorporated into the FG-DVC model, allows obtaining rates and yields with the instantaneous heating rate effect. Afterward, the next CFD simulation is carried out with optimized kinetic parameters for global models. The optimization is performed through the minimization of the objective function that is found to be the most effective approximation method (Sub-chapter 4.3.5). The procedure is repeated until a converged solution is obtained - heating rates, volatile composition and their rate of release do not change with consecutive iterations. Finally, obtained optimized results, based on the FG-DVC approach, are confronted with the non-optimized results, with experimental data, and with the CFD-built-in CPD model. One of the most important benefits of the presented procedure is its versatility. It can be used in the optimization of other phenomena, provided that both advanced and global models are available. Moreover, the range of applicability of this procedure depends only on the phenomenological models, which the optimization is based on.

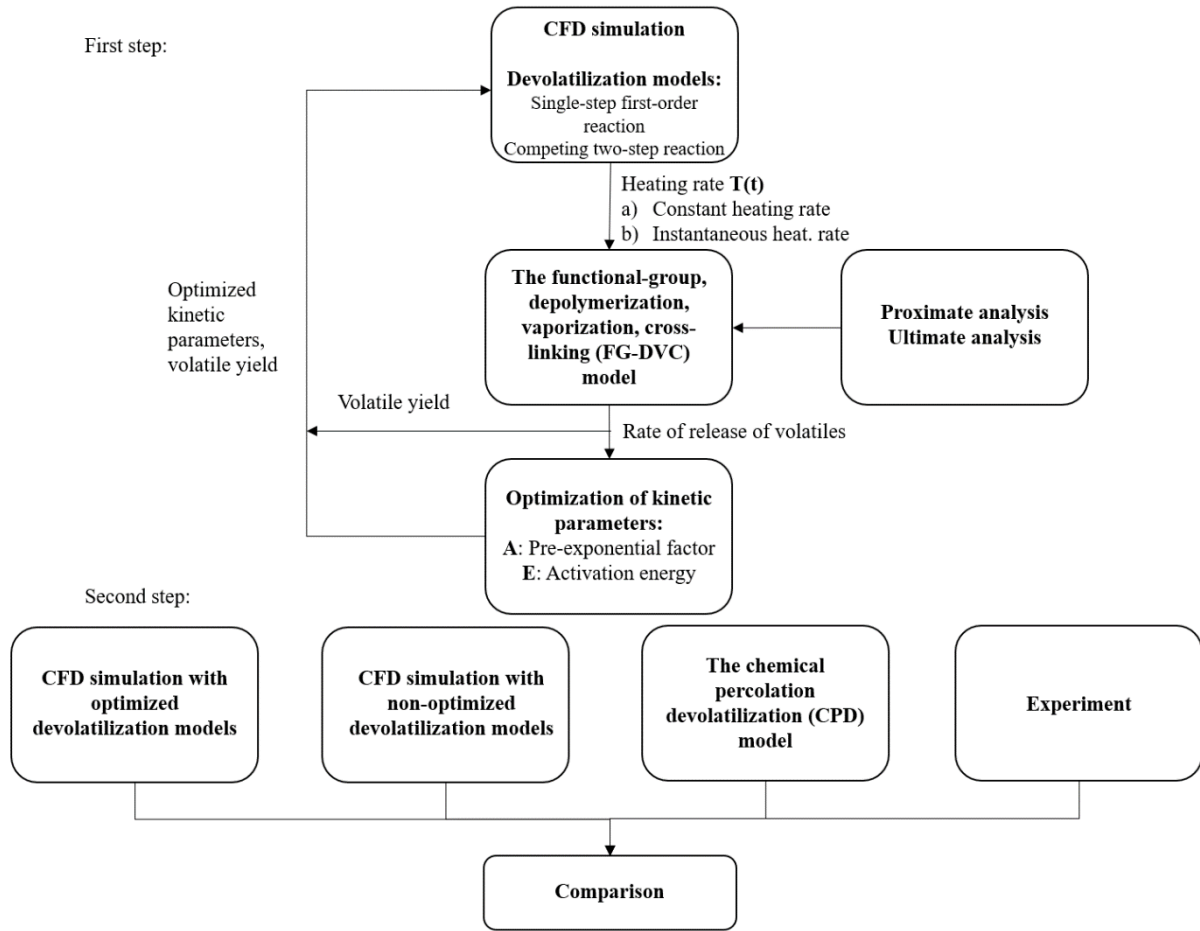


Figure 4.1. Optimization procedure of global devolatilization models [224].

### 4.3 Optimization of kinetic parameters

One of the crucial modules of the demonstrated optimization procedure is related to data extraction from the complex network models and its approximation with simple global models. This section describes the comparison of mathematical methods to derive the pre-exponential factor and activation energy. In the first instance, one must consider the solution strategy of the global models during CFD simulation particle tracking. Since there is no direct analytical integral of the  $Ae^{-E/RT}$  component, integration of Eq. (2.1) has only an approximate analytical solution. Assuming that particle temperature does not change significantly in the consecutive integration time steps, a recursive formula can be obtained through an Euler method. Taking SFOR as an example, the solution has the following form:

$$V(t + \Delta t) = V(t) \exp(-k\Delta t) + V_{total}(1 - \exp(-k\Delta t)) \quad (4.1)$$

The C2SM model is being integrated with the similar approach:

$$V = \int_0^t (a_1 k_1(\tau) + a_2 k_2(\tau)) \exp\left(-\int_0^\tau (k_1(t') + k_2(t')) dt'\right) d\tau \quad (4.2)$$

Let us define a standard least-squares objective function used to quantify the difference between the above models' predictions Eq. (4.1), Eq. (4.2), and detailed models' data to be

minimized over SFOR and C2SM. The optimization of kinetic parameters is based on the minimization of the objective function:

$$OF(x_k) = \frac{1}{N_{hr}} \sum_{i=1}^{N_{hr}} \left( \frac{\sum_{j=1}^{N_{t,j}} (Y_{i,j}^{net} - Y_{i,j}^{emp}(x_k))^2}{N_{t,i} (\max(Y_{i,j}^{net}))^2} \right) \quad (4.3)$$

where:  $Y^{net}$  is the volatile yield from the complex network model (FG-DVC),  $Y^{emp}$  is the volatile yield from the empirical model obtained from Eq. (4.1) and Eq. (4.2),  $x_k$  are the model parameters (the pre-exponential factor, activation energy),  $N_{hr}$  is the number of particle heating rates and  $N_{t,j}$  is the number of discrete time steps. The solution is obtained based on Levenberg-Marquardt fitting routine for multiple heating rates. The objective function of the SFOR model that was minimized - Eq. (4.3), is depicted in Figure 4.2. It is the function of two model parameters ( $x_k$ ), namely of the pre-exponential factor ( $A$ ) and activation energy ( $E$ ), visualized within the specified intervals of  $A$  ( $10^5 - 10^6$  1/s) and  $E$  ( $10^4 - 10^5$  J/mol). The values of  $A$  and  $E$  within these intervals are generally encountered in the literature [75,120–123].

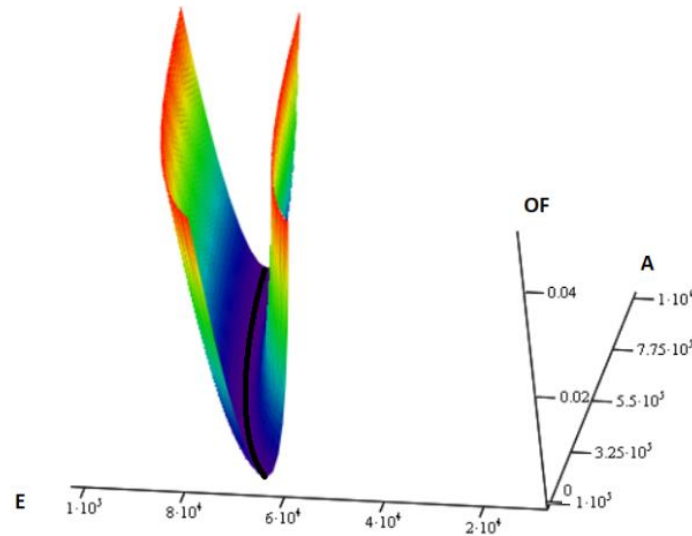


Figure 4.2. Objective function visualization of the SFOR model ( $A$  - 1/s,  $E$  - J/mol). Black line depicts the compensation effect [224].

The black line that was additionally added refers to the set of kinetic parameters ( $A$ ,  $E$ ), for which the objective function takes the minimum value. This observation can be related to the compensation effect. This phenomenon was already mentioned by [225–229] and was defined by [225] as a given set of data that can be fitted equally well by more than one pair of kinetic parameters ( $A$ ,  $E$ ). The effect of multiple minima indicates that for each set of kinetic parameters, for which the objective function reaches a minimum, the volatile yield predicted by the global model  $Y^{emp}$  approximates the volatile yield from the complex model  $Y^{net}$  equally well. The compensation effect explains why the same set of data can yield different kinetic parameters depending upon the method used to extract them, and this may partly explain the wide variation of values reported in the literature [230]. In the below sub-chapters an analysis of different approximation methods is presented.

### 4.3.1 Kinetic approximations – Linear approximation

Proper kinetic data approximation from the complex models is a crucial stage of the calibration procedure. This section compares different methods and their accuracy on the basis of the SFOR model. Considering that  $\frac{dV}{dt} = k(V_{total} - V)$  the reaction rate coefficient has the following form:

$$k = \frac{dV}{dt} \cdot \frac{1}{V_{total} - V} \quad (4.4)$$

Taking the logarithm of both sides of Arrhenius relation:  $k = A \cdot \exp\left(-\frac{E}{RT}\right)$ , the final form of the relation to work with is as follows:

$$\ln(k) = -\frac{E}{R} \cdot \frac{1}{T} + \ln(A) \quad (4.5)$$

which is analogous to the form of the linear function :  $y = ax + b$  where  $y$  is  $\ln(k)$  and  $x$  is  $\frac{1}{T}$ ,  $-\frac{E}{R}$  is the slope and  $\ln(A)$  is the y-intercept coefficient. The visualization can be seen in Figure 4.3.

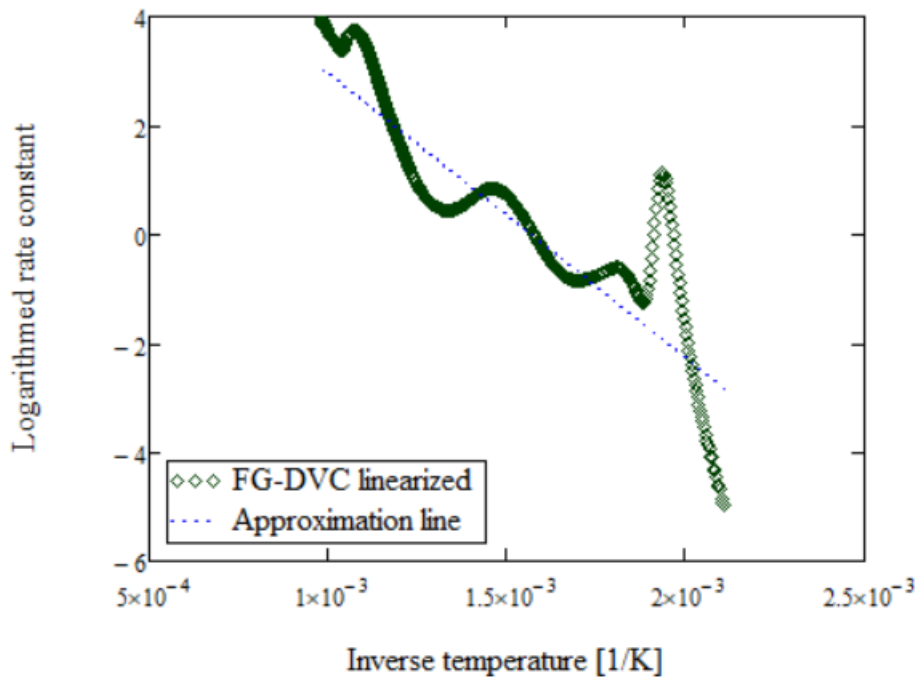


Figure 4.3. Linear approximation of FG-DVC yield data with respect to the inverse temperature (1/K).

### 4.3.2 Kinetic approximations – Second Linear approximation

In the second linear approximation method, the SFOR model was expressed as a function of a conversion degree:  $\alpha = \frac{V}{V_{total}}$

$$\frac{d\alpha}{dt} = k(1 - \alpha) \quad (4.6)$$

For non-isothermal conditions, when the particle temperature varies in time, assuming a constant heating rate:  $\beta = \frac{dT}{dt}$  the Eq. (4.6) is further modified into:

$$\beta \frac{d\alpha}{dT} = k(1 - \alpha) = A \cdot \exp\left(-\frac{E}{RT}\right) (1 - \alpha) \quad (4.7)$$

The calculation of pre-exponential factor and activation energy, in this case, requires the use of variational methods according to the form of the Eq. (4.7) that is used (integral or differential form). For the integration method, the equation takes the form:

$$\int_0^\alpha \frac{d\alpha}{1 - \alpha} = \frac{A}{\beta} \int_{T_0}^T \exp\left(-\frac{E}{RT}\right) dT \quad (4.8)$$

Further by applying the approximation of the temperature integral Eq. (4.9)

$$\int_{T_0}^T \exp\left(-\frac{E}{RT}\right) dT \approx \frac{R}{E} T^2 \exp\left(-\frac{E}{RT}\right) \quad (4.9)$$

and taking the logarithm of both sides it is possible to obtain:

$$\ln\left(\frac{-\ln(1 - \alpha)}{T^2}\right) = -\frac{E}{R} \cdot \frac{1}{T} + \ln\left(\frac{AR}{\beta E}\right) \quad (4.10)$$

As in the previous case the Eq. (4.5) can be written in the form of the linear function:  $y=ax+b$  where  $y$  is the left-hand-side of the equation,  $x$  is  $\frac{1}{T}$ ,  $a$  is  $-\frac{E}{R}$  and  $b$  is  $\ln\left(\frac{AR}{\beta E}\right)$ . The final approximation results are presented in Figure 4.4.



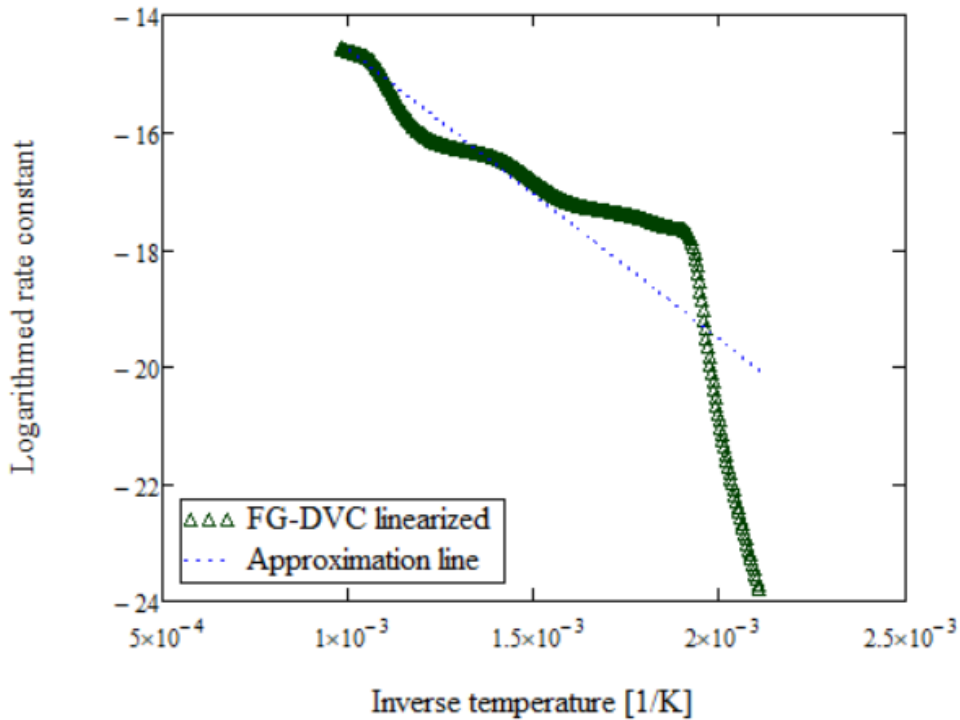


Figure 4.4. Second linear approximation of the FG-DVC data with respect to the inverse temperature ( $1/K$ ).

### 4.3.3 Kinetic approximations – exponential approximation

The third approximation treated the reaction rate to be constant. By calculating the derivative of the reaction rate  $k$  within the intervals, where the reaction rate was the fastest it was possible to determine the kinetic parameters  $A$  and  $E$ , for which the derivative  $\frac{dk}{dt}$  reached maximum – Figure 4.5.

$$\frac{dk}{dt} = \left(\frac{T}{t}\right) \cdot A \cdot \exp\left(-\frac{E}{RT}\right) \cdot \frac{E}{RT} \quad (4.11)$$

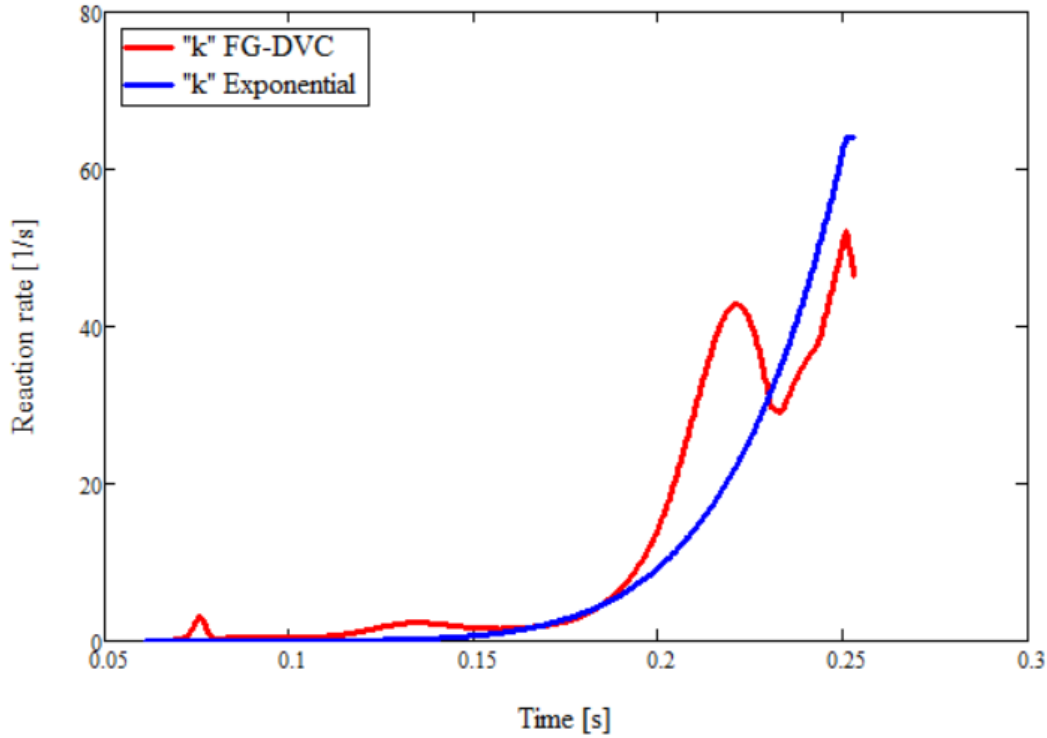


Figure 4.5. Exponential approximation of the reaction rate constant (1/s) obtained from FG-DVC data with respect to temperature (K).

#### 4.3.4 Minimization of the objective function

The last approach is based on the minimization of the objective function Eq. (4.12) which is a function of kinetic parameters.

$$OF(x_k) = \frac{1}{N_{hr}} \sum_{i=1}^{N_{hr}} \left( \frac{\sum_{j=1}^{N_{t,j}} (Y_{i,j}^{net} - Y_{i,j}^{emp}(x_k))^2}{N_{t,i} (\max(Y_{i,j}^{net}))^2} \right) \quad (4.12)$$

The objective function incorporated in this work was already studied by Vascellari et al. [77,94,95] and has provided satisfactory results.

#### The effect of multiple heating rates:

The key aspect related to the minimization of the objective function regards the possibility to account for multiple particle heating rates. As it was mentioned in the literature review, the detailed devolatilization models, such as FG-DVC, CPD, or Flashchain describe the ultimate volatile yield for a wide range of heating rates. On the contrary, the single-step SFOR approach cannot handle it due to the constant  $V_{total}$  term. The two-step C2SM model managed to follow the trend of the final yield with respect to the multiple particle heating rates. Figure 4.6 and Figure 4.7 present the effect of multiple heating rates of SFOR and C2SM, respectively with regard to the detailed FG-DVC model. Kinetic parameters for SFOR and C2SM were obtained by the minimization of the objective function for three heating rates. It is evident that C2SM is a much more accurate approach than SFOR, especially, when one considers polydisperse particles where each particle is subjected to a different heating rate. It is, however, important to

mention that although the ultimate volatile yield is rate- and temperature-dependent, in ANSYS Fluent it is artificially restrained up to a pre-defined value, in order to keep the mass and energy balance closed.

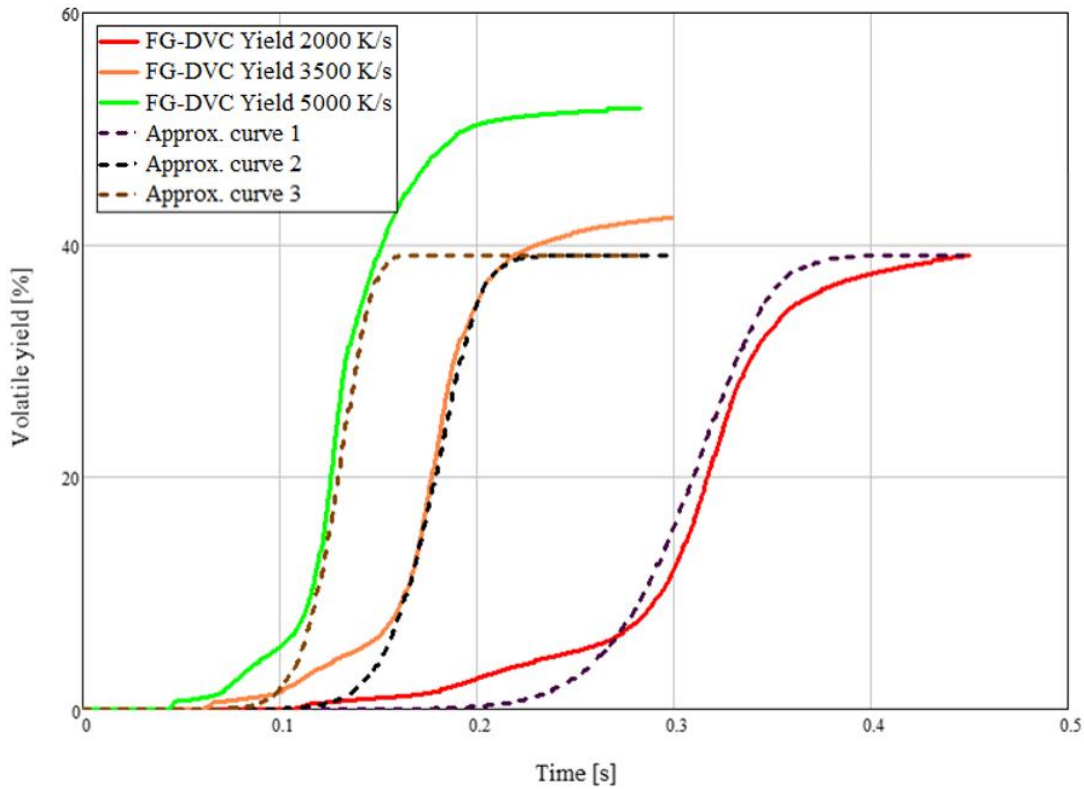


Figure 4.6. Calibration of the SFOR model - Volatile yield for three randomly taken heating rates (2000, 3500, 5000 K/s) (Continuous lines – FGDVC yields, dashed lines – SFOR yields).

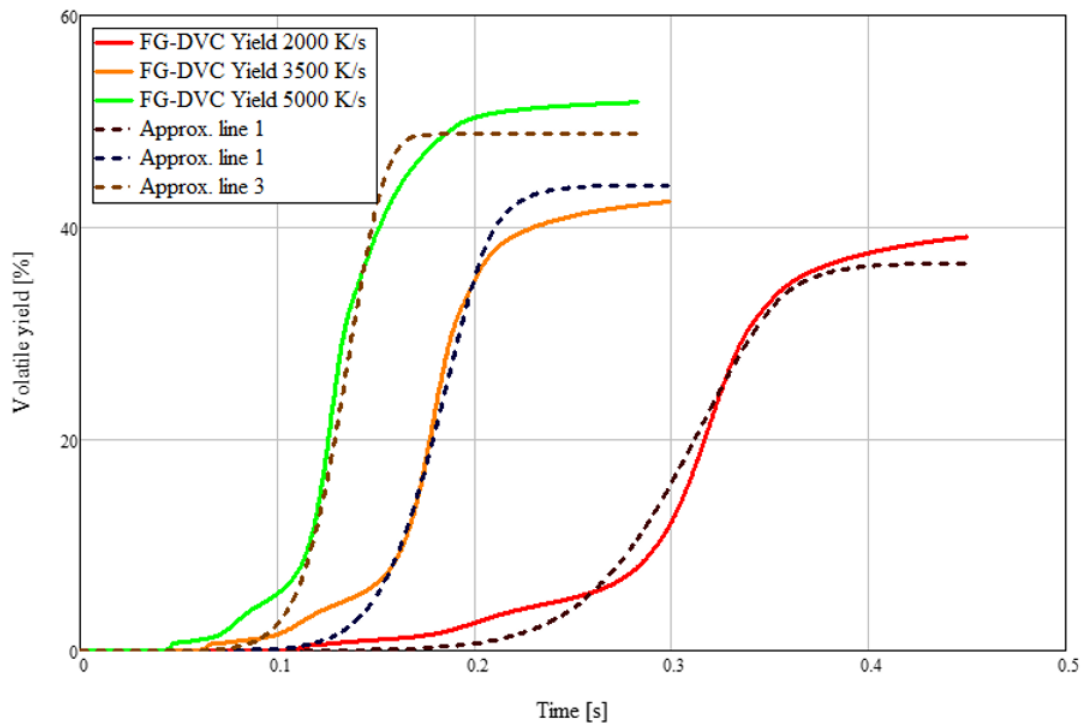


Figure 4.7. Calibration of the Kobayashi model - Volatile yield for three randomly taken heating rates (2000, 3500, 5000 K/s) (Continuous lines – FGDVC yields, dashed lines – Kobayashi yields)

### 4.3.5 Comparison of the approximation methods

Figure 4.8 presents four approximation curves of reaction rate  $k$  as a function of temperature. The final assessment of the efficiency of applied approximation methods is based on the results presented in Figure 4.9 and Table 4.1.

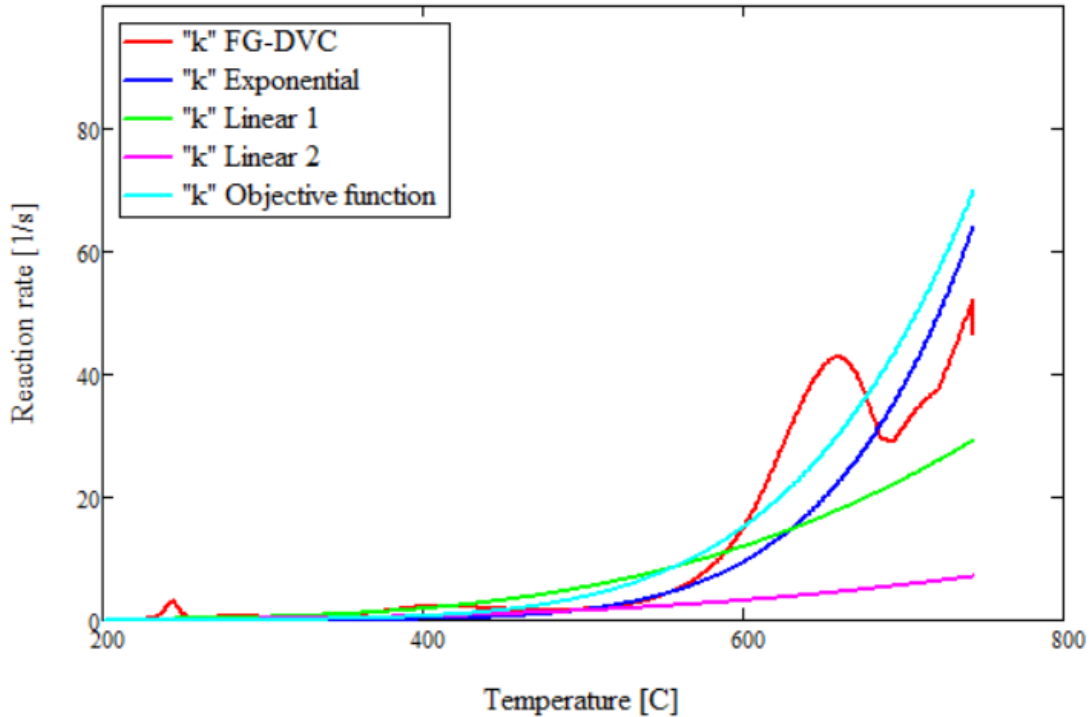


Figure 4.8. Approximation curves of reaction rate coefficient (1/s) for aforementioned methods with respect to temperature (C).

Figure 4.9 presents the release of volatiles with respect to time. The red curve is obtained directly from the FG-DVC approach. The rest of the curves incorporate Eq. (4.1), to obtain the volatile yield. Kinetic parameters:  $A$  and  $E$ , calculated differently through the investigated approximation methods are the only elements that differ in these curves. “Linear 1”, “Linear 2”, “Exponential”, “Objective function” approximations of kinetic parameters are obtained through the linear approximation - Eq. (4.5), the linear second approximation - Eq. (4.10), Exponential approximation – Eq. (4.11) and minimization of the objective function - Eq. (4.12), respectively. “Linear 1”, “Exponential” and “Objective function” approximation curves are relatively close to each other, but it is the “Objective function” approximation that has the highest coefficient of determination (Table 4.1).

Table 4.1. Coefficients of determination [224].

Coefficient of determination	$Yield_{linear1}$	$Yield_{linear2}$	$Yield_{exponential}$	$Yield_{objective\ function}$
$r^2$	0.988	0.921	0.981	0.997

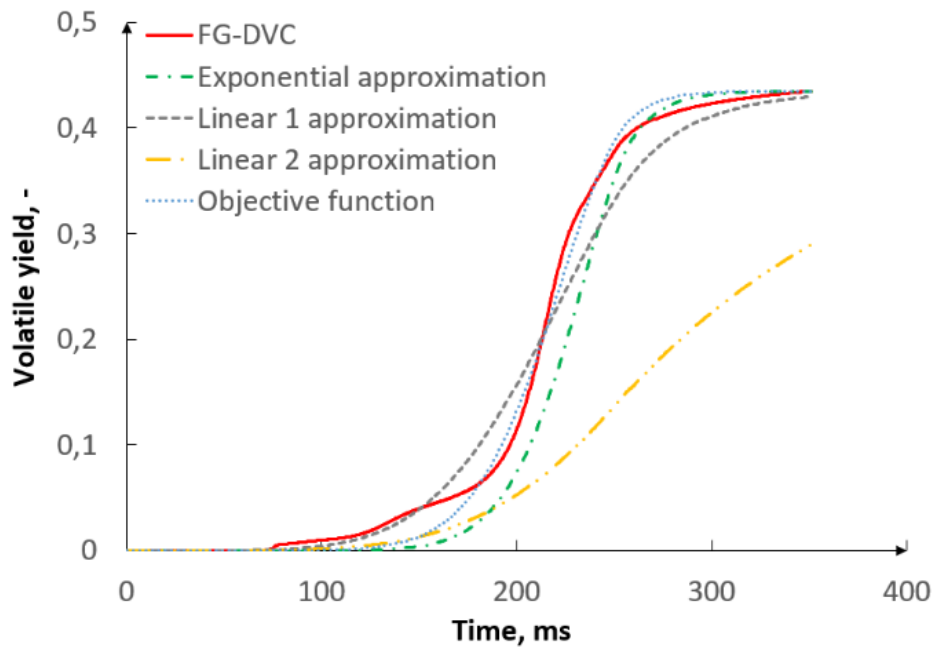


Figure 4.9. Volatile yield curves (%wt) with respect to time, obtained by different approximation methods [224].

#### 4.4 Optimization of volatile composition

Devolatilization consists of the primary and the secondary step. As the coal particle is heated in the absence of oxygen, tar and light gases are initially driven out of the particle and a solid residue remains. These light gases are generally oxides ( $\text{CO}_2$ ,  $\text{CO}$ ,  $\text{H}_2\text{O}$ ) and light hydrocarbons ( $\text{C}_1\text{-C}_4$ ) [55,56]. Tar is generally defined as the volatiles that condense to a solid or liquid at room temperature. All these species have different devolatilization rate constants.

In the CFD modelling, it was assumed that volatiles are produced as a single compound that instantaneously breaks up into tar, light hydrocarbons,  $\text{CO}$ ,  $\text{CO}_2$  and  $\text{H}_2\text{O}$ . FG-DVC calculates the devolatilization rate of tars and other species.

Secondary devolatilization is the further break-down and reorganization of tars. Some researchers incorporate that phenomena in the CFD simulations of pulverized coal combustion by assuming that tar decomposes to soot, light hydrocarbons,  $\text{H}_2$ , and  $\text{CO}$  [231]. An assumption can be made that the rate of secondary tar decomposition is equal to the rate of primary devolatilization. The produced light hydrocarbons ( $\text{C}_m\text{H}_n$ ) are considered to have the same composition as those produced with primary volatiles. Soot is assumed to be pure carbon. The pathway of devolatilization is demonstrated in Figure 4.10.

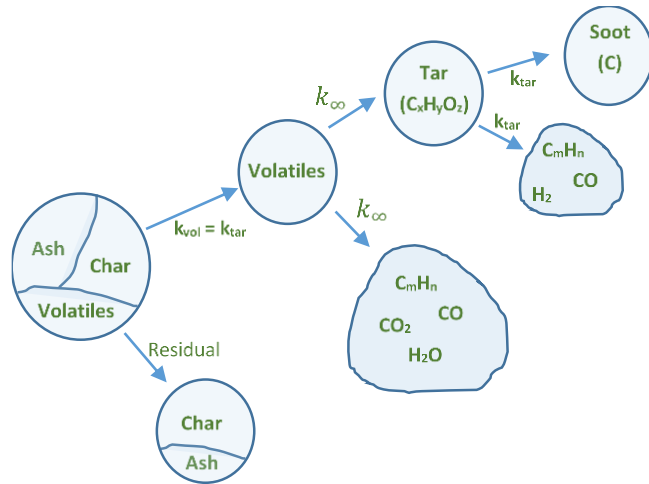


Figure 4.10. Devolatilization modelling approach [224].

In this dissertation, the secondary pyrolysis is not considered and tar is assumed to be a  $C_xH_yO_z$  molecule with the main component -  $C_7$  [232,233], whereas the light gases are treated as a  $C_mH_n$  molecule. Any detailed chemical mechanisms for heavy hydrocarbon conversion are considered too computationally expensive. The results along with the proximate and ultimate analysis of coals for both gasification and pyrolysis are given in Table 4.2.

Table 4.2. Coal analysis [133,210] and FG-DVC output data for two examined coals [224].

Calenturitas coal - coal pyrolysis in the drop tube				Utah coal - coal gasification in the BYU reactor					
<b>Proximate analysis (wt%, ar) [133]</b>				<b>Proximate analysis (wt%, ar) [210]</b>					
Ash	Volatiles Matter	Moisture	Fixed Carbon	Ash	Volatiles Matter	Moisture	Fixed Carbon		
7.1	39.1	6.8	47.0	8.3	45.6	2.4	43.7		
<b>Ultimate analysis (wt%, daf) [133]</b>				<b>Ultimate analysis (wt%, daf) [210]</b>					
C	H	N	S	O	C	H	N	S	O
77.7	5.0	1.4	0.6	15.3	77.6	6.6	1.3	0.6	13.9
<b>FG-DVC high-temperature yield (wt%, db) 1073K case</b>				<b>FG-DVC high-temperature yield (wt%, db)</b>					
Volatiles		Char		Volatiles		Char			
39.9		52.5		47.2		44.3			
<b>Volatiles composition from FG-DVC (wt%) 1073K case</b>				<b>Volatiles composition from FG-DVC (wt%)</b>					
$H_2O$	$CO$	$CO_2$	$C_mH_n$	$C_xH_yO_z$	$H_2O$	$CO$	$CO_2$	$C_mH_n$	$C_xH_yO_z$
15.5	1.2	1.4	11.3	70.6	14.0	8.9	2.7	14.9	59.5
<b>Empirical formula for light hydrocarbons (<math>C_mH_n</math>) and tar (<math>C_xH_yO_z</math>) 1073K case</b>				<b>Empirical formula for light hydrocarbons (<math>C_mH_n</math>) and tar (<math>C_xH_yO_z</math>)</b>					
$C_mH_n$ (gas)		$C_xH_yO_z$ (tar)		$C_mH_n$ (gas)		$C_xH_yO_z$ (tar)			
m=1, n=2.88		x=7, y=11.27, z=0.91		m=1, n=6.33		x=7, y=10.61, z=0.87			

Knowing the volatile fraction of dry-ash-free (daf) coal ( $f_{volatile}$ ) and assuming that residual char is pure carbon with known lower heating value  $LHV_{char}$ , one can calculate the lower heating value of volatiles ( $LHV_{volatile}$ ).

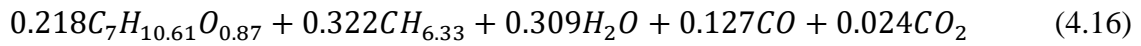
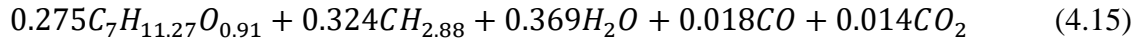
$$LHV_{volatile} = \frac{LHV_{coal_{daf}} - f_{char} \cdot LHV_{char}}{f_{volatile}} \quad (4.13)$$

The lower heating value of tars was calculated assuming the lower heating value of light hydrocarbons to be approximately equal to that of methane ( $LHV_{gas} = 50$  MJ/kg).

$$LHV_{tar} = \frac{LHV_{volatile} - (y_{gas} \cdot LHV_{gas} + y_{CO} \cdot LHV_{CO})}{y_{tar}} \quad (4.14)$$

where  $y_{gas}$ ,  $y_{tar}$ ,  $y_{CO}$  stand for the mass fraction in volatiles and  $LHV_{CO}$  is the known lower heating value of CO. The above procedure assumes that individual components are independent and non-interacting. In the real process, they undergo structural and chemical transformations during devolatilization, which affect the amount of energy stored in chemical bonds.

The final volatile composition on a molar basis for coal pyrolysis and coal gasification is shown in Eq. (4.15) and Eq. (4.16), respectively.



#### 4.5 Coal gasification simulation – brief model setup

The mathematical model used to study the entrained flow coal gasification process is based on the commercial CFD software Ansys Fluent [215] which incorporates the finite-volume method. The gas phase is modeled assuming an Eulerian approach. Discrete phase trajectories are calculated using the Lagrangian formulation and the coupling between the phases is introduced through particle sources of Eulerian gas-phase equations [216]. Simulation of the following processes takes place in the reactors: laminar or turbulent flow, moisture evaporation, devolatilization, gas-phase reactions, char surface reactions, particle, and radiative transport. Turbulence is modeled according to the realizable k- $\epsilon$  approach [218]. The dispersion of particles due to turbulence is considered with a stochastic tracking model [234]. Radiation is modeled with the P-1 approach [222].

Devolatilization is modeled according to the optimization procedure, as shown in Figure 4.1. Three devolatilization models are used. For the global approach, the C2SM approach is utilized. For the detailed approach, both FG-DVC and CPD models are used. FG-DVC approach serves as the basis of the optimization procedure. It is used independently of the CFD. The CPD model is used within the CFD software as an additional comparison of the results, apart from optimized, non-optimized, and experimental data (Figure 4.1 - Second step). It must be underlined that the CFD-embedded CPD model provides only the release rate of volatiles. Hence, the final volatile yield for the CPD model is taken from the FG-DVC approach. Input parameters for the FG-DVC model are interpolated from among input parameters of the three

nearest library coals (triangular interpolation) in the van Krevelen diagram [235], based on the proximate and ultimate analysis of the examined coal. Parameters for the CPD model are estimated using the Genetti et al.'s [236] correlation, which was found to provide satisfactory results in the literature considering combustion/gasification aspects [95,97,237,238].

The following gas-phase and char conversion reactions with the kinetic parameters are considered for coal gasification (Table 4.3):

Table 4.3. Kinetic parameters for gas-phase and surface reactions [224].

Reactions:	Kinetic parameters:		Ref.
	A - kg/s Pa	E - J/kmol	
<b>Surface reactions:</b>			
$C + 0.5O_2 \rightarrow CO$	$A = 0.005$	$E = 7.4 \cdot 10^7$	[77]
$C + CO_2 \rightarrow 2CO$	$A = 0.0635$	$E = 1.62 \cdot 10^8$	[77]
$C + H_2O \rightarrow CO + H_2$	$A = 0.0019$	$E = 1.47 \cdot 10^8$	[77]
<b>Gas-phase reactions:</b>			
$C_mH_n + \frac{m}{2}O_2 \rightarrow mCO + \frac{n}{2}H_2$	$A = 4.4 \cdot 10^{11}$	$E = 1.25 \cdot 10^8$	[87]
$C_xH_yO_z + \frac{x-z}{2}O_2 \rightarrow xCO + \frac{y}{2}H_2$	$A = 4.4 \cdot 10^{11}$	$E = 1.25 \cdot 10^8$	[87]
$C_mH_n + H_2O \rightarrow mCO + \left(\frac{n}{2} + 1\right)H_2$	$A = 3 \cdot 10^8$	$E = 1.25 \cdot 10^8$	[87]
$C_xH_yO_z + (x-z)H_2O \rightarrow xCO + \left(\frac{y}{2} + x - z\right)H_2$	$A = 3 \cdot 10^8$	$E = 1.25 \cdot 10^8$	[87]
$CO + H_2O \rightarrow CO_2 + H_2$	$A = 2.75$	$E = 8.38 \cdot 10^7$	[142]
$CO + 0.5O_2 \rightarrow CO_2$	$A = 2.24 \cdot 10^{12}$	$E = 1.67 \cdot 10^8$	[87]

It was assumed that the reaction kinetics of  $C_xH_yO_z$  and  $C_mH_n$  with  $O_2$  and  $H_2O$  is similar to the kinetics of light hydrocarbon molecules, such as  $CH_4$  [87]. The choice is justified because these reaction rates do not vary largely [105,106].

The gas-phase chemical kinetics are resolved with finite rate considerations in the case of laminar flow. The turbulence-chemistry interaction was taken into account by assuming infinitely fast chemistry which originates from the observation that most species produced during combustion rapidly reach chemical equilibrium at high temperatures.

The coal gasification process is simulated in the reactor shown in Figure 4.11. It is a one-stage atmospheric oxygen-blown entrained flow reactor with a non-swirling flow at Brigham Young University. It is 1.8 m long with a diameter of 20 cm. Coal is injected in the primary stream with a gas that consists of  $O_2$ , Ar, and  $H_2O$ . In the secondary stream,  $H_2O$  is injected solely. It is the only known to authors gasifier, where apart from averaged outlet data, in-reactor species measurements are available. The numerical model is validated against the experimental data of Smith et al. [210].

Bituminous pulverized coal from Utah is studied. Its proximate and ultimate analysis are shown in Table 4.2. This particular coal was chosen because the experimental results were the most stable during different tests [210].

The boundary conditions with gas molar fraction percentages are presented in Table 4.4. The particle size follows a Rosin-Rammler distribution. The parameters used in this work are



as follows: the minimum, mean and maximum diameters are 1, 36, and 80  $\mu\text{m}$ , respectively. The spread parameter is equal to 1.033. Kinetic parameters for gasification and gas-phase reactions of coal were taken from the literature and are presented in Table 4.3. The geometry of the reactor is discretized using a 2D axisymmetric grid composed of about 100 000 rectangular cells. The grid independence study is performed. The SIMPLE [239] algorithm is used for pressure-velocity coupling. Second-order schemes are used for spatial discretization. The weighted-sum of gray gas (WSGG) model [215] is used for the calculation of the gas absorption coefficient.

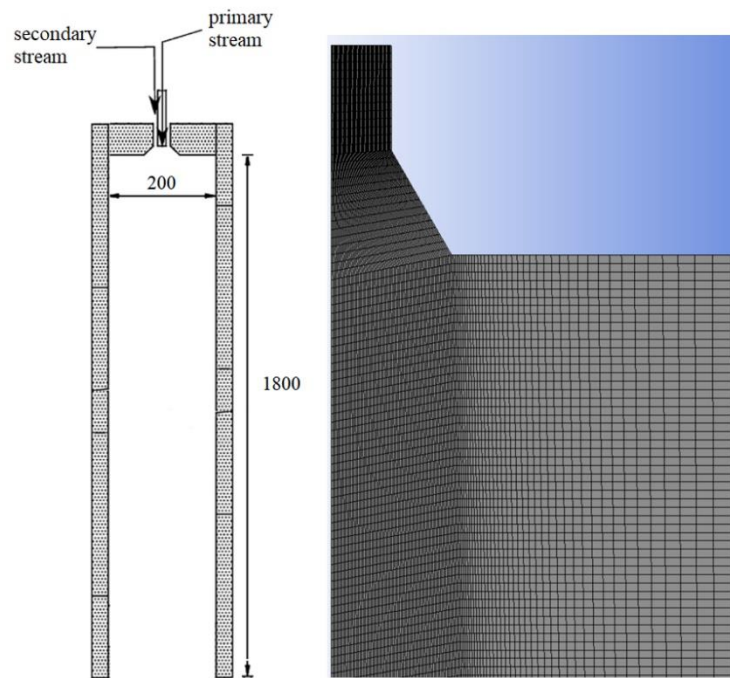


Figure 4.11. BYU gasifier geometry with axisymmetric mesh [210].

Table 4.4. Boundary conditions for the BYU reactor [210].

<b>Boundary conditions:</b>			
<b>1<sup>st</sup> stage</b>	<b>26.24 kg/h</b>	<b>Inlet temp.</b>	<b>Wall temp.</b>
O <sub>2</sub>	85 %	367 K	
Ar	12.6 %	367 K	
H <sub>2</sub> O	2.4 %	367 K	
<b>2<sup>nd</sup> stage, kg/h</b>	<b>6.62</b>	<b>450 K</b>	<b>1500 K</b>
H <sub>2</sub> O	100 %	450 K	
<b>Utah bituminous coal, kg/h</b>	<b>23.88 kg/h</b>	<b>300 K</b>	

## 4.6 Coal pyrolysis simulation – brief model setup

With regard to the model description of gasification, coal pyrolysis simulation considers the laminar flow, devolatilization, particle transport, and radiative transport. Radiation is modeled with the discrete ordinate method [223]. Devolatilization is modeled according to the

optimization procedure, shown in Figure 4.1, in the same way, as it was presented for coal gasification. In this case, however, apart from the C2SM approach, authors additionally examine the SFOR model. The numerical model is validated against the experimental data of Authier et al. [133] who studied coal pyrolysis under laminar flow conditions. Coal pyrolysis simulations are based on the drop tube furnace at LGRE - University of Haute-Alsace (Figure 4.12) [133]. Its geometry is incorporated in the CFD model. The reactor is a vertical cylinder with an inner diameter of 50 mm and a length of 1.4 m. The furnace is electrically heated by resistances. Reference temperatures of 1073K, 1173K, 1473K, and 1673K with the 70 cm reactor length, are investigated. The gas flow inside the reactor is laminar. The pressure is equal to 0.1 MPa.

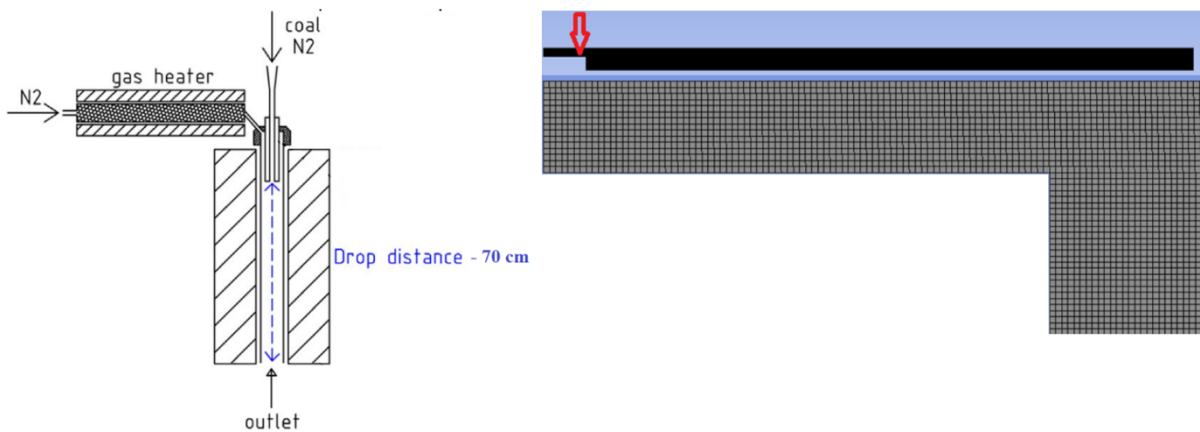


Figure 4.12. Drop tube furnace (DTF) geometry at LGRE with axisymmetric mesh [133].

The coal powder is injected continuously at the top of the drop tube carried by a nitrogen stream ( $30\text{L(stp)h}^{-1}$ ) at the temperature of 300K. The secondary stream contains nitrogen ( $370\text{L(stp)h}^{-1}$ ) heated to the temperature of 1173K. General boundary conditions are shown in Table 4.5. It can be noticed that the study regards four different wall temperatures. Thus the devolatilization process is examined in four different operating reactor conditions. The particle size follows a Rosin - Rammler distribution. The parameters used in this work are as follows: the minimum, mean and maximum diameters are 40, 55, and 80  $\mu\text{m}$ , respectively. The spread parameter is equal to 8.

Table 4.5. Boundary conditions for the LGRE gasifier [133].

<b>Boundary conditions:</b>				
	<b>Inlet</b>	<b>streams:</b>	<b>Inlet temperature [K]</b>	<b>Wall temperatures [K]</b>
	<b>[kg/s]</b>			
Primary:				
Calenturitas coal/	$1.39 \cdot 10^{-6}$		300	
C-coal				1073, 1173, 1473, 1673
Primary: N <sub>2</sub>	$1.042 \cdot 10^{-5}$		300	
Secondary: N <sub>2</sub>	0.000128		1173	

The geometry of the reactor is discretized using a 2D axisymmetric grid composed of about 50 000 rectangular cells. The pressure-based solver under steady-state conditions is employed. The SIMPLE [239] algorithm is used for pressure-velocity coupling. Gradients used to discretize the convection and diffusion terms in the flow conservation equations are computed according to the least-squares cell-based method [215]. Convective fluxes in all transport equations are discretized according to the second-order upwind scheme. The weighted-sum of gray gas (WSGG) model is used for the calculation of the gas absorption coefficient.

## **4.7 Results and discussion**

### **4.7.1 Coal gasification results**

The optimization of global devolatilization models was performed through the iterative procedure. Hence, the simulation results will be presented for each iteration step. It will allow us to depict the direct impact of the optimized kinetic parameters. It must be underlined that total volatile yield and composition are updated in the course of the optimization procedure next to kinetic parameters (Figure 4.1). Figure 4.13 presents CO and H<sub>2</sub> mole fraction distribution along the reactor centerline. It can be noticed that major species concentration obtained with non-optimized default kinetic parameters significantly deviates from optimized parameters as well as from experimental data. This observation is particularly strong in the near-burner region. The impact of optimization of kinetic parameters and consequently of the application of different devolatilization rates and yields are not significant, with regard to final syngas composition. The same conclusion was drawn by [77,123]. But the impact of different devolatilization rates and yields in the flame vicinity is significant. It proves that the outlet species measurement data only do not provide enough information to confirm the efficiency of the incorporated model. Many of the latest papers rely solely on the outlet data. But the detailed, in-reactor measurements are required. It can be noticed that each consecutive iteration shows a closer agreement with the advanced CPD model. The same trend can be seen for the CO<sub>2</sub> mole fraction distribution (Figure 4.13). The optimization procedure preserves the accuracy of the advanced network model while obtaining closer agreement with experimental data. The H<sub>2</sub>O composition (Figure 4.13) shows the worst agreement in the near-burner region, but it must be underlined, that the experimental data for this species were not available, and had to be calculated from the hydrogen balance [77]. This calculation, however, leads to an  $\pm 14\%$  uncertainty owing to the reported uncertainty in the char ash analysis [77], especially in the flame region. Nonetheless, the positive effect of the optimization performance can be noticed. Figure 4.14 and Figure 4.15 show the temperature prediction inside the reactor. As in the case of major species, the high-efficiency performance of the procedure can be seen in the flame estimation. Similar results for the CPD and the optimized empirical C2SM model can be noticed. On the other hand, entirely different flame prediction obtained by the C2SM model with standard parameters can be seen.

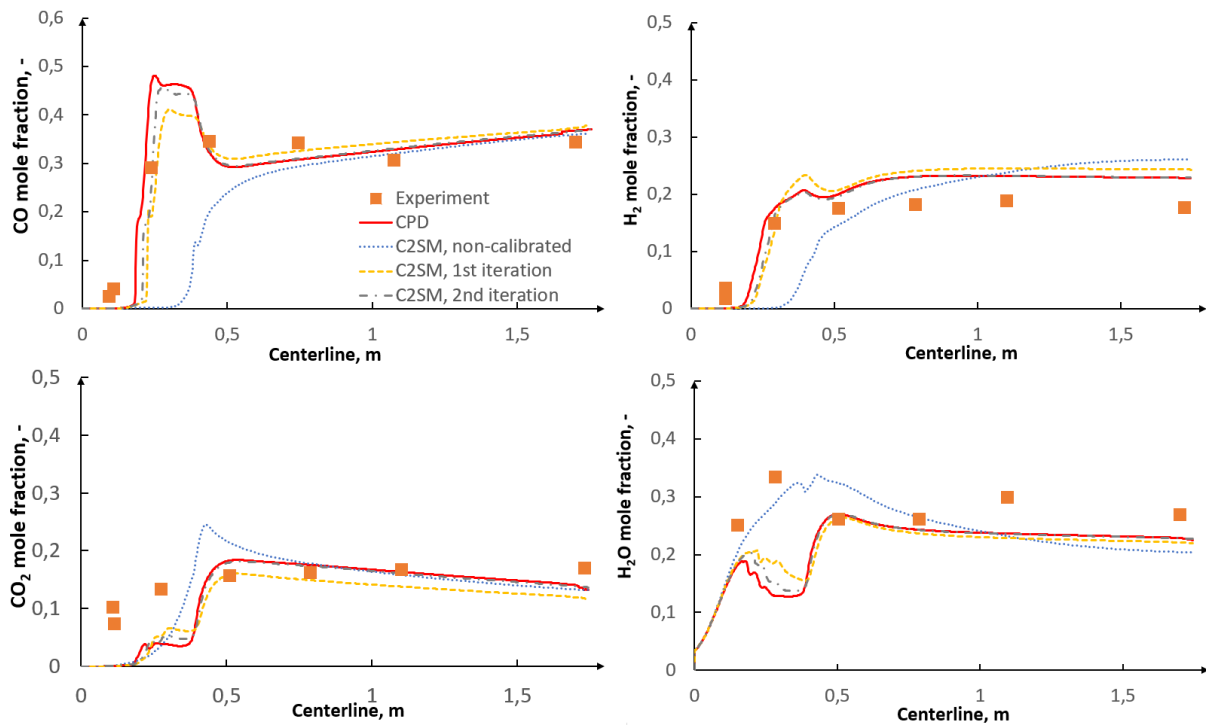


Figure 4.13. CO, H<sub>2</sub>, CO<sub>2</sub> and H<sub>2</sub>O mole fraction distribution along the centerline for consecutive iterations and for the CPD model [224].

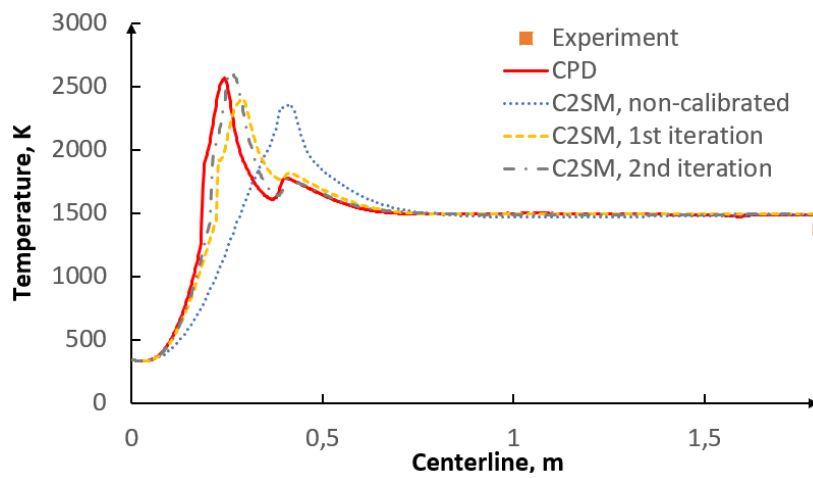


Figure 4.14. Temperature distribution along the centerline for consecutive iterations and for CPD [224].

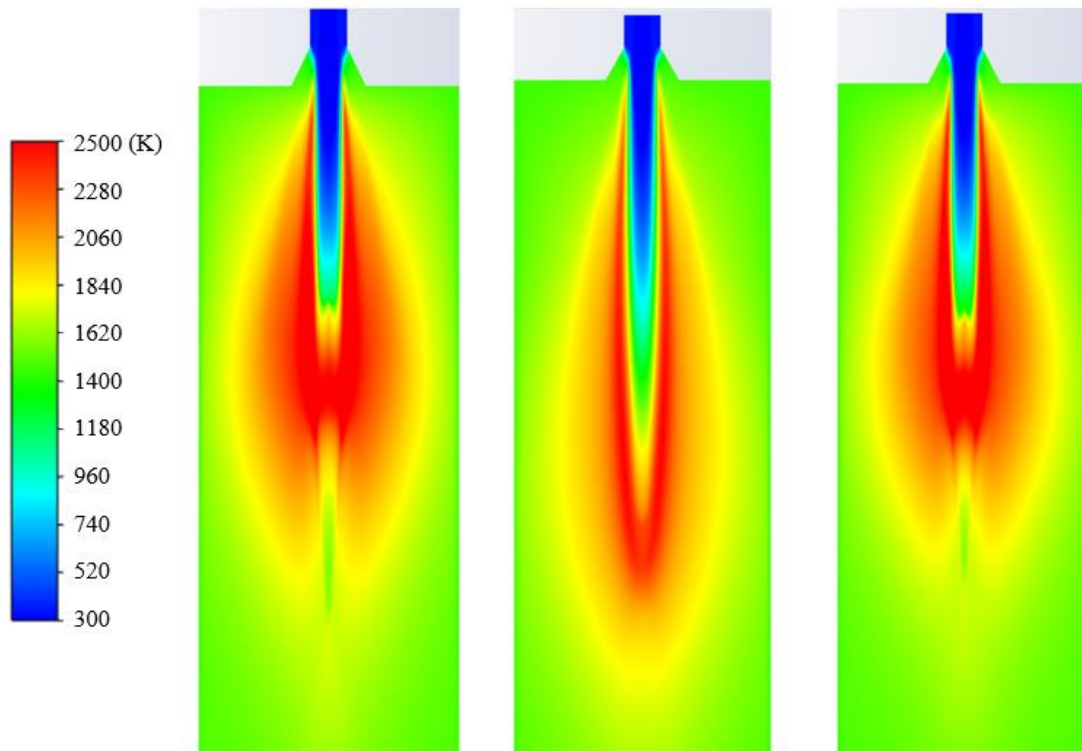


Figure 4.15. Temperature contour inside the BYU reactor. (Left: CPD model, Middle: C2SM with non-optimized kinetic parameters, Right: C2SM with optimized parameters) [224].

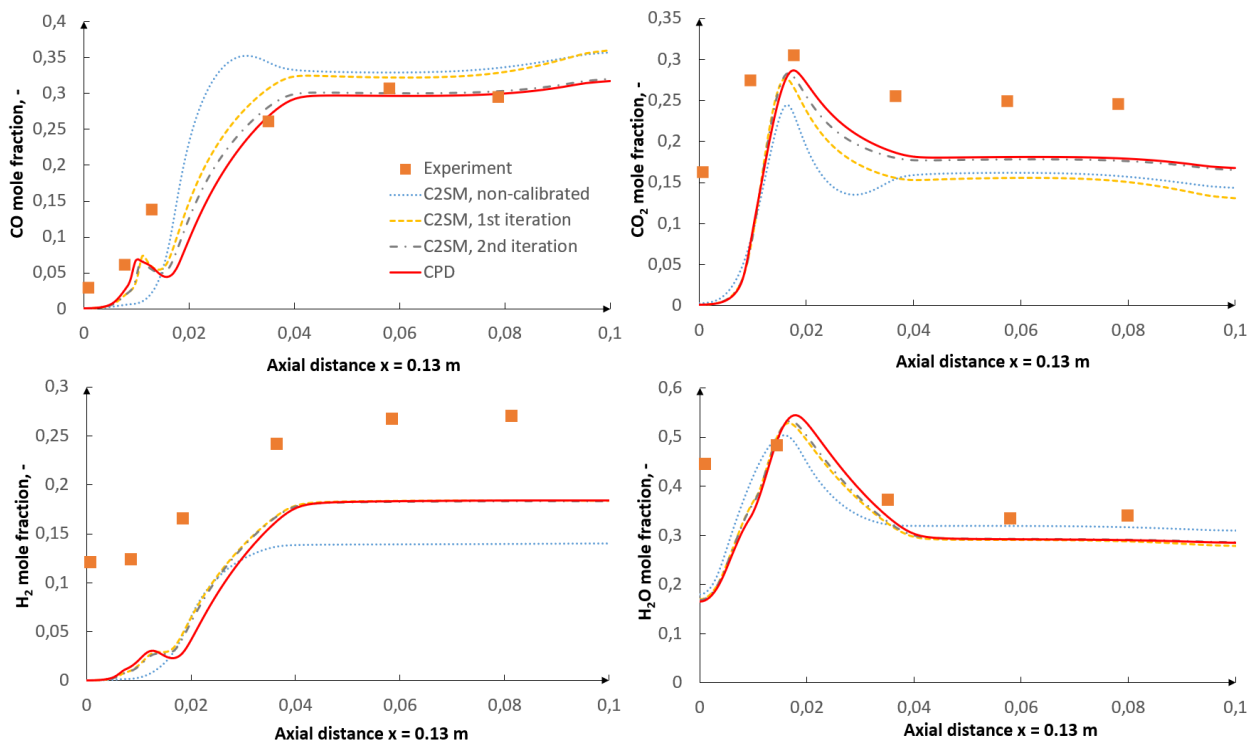


Figure 4.16. CO, H<sub>2</sub>, CO<sub>2</sub> and H<sub>2</sub>O mole fraction distribution along the axial distance  $x = 0.13$  m for consecutive iterations and for the CPD model [224].

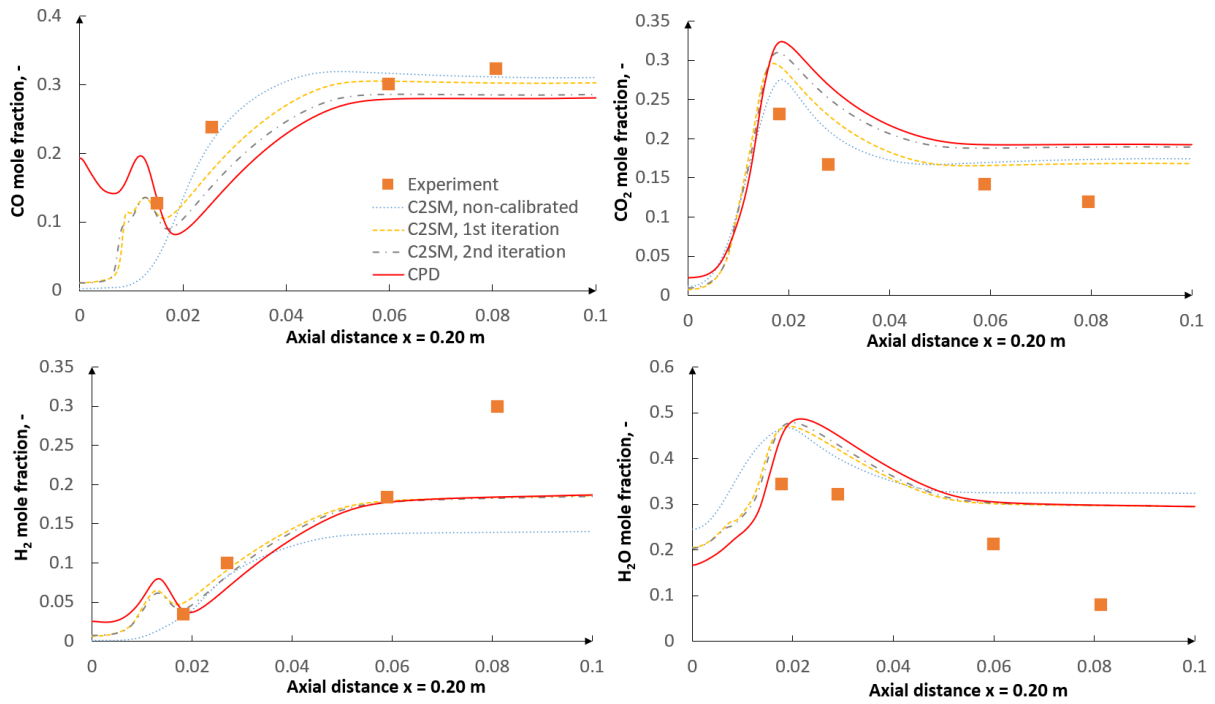


Figure 4.17. CO, H<sub>2</sub>, CO<sub>2</sub> and H<sub>2</sub>O mole fraction distribution along the axial distance  $x = 0.20$  m for consecutive iterations and for the CPD model.

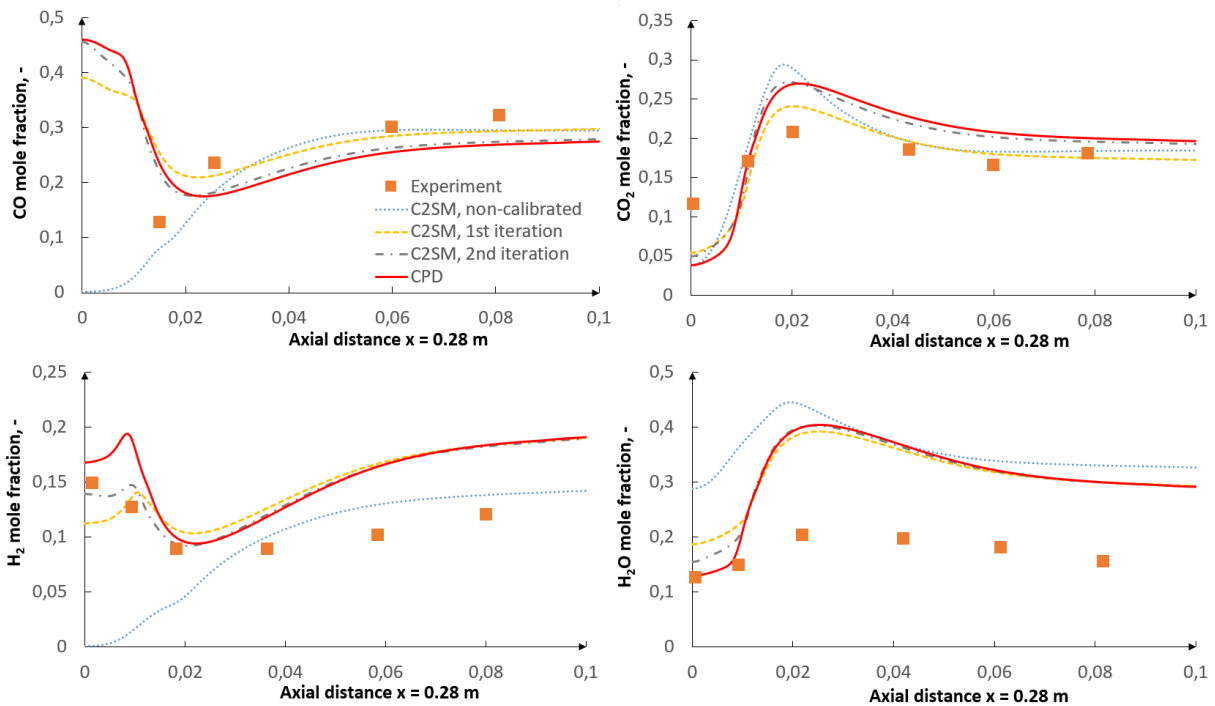


Figure 4.18. CO, H<sub>2</sub>, CO<sub>2</sub> and H<sub>2</sub>O mole fraction distribution along the axial distance  $x = 0.28$  m for consecutive iterations and for the CPD model [224].

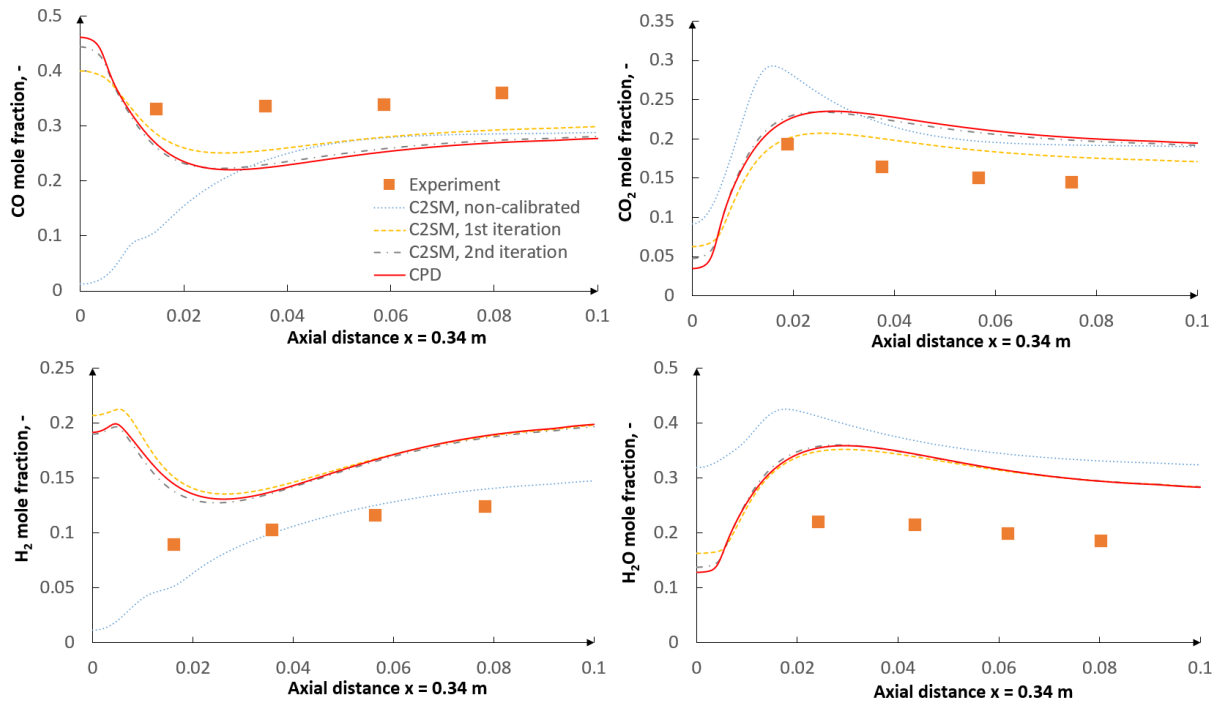


Figure 4.19. CO, H<sub>2</sub>, CO<sub>2</sub> and H<sub>2</sub>O mole fraction distribution along the axial distance  $x = 0.34$  m for consecutive iterations and for the CPD model.

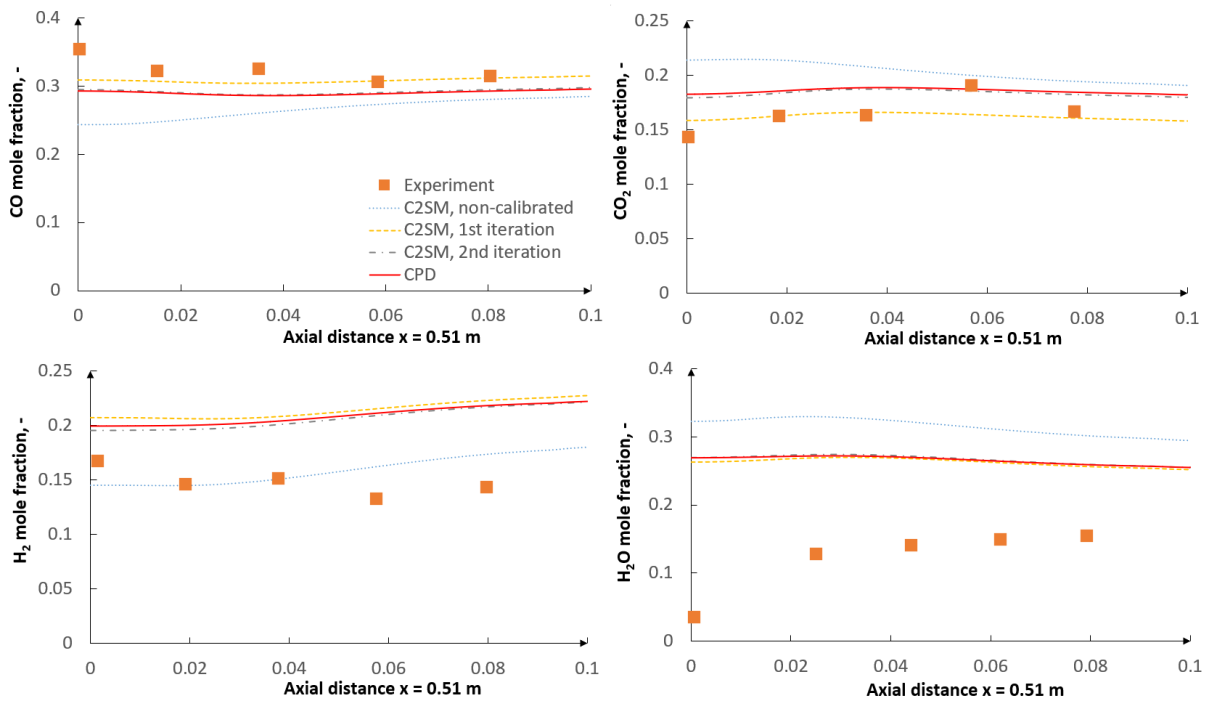


Figure 4.20. CO, H<sub>2</sub>, CO<sub>2</sub> and H<sub>2</sub>O mole fraction distribution along the axial distance  $x = 0.51$  m for consecutive iterations and for the CPD model.

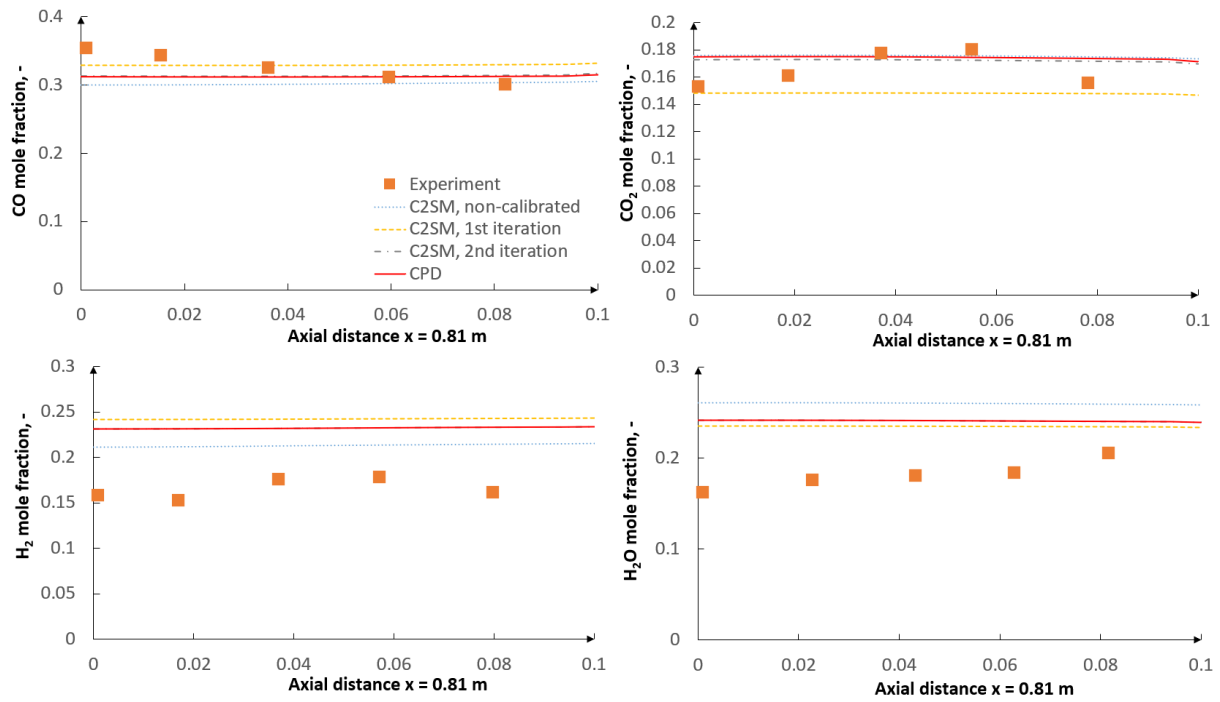


Figure 4.21. CO, H<sub>2</sub>, CO<sub>2</sub> and H<sub>2</sub>O mole fraction distribution along the axial distance  $x = 0.81$  m for consecutive iterations and for the CPD model.

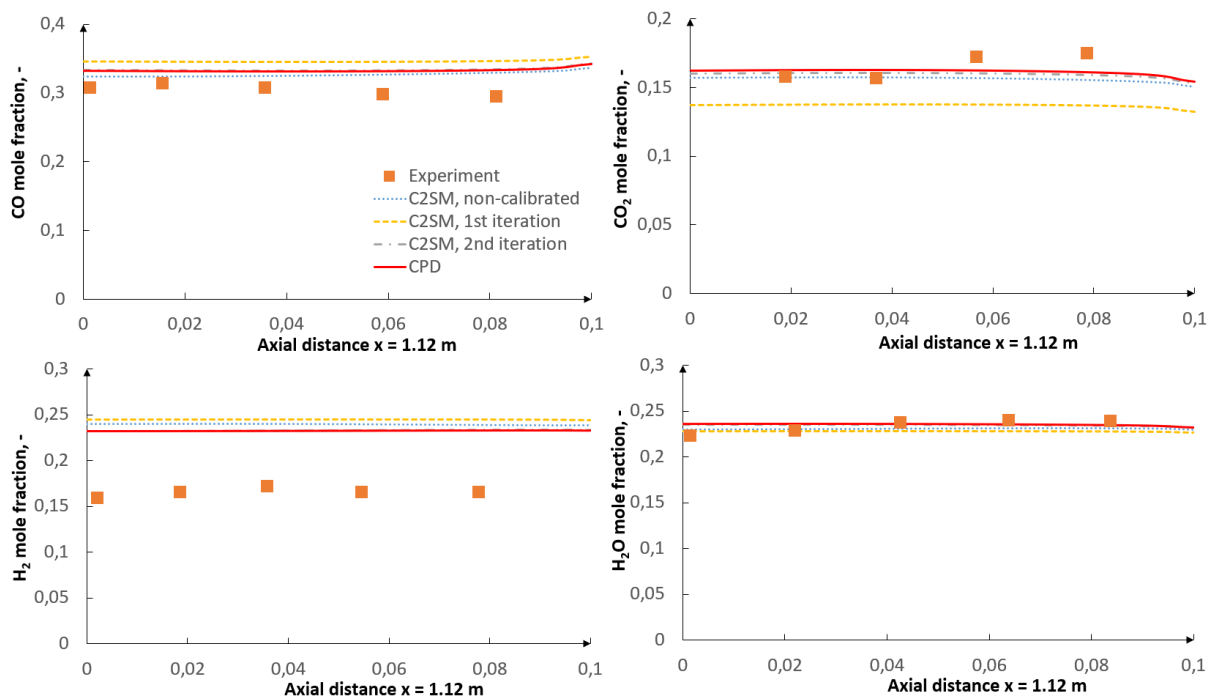


Figure 4.22. CO, H<sub>2</sub>, CO<sub>2</sub> and H<sub>2</sub>O mole fraction distribution along the axial distance  $x = 1.12$  m for consecutive iterations and for the CPD model [224].

Figure 4.16, Figure 4.18, Figure 4.22, Figure 4.19, Figure 4.20, Figure 4.21 and Figure 4.22 present the concentration of the main species in seven radial traverses. These traverses are visualized in Figure 4.23. The value of 0 in the horizontal ordinate indicates that the concentration is measured in the centerline. The value of 0.1 means that the concentration is measured close to the reactor wall.



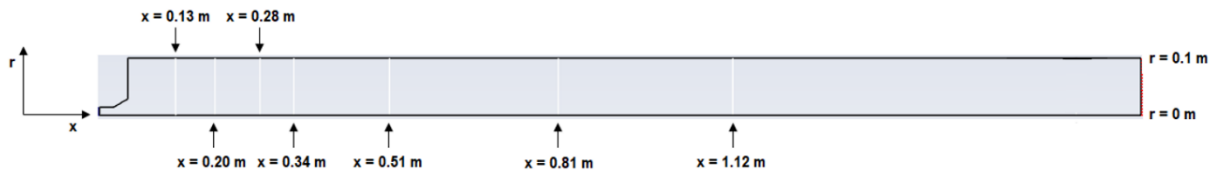


Figure 4.23. Seven radial traverses:  $x = 0.13$  m,  $x = 0.20$  m,  $x = 0.28$  m,  $x = 0.34$  m,  $x = 0.51$  m,  $x = 0.81$  m,  $x = 1.12$  m.

A general improvement in agreement with experimental data can be noticed. As already mentioned, the H<sub>2</sub>O data points are calculated from hydrogen balance and are not directly measured. Consequently, the agreement or lack of it with experimental data, should not be considered as highly credible. Obtained results prove that the devolatilization process is very important in the accurate prediction of flame properties and major species production in the near-burner region for coal gasification. Inappropriate estimation of kinetic parameters may lead to flame lift-off, unstable working conditions, and consequently to the reduction of the process efficiency. As a result, further detailed research is carried out that regards the impact of the optimization procedure directly in coal pyrolysis (Chapter 4.7.2).

#### 4.7.2 Coal pyrolysis results

This sub-chapter discusses the volatile yield with respect to time for different wall temperatures equal to 1073, 1173, 1473, 1673 K calculated with the CFD technique utilizing SFOR, C2SM, and the CPD model implemented in the CFD code. Computations are compared with the measurements of coal volatile yield [133]. The complexity of obtaining volatile evolution experimental data in the drop tube reactor must be underlined [78]. The mass loss was determined by the standard ash tracer method that assumes the ashes from coal to be inert. It was shown that DTF reactors often cause higher errors than the thermogravimetric analysis (TGA). There are several sources of potential inherent error associated with: ash tracer method, particle deposition on reactor walls, coal properties effect, difficulties in measuring wall temperature profile, or precision of coal feeder. In Figure 4.25 for the low wall temperature case (1073K), one can observe some inaccuracies in the experiment, where a drop in the volatile yield was reported in the last measurement point. Additionally, the direct measurement of coal samples in the reactor is complicated and unreliable, non-interfering methods are usually not available. Hence, the particle temperature-time histories are calculated in this research only with the CFD technique.

Figure 4.24 and Figure 4.25 depict the iterative optimization process of global SFOR and C2SM models. For the SFOR approach, a maximum of four iterations were enough to obtain convergence, whereas, for the C2SM model, a minimum of three iterations were necessary. Subsequent iterations have only overlapped the previous ones. In addition, it can be observed that each consecutive iteration for each wall temperature, provides closer agreement of the release rate of volatiles with the detailed CPD model (the curve slope). As it was already mentioned, due to the fact that the software version of the CPD model does not provide information about the volatile yield, it is therefore taken from the FG-DVC approach. Hence, the comparison between global models (SFOR, C2SM) and the CPD model should be directed only at the volatiles release rate.

A very high coal reactivity was observed for the highest wall temperatures (1173, 1473, 1673 K) in the experiment (Figure 4.24 and Figure 4.25). A close agreement was found between the simulation and the experimental results in those cases. The total volatile yield along with its composition was taken from the FG-DVC and was optimized simultaneously with kinetic parameters (Figure 4.1). However, for each of the examined cases (Figure 4.24 and Figure 4.25), the FG-DVC approach underestimates the final volatile yield and the optimization procedure reproduces this error. This underestimation is most significant for the lowest wall temperature case (1073 K case in Figure 4.25). For this reason, further analysis of this case should be performed.

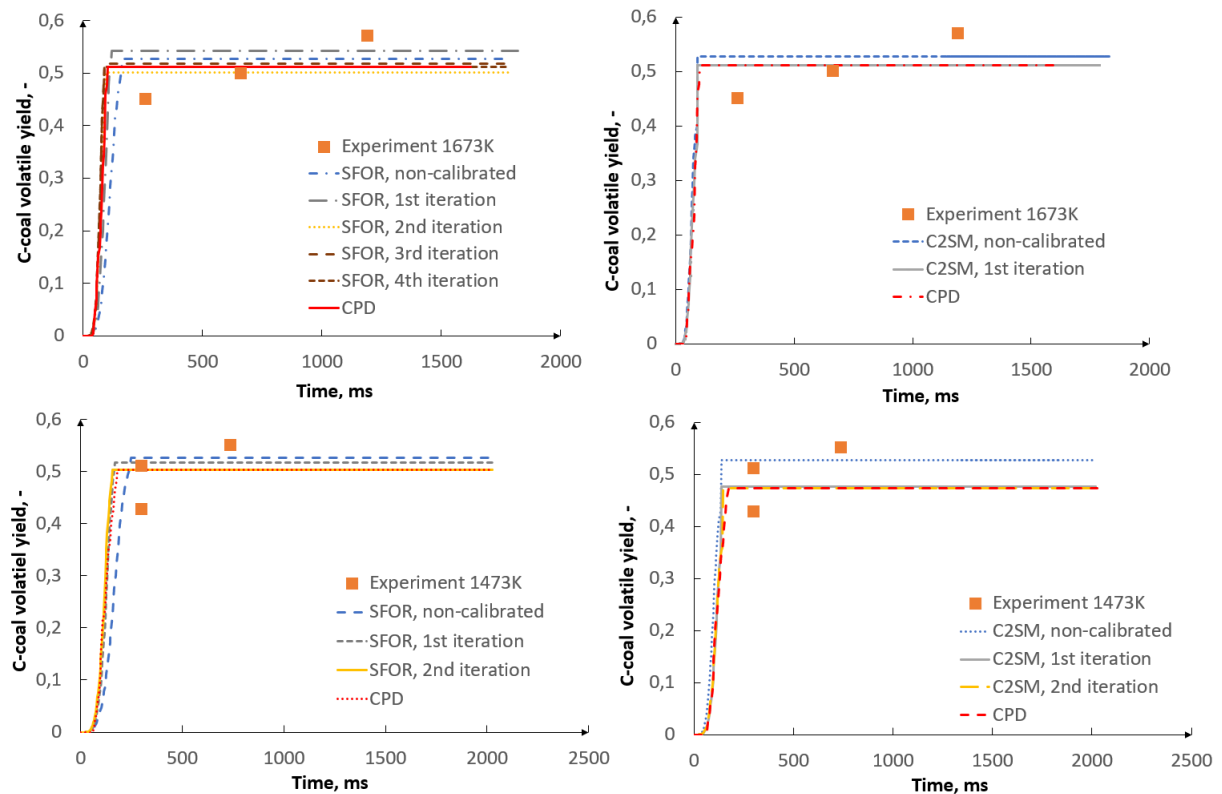


Figure 4.24. Volatile yield of the Calenturitas coal for the SFOR, C2SM, CPD models (dry-ash-free), Wall temperature: 1473, 1673 K [224].

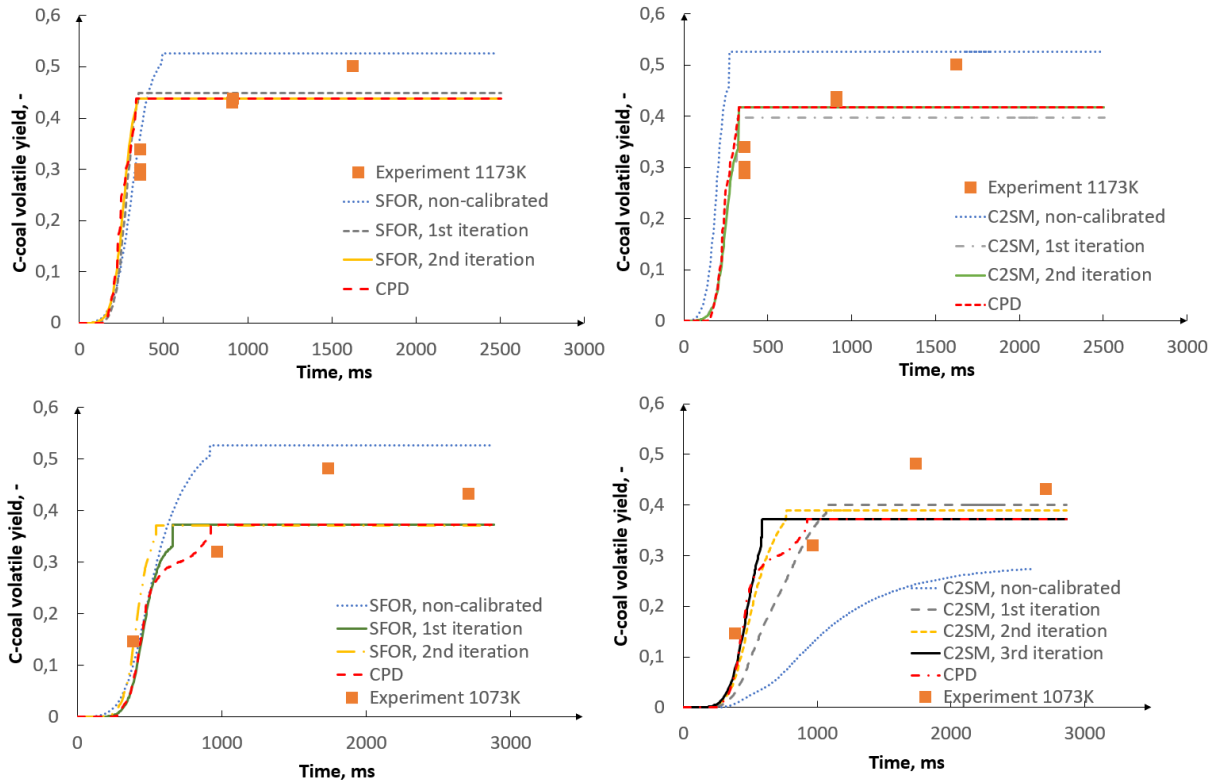


Figure 4.25. Volatile yield of the Calenturitas coal for the SFOR, C2SM, CPD models (dry-ash-free), Wall temperature: 1073, 1173 K [224].

Figure 4.26a depicts the volatile yield obtained by CPD and FG-DVC for the wall temperature 1073 K with the final volatile yield taken from the FG-DVC approach. A close match that is also characterized by a non-linear volatile matter evolution, can be observed. On the other hand, Figure 4.26b depicts the volatile yield from the CPD model by taking the final volatile yield not from FG-DVC, but from the experiment. In this case, a very high agreement between the model and experimental data can be noticed. Based on these two figures, one can conclude that both detailed approaches provide a similar prediction of the volatiles release rate, but the final volatile yield obtained by the FG-DVC approach is significantly underestimated. Figure 4.26b proves the relatively small influence of CFD inherent errors on the model prediction. At the same time, it confirms that the biggest issue related to the lack of accuracy between the numerical and experimental data, especially in Figure 4.25 and Figure 4.26, originates from the inaccurate prediction of the final volatile yield by the FG-DVC model.

The discrepancy between the detailed FG-DVC model and experimental results might be related to the fact that the evaluation of the kinetic rates originates from TGA at relatively slow heating rates. TGA results are often criticized that the data are not directly applicable to high heating rate applications [240]. Additionally, the final temperatures are higher in DTF or industrial applications compared to TGA. One source of inherent FG-DVC error is associated with the extrapolation strategy of TGA kinetic data to high heating rate conditions. Since the steepness of the FG-DVC curve almost does not change at different heating rates, Figure 4.24 and Figure 4.25 suggest that extrapolation is based mainly on the activation energy variation and not on the pre-exponential factor.

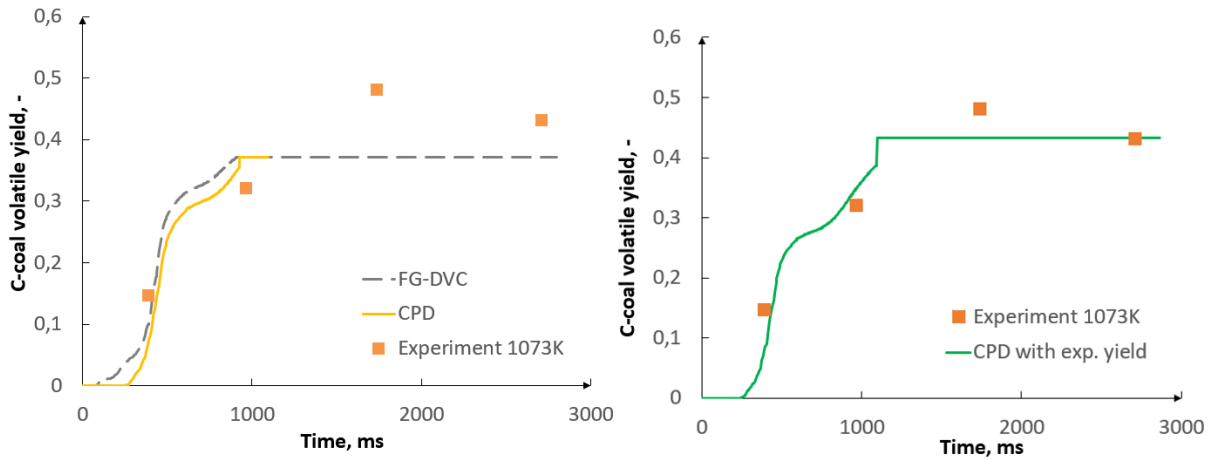


Figure 4.26. Volatile yield of the Calenturitas coal for the wall temperature: 1073K. Left: FG-DVC and CPD models with the final volatile yield taken from FG-DVC. Right: CPD model with the final volatile yield taken from the experiment [224].

### 4.7.3 Constant heating rate vs instantaneous heating rate

This sub-chapter presents the comparison of two heating rate assessment methods. As it was mentioned, the constant heating rate (linear heating) is a devolatilization-time-averaged value which is calculated from the CFD particle thermal history as a ratio of the total change in temperature during the devolatilization process to its time of duration. The instantaneous heating rate considers the detailed CFD particle thermal history without the averaging effect. As a result, after the incorporation of both constant and instantaneous heating rates into FG-DVC, one obtains two volatile yield curves (Figure 4.27).

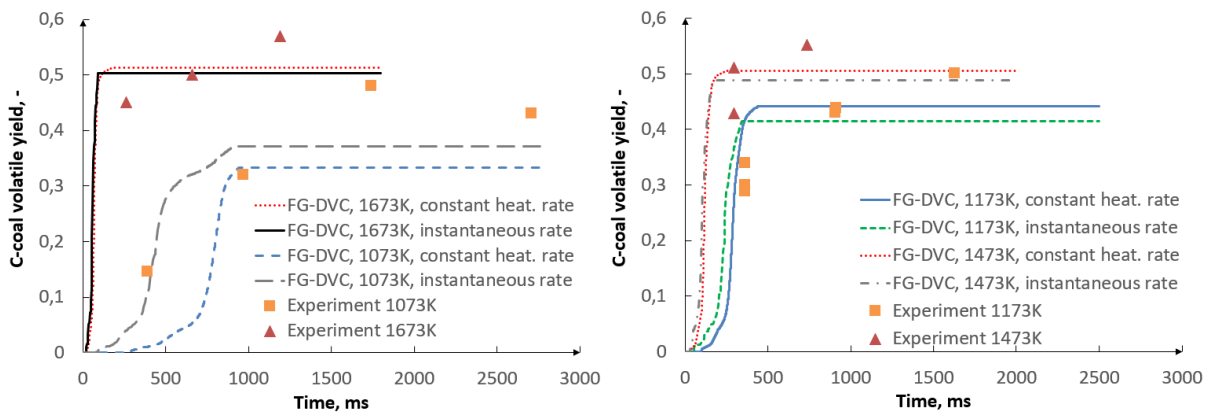


Figure 4.27. Volatile yield of the Calenturitas coal as a function of time for the devolatilization-time-averaged heating rate and for the instantaneous heating rate. Wall temperatures: 1073K, 1173K, 1473K, 1673K [224].

Figure 4.27 shows the comparison of both heating rate representation methods based on the volatile yield obtained from the FG-DVC approach for each wall temperature case. For higher temperatures and heating rates, the difference between the constant devolatilization-time-averaged heating rate and the instantaneous heating rate decreases. The most substantial discrepancy can be seen for the wall temperature of 1073K, whereas the marginal difference concerns the case with the wall temperature equal to 1673 K. It can be concluded that for low

heating rates, the entire particle thermal history should be provided to estimate the instantaneous particle heating rate during devolatilization.

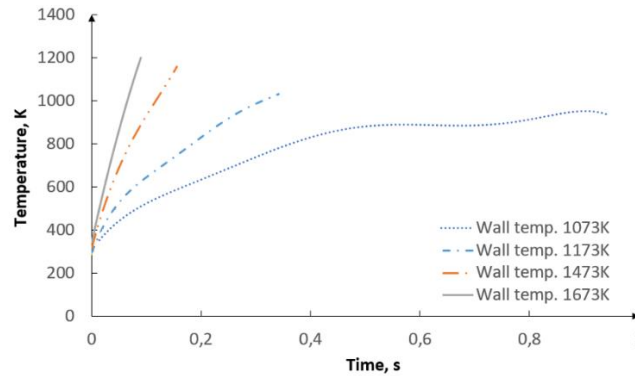


Figure 4.28. Particle temperature of the Calenturitas coal as a function of devolatilization time for different wall temperatures.

Figure 4.28 explains the reason for accuracy improvement at the lowest wall temperature case (1073 K) when the instantaneous particle heating rate is incorporated in the optimization procedure (Figure 4.27). Figure 4.28 depicts that one potential source of model inaccuracy is related to a change in particle thermal history curve shape as the wall temperature (particle heating rate) drops. One can observe that particle thermal history is almost linear only for the highest wall temperatures. In this case, the constant average heating rate can be assumed in the optimization procedure and there is an insignificant improvement associated with the implementation of instantaneous particle heating rate compared to the average one (Figure 4.27). However, for lower wall temperatures, the shape departs from the straight line and the constant heating rate assumption might introduce a significant error. The detailed particle history should be considered.

#### 4.7.4 Model quality estimation

The effect of the optimization procedure has also been quantitatively measured. The accuracy of the optimization procedure has been additionally assessed with error analysis. A maximum and average value of absolute errors for non-optimized and optimized models are presented. The absolute error is defined as:

$$\Delta e = |x_{exp} - x_{num}| \quad (4.17)$$

where  $x_{exp}$  and  $x_{num}$  are the experimental and numerical values of the specific variable (e.g. volatile yield, CO/H<sub>2</sub>/CO<sub>2</sub>/H<sub>2</sub>O mole fraction), respectively. The error analysis is performed for exemplary figures for the stepwise iterations of the global model and for the advanced CPD model.

Table 4.6. Error analysis of volatile yield for wall temperature of 1073K, 1173K, 1473K and 1673K – Devolatilization in an inert atmosphere – C2SM (Figure 4.24, Figure 4.25).

Iteration s	Volatile yield for wall temperature of 1073 K		Volatile yield for wall temperature of 1173 K		Volatile yield for wall temperature of 1473 K		Volatile yield for wall temperature of 1673 K	
	Max $\Delta e$ [%]	Av. $\Delta e$ [%]	Max $\Delta e$ [%]	Av. $\Delta e$ [%]	Max $\Delta e$ [%]	Av. $\Delta e$ [%]	Max $\Delta e$ [%]	Av. $\Delta e$ [%]
0	23.7	18.1	22.6	11.5	5.3	3.9	7.5	4.9
1	11.9	6.3	10.2	7.8	7.6	3.8	6.0	4.4
2	9.0	6.6	11.7	7.2	7.6	3.8	-	-
3	10.8	5.7	-	-	-	-	-	-
CPD model	10.6	5.3	11.7	7.2	7.6	3.8	6.0	4.4

Table 4.7. Error analysis of volatile yield for wall temperature of 1073K, 1173K, 1473K and 1673K – Devolatilization in an inert atmosphere – SFOR (Figure 4.24, Figure 4.25).

Iteration s	Volatile yield for wall temperature of 1073 K		Volatile yield for wall temperature of 1173 K		Volatile yield for wall temperature of 1473 K		Volatile yield for wall temperature of 1673 K	
	Max $\Delta e$ [%]	Av. $\Delta e$ [%]	Max $\Delta e$ [%]	Av. $\Delta e$ [%]	Max $\Delta e$ [%]	Av. $\Delta e$ [%]	Max $\Delta e$ [%]	Av. $\Delta e$ [%]
0	20.7	8.6	9.2	4.5	5.6	3.9	7.9	5.1
1	10.8	5.3	5.2	3.3	4.9	4.1	9.3	5.4
2	10.8	5.3	6.3	3.1	4.7	4.1	6.8	4.1
3	-	-	-	-	-	-	7.0	4.7
4	-	-	-	-	-	-	6.4	4.5
CPD model	10.8	5.3	6.3	3.1	4.7	4.1	6.4	4.5

Table 4.8. Error analysis of CO, H<sub>2</sub>, CO<sub>2</sub> and H<sub>2</sub>O concentration along the centerline of the BYU reactor – gasification (Figure 4.13).

Iterations	CO		H <sub>2</sub>		CO <sub>2</sub>		H <sub>2</sub> O	
	Max $\Delta e$ [%]	Av. $\Delta e$ [%]	Max $\Delta e$ [%]	Av. $\Delta e$ [%]	Max $\Delta e$ [%]	Av. $\Delta e$ [%]	Max $\Delta e$ [%]	Av. $\Delta e$ [%]
0	28.8	8.3	14.7	5.5	10.1	5.5	6.7	4.8
1	10.1	3.7	6.7	3.9	10.2	5.0	14.7	5.9
2	4.1	2.9	5.2	3.3	10.2	4.8	18.1	6.3
CPD model	4.1	2.4	5.1	3.5	10.2	5.0	20.5	6.7

Table 4.9. Error analysis of CO, H<sub>2</sub>, CO<sub>2</sub> and H<sub>2</sub>O concentration along radial traverse x=0.13 of the BYU reactor – gasification (Figure 4.16).

Iterations	CO		H <sub>2</sub>		CO <sub>2</sub>		H <sub>2</sub> O	
	Max Δe [%]	Av. Δe [%]	Max Δe [%]	Av. Δe [%]	Max Δe [%]	Av. Δe [%]	Max Δe [%]	Av. Δe [%]
0	11.6	5.8	13.0	11.9	17.4	11.2	26.4	7.3
1	7.7	3.9	11.9	9.8	17.4	11.0	28.1	8.7
2	8.1	3.0	11.9	9.8	17.4	9.4	27.9	8.4
CPD model	7.9	2.5	13.0	10.2	17.4	9.1	27.9	8.1

Table 4.10. Error analysis of CO, H<sub>2</sub>, CO<sub>2</sub> and H<sub>2</sub>O concentration along radial traverse x=0.28 of the BYU reactor – gasification (Figure 4.18).

Iterations	CO		H <sub>2</sub>		CO <sub>2</sub>		H <sub>2</sub> O	
	Max Δe [%]	Av. Δe [%]	Max Δe [%]	Av. Δe [%]	Max Δe [%]	Av. Δe [%]	Max Δe [%]	Av. Δe [%]
0	5.5	3.4	14.8	6.0	7.9	3.6	24.0	18.5
1	12.6	4.7	6.4	3.7	6.2	2.6	18.1	12.5
2	8.8	5.7	6.3	3.2	6.6	3.6	19.5	12.0
CPD model	10.2	6.6	6.3	4.1	8.0	4.1	19.5	11.2

Table 4.11. Error analysis of CO, H<sub>2</sub>, CO<sub>2</sub> and H<sub>2</sub>O concentration along radial traverse x=1.12 of the BYU reactor – gasification (Figure 4.22).

Iterations	CO		H <sub>2</sub>		CO <sub>2</sub>		H <sub>2</sub> O	
	Max Δe [%]	Av. Δe [%]	Max Δe [%]	Av. Δe [%]	Max Δe [%]	Av. Δe [%]	Max Δe [%]	Av. Δe [%]
0	3.6	2.2	8.2	7.5	1.9	0.9	0.9	0.6
1	5.4	4.3	8.6	8.0	3.8	2.8	1.2	0.7
2	4.0	2.9	7.2	6.7	1.5	0.8	1.2	0.6
CPD model	4.0	2.9	7.2	6.7	1.3	0.8	1.2	0.6

Table 4.12. Error analysis of volatile yield for wall temperature of 1073K – Devolatilization in an inert atmosphere – CPD and FG-DVC (Figure 4.26).

Models	Volatile yield for wall temperature of 1073 K	
	Max Δe [%]	Av. Δe [%]
FG-DVC	10.9	5.5
CPD	11.0	5.1
CPD with exp. yield	4.9	1.7

Table 4.13. Error analysis of volatile yield for wall temperature of 1073K, 1173K, 1473K, 1673K – Devolatilization in an inert atmosphere – the constant heating rate and the instantaneous heating rate (Figure 4.27).

Heating rate	Volatile yield for wall temperature of 1073 K		Volatile yield for wall temperature of 1173 K		Volatile yield for wall temperature of 1473 K		Volatile yield for wall temperature of 1673 K	
	Max $\Delta e$ [%]	Av. $\Delta e$ [%]	Max $\Delta e$ [%]	Av. $\Delta e$ [%]	Max $\Delta e$ [%]	Av. $\Delta e$ [%]	Max $\Delta e$ [%]	Av. $\Delta e$ [%]
Constant heating rate	14.9	10.0	11.7	6.1	4.2	4.2	6.8	4.7
Instantaneous heating rate	11.3	5.6	8.5	6.1	6.1	4.1	6.2	4.1

The results from the tables confirm the increase of agreement between numerical and experimental data. For some cases, the improvement was significant, whereas for some cases it was marginal. One may observe that three cases have been highlighted where the optimization procedure decreased the agreement. However, two of these cases regard the  $H_2O$  concentration in gasification (Table 4.8 and

Table 4.9) where the experimental data points were calculated from hydrogen balance and were not directly measured. The third case (Table 4.10) considers CO mole fraction along the radial traverse  $x = 0.28$  m. Although it may seem that the error for the non-optimized model is the lowest, Figure 4.13 in the manuscript indicates that the CO mole fraction at  $x = 0.28$  m in the centerline for the non-optimized model (blue line) is equal to 0. It is untrue when one considers Figure 4.18, and the experimental CO concentration for  $x \approx 0.28$ , where a value higher than 0.3, is expected. Therefore, the positive effect of the optimization procedure should also be attributed to this case.

## 4.7.5 Conclusions

An optimization procedure for the SFOR and C2SM devolatilization models, based on the FG-DVC approach, was presented. The following conclusions can be drawn:

- The use of the optimization procedure resulted in better agreement between the model results and the experimental data for both coal pyrolysis and coal gasification.
- The constant devolatilization-time-averaged heating rate approach is inaccurate for devolatilization in low heating rate conditions. The entire particle thermal history with the instantaneous heating rate description should be provided. At higher heating rates (higher than 10 000 K/s), the constant devolatilization-time-averaged heating rate approach yields similar results as the instantaneous particle heating rate approach. For this reason, the global gasification models were optimized using the averaged heating rate.
- The FG-DVC model inaccurately estimates the final volatile yield for a wide range of heating rates. Moreover, the steepness of the FG-DVC curve almost does not change at different heating rates. This suggests that the extrapolation from TGA is based mainly on the activation energy variation and not on the pre-exponential factor.



- Devolatilization proved to have a crucial role in the gasification process simulations. The optimized models predicted the gas production rate and the composition and temperature of the gas differently (especially in the near-burner region) than the standard non-optimized models. This confirms devolatilization sensitivity to operating conditions and proves the importance of kinetic parameters in the accurate simulation of the entire gasification process.

## 5. Gas phase modeling

The results from this chapter have been published in [241]

[241] Mularski J., Modliński N. Impact of Chemistry – Turbulence Interaction Modeling Approach on the CFD Simulations of Entrained Flow Coal Gasification. *Energies* 2020;13:6467. <https://doi.org/10.3390/en13236467>  
*MNiSW (2019-2021): 140 pts, IF (2019): 2.702*

### 5.1 Introduction

On the basis of the literature review by Mularski et al. [31], a conclusion was drawn that the majority of authors utilized global combustion mechanisms and turbulence-chemistry interaction approaches the same as in coal combustion studies. However, these processes differ substantially. Unlike in conventional combustion, where infinitely fast chemistry is generally assumed, in the case of gasification there is an extended reacting flow region with lower temperatures where chemical reaction rates are comparable to turbulent mixing rates. For example, CO does oxidize rapidly at high temperatures with oxygen supply but does not oxidize so well at the cooler temperatures or less intensive mixing conditions. Such conditions are common in entrained flow gasifiers. Additionally, at high temperatures, the dissociation reactions are promoted. For such systems, it is necessary to use more detailed and complex approaches, which usually require the adoption of finite-rate chemistry. Therefore the interaction between the turbulent effects and the reaction chemistry needs to be accurately described. On top of that, no study was found that would thoroughly investigate and compare the gas phase models strictly in gasification conditions to be able to assess their accuracy with respect to combustion. On this basis, I have decided to study these aspects thoroughly.

Some authors considered the influence of the gas phase stage in MILD combustion [97,242] or PCC combustion [243]. Only one publication was found that considered the impact of the gas phase stage strictly in gasification conditions [98], but it accounted for only the comparison between the finite-rate model and the finite-rate/eddy dissipation model. Therefore, one of the objectives of the dissertation was to thoroughly investigate the direct impact of the gas-phase stage modeling on the entire entrained flow gasification process.

This chapter examines the impact of different chemistry-turbulence interaction approaches on the accuracy of simulations of coal gasification in entrained flow reactors. Infinitely fast chemistry is compared with the eddy dissipation concept considering the influence of turbulence on chemical reactions. Additionally, an ideal plug flow reactor study

and a perfectly stirred reactor study are carried out to estimate the accuracy of chosen simplified chemical kinetic schemes in comparison with two detailed mechanisms. The most accurate global approach and the detailed one are further implemented in the CFD code. Special attention is paid to the water-gas shift reaction, which is found to have a key impact on the final gas composition. Three different reactors are examined: a pilot-scale Mitsubishi Heavy Industries reactor, a laboratory-scale reactor at Brigham Young University, and a Conoco-Philips E-gas reactor. The aim of this research was to assess the impact of gas-phase combustion model accuracy on gasification simulations and to find which mechanisms are more suitable for reproducing the entrained flow gasification process. It turned out that the advanced turbulence-chemistry models with the complex kinetic mechanisms showed the best agreement with the experimental data.

## 5.2 Mathematical model – brief setup

A summary of the models applied to the reactors is presented in Table 5.1.

Table 5.1. Summary of applied models [241].

Models	BYU gasifier	MHI gasifier	E-gas gasifier
<b>Devolatilization:</b>	<ul style="list-style-type: none"> <li>• CPD [5,7,52]</li> <li>• FG-DVC [8]</li> </ul>	<ul style="list-style-type: none"> <li>• SFOR [37–40]</li> <li>• FG-DVC</li> </ul>	<ul style="list-style-type: none"> <li>• C2SM [39]</li> <li>• FG-DVC</li> </ul>
<b>Gas phase:</b>	<ul style="list-style-type: none"> <li>• Global reaction approach with finite-rate/eddy dissipation model</li> <li>• Global reaction approach with eddy dissipation concept</li> <li>• Detailed GRI-Mech mechanism with eddy dissipation concept</li> </ul>		
<b>Char conversion:</b>	<ul style="list-style-type: none"> <li>• Multiple surface reaction model [168]</li> </ul>		
<b>Turbulence:</b>	<ul style="list-style-type: none"> <li>• Realizable k-<math>\epsilon</math> model [218]</li> </ul>		
<b>Radiation:</b>	<ul style="list-style-type: none"> <li>• Discrete ordinate method [223]</li> </ul>		
<b>Gas absorption coefficient:</b>	<ul style="list-style-type: none"> <li>• Weighted sum of gray gas model [215]</li> </ul>		
<b>Pressure-velocity coupling</b>	<ul style="list-style-type: none"> <li>• SIMPLE [239]</li> </ul>		

Devolatilization is modeled for each of the reactors according to the Mularski and Modliński optimization procedure [224]. This approach considers the effect of operating conditions (heating rate, fuel properties) on the volatile matter release [78]. The optimization process (Figure 4.1) yields kinetic parameters (the pre-exponential factor and activation energy) for SFOR and C2SM, based on FG-DVC results, through the minimization of the objective function. FG-DVC is used independently of CFD, as a stand-alone model. Moreover, it estimates the volatile yield which is then incorporated into CFD. The reason why the three different devolatilization models are used (CPD, SFOR, C2SM) lies in the complexity of the particular reactors. The MHI reactor required the longest simulation time while the BYU gasifier required the lowest computational cost. The global empirical models (SFOR, C2SM) allowed us to reduce the computational effort.

Modeling turbulent reactive flow requires extensive computational resources. The cost rises with the number of chemical species involved in the kinetic mechanism. The detailed

chemistry is adopted for combustion systems only in the case of simple geometries and fuels that incorporate a small number of species. For efficient computations, the chemical kinetics mechanisms incorporated in the CFD simulations need to be as small as possible. Solid fuels devolatilization products are composed of hydrocarbons for which a comprehensive mechanism is not available. For this reason, simplified kinetic mechanisms were developed. The global reaction mechanisms demonstrated in Table 5.2 are the most convenient and hence considered in this dissertation.

Table 5.2. Investigated global reaction mechanisms [241].

Reaction:	A (s-m-kmol)	T <sub>b</sub>	E <sub>a</sub> (J/kmol)
Mechanism 1			
H <sub>2</sub> + 0.5O <sub>2</sub> → H <sub>2</sub> O	6.8e15	0	1.67e08
CH <sub>4</sub> + 0.5O <sub>2</sub> → CO + 2H <sub>2</sub>	0.44e12	0	1.2552e08
CH <sub>4</sub> + H <sub>2</sub> O → CO + 3H <sub>2</sub>	0.30e09	0	1.2552e08
CO + H <sub>2</sub> O = CO <sub>2</sub> + H <sub>2</sub>	0.275e10	0	8.368e07
CO + 0.5O <sub>2</sub> → CO <sub>2</sub>	2.24e12	0	1.67e08
Mechanism 2			
H <sub>2</sub> + 0.5O <sub>2</sub> → H <sub>2</sub> O	0.10e07	0	8.368e07
CH <sub>4</sub> + 0.5O <sub>2</sub> → CO + 2H <sub>2</sub>	0.44e12	0	1.2552e08
CH <sub>4</sub> + H <sub>2</sub> O → CO + 3H <sub>2</sub>	0.30e09	0	1.2552e08
CO + H <sub>2</sub> O = CO <sub>2</sub> + H <sub>2</sub>	0.275e10	0	8.368e07
Mechanism 3			
H <sub>2</sub> + 0.5O <sub>2</sub> → H <sub>2</sub> O	1.00e07	0	8.368e06
CO + 0.5O <sub>2</sub> → CO <sub>2</sub>	5.42e09	0	1.2552e08
CH <sub>4</sub> + 1.5O <sub>2</sub> → CO + 2H <sub>2</sub> O	7.28e09	0.5	1.6736e08
Mechanism 4			
CH <sub>4</sub> + 0.5O <sub>2</sub> → CO + 2H <sub>2</sub>	3.80e07	0	5.5463e07
CH <sub>4</sub> + 1.5O <sub>2</sub> → CO + 2H <sub>2</sub> O	2.33e11	0.5	1.6737e08
CO + 0.5O <sub>2</sub> → CO <sub>2</sub>	1.30e11	0	1.252e08
Surface reactions for each mechanism			
C(s) + 0.5O <sub>2</sub> → CO	5.09e+08	0	1.79e04
C(s) + CO <sub>2</sub> → 2CO	6.35e+09	0	3.87e04
C(s) + H <sub>2</sub> O → CO + H <sub>2</sub>	1.90e07	0	3.51e04

Mechanism 1 and Mechanism 2 are based on [105], but Mechanism 1 additionally incorporates the reaction of CO oxidation to CO<sub>2</sub> [106]. Mechanism 1 was often employed in gasification modeling. Mechanism 3 works under the assumption of a water-gas shift equilibrium. Mechanism 4 is mainly based on the one described in [139]. All of the examined approaches consider CH<sub>4</sub> to represent the reactions of hydrocarbons and tar.

### 5.2.1 Plug flow reactor study

Reduced mechanisms are mostly applied to decrease the computational effort. Their application is usually associated with accuracy loss, thus making the simulations unreliable. An effective solution is to compare global mechanisms with either experimental measurements or

validated complex kinetic mechanisms. In the present paper, the global hydrocarbon combustion mechanisms were compared with the detailed CRECK mechanism (1999 elementary chemical reactions, 115 species) [10,244] and with the detailed GRI-Mech 3.0 mechanism (325 elementary chemical reactions, 53 species) [9].

The objective of this section is to characterize the behavior of global reaction mechanisms under high-temperature gasification conditions. An investigation was carried out to indicate which global mechanism has the highest accuracy. The chosen detailed mechanisms were validated in various conditions. It must be mentioned that the validation range of GRI-Mech for pressure is up to 10 atm, whereas the validation range of CRECK is up to 100 atm. An additional comparison of these two approaches is made for pressures above 10 atm. This validation was necessary since GRI-Mech can be implemented into the CFD model, while CRECK is simply too large to be used in 3-D reactive flow simulations due to computational effort.

The analysis provided almost identical results of GRI-Mech and CRECK for all examined conditions – (See sub-chapters 5.3.1 and 5.3.2). Owing to the fact that GRI-Mech is less computationally expensive, it will further serve as reference data. As a result, I will assume that the global mechanism from Table 5.2 which results will be closest to GRI-Mech 3.0 brings the highest level of confidence.

The calculations have been carried out with an in-house plug flow model. The calculations utilized GSL (GNU Scientific Library) libraries to solve the system of stiff differential equations. The basic assumption of the plug flow reactor model is that the fluid is perfectly mixed in the direction perpendicular to the axis and that axial diffusive transport is negligible.

Table 5.3 presents the input parameters for PFR.

Table 5.3. Input parameters for PFR [241].

Fuel mixture, mole fraction	Oxidizer mixture, mole fraction	Equivalence ratio	Initial gas temperature
C(s) – 0.677	H <sub>2</sub> O – 0.22	2.2	800 K
CH <sub>4</sub> – 0.284	N <sub>2</sub> – 0.10		
CO – 0.039	O <sub>2</sub> – 0.68		

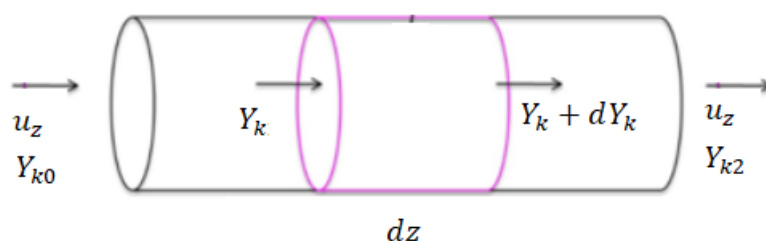


Figure 5.1. Sketch map of plug flow reactor [241].

The species continuity equation for the steady, constant cross-sectional plug flow is described as:

$$\rho u_z \frac{dY_k}{dz} = R_k \quad (5.1)$$

where  $\rho$  is density,  $u_z$  is velocity in z direction,  $Y_k$  is mass fraction of species k,  $dz$  is differential thickness of fluid plug and  $R_k$  is reaction rate.

### 5.2.2 Ideal perfectly stirred reactor study

The perfectly stirred reactor study is the second part of the ideal reactors study where global mechanisms from Table 5.2 are compared with detailed mechanisms in terms of the accuracy in temperature distribution or molar fraction distribution of the main syngas components. The basic assumption of the perfectly stirred reactor model is that the perfect mixing (homogeneity) is achieved inside the control volume – Figure 5.2. Thus the properties are spatially uniform inside a control volume.

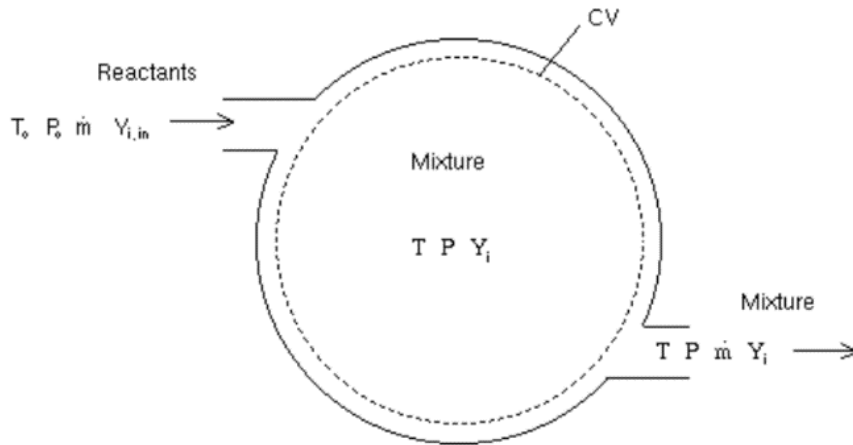


Figure 5.2. Sketch map of perfectly stirred reactor [241].

The species continuity equation for the steady-state case is as follows:

$$R_i = \frac{\rho}{\tau} (Y_{i,out} - Y_{i,in}) \quad (5.2)$$

where  $\tau$  is the residence time,  $Y_{i,out}$  and  $Y_{i,in}$  are the mass fractions of species at the outlet and inlet, respectively.

Table 5.4 presents the input parameters for PSR.

Table 5.4. Input parameters for PSR [241].

Fuel mixture, mole fraction	Oxidizer mixture, mole fraction	Equivalence ratio	Gas temperatures	Pressure
C(s) – 0.284 CH <sub>4</sub> – 0.677 CO – 0.039	H <sub>2</sub> O – 0.22 N <sub>2</sub> – 0.10 O <sub>2</sub> – 0.68	2.2	1500 K, 1750 K, 2000 K, 2250 K, 2500 K, 2800 K	20 atm

The examined conditions concern the gasification process conditions (equivalence ratio is equal to 2.2). The operating pressure was assumed to be equal to 20 atm. The analysis is conducted for six temperatures - 1500 K, 1750 K, 2000 K, 2250 K, 2500 K, 2800 K. The results are presented in sub-chapter 5.3.2.

### 5.2.3 CFD study

#### a) BYU reactor

The BYU reactor is a one-stage, atmospheric, oxygen-blown entrained flow reactor with a non-swirling flow (Figure 4.11). It is 1.8 m long and has a diameter of 20 cm. Bituminous pulverized coal from Utah was used in the investigations. The ultimate and proximate analyses are presented in Table 5.5.

Coal was injected in the primary stream with a gas consisting of O<sub>2</sub>, Ar, and H<sub>2</sub>O. The secondary stream contained only H<sub>2</sub>O. The mass flow rates with molar fractions are presented in Table 5.6. The particle size followed the Rosin-Rammler distribution.

The parameters used in this study were as follows. The minimum, mean and maximum diameters were 1, 36, and 80 μm, respectively. The spread parameter was equal to 1.033. The kinetic parameters of the heterogeneous and homogeneous reactions were taken from the literature and are presented in Table 5.9. The geometry of the reactor was discretized using a 2D axisymmetric grid consisting of approximately 100 000 rectangular cells. A grid independence study was carried out. The numerical model was validated against the experimental data of Smith et al. [210].

#### b) MHI reactor

The MHI reactor is a 200 tons/day, two-stage, air-blown and pressurized Mitsubishi entrained flow gasifier with a swirling flow (Figure 5.3). The reactor is 13 m long. It has three stages of dry-feed injectors. Two of them are located in the combustion region and the third one is in the reductor. Bituminous pulverized coal from Taiheiyo (TH) was used in the investigations. Its proximate and ultimate analyses are shown in Table 5.5.

Coal was injected with air in the 1<sup>st</sup> stage. Recycled char was injected through the second-stage injectors in the combustion region. The third-stage injectors were supplied with coal and air. The mass flow rates are presented in Table 5.7. The particle size followed the Rosin-Rammler distribution. The minimum, mean and maximum diameters were 4, 25, and 150 μm, respectively. The spread parameter was equal to 0.74. The kinetic parameters for the coal gasification reactions were taken from the literature – Table 5.9. The geometry of the reactor was discretized using a 3D planar grid consisting of approximately 530 000 elements. A grid independence study was carried out. The numerical model was validated against the experimental data of Chen et al. [104] and Watanabe et al. [80].

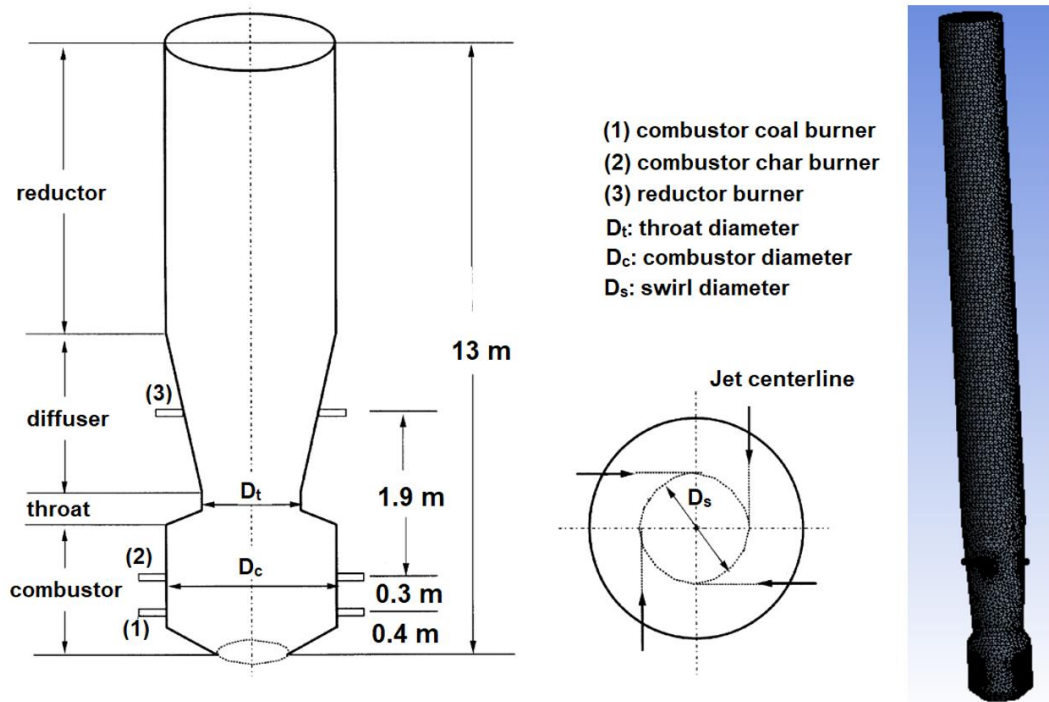


Figure 5.3. MHI reactor geometry with mesh [87].

### c) Conoco-Philips E-gas reactor

The Conoco-Philips E-gas reactor is a 2400 tons/day, two-stage, oxygen-blown, and pressurized entrained flow gasifier (Figure 5.4). It is 12 meters long. It has two stages of feed injectors. One of them is located in the combustor region and the second one in the throat. The combustor consists of an 8 m long horizontal cylinder with a diameter of 2 m. The first-stage injectors are located at each end of the combustor tube. Pulverized coal from Illinois was used in the investigations. Its proximate and ultimate analyses are shown in Table 5.5.

Coal-water slurry, oxygen, and a small amount of nitrogen were injected in the 1<sup>st</sup> stage. In the 2<sup>nd</sup> stage, only coal-water slurry was injected. The mass flow rates are presented in Table 5.8. The particle size was uniform and equal to 100  $\mu\text{m}$ . The kinetic parameters are presented in Table 5.9. The geometry of the reactor was discretized using a 3D planar grid consisting of approximately 360 000 elements. A grid independence study was carried out. The numerical model was validated against the data of Shi et al. [81] and Labbafan et al. [96].

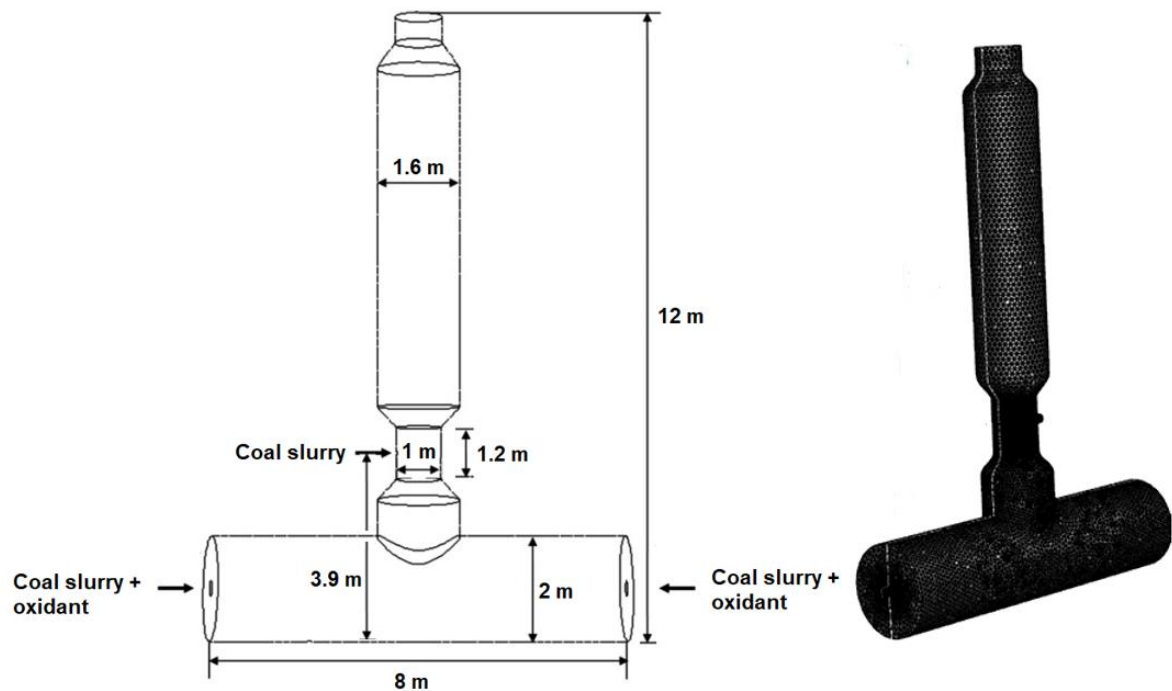


Figure 5.4. Conoco-Philips E-gas reactor geometry with mesh [81,96].

Table 5.5. Proximate and ultimate analyses of coals for three reactors.

Proximate analysis, as received			
	Utah bit. coal, % BYU reactor	TH coal, % MHI reactor	Illinois coal, % E-gas reactor
Volatile matter	45.6	46.8	35.0
Fixed carbon	43.7	35.8	44.2
Ash	8.3	12.1	9.7
Moisture	2.4	5.3	11.1
Ultimate analysis, % dry-ash-free			
C	77.6	77.6	80.5
H	6.56	6.5	5.7
N	1.42	1.78	1.6
S	0.55	0.22	3.5

Table 5.6. Mass flow rates of coal and gas with molar composition for BYU reactor.

<b>1<sup>st</sup> stage, kg/h</b>	26.24
O <sub>2</sub>	0.85
Ar	0.126
H <sub>2</sub> O	0.024
<b>2<sup>nd</sup> stage, kg/h</b>	6.62
H <sub>2</sub> O	1
Utah bituminous coal, kg/h	23.88



Table 5.7. Mass flow rates of coal and gas for MHI reactor.

Mass flow rates of coal in three-stage injectors, kg/s	
1 <sup>st</sup> stage – coal	0.472
2 <sup>nd</sup> stage – char	1.112
3 <sup>rd</sup> stage – coal	1.832
Mass flow rates of air, kg/s	
1 <sup>st</sup> stage	4.708
2 <sup>nd</sup> stage	4.708
3 <sup>rd</sup> stage	1.832

Table 5.8. Mass flow rates of coal and oxidant for E-gas reactor.

Mass flow rates of coal in three-stage injectors, kg/s	
1 <sup>st</sup> stage – coal	21.7
1 <sup>st</sup> stage – water	9.3
2 <sup>nd</sup> stage – coal	6.1
2 <sup>nd</sup> stage – water	2.6
Mass flow rates of oxidant, kg/s	
1 <sup>st</sup> stage (0.95 O <sub>2</sub> , 0.05 N <sub>2</sub> )	22.9
2 <sup>nd</sup> stage	0

Table 5.9. Kinetic parameters for surface reactions and gas-phase reactions (global reaction approach).

Reactions:	Kinetic parameters: A – kg/s Pa, E- J/kmol		
	BYU reactor	MHI reactor	E-gas reactor
<b>Surface reactions:</b>			
$C(s) + 0.5O_2 \rightarrow CO$	$A = 0.005$ $E = 7.4 \cdot 10^7$ [77]	$A = 0.052$ $E = 6.1 \cdot 10^7$ [104]	$A = 0.052$ $E = 6.1 \cdot 10^7$ [104]
$C(s) + CO_2 \rightarrow 2CO$	$A = 0.0635$ $E = 1.62 \cdot 10^8$ [77]	$A = 0.0732$ $E = 1.125 \cdot 10^8$ [104]	$A = 0.0732$ $E = 1.125 \cdot 10^8$ [104]
$C(s) + H_2O \rightarrow CO + H_2$	$A = 0.0019$ $E = 1.47 \cdot 10^8$ [77]	$A = 0.0782$ $E = 1.15 \cdot 10^8$ [104]	$A = 0.0782$ $E = 1.15 \cdot 10^8$ [104]
<b>Gas-phase reactions:</b>			
$C_xH_yO_z + \frac{x-z}{2}O_2 \rightarrow xCO + \frac{y}{2}H_2$	$A = 4.4 \cdot 10^{11}$ $E = 1.25 \cdot 10^8$ [87]	$A = 4.4 \cdot 10^{11}$ $E = 1.25 \cdot 10^8$ [87]	$A = 4.4 \cdot 10^{11}$ $E = 1.25 \cdot 10^8$ [87]
$C_xH_yO_z + (x-z)H_2O \rightarrow xCO + \left(\frac{y}{2} + x-z\right)H_2$	$A = 3 \cdot 10^8$ $E = 1.25 \cdot 10^8$ [87]	$A = 3 \cdot 10^8$ $E = 1.25 \cdot 10^8$ [87]	$A = 3 \cdot 10^8$ $E = 1.25 \cdot 10^8$ [87]
$C_mH_n + \frac{m}{2}O_2 \rightarrow mCO + \frac{n}{2}H_2$	$A = 4.4 \cdot 10^{11}$ $E = 1.25 \cdot 10^8$ [87]	$A = 4.4 \cdot 10^{11}$ $E = 1.25 \cdot 10^8$ [87]	$A = 4.4 \cdot 10^{11}$ $E = 1.25 \cdot 10^8$ [87]
$C_mH_n + H_2O \rightarrow mCO + \left(\frac{n}{2} + 1\right)H_2$	$A = 3 \cdot 10^8$ $E = 1.25 \cdot 10^8$ [87]	$A = 3 \cdot 10^8$ $E = 1.25 \cdot 10^8$ [87]	$A = 3 \cdot 10^8$ $E = 1.25 \cdot 10^8$ [87]

$CO + H_2O \rightarrow CO_2 + H_2$	$A = 2.75$ [91] $E = 8.38 \cdot 10^7$ [105]	$A = 2.75 \cdot 10^9$ $E = 8.38 \cdot 10^7$ [105]	$A = 2.75$ [91] $E = 8.38 \cdot 10^7$ [105]
$CO + 0.5O_2 \rightarrow CO_2$	$A = 2.24 \cdot 10^{12}$ $E = 1.67 \cdot 10^8$ [106]	$A = 2.24 \cdot 10^{12}$ $E = 1.67 \cdot 10^8$ [106]	$A = 2.24 \cdot 10^{12}$ $E = 1.67 \cdot 10^8$ [106]
$H_2 + 0.5O_2 \rightarrow H_2O$	$A = 6.8 \cdot 10^{15}$ $E = 1.67 \cdot 10^8$ [87]	$A = 6.8 \cdot 10^{15}$ $E = 1.67 \cdot 10^8$ [87]	$A = 6.8 \cdot 10^{15}$ $E = 1.67 \cdot 10^8$ [87]

It was assumed that the reaction kinetics of  $C_xH_yO_z$  and  $C_mH_n$  with  $O_2$  and  $H_2O$  were similar to those of light hydrocarbon molecules, such as  $CH_4$  [87]. The choice is justified because these reaction rates do not vary greatly [105,106]. It is also apparent that the reaction kinetics of the gas phase is almost identical for the three examined reactors.

## 5.3 Results and discussion

### 5.3.1 Plug flow results

Figure 5.5a shows the temperature distribution in the PFR. One can notice that only Mechanisms 1 and 4 show close agreement with the GRI-Mech approach. Figure 5.5b, Figure 5.5c, Figure 5.5d show the  $O_2$ ,  $CO$ , and  $H_2$  mole fraction distributions. In this case, Mechanism 1 also reproduces the results with the highest accuracy with regard to GRI-Mech. Mechanism 2 exhibits the worst accuracy. As regards Figure 5.6, which depicts the  $CO_2$ ,  $H_2O$ , and  $C(s)$  mole fraction distributions, Mechanism 1 also shows the best agreement with GRI-Mech, whereas Mechanism 2 reproduces the results with the worst accuracy. On the basis of these figures, one can draw the conclusion that Mechanism 2 is the only examined mechanism that does not consider the oxidation reaction of  $CO$  ( $CO + 0.5O_2 \rightarrow CO_2$ ). The lack of this reaction substantially impacts the results. Moreover, for each distribution (Figure 5.5, Figure 5.6) the results from Mechanisms 1 and 2 begin to converge after the distance of 500 mm. One can conclude that the impact of the  $CO$  oxidation reaction is most significant within the distance of 0-500 mm. With respect to GRI-Mech, Mechanisms 3 and 4 show poor agreement as well. It is evident that these approaches do not consider the water-gas shift reaction. The results from the CFD analysis confirm the great importance of this reaction in the accurate prediction of the gasification process. Therefore, one can ultimately conclude that, as regards the global reaction mechanisms, the  $CO + 0.5O_2 \rightarrow CO_2$  reaction and the  $CO + H_2O \rightarrow CO_2 + H_2$  reaction has a substantial impact on the gas phase in gasification.

Figure 5.6c shows the consumption of  $C(s)$  in the reactor. The strong impact of the gas-phase reactions on the char consumption rate is apparent.

Judging by the overall accuracy, based on the error analysis, it is evident that Mechanism 1 shows the closest agreement with GRI-Mech and CRECK.

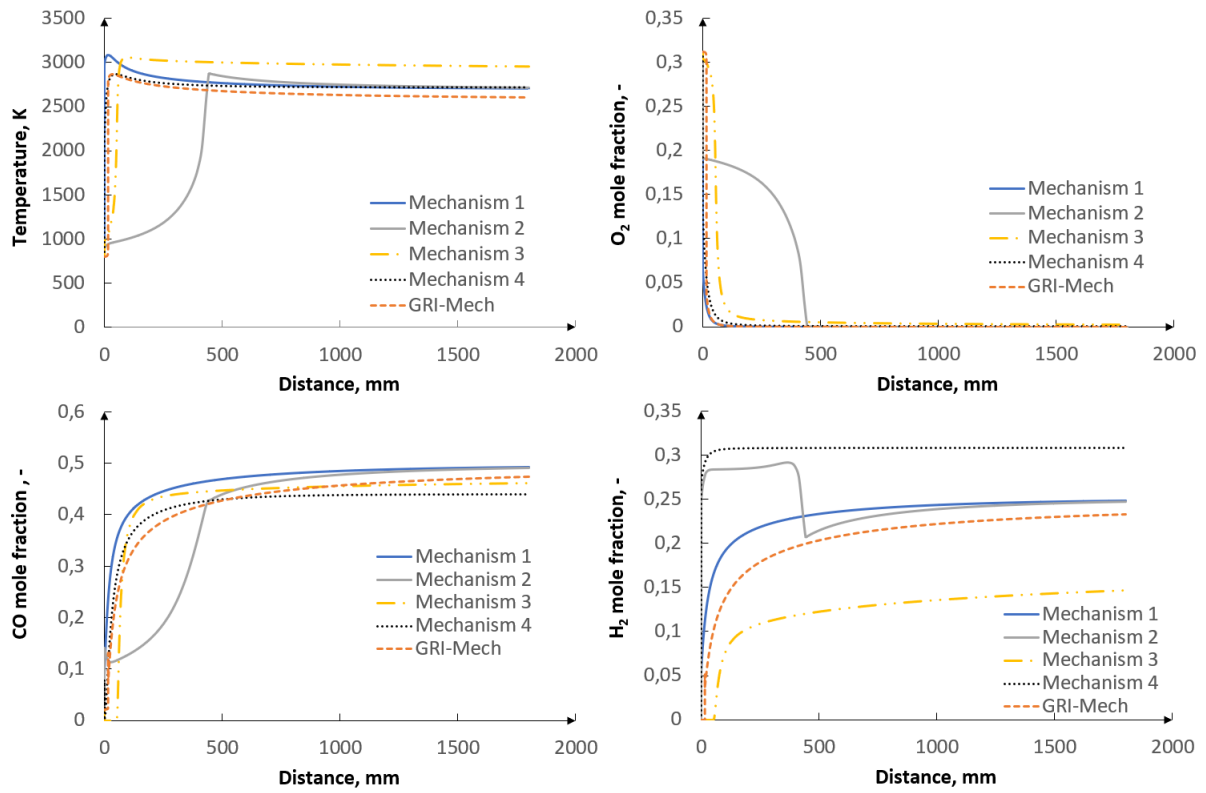


Figure 5.5. Temperature distribution and O<sub>2</sub>, CO and H<sub>2</sub> mole fraction distributions in PFR for each mechanism (Table 5.2) [241].

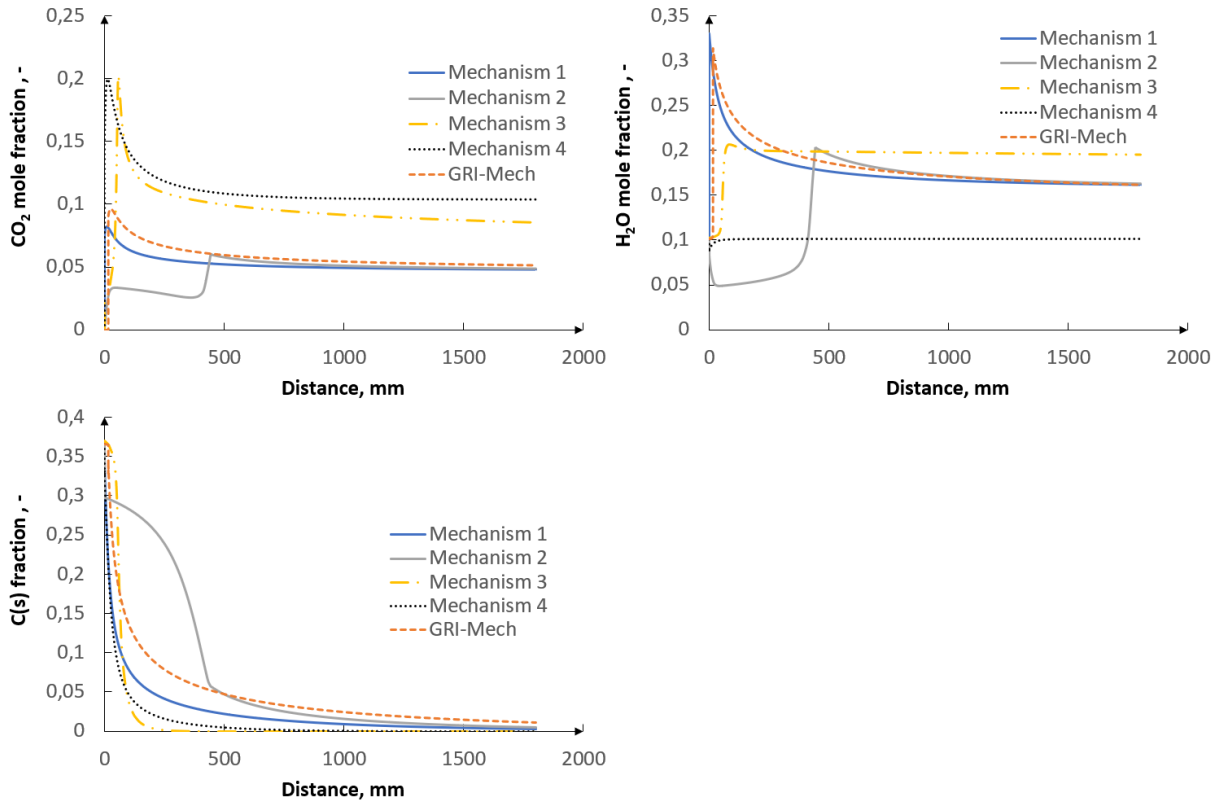


Figure 5.6. CO<sub>2</sub>, H<sub>2</sub>O and C(s) mole fraction distributions in PFR for each mechanism (Table 5.2) [241].

Figure 5.7 presents the exemplary results of GRI-Mech and CRECK for two pressures that are outside of the optimization range of GRI-Mech for CO, H<sub>2</sub>, CO<sub>2</sub> mole fractions, and temperature distributions in PFR. An excellent agreement can be noticed proving that GRI-Mech can be surely utilized in high-pressure conditions.

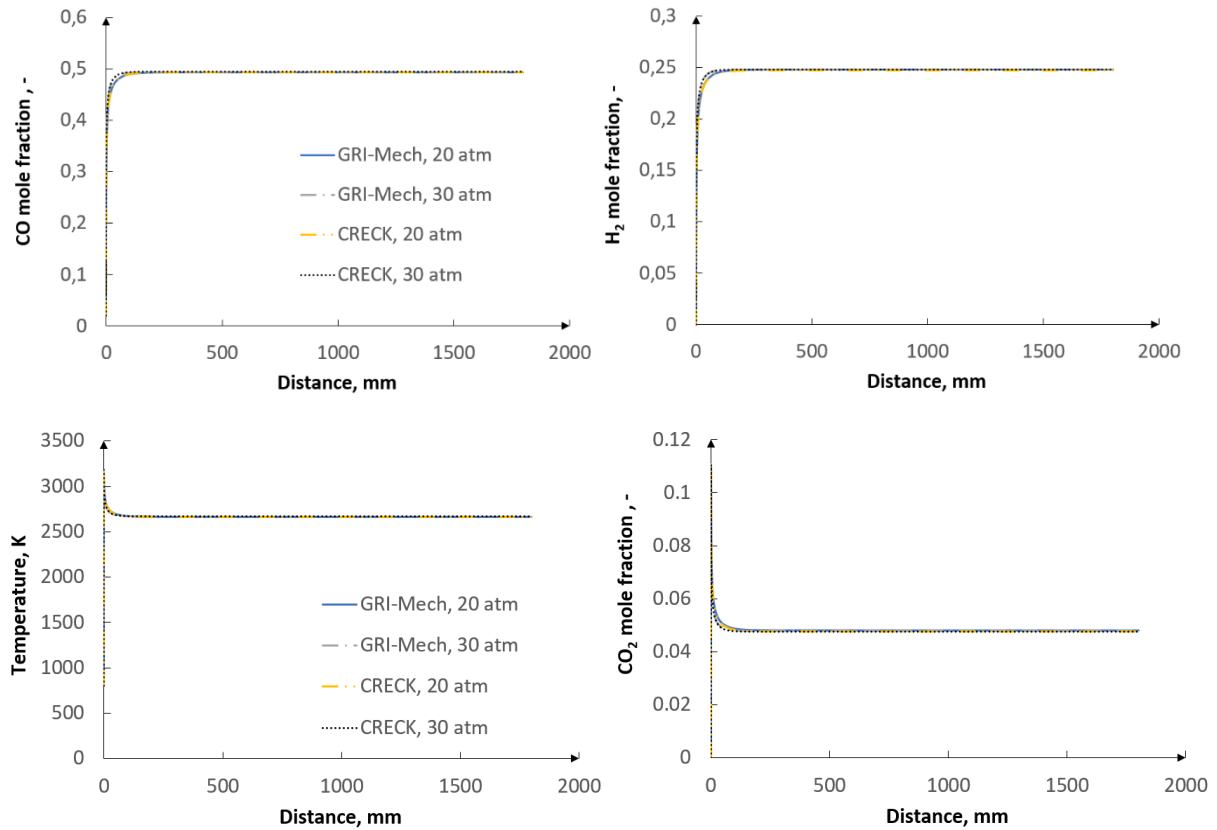


Figure 5.7. CO, H<sub>2</sub>, Temperature and CO<sub>2</sub> mole fraction distributions in PFR for GRI-Mech and CRECK [241].

### 5.3.2 Perfectly stirred reactor results

Judging by Figure 5.8, one can notice an extremely close agreement of GRI-Mech, CRECK, and global Mechanism 1 for five out of six temperatures. For 1500 K there is a slight disagreement between these mechanisms. Mechanisms 3 and 4 depict the worst accuracy with respect to the detailed mechanisms. Mechanism 2 provides a relatively close agreement for temperatures higher than 2000 K. As regards the decreasing char fraction due to heterogeneous reactions, one can also observe a very close agreement between GRI-Mech, CRECK, and Mechanism 1. Considering the plug flow reactor study and the perfectly stirred reactor study, in both examined cases Mechanism 1 exhibited the highest agreement with the detailed mechanisms. On this basis, Mechanism 1 will be further investigated as the main global approach in the CFD study. Based on the flow regime, the plug flow reactor relates to the BYU gasifier, whereas the perfectly stirred reactor relates to the MHI and E-gas gasifiers.

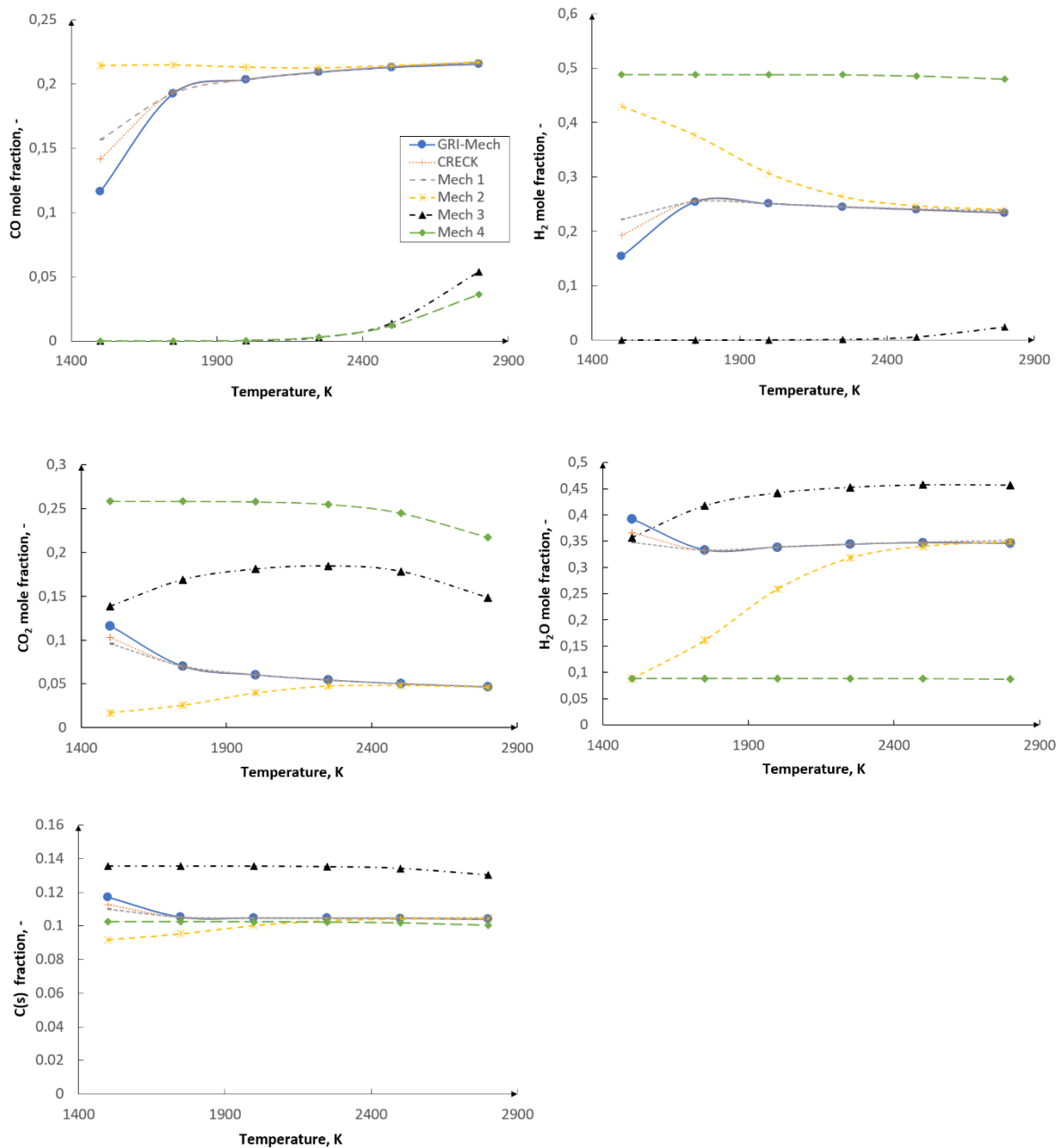


Figure 5.8. CO, H<sub>2</sub>, CO<sub>2</sub>, H<sub>2</sub>O and C(s) mole fraction distributions in PSR for global and detailed mechanisms [241].

### 5.3.3 CFD results

The results for each of the reactors are presented for the three cases:

- the global reaction approach with the finite-rate/eddy dissipation model (Global, F-R/EDM),
- the global reaction approach with the eddy dissipation concept (Global, EDC),
- the detailed GRI-Mech mechanism with the eddy dissipation concept (GRI-Mech, EDC).

The global reaction approach is the extended Mechanism 1.

The fourth case: the GRI-Mech mechanism with the finite-rate/eddy dissipation model (GRI-Mech, F-R/EDM) is not considered. GRI-Mech is a radical-reaction approach with reversible reactions which the finite-rate/eddy dissipation model cannot handle.

### BYU gasifier

Figure 5.9 presents the molar fraction distribution of the main gas components (CO, H<sub>2</sub>, CO<sub>2</sub>, and H<sub>2</sub>O) along the centerline inside the reactor. A strong impact of the examined gas-phase modeling approaches on the gas composition inside the reactor, especially in the flame region, is visible. (Global, EDC) and (GRI-Mech, EDC) show closer agreement with each other than (Global, F-R/EDM) with (Global, EDC). This indicates that the turbulence-chemistry interaction has a greater impact on the gas composition than the reaction mechanisms. Considering the accuracy of the analyzed approaches, the GRI-Mech mechanism with the eddy dissipation concept yields the most accurate results with regard to the experimental data. (Global, F-R/EDM) predicts a strong peak in the CO yield in the flame region. On the other hand, the CO<sub>2</sub> and H<sub>2</sub>O yields in the flame region estimated by (Global, F-R/EDM) are strongly underpredicted.

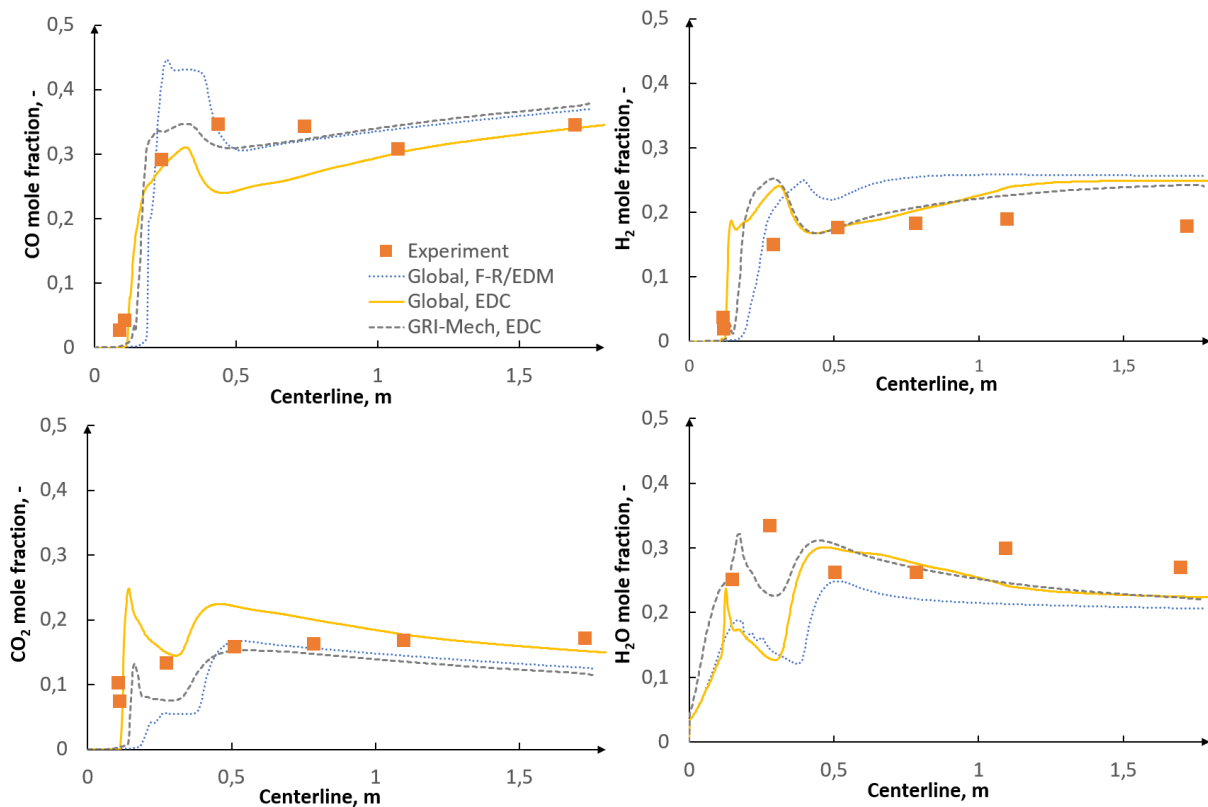


Figure 5.9. CO, H<sub>2</sub>, CO<sub>2</sub> and H<sub>2</sub>O mole fraction distributions along centerline for three gas-phase modeling approaches – BYU reactor [241].

Figure 5.11 - Figure 5.18 show the gas concentration along the radial traverses  $x = 0.13$  m,  $x = 0.20$  m,  $x = 0.28$  m,  $x = 0.34$  m,  $x = 0.51$  m,  $x = 0.81$  m,  $x = 1.12$  m and  $x = 1.73$  m. The traverses are visualized in Figure 5.10. The value of 0 in the horizontal ordinate indicates that the concentration is measured along the centerline. The value of 0.1 means that the concentration is measured close to the reactor wall.

The models show great variations, especially for  $x = 0.13$  m and  $x = 0.28$  m in the flame region. (GRI-Mech, EDC) yielded most accurate results with regard to the experimental data. The recirculation zone was relatively well predicted, especially for CO and CO<sub>2</sub>. While for the centerline (Global, EDC) provided reasonable results, for the radial traverses it yielded poor results with respect to other numerical results and the experimental data.

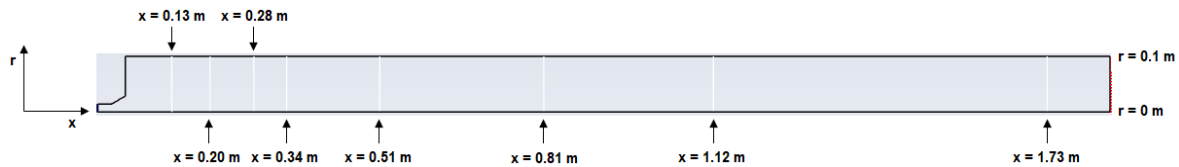


Figure 5.10. Map of radial traverses in BYU reactor.

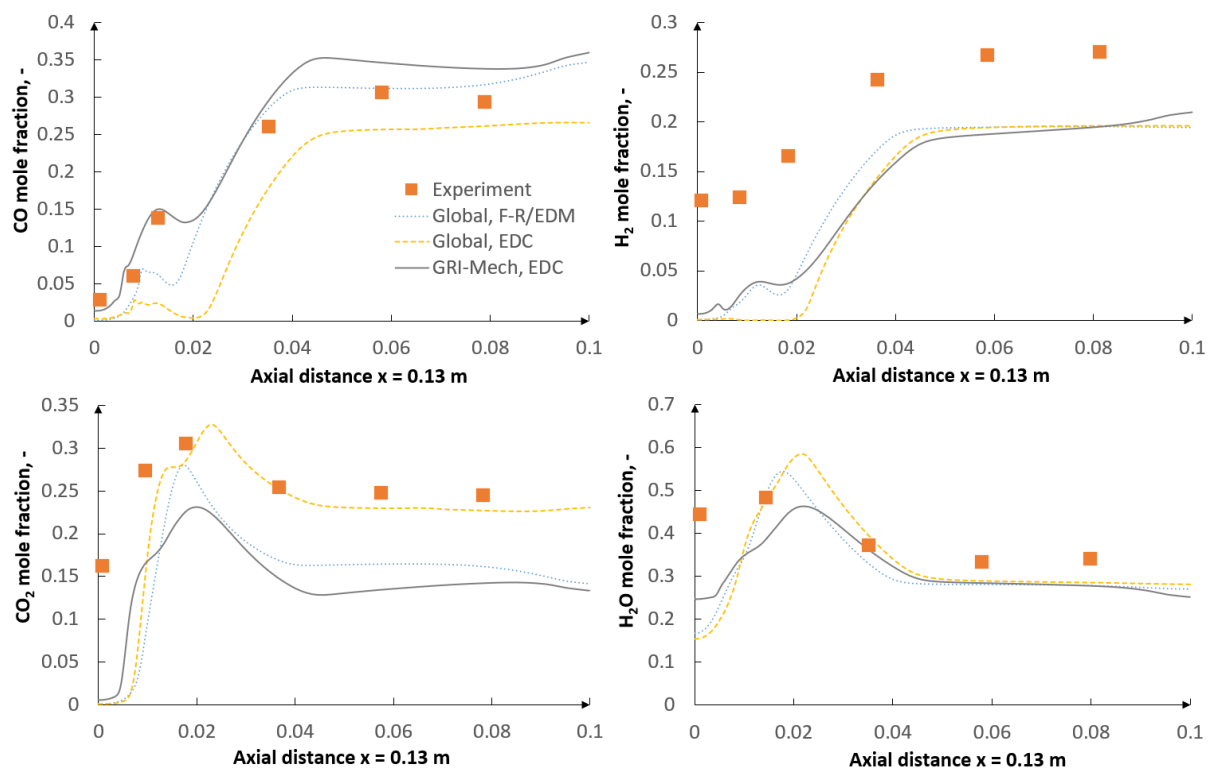


Figure 5.11. CO, H<sub>2</sub>, CO<sub>2</sub> and H<sub>2</sub>O mole fraction distributions along axial distance  $x = 0.13$  m for three gas-phase modeling approaches – BYU reactor [241].

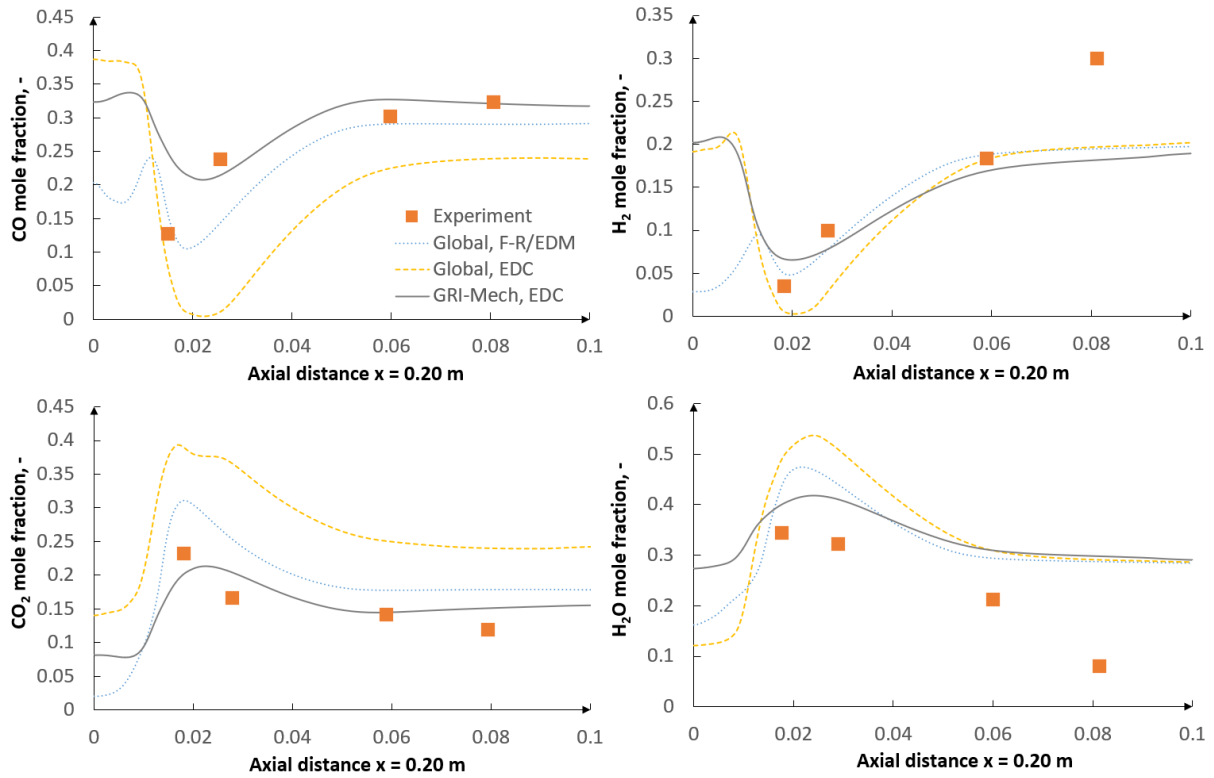


Figure 5.12. CO, H<sub>2</sub>, CO<sub>2</sub> and H<sub>2</sub>O mole fraction distributions along axial distance  $x = 0.20$  m for three gas-phase modeling approaches – BYU reactor.

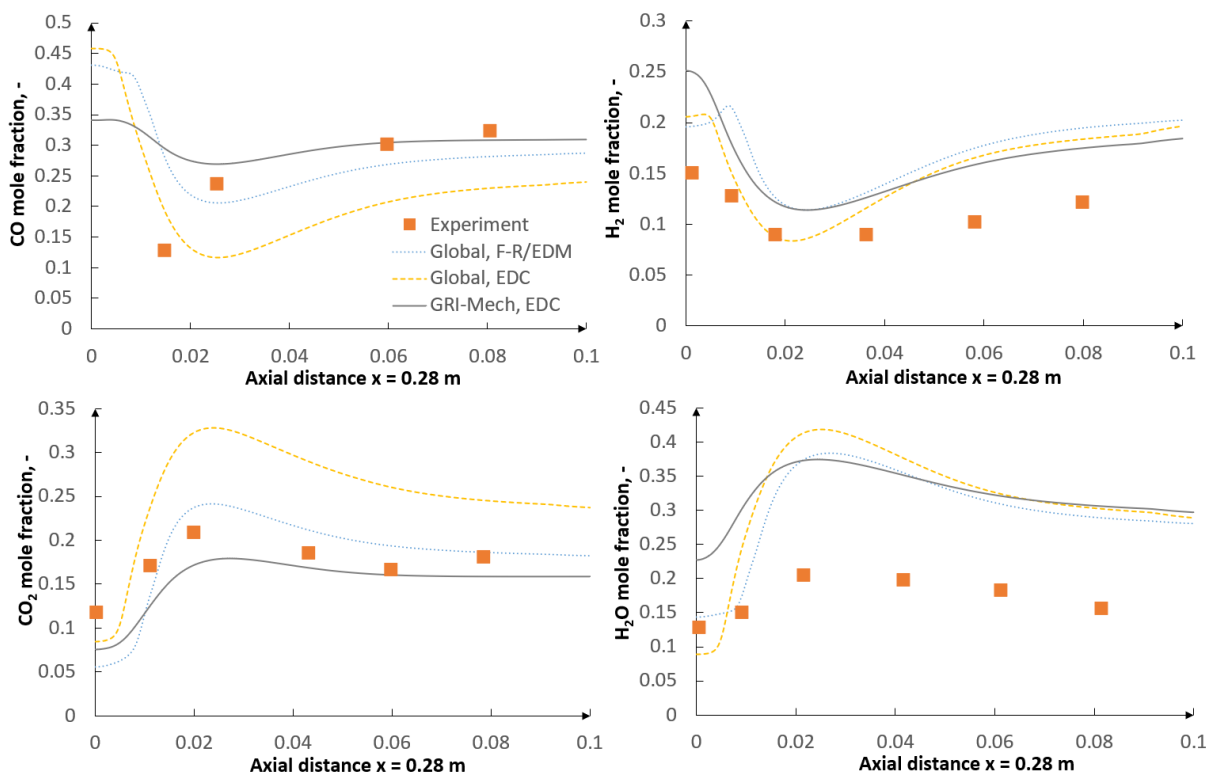


Figure 5.13. CO, H<sub>2</sub>, CO<sub>2</sub> and H<sub>2</sub>O mole fraction distributions along axial distance  $x = 0.28$  m for three gas-phase modeling approaches – BYU reactor [241].



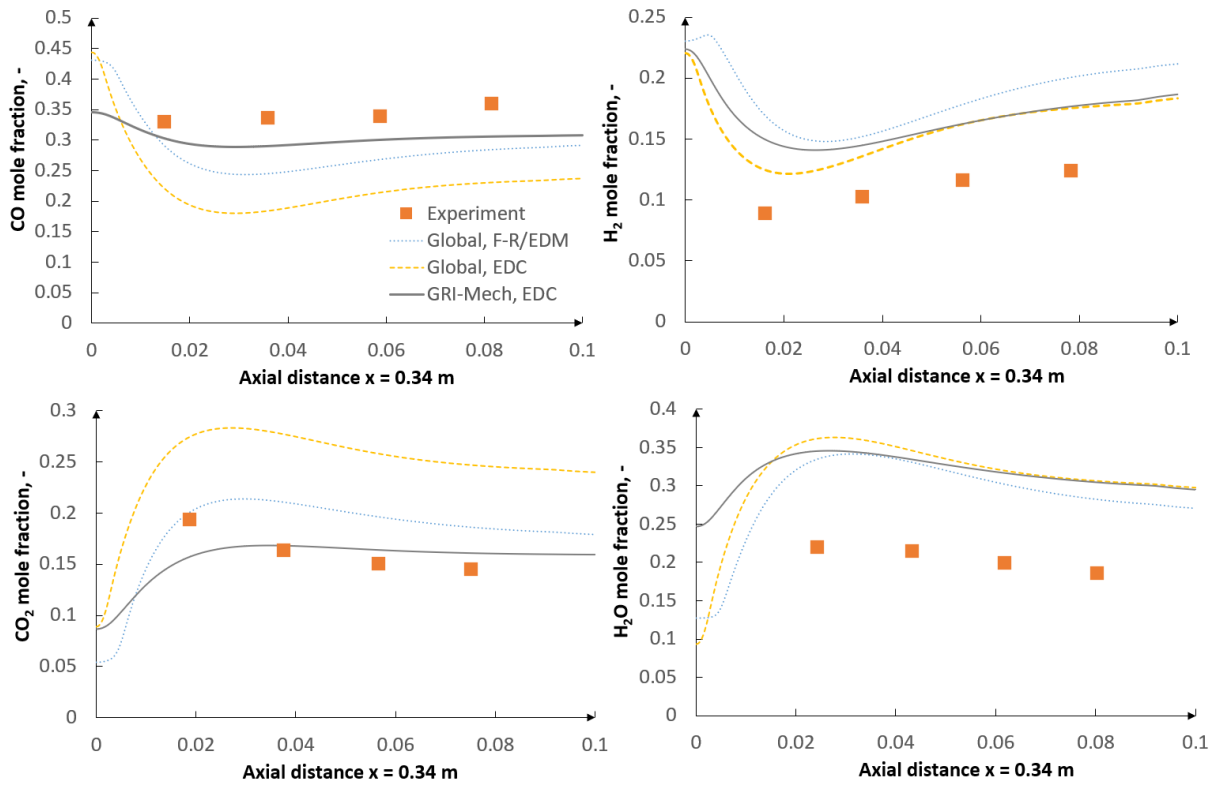


Figure 5.14. CO, H<sub>2</sub>, CO<sub>2</sub> and H<sub>2</sub>O mole fraction distributions along axial distance  $x = 0.34$  m for three gas-phase modeling approaches – BYU reactor.

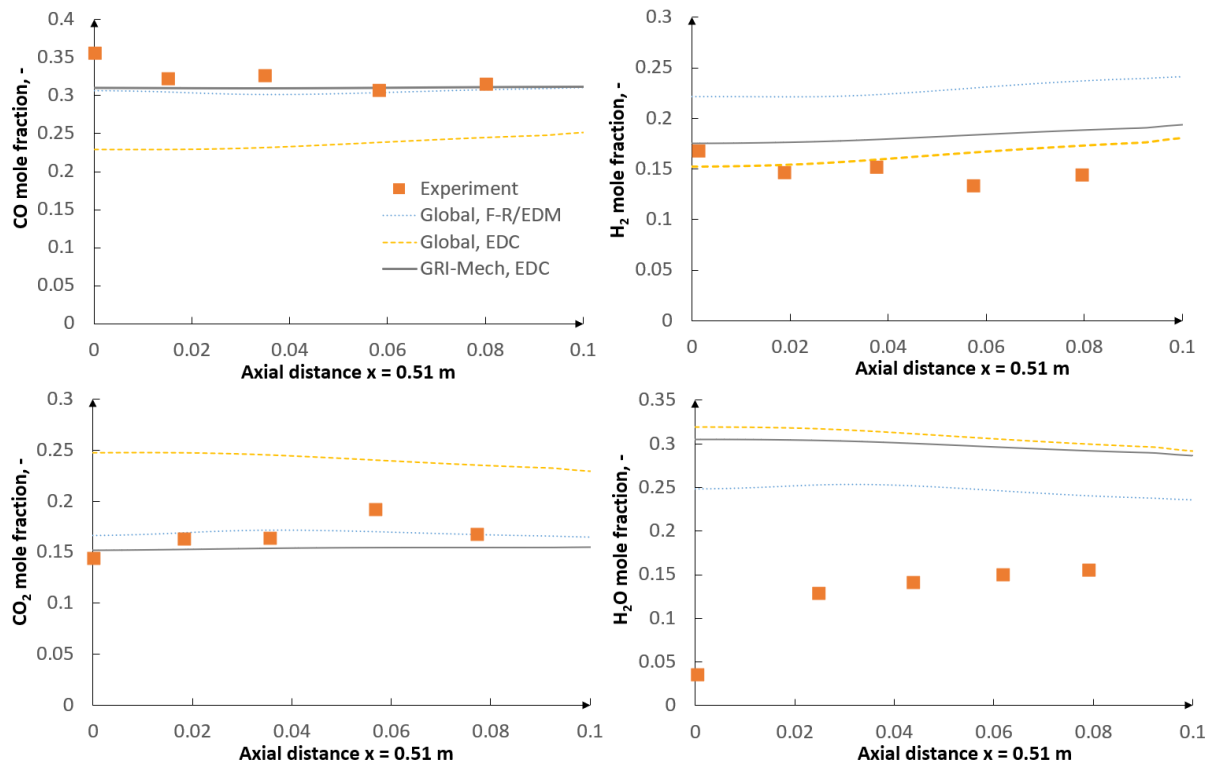


Figure 5.15. CO, H<sub>2</sub>, CO<sub>2</sub> and H<sub>2</sub>O mole fraction distributions along axial distance  $x = 0.51$  m for three gas-phase modeling approaches – BYU reactor.

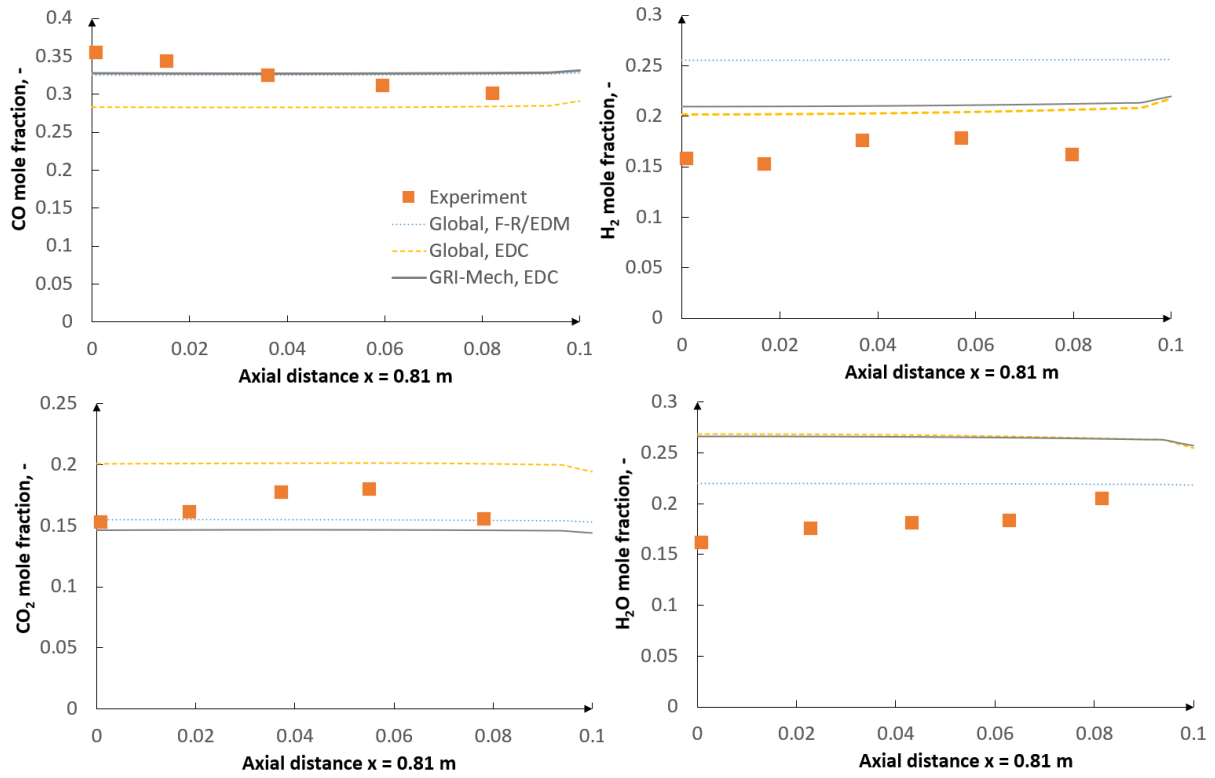


Figure 5.16. CO, H<sub>2</sub>, CO<sub>2</sub> and H<sub>2</sub>O mole fraction distributions along axial distance  $x = 0.81$  m for three gas-phase modeling approaches – BYU reactor.

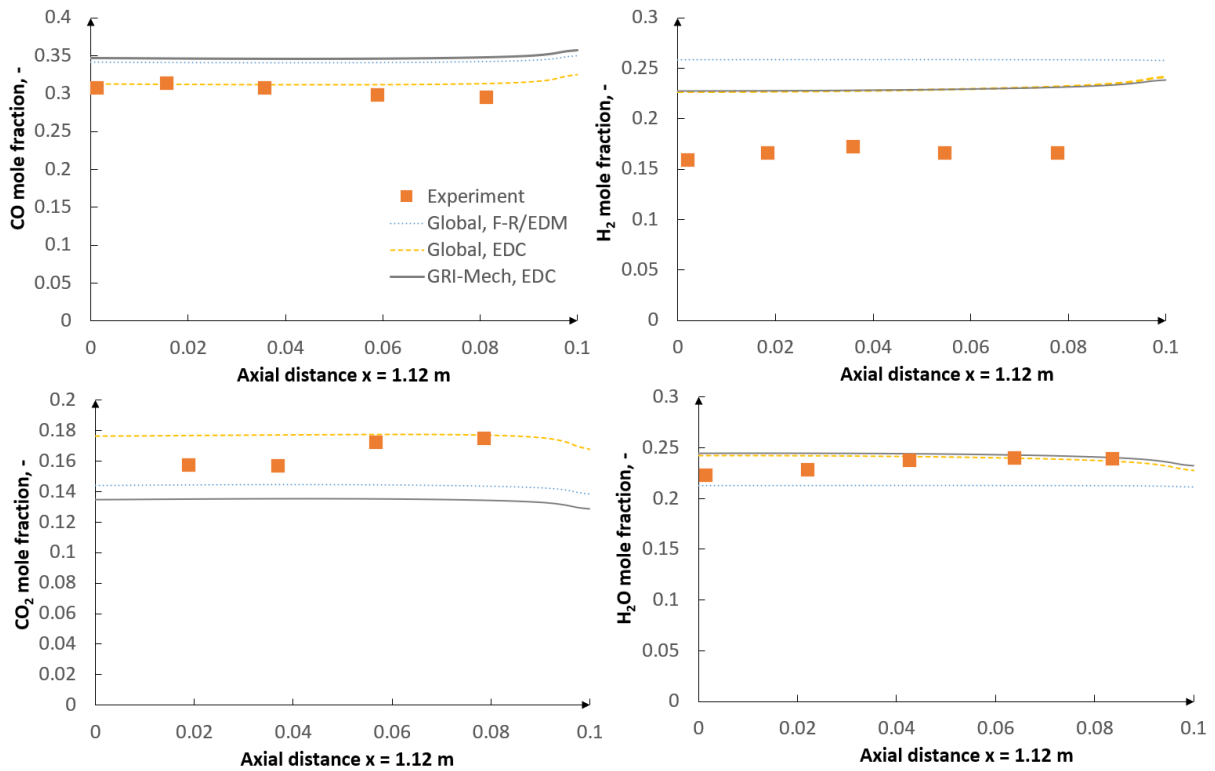


Figure 5.17. CO, H<sub>2</sub>, CO<sub>2</sub> and H<sub>2</sub>O mole fraction distributions along axial distance  $x = 1.12$  m for three gas-phase modeling approaches – BYU reactor [241].

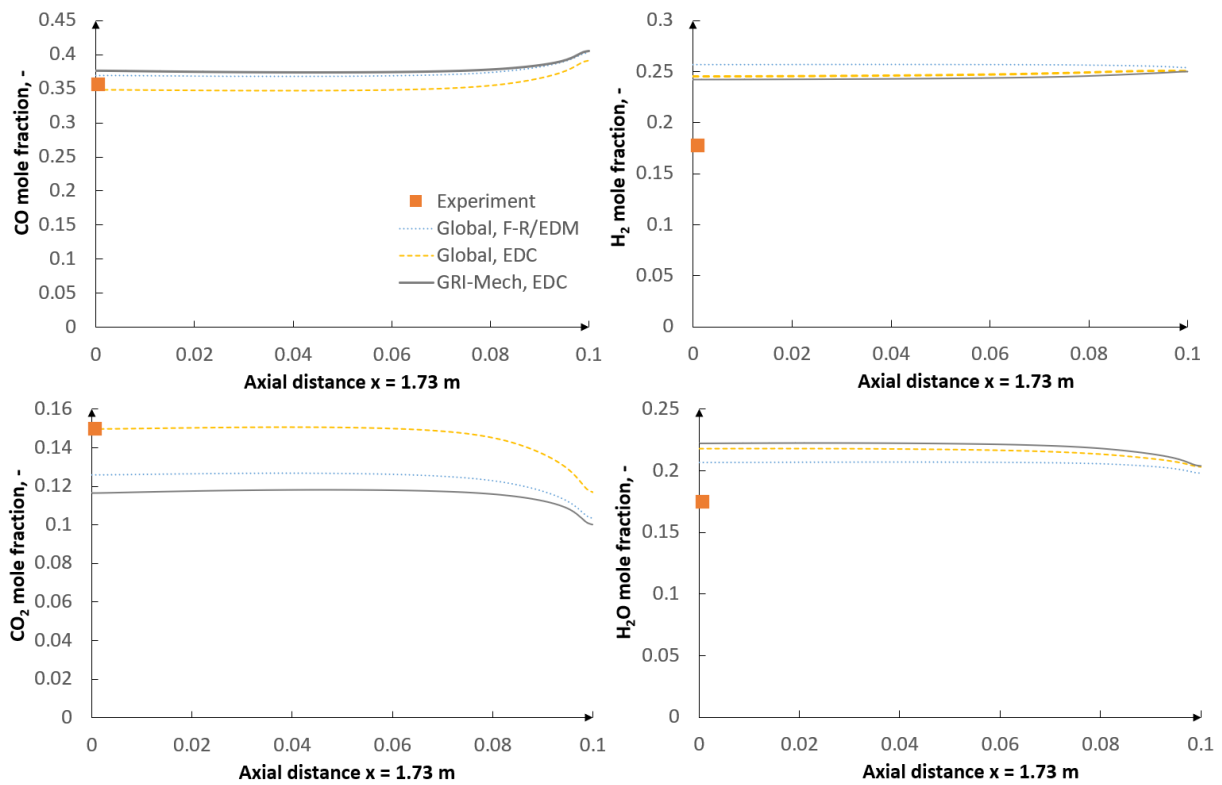


Figure 5.18. CO, H<sub>2</sub>, CO<sub>2</sub> and H<sub>2</sub>O mole fraction distributions along axial distance  $x = 1.73$  m for three gas-phase modeling approaches – BYU reactor.

### MHI gasifier

Figure 5.19 shows the mole fraction distribution of the main gas components in the MHI reactor. One can see a considerable increase in CO and H<sub>2</sub> concentration in the second stage of the reactor where endothermic gasification reactions prevail. On the other hand, the CO<sub>2</sub> and H<sub>2</sub>O content gradually decrease as CO<sub>2</sub> and H<sub>2</sub>O react with char to form CO and H<sub>2</sub>. The GRI-Mech mechanism with the eddy dissipation concept turned out to be the most accurate approach when estimating CO and CO<sub>2</sub> concentration with respect to the outlet experimental data. However, the H<sub>2</sub> concentration was underpredicted by GRI-Mech. Its concentration was properly reproduced by the (Global, EDC) approach. It should be noted that GRI-Mech is not optimized for such high pressures. Therefore, one of the objectives of this study was to incorporate GRI-Mech in conditions outside the optimized range and to see the level of accuracy. GRI-Mech was found to yield reasonable results despite being outside the optimized range. However, in order to further increase the accuracy, future research on GRI-Mech optimization for higher pressures is needed.

As regards H<sub>2</sub>O concentration, no outlet experimental data points were available. (GRI-Mech, EDC) predicts H<sub>2</sub>O molar concentration at the reactor outlet to be at 4-5%. (Global, F-R/EDM) and (Global, EDC) do not predict any amount of H<sub>2</sub>O. This effect was attributed to the kinetics of the water-gas shift (WGS) reaction. In the case of the MHI gasifier, a very high reaction rate had to be assumed for the global reaction approach in order to match the experimental data. This results in the consumption of all the H<sub>2</sub>O. GRI-Mech, on the other hand, does not incorporate this reaction directly because the gas phase is modeled via radical

reactions.

Figure 5.19 also shows, as in the case of the BYU reactor, a relatively strong impact of the applied gas-phase modeling approaches on gas composition. Both the eddy dissipation concept and the finite-rate/eddy dissipation model yield similar results for CO and H<sub>2</sub>O concentrations along the centerline. In the case of CO<sub>2</sub> concentration, a substantial difference can be observed in the combustor region, where the eddy dissipation concept predicts a much higher concentration. Unfortunately, no experimental measurements in the combustor were available to confront the data. The most significant difference was noticed for H<sub>2</sub> concentration.

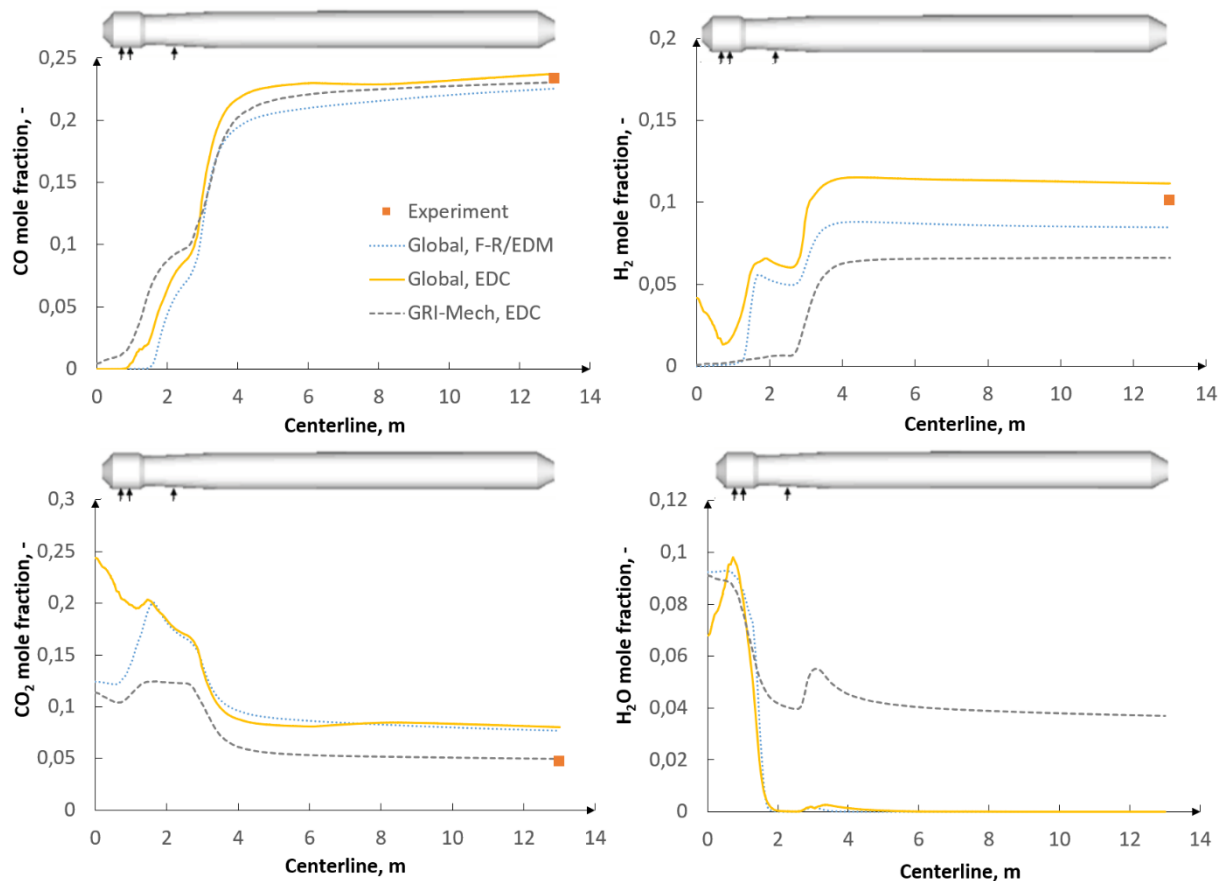


Figure 5.19. CO, H<sub>2</sub>, CO<sub>2</sub> and H<sub>2</sub>O mole fraction distributions along centerline for three gas-phase modeling approaches – MHI reactor [241].

Figure 5.20 illustrates the temperature distribution along the centerline of the reactor. One can notice a substantial difference between the examined approaches in the combustor region. GRI-Mech yielded the most accurate results, predicting also lower temperatures than the global reaction approaches. A lower temperature predicted by GRI-Mech, in comparison with the other numerical approaches, indicates a lower CO<sub>2</sub> concentration in the combustor (Figure 5.19).

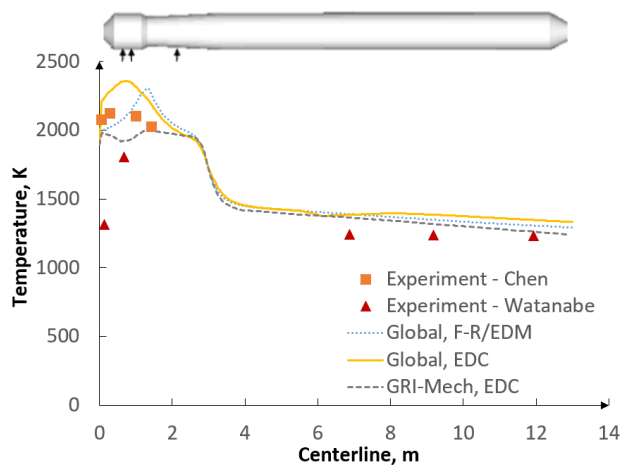


Figure 5.20. Temperature distribution along centerline for three gas-phase modeling approaches – MHI reactor [241].

### E-gas gasifier

Figure 5.21 shows the gas composition along the centerline for the E-gas reactor. As in the MHI reactor, an increase in CO and H<sub>2</sub> gas content can be noticed in the 2<sup>nd</sup> stage of the E-gas reactor due to gasification reactions with CO<sub>2</sub> and H<sub>2</sub>O. As a result, the CO<sub>2</sub> and H<sub>2</sub>O content in the 2<sup>nd</sup> stage gradually decreases. The CO<sub>2</sub> content is the highest in the combustor due to the relatively high O<sub>2</sub> concentration where the complete oxidation of C with O<sub>2</sub> occurs. GRI-Mech with EDC is found to yield the most accurate results with regard to the outlet data obtained in [81]. The global reaction approach with the finite-rate/eddy dissipation model reproduces the results with the worst accuracy.

Figure 5.22 shows the temperature distribution along the centerline of the reactor. One can notice that the GRI-Mech mechanism predicts lower temperatures in the combustor. The same is observed for the MHI reactor. The results confirm a substantial influence of the gas-phase modeling approaches on gas composition and temperature distribution.

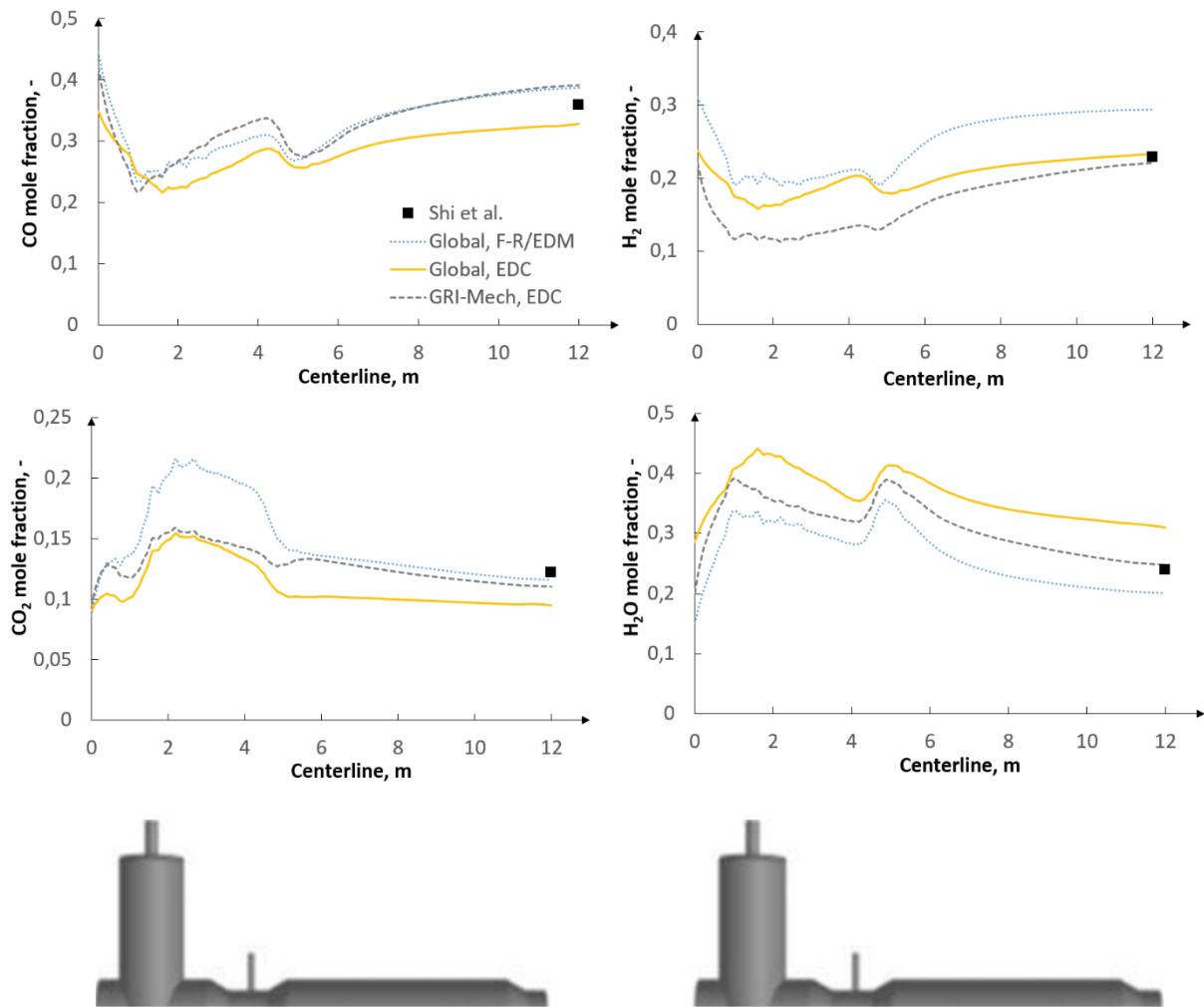


Figure 5.21. CO, H<sub>2</sub>, CO<sub>2</sub> and H<sub>2</sub>O mole fraction distributions along centerline for three gas-phase modeling approaches – E-gas reactor [241].

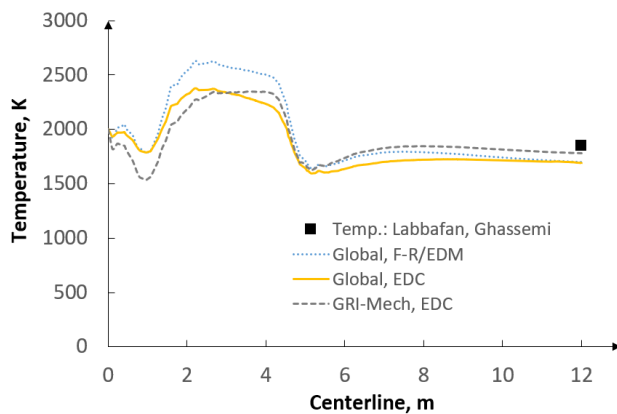


Figure 5.22. Temperature distribution along centerline for three gas-phase modeling approaches – E-gas reactor [241].

### Water-gas shift reaction

As regards the global reaction approach, the water-gas shift (WGS) reaction was observed to have a significant influence on the final gas composition. According to the literature review [80,88,101,108,114,120,125,130,158], the kinetic parameters for this reaction originate from

the Jones-Lindstedt approach [105]. However, some authors modified the pre-exponential factor from this reaction [75,86,87,91,108] in order to match the experimental data. The reason lies in the fact that the rate from the Jones-Lindstedt mechanism was obtained under catalytic conditions which, in many cases, turned out to be too fast for gasification. The present study analyzes the behavior of the WGS reaction in three different gasification conditions. For the BYU gasifier, where the maximum flame temperature reached 2800 K, the kinetic parameters had to be very low to match the experimental data. The pre-exponential factor was assumed to be equal to 2.75. This value was taken from the study of Lu and Wang [91]. As regards the MHI reactor, where the maximum flame temperature was below 2400 K, the pre-exponential factor was assumed to be equal to  $2.75 \cdot 10^9$  and was taken from [86]. In the case of the E-gas gasifier, the flame temperature was observed to be above 3000 K and the pre-exponential factor was also assumed to be equal to 2.75 (Table 5.10). This observation confirms a very important feature of the WGS reaction, i.e. decreasing conversion with increasing temperature. However, such a wide range of pre-exponential factors (from 2.75 to  $2.75 \cdot 10^9$ ) makes it necessary to properly optimize this reaction rate prior to any numerical simulation.

Figure 5.23 shows the final gas composition for the (Global, F-R/EDM) approach at the BYU and E-gas reactor outlets for two pre-exponential factors ( $A = 2.75$  and  $A = 2.75 \cdot 10^9$ ) of the WGS reaction. One can notice a substantial difference in the gas composition at the reactor outlet, which confirms a strong dependence of this reaction on the operating conditions inside the gasifier. The pre-exponential factor value used for the MHI reactor ( $A = 2.75 \cdot 10^9$ ) failed to correctly reproduce the outlet results for the BYU and E-gas gasifiers. The necessity of the proper optimization of the WGS rate can be overcome by directly implementing the GRI-Mech mechanism which was found to be the most accurate approach for each of the reactors. This is because GRI-Mech does not directly account for the WGS reaction as it is a radical-reaction approach. Further research concerning GRI-Mech applicability to higher temperatures and pressures would allow increasing its accuracy of predictions considering that the operating pressures in the MHI and E-gas reactors were outside of the optimized range for GRI-Mech.

Table 5.10. Kinetic parameters of WGS reaction [241].

Reactor	MHI	BYU	E-Gas
<b>Oxidant</b>	air	O <sub>2</sub>	O <sub>2</sub>
<b>Maximum flame temperature</b>	< 2400 K	< 2800 K	> 3000 K
<b>Kinetic parameters of WGS reaction</b>	$A = 2.75 \cdot 10^9$	$A = 2.75$	$A = 2.75$
<b>A – kg/s Pa, E – kJ/mol</b>	$E = 83.8$	$E = 83.8$	$E = 83.8$

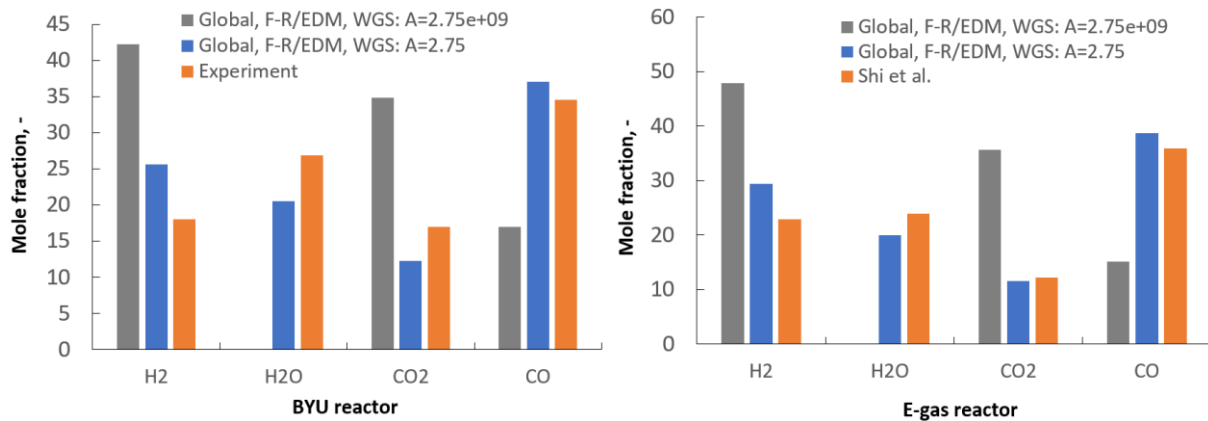


Figure 5.23. BYU reactor and E-gas reactor outlet syngas composition [241].

## 5.4 Conclusions

A plug flow reactor study, a perfectly stirred reactor study, and a CFD analysis were carried out to investigate the impact of chemical reaction mechanisms and turbulence-chemistry interaction approaches on coal gasification in entrained flow reactors with the aim of understanding which mechanisms are more accurate and suitable for gasification. The conclusions are as follows:

- (1) Among the studied global reaction mechanisms in ideal PFR and PSR reactors, Mechanism 1 exhibited the highest agreement with regard to the detailed GRI-Mech and CRECK mechanisms.
- (2) An excellent agreement between the detailed GRI-Mech and CRECK mechanisms could be noticed in the PFR and PSR reactors. Additionally, GRI-Mech was found to yield accurate results for pressure conditions outside of its validation range based on the comparison with CRECK.
- (3) As regards the CFD study, the examined reaction mechanisms and turbulence-chemistry interaction approaches were found to have a significant impact on gas composition and temperature distribution inside the studied gasifiers.
- (4) The detailed GRI-Mech mechanism with the eddy dissipation concept yielded the most accurate results with regard to the experimental data. The global reaction approach with the finite-rate/eddy dissipation model reproduced the results with the worst accuracy, even though it was found to be the approach most widely used in the literature.
- (5) GRI-Mech was found to predict lower temperatures and especially CO<sub>2</sub> and H<sub>2</sub> concentrations in the flame region than the global reaction mechanism.
- (6) Higher disagreement between the detailed and the global reaction mechanism approach was more remarkable in the CFD study than in the ideal reactor studies (PFR, PSR).
- (7) From among the gas-phase reactions, the water-gas shift (WGS) reaction and the CO oxidation reaction were found to significantly depend on the operating conditions inside the reactors.



## 6. Optimization procedure of char conversion

The results from this chapter have been published in [245].

[245] Mularski J., Modliński N. Entrained-flow Coal Gasification Process Simulation with the Emphasis on Empirical Char Conversion Models Optimization Procedure.

Energies 2021;14:1729. <https://doi.org/10.3390/en14061729>

*MNiSW (2019-2021): 140 pts, IF (2019): 2.702*

### 6.1 Introduction

On the basis of the literature review by Mularski et al. [31], one could have observed a variety of char conversion models starting with the most basic ones as the kinetic-diffusion models and ending with the most complex ones as the detailed CBK/E and CBK/G approaches. The kinetic-diffusion models, due to their simplicity, robustness, and numerical stability, were found to be the most widely applied models in the literature. They yielded reasonable although not highly accurate results in terms of the temperature distribution or syngas composition, but the char conversion was mostly inaccurately estimated. Moreover, it was found that the majority of authors incorporated the same set of kinetic parameters for different reactors with different operating conditions. Following the strategy presented in chapter 4 for devolatilization, the results of advanced models can be applied for optimizing the kinetic parameters of simplified models for a well-defined range of operating conditions. The process of optimizing kinetic parameters is performed through the minimization of the objective function, which was found to be the most accurate approximating method among the examined ones in chapter 4. The results are confronted with the experimental data of Smith et al. [210] for the BYU reactor which was also investigated in chapters 4 and 5.

### 6.2 Optimization procedure

The main idea of the optimization procedure is presented in Figure 6.1. At first, a CFD simulation is carried out with literature-taken kinetic parameters for the global kinetic-diffusion model. In the next step, CFD results provide specific input data for CBK, such as O<sub>2</sub> % volume distribution, gas temperature, wall temperature, and particle residence time. Additionally, operating pressure, fuel properties from proximate and ultimate analyses, and particle size are provided. It must be mentioned that CBK can handle only monodisperse particles. Therefore only the mean particle sizes were investigated. The main results of interest are the reaction rate of char-O<sub>2</sub> (obtained from CBK/E), one reaction rate as the sum of char-CO<sub>2</sub>, char-H<sub>2</sub>O, and char-H<sub>2</sub> reactions (obtained from CBK/G), and char conversion factor due to the oxidation reaction and overall gasification reaction. Afterward, an optimization of kinetic parameters (activation energy, pre-exponential factor, temperature exponent) is performed through the minimization of the objective function. Newly obtained pre-exponential factor, activation energy, and temperature exponent are further applied into CFD. In this case, one iteration was enough to obtain convergence. The second step of the procedure considered the comparison of

the results with optimized kinetic parameters and non-optimized (literature-taken) parameters based on the experimental data.

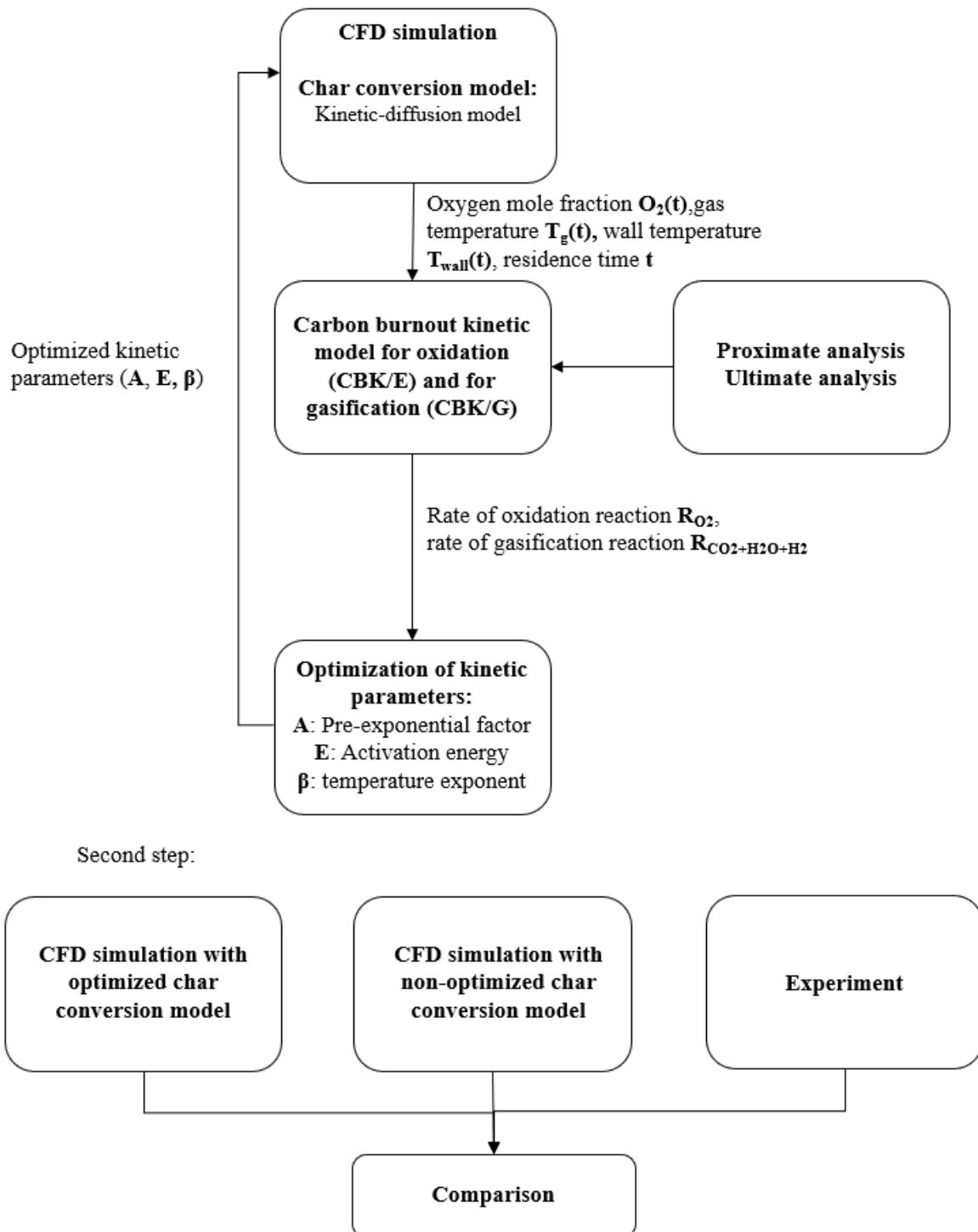


Figure 6.1. Optimization procedure of char conversion models [245].

### 6.3 Optimization of kinetic parameters

Optimization of kinetic parameters is performed through Eq. (6.1). The analyzed kinetic-diffusion model is presented in detail in chapter 2.4.1. It is described by Eq. (2.39).

$$OF(x_k) = \frac{\sum_{j=1}^{N_{t,j}} (R_{i,j}^{net} - R_{i,j}^{emp}(x_k))^2}{N_{t,i}} \quad (6.1)$$

where:  $R^{net}$  is the reaction rate from the complex model (CBK/E and CBK/G),  $x_k$  are the model parameters (the pre-exponential factor, activation energy, temperature exponent),  $N_{t,j}$  is the number of discrete time steps. The solution is obtained based on Levenberg-Marquardt fitting routine.  $R^{emp}$  is the reaction rate from the empirical model obtained from Eq. (2.40), assuming the reaction order to be equal to one. The unit of it is in  $\frac{g}{cm^2s}$ . The final form of the Eq. (2.40) is as follows:

$$R^{emp} = \frac{p_n}{\frac{1}{D_0} + \frac{1}{R_{kin}}} \quad (6.2)$$

where  $p_n$  is the partial pressure of gasifying agent,  $D_0$  is the diffusion rate coefficient and  $R_{kin}$  is the kinetic rate defined by the Arrhenius equation – Eq. (2.43). Eq. (6.2) is calculated for the  $C+0.5O_2 \rightarrow CO$  reaction,  $C+CO_2 \rightarrow 2CO$  reaction, and the  $C+H_2O \rightarrow CO+H_2$  reaction. The  $C+2H_2 \rightarrow CH_4$  reaction in the global model is not taken into account. Based on the literature it was found that its impact is negligible. It is important to mention that the objective function is calculated twice. The first case considers oxidation with the CBK/E model, where  $R^{net}$  provides the reaction rate for oxidation reaction. The second case regards gasification with CBK/G model, where  $R^{net}$  provides the final rate as the sum of all gasification reactions. The reaction rate from the CBK/E model is given in units  $\frac{g}{cm^2s}$  whereas the reaction rate from the CBK/G model is given in units  $\frac{1}{s}$ . On this basis, it is necessary to convert the reaction rate given in  $1/s$  also into  $\frac{g}{cm^2s}$ . The following relation is applied [94]:

$$R^{net} \left[ \frac{g}{cm^2s} \right] = \frac{\rho_c d_p}{6(1-X)} R^{net} \left[ \frac{1}{s} \right] \quad (6.3)$$

where  $\rho_c$  is the particle density,  $d_p$  is the particle diameter,  $X$  is the char conversion and  $R^{emp}$  is the reaction rate in unit  $1/s$ . Particle density and char conversion are also obtained from the CBK/G model. The reason why this is a two-step process lies in the fact that the char- $O_2$  reaction completely dominates the process as long as the  $O_2$  concentration is greater than approximately 500 ppm [11,12]. Therefore char combustion and char gasification occur consecutively.

## 6.4 Coal gasification simulation – brief model setup

The CFD model setup is very similar to the one presented in chapter 4.5 for the optimization of devolatilization. Data from proximate and ultimate analyses for the Utah coal are presented in Table 4.2. The investigated BYU reactor is depicted in Figure 4.11. The gas-phase reactions for the global approach are summarized in Table 4.3. Boundary conditions are presented in Table 4.4. The summary of applied models is presented in Table 6.1.

Table 6.1. Summary of applied models [245].

<b>Models</b>	
Devolatilization:	Competing two-step reaction mechanism (C2SM) [39]
Gas phase:	Global reaction approach with finite-rate/eddy dissipation model [151]
Char conversion:	Kinetic-diffusion model [168]
Turbulence:	Realizable k-ε model [218]
Radiation:	Discrete ordinate method [215], Weighted sum of gray gas model [215]
Particle tracking:	Discrete phase model, Discrete random walk model [234]
Pressure-velocity coupling	Semi-implicit method for pressure linked equations (SIMPLE) [239]

The research considers modified kinetic parameters for the surface reactions based on CBK/E and CBK/G models, literature-taken parameters of Chen et al. [104] which the optimization was initialized with, and additional three sets of parameters for the comparison - Table 6.2.

Table 6.2. Surface reactions kinetic parameters [245].

Reactions	Kinetic parameters	Literature parameters 1 [104]	Optimized parameters based on PC coal lab	Literature parameters 2 [87]	Literature parameters 3 [77]	Literature parameters 4 [77]
C+0.5O <sub>2</sub> →CO	A	0.052	1.298e-03	2.3	0.005	0.005
	E	6.1e07	1.324e08	9.23e07	7.4e07	7.4e07
	β	0	1.233	1	0	0
C+CO <sub>2</sub> →2CO	A	0.0732	0.066	4.4	0.3493	0.0635
	E	1.125e08	1.385e08	1.62e08	2.36e08	1.62e08
	β	0	-0.263	1	0	0
C+H <sub>2</sub> O→CO+H <sub>2</sub>	A	0.0782	1.877e-03	1.33	61.484	0.0019
	E	1.5e08	1.588e08	1.47e08	3.16e08	1.47e08
	β	0	-0.124	1	0	0

## 6.5 Results and discussion

The results are divided into three parts: the first part regards the char conversion optimization procedure results. The second part regards the CFD results with literature-taken kinetic parameters and modified parameters obtained from the optimization procedure by means of the CBK/E and CBK/G models. The third part considers the extra results of the modified parameters obtained by means of two gas-phase modeling approaches that were thoroughly discussed in chapter 5: a) the global reaction approach with finite-rate/eddy dissipation model and b) detailed GRI-Mech mechanism with eddy dissipation concept. The global reaction approach with the finite-rate/eddy dissipation model was used in the current

analysis of the impact of different char conversion kinetic parameters on coal gasification simulations, in order to save the computational effort. In Chapter 5 it turned out that the GRI-Mech mechanism with the eddy dissipation concept yielded the most accurate results, while the global reaction approach with finite-rate/eddy dissipation model yielded the least accurate, yet reasonable results. However, the detailed GRI-Mech mechanism is the most complex approach and it requires considerable computing power. Therefore, it was decided that the GRI-Mech approach will be applied only for the modified kinetic parameters from Table 6.2 as a comparison with the global approach with the finite-rate/eddy dissipation model.

### 6.5.1 Optimization procedure - results

The results consider the optimization of kinetic parameters for the kinetic-diffusion model based on the reaction rates from the CBK/E and CBK/G models. Figure 6.2 presents the reaction rates of CBK/E and kinetic-diffusion model with literature-taken kinetic parameters from Chen et al. [104]. These values can be found in Table 6.2. One can notice that the O<sub>2</sub> consumption rate is strongly overpredicted by the kinetic-diffusion model with literature-taken kinetic parameters with respect to the detailed CBK/E approach. Figure 6.3 depicts modified reaction rates of the kinetic-diffusion model obtained through the minimization of the objective function. One can observe a relatively reasonable agreement. The final coefficient of determination is equal to 96.1 %.

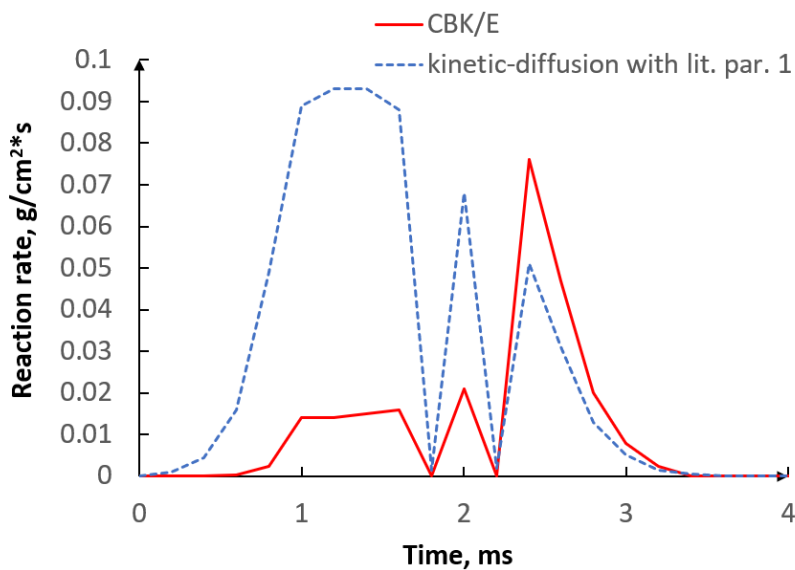


Figure 6.2. Reaction rates of CBK/E and kinetic-diffusion model with lit. parameters no. 1 [245].

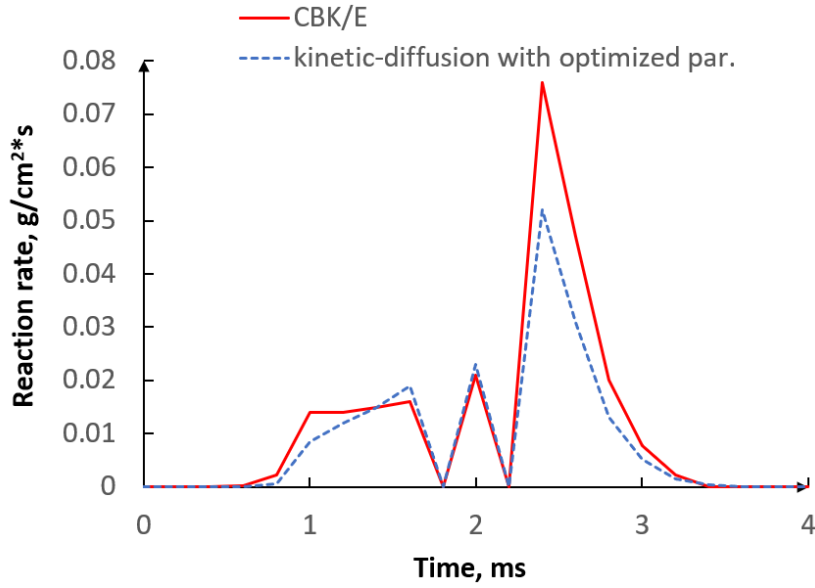


Figure 6.3. Reaction rate of CBK/E and optimized kinetic-diffusion model [245].

As regards the optimization of gasification, the first step in the optimization process required proper estimation of the frequency factor for surface oxide desorption in the CBK/G model [12]. The CBK/G version implemented into NEA’s PC Coal lab accounts for an empirical correlation, linking the kinetic parameters in the model with the daf carbon content of the parent coal [246].

$$A_{70} = 10^{0.1C_{daf}-0.64} \quad (6.4)$$

Where  $A_{70}$  is the frequency factor,  $C_{daf}$  is coal carbon content in dry-ash-free (daf) wt%.

However, while analyzing the performance of CBK/G for a large dataset of 228 coals with conversion ranging from 0% to 100%, a substantial scatter with respect to the experiments was observed. It concerned especially low and high conversion levels. It was concluded that the empirical relation only depicted the overall tendency in the gasification reactivity with the coal rank. In order to obtain data of high accuracy, experimental data are necessary to scale the empirical correlation. As a result, instead of applying Eq. (6.4), the frequency factor was scaled on the basis of the char conversion experiment of the Illinois coal [247], which is close to the analyzed in the present study Utah coal, based on the Van Krevelen diagram - Figure 6.4.

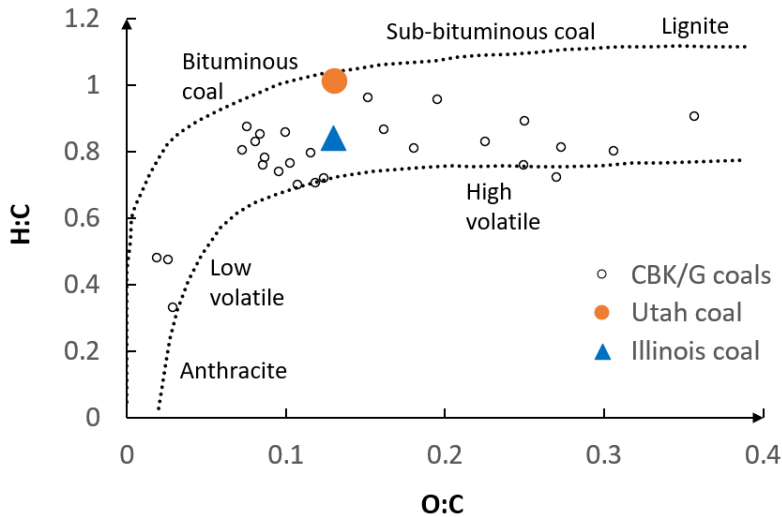


Figure 6.4. Location of the coals in the van Krevelen diagram. The plot also reports coal database used for CBK/G validation [12].

The results of the modified CBK/G model for the Illinois coal are presented in Figure 6.5. The scaled frequency factor, for which the model results coincide with experimental data [247], is further incorporated in the calculations. Figure 6.5 additionally presents the results of the CBK/G original model with the frequency factor obtained from Eq. (6.4). It is evident that in order to obtain accurate char conversion prediction even with the detailed CBK/G model, experimental data are required.

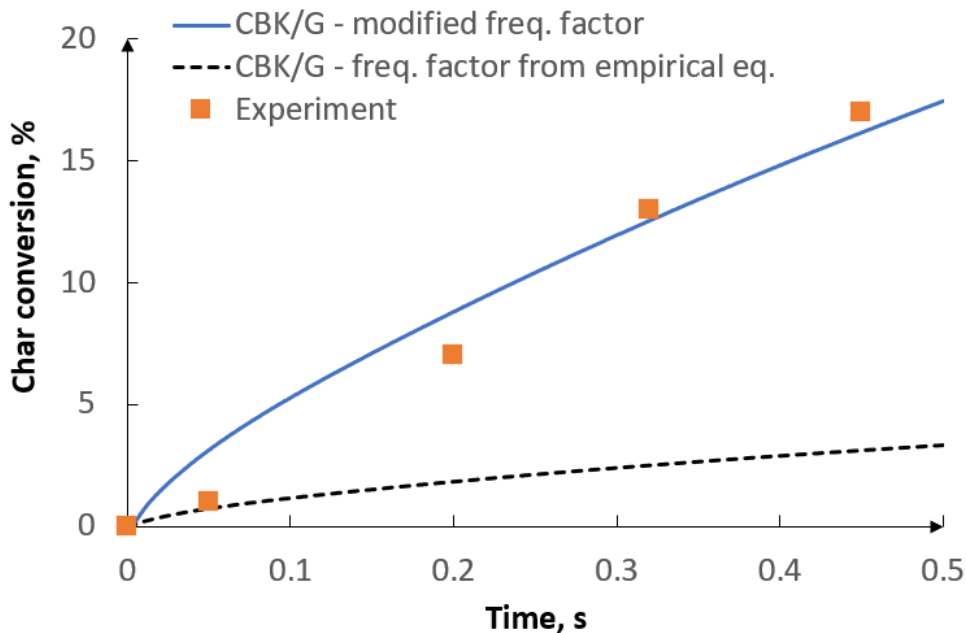


Figure 6.5. Char conversion of the Illinois coal as a function of the residence time in a drop tube furnace. Gas temp - 1727K, Composition: 21% CO<sub>2</sub>, 79% N<sub>2</sub> [245].

Figure 6.6 presents the gasification reaction rate of the modified CBK/G and the reaction rate of the kinetics-diffusion model with literature parameters. Owing to the fact that

the reaction rate from the CBK/G model is actually the sum of the reaction rates from all gasification reactions, the blue curve in Figure 6.6 and Figure 6.7 is the sum of the reaction rates from the  $C+CO_2 \rightarrow 2CO$  reaction and the  $C+H_2O \rightarrow CO+H_2$  reaction. As it was mentioned, based on the literature, the reaction rate from the  $C+2H_2 \rightarrow CH_4$  reaction is very small and hence it is not taken into account. Therefore it has been assumed the final reaction rate is defined as follows:

$$R_{CO_2+H_2O+H_2} = R_{CO_2} + R_{H_2O} \quad (6.5)$$

The choice is relevant because at atmospheric pressures separated active sites for  $CO_2$  and  $H_2O$  can be assumed and consequently, the total reaction rate can be the sum of the individual rates [189,190,200].

Based on the results, one can notice a strong overprediction by the global model. In such a case, the char conversion factor would be strongly overpredicted. Figure 6.7 depicts the optimized global model based on the results of CBK/G. In this case, a coefficient of determination is equal to 97.2 %. The modified kinetic parameters can be found in Table 6.2.

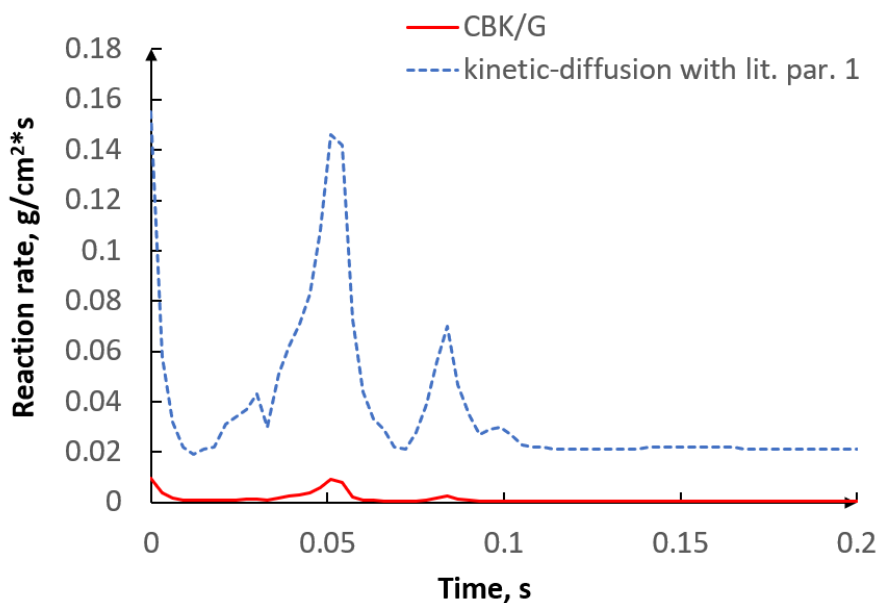


Figure 6.6. Reaction rates of CBK/G and kinetic-diffusion model with literature-taken parameters [245].



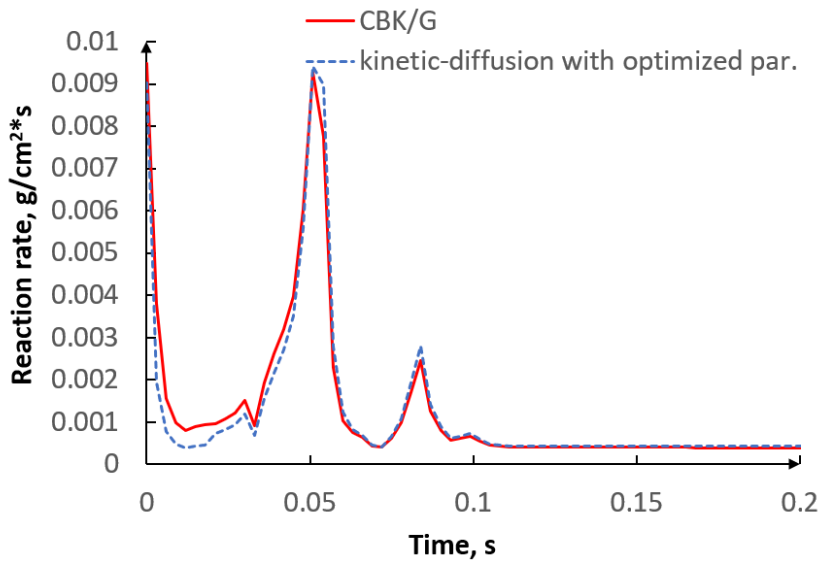


Figure 6.7. Reaction rate of CBK/G and modified reaction rate of the kinetic-diffusion model [245].

Figure 6.8 and Figure 6.9 depict the reaction rate of char oxidation and char gasification for the global kinetic diffusion model with literature parameters from Table 6.2. One can observe a very strong impact of the applied parameters on the reaction rate. In Figure 6.9 the results have not been presented in one graph because the reaction rates with literature parameters 3 and 4 are an order of magnitude smaller and they would not be visible. It is clear that prior to any simulation, char conversion parameters have to be carefully adjusted in order to accurately predict the behavior of the rate of surface reactions.

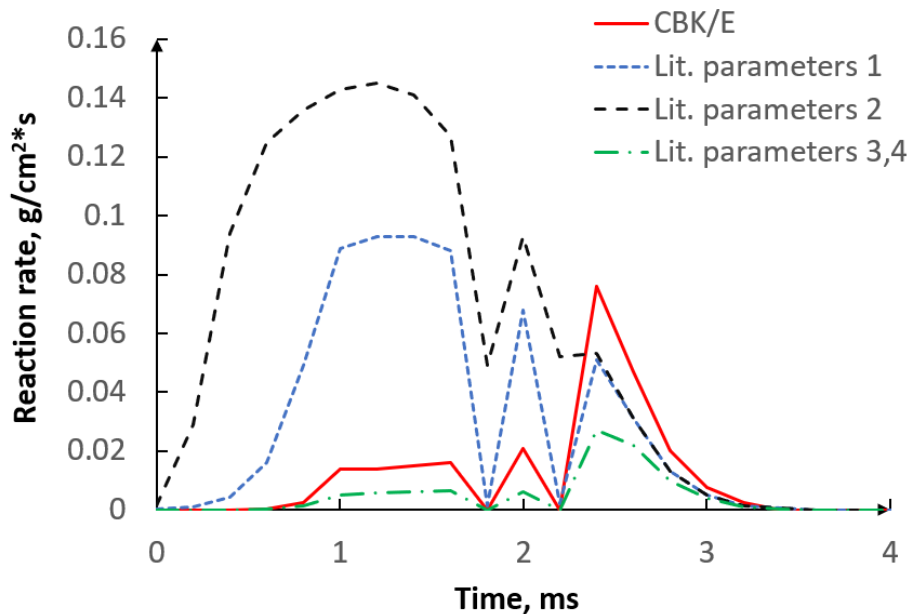


Figure 6.8. Comparison of oxidation reaction rates for global model with literature parameters [245].

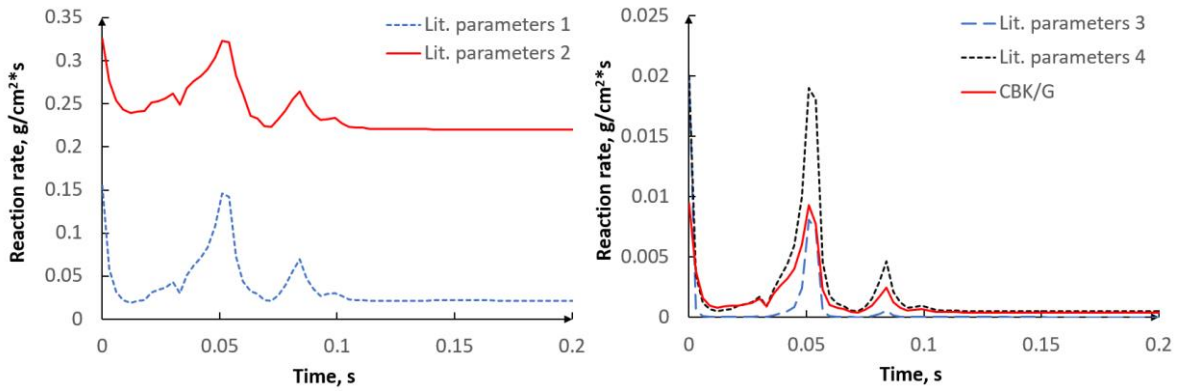


Figure 6.9. Comparison of gasification reaction rates for global model with literature parameters [245].

### 6.5.2 CFD results

This section presents the CFD results for the BYU reactor focusing on the char conversion aspect. Four sets of literature-taken kinetic parameters and one set of parameters optimized based on the CBK model are analyzed. Figure 6.10 presents the molar fraction concentrations of CO, H<sub>2</sub>, CO<sub>2</sub>, and H<sub>2</sub>O along the centerline of the BYU reactor.

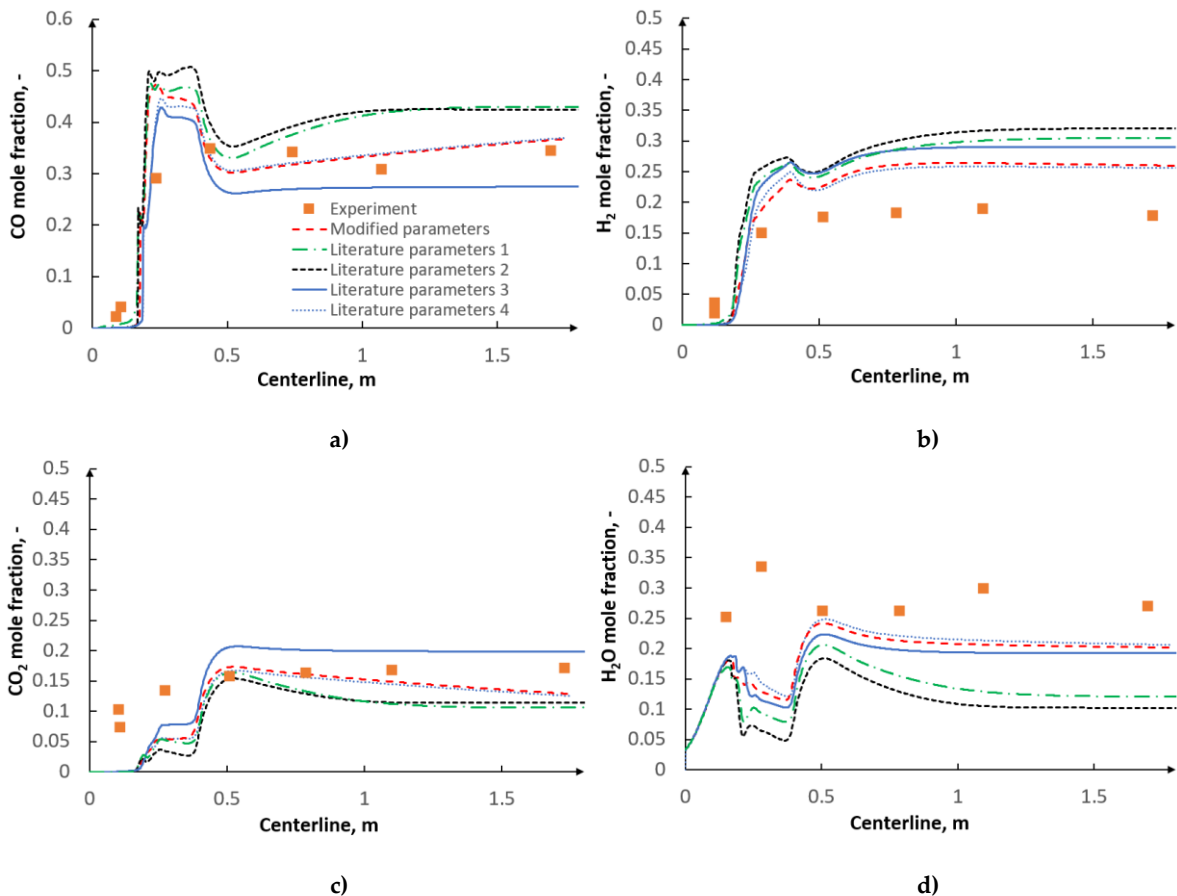


Figure 6.10. CO, H<sub>2</sub>, CO<sub>2</sub> and H<sub>2</sub>O mole fraction distribution along the centerline for five different sets of kinetic parameters [245].

An extreme impact of the applied kinetic parameters on the overall gas composition can be observed. One can notice that the slope of the curves varies in the reforming zone which corresponds to the strength of the gasification reactions. Judging by Figure 6.8 and Figure 6.9, the second set of parameters provides the highest reaction rate. As a result, in Figure 6.10 for the second set of kinetic parameters, the CO and H<sub>2</sub> mole fraction curves have the highest slope in the reforming zone and consequently, the highest amount of CO and H<sub>2</sub> produced, while the lowest amount of CO<sub>2</sub> and H<sub>2</sub>O. As for the third set of kinetic parameters, the gasification rate is the slowest (Figure 6.8 and Figure 6.9), hence the lowest slope of the CO mole fraction curve in the reforming zone and the smallest amount of the final CO produced. One can observe that the optimized kinetic parameters and the fourth set of literature-taken parameters are the most accurate ones with respect to the experimental results. The phenomenon that a given set of data can be fitted equally well by more than one pair of kinetic parameters is referred to as the compensation effect. It was already mentioned by [225–229]. The impact of gasification reactions is less pronounced in the lean zone and at the beginning of the flame zone where devolatilization and char oxidation prevail. However, the contribution of these reactions in these zones is also non-negligible. Figure 6.11 depicts the devolatilization process of particles with 6 representative diameters. For clarity, each sub-figure consists of 50 particles. A considerable influence of the particle diameter on the onset of devolatilization and the overall time of devolatilization can be observed. The sooner the volatiles are released, the sooner the surface reactions begin to occur. One can notice that the axial distance for which the volatiles are released varies from  $x = 0.2$  m to  $x = 0.5$  m. Therefore, different kinetics of the surface reactions will result in different strength of the surface reactions in this region. As a result, different amounts of CO, H<sub>2</sub>, CO<sub>2</sub>, and H<sub>2</sub>O are to be expected. Judging by Figure 6.11a-c it is evident that for smaller particles the recirculation is much more intense. As regards Figure 6.12, the applied kinetic parameters have also a non-negligible effect on the temperature distribution inside the reactor. Due to more intensive gasification reactions and their endothermic character for lit. parameters no. 2 and no. 3, the temperature is substantially lower, especially, in the reforming zone where gasification reactions dominate.

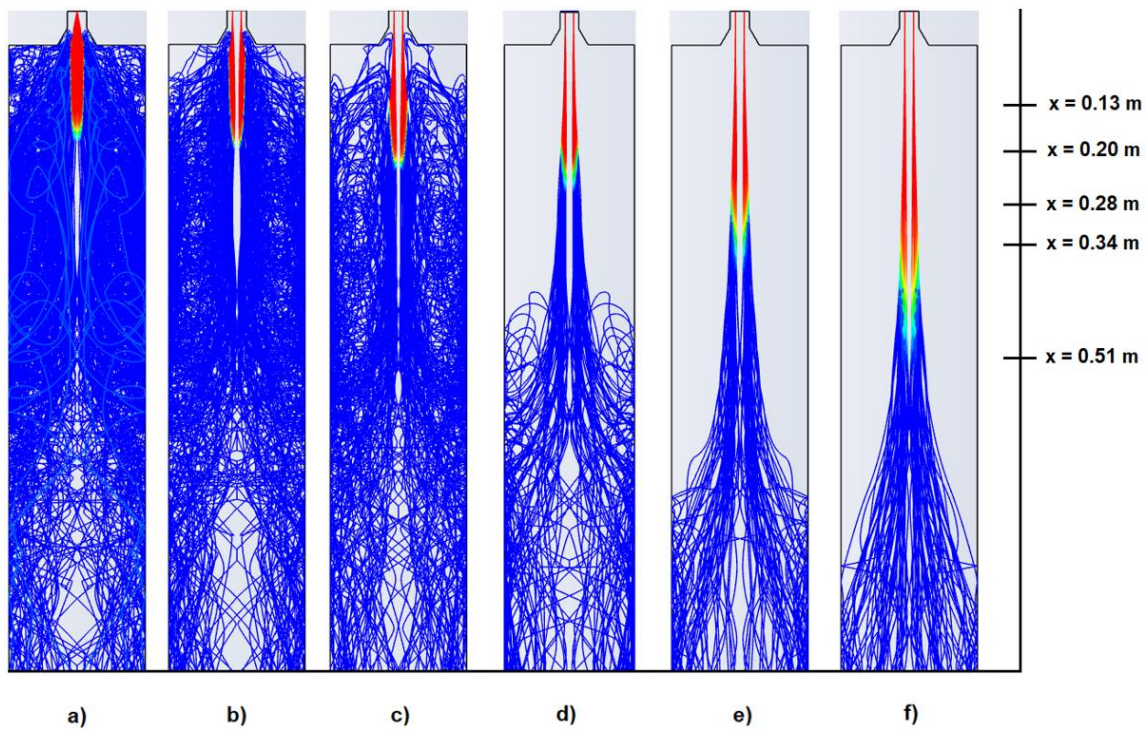


Figure 6.11. Particle tracks of volatiles mass fraction for the optimized kinetic-diffusion model during devolatilization of 50 particles for 6 representative diameters a)  $1\ \mu\text{m}$ , b)  $17\ \mu\text{m}$ , c) mean -  $36\ \mu\text{m}$ , d)  $51\ \mu\text{m}$ , e)  $77\ \mu\text{m}$ , f)  $85\ \mu\text{m}$  [245].

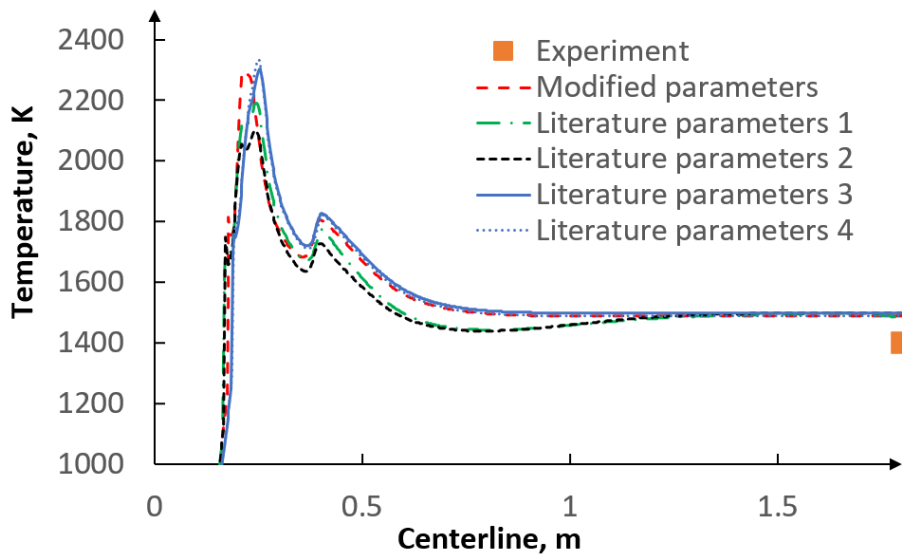


Figure 6.12. Temperature distribution along the centerline for five different sets of kinetic parameters [245].

Table 6.3 presents the char conversion factor for the surface reaction model with kinetic parameters from Table 6.2. As it was already mentioned, CBK/E and CBK/G models can handle only monodisperse particles. Therefore the optimized kinetic parameters inherently correspond to the mean particle diameter. On this basis, Table 6.3 regards both the mean particle diameter comparison and all particle fractions with regard to the experiment. Judging by the results, the optimized kinetic parameters for the mean particle diameter are in excellent agreement with the experiment. Char conversion factors for all particle fractions for optimized parameters and

literature parameters no. 4 are in reasonable agreement with the experiment. Future enhancement of CBK/E and CBK/G models to account for polydisperse particles would improve the accuracy of simulations, providing more exact reaction rates. As a result, optimized kinetic parameters would directly correspond to all particle fractions.

Table 6.3. Char conversion degree for surface reaction model with different kinetic parameters [245].

	Char conversion degree %		
	Simulation results Mean particle diameter - 36 $\mu\text{m}$	Simulation results all particle fractions 1 - 85 $\mu\text{m}$	Experiment All particle fractions 1 - 85 $\mu\text{m}$
Literature parameters 1	100 %	100 %	
Optimized parameters	83 %	77 %	
Literature parameters 2	100 %	99 %	82%
Literature parameters 3	27 %	59 %	
Literature parameters 4	80 %	74 %	

The accuracy of the optimization procedure for the axial in-reactor gas composition (Figure 6.10) has been additionally assessed with error analysis. A maximum and average value of absolute errors for non-optimized and optimized models are presented. The absolute error is defined as:

$$\Delta e = |x_{exp} - x_{num}| \quad (6.6)$$

where  $x_{exp}$  and  $x_{num}$  are the experimental and numerical values of the specific variable (e.g. CO/H<sub>2</sub>/CO<sub>2</sub>/H<sub>2</sub>O mole fraction), respectively.

Table 6.4 presents the quantitative assessment of the procedure. Judging by the results, the application of the modified parameters and literature parameters no. 4 results in one of the lowest errors with respect to the experimental data.

Table 6.4. Error analysis of CO, H<sub>2</sub>, CO<sub>2</sub> and H<sub>2</sub>O concentration along the centerline - Figure 6.10 [245].

Kinetic parameters	CO		H <sub>2</sub>		CO <sub>2</sub>		H <sub>2</sub> O	
	Max $\Delta e$ [%]	Av. $\Delta e$ [%]	Max $\Delta e$ [%]	Av. $\Delta e$ [%]	Max $\Delta e$ [%]	Av. $\Delta e$ [%]	Max $\Delta e$ [%]	Av. $\Delta e$ [%]
Lit. parameters 1	17.91	6.74	12.80	7.89	10.22	5.87	16.82	11.84
Mod. parameters	18.48	4.82	7.95	5.47	10.15	4.72	20.22	9.58
Lit. parameters 2	20.20	7.94	14.40	8.98	10.15	5.98	19.73	13.04
Lit. parameters 3	11.11	5.71	11.36	7.51	10.14	5.38	19.24	10.35
Lit. parameters 4	12.50	4.90	8.33	5.40	10.16	4.77	20.68	8.99

Figure 6.13 - Figure 6.20 present molar fraction gas concentrations along radial traverses for  $x=0.13\text{m}$ ,  $x=0.2\text{m}$ ,  $x=0.28\text{m}$ ,  $x=0.34\text{m}$ ,  $x=0.51\text{m}$ ,  $x=0.81\text{m}$ ,  $x=1.12\text{m}$  and  $x=1.73\text{m}$ . These traverses are visualized in Figure 5.10. In most of the cases, the model results with optimized kinetic parameters are in closest agreement with experimental data. As mentioned,  $\text{H}_2\text{O}$  mole fraction results are calculated from hydrogen balance and should not be considered as credible reference data. The impact of the applied parameters on the radial distribution is less substantial than for the axial distribution. This observation is sensible because the gasification reactions that dominate in the reforming zone proceed axially along with the mainstream. Another observation regards the changes in radial concentration. One may notice that from the axial distance  $x = 0.51\text{ m}$  the molar distribution of species stabilizes in the radial direction. There are insignificant changes in the yield. It means that the gasification reactions which begin to dominate in the reforming zone are radially uniform. On the other hand, substantial changes in the radial direction (Figure 6.13 - Figure 6.16) for axial distances  $x < 0.51\text{ m}$  can be observed. These changes are most abrupt up to the radial distance of  $0.04\text{ m}$ . This is the boundary of the flame - Figure 6.21.

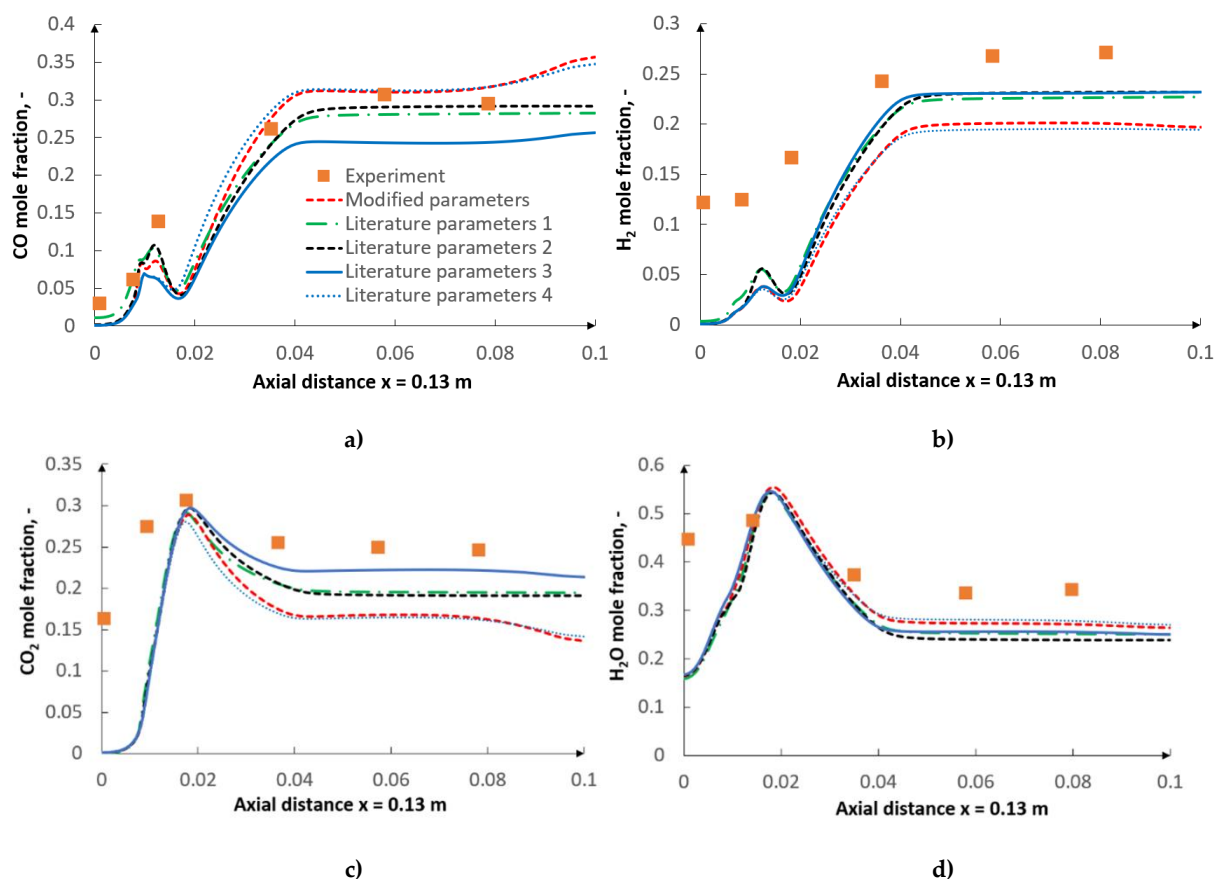


Figure 6.13.  $\text{CO}$ ,  $\text{H}_2$ ,  $\text{CO}_2$  and  $\text{H}_2\text{O}$  mole fraction distribution along the radial traverse  $x=0.13\text{m}$  for five different sets of kinetic parameters [245].

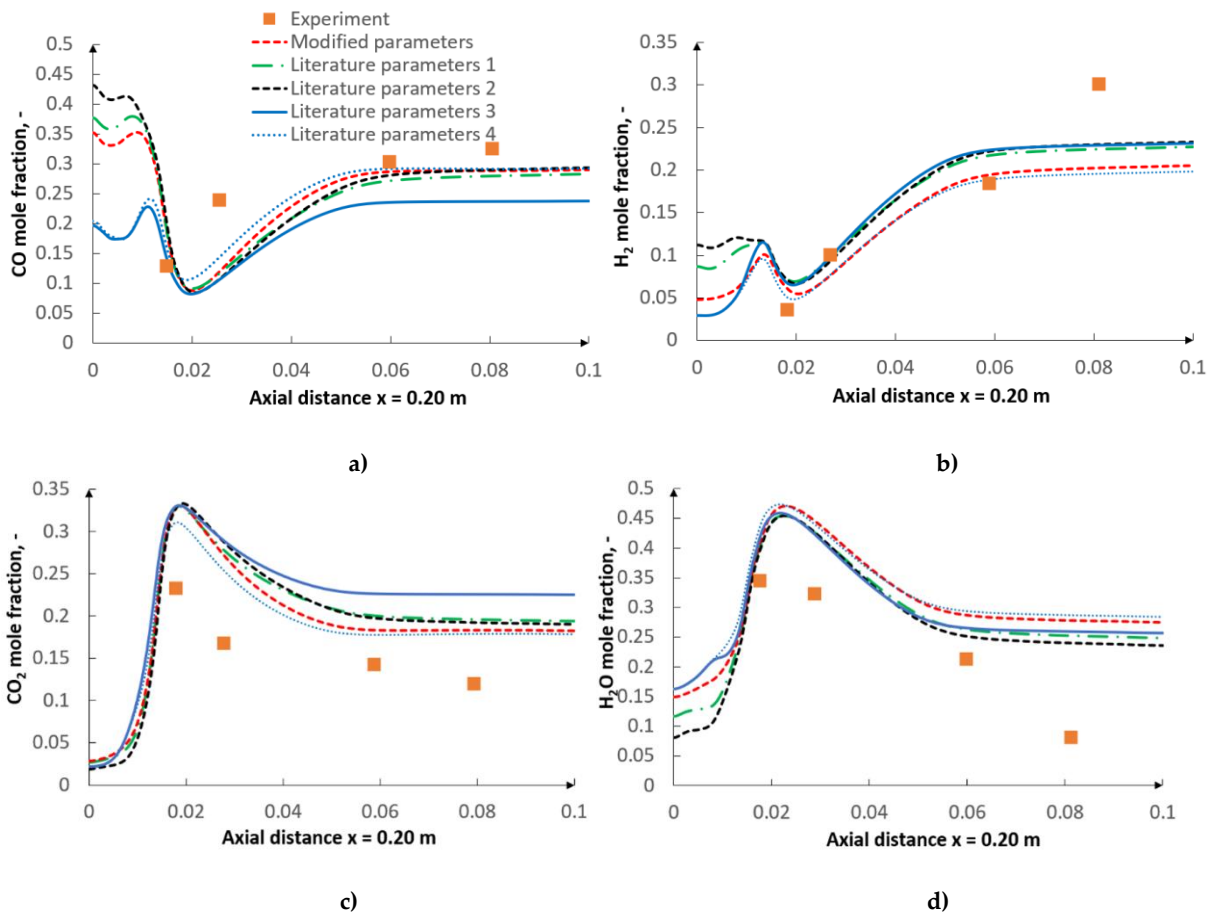
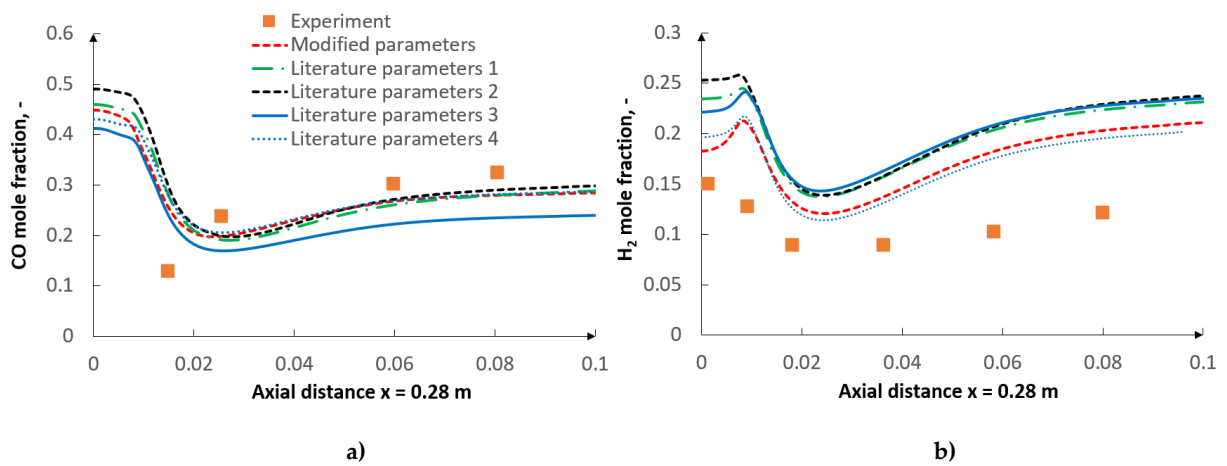


Figure 6.14. CO,  $\text{H}_2$ ,  $\text{CO}_2$  and  $\text{H}_2\text{O}$  mole fraction distribution along the radial traverse  $x=0.20\text{m}$  for five different sets of kinetic parameters [245].



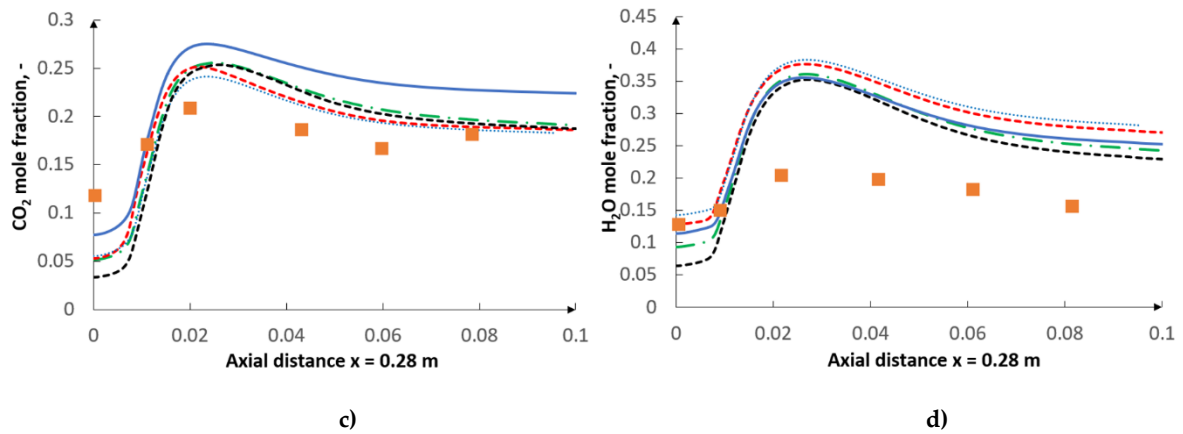


Figure 6.15.  $CO$ ,  $H_2$ ,  $CO_2$  and  $H_2O$  mole fraction distribution along the radial traverse  $x=0.28m$  for five different sets of kinetic parameters [245].

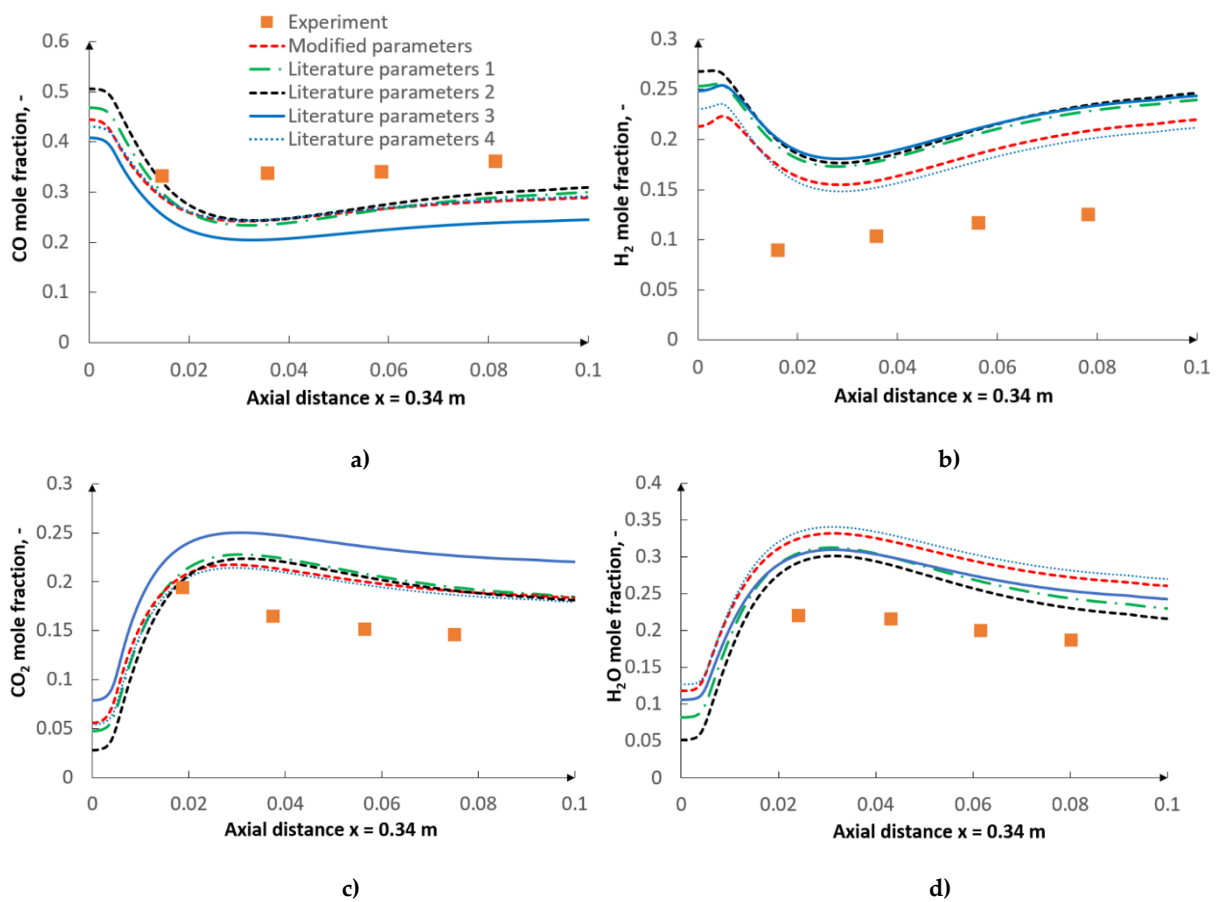


Figure 6.16.  $CO$ ,  $H_2$ ,  $CO_2$  and  $H_2O$  mole fraction distribution along the radial traverse  $x=0.34m$  for five different sets of kinetic parameters [245].



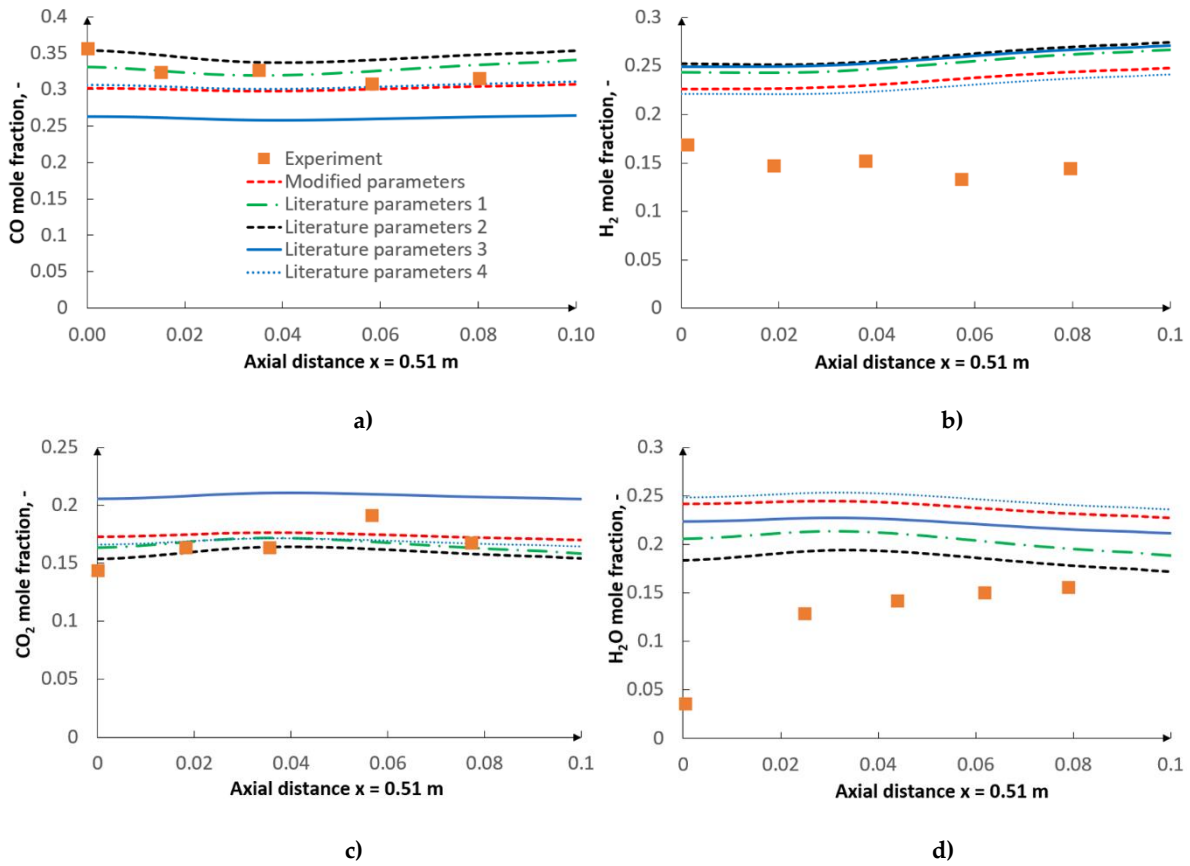


Figure 6.17.  $\text{CO}$ ,  $\text{H}_2$ ,  $\text{CO}_2$  and  $\text{H}_2\text{O}$  mole fraction distribution along the radial traverse  $x=0.51\text{m}$  for five different sets of kinetic parameters [245].

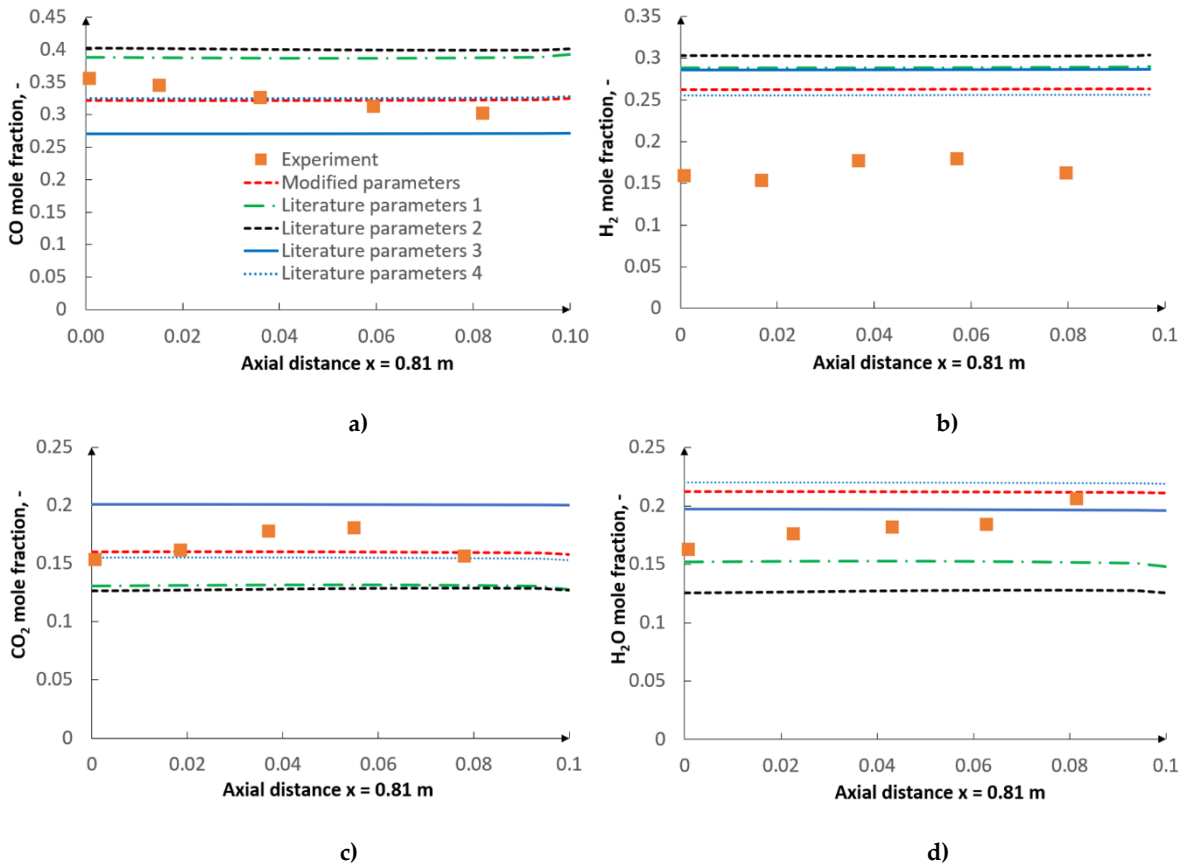


Figure 6.18. CO, H<sub>2</sub>, CO<sub>2</sub> and H<sub>2</sub>O mole fraction distribution along the radial traverse  $x=0.81\text{m}$  for five different sets of kinetic parameters [245].

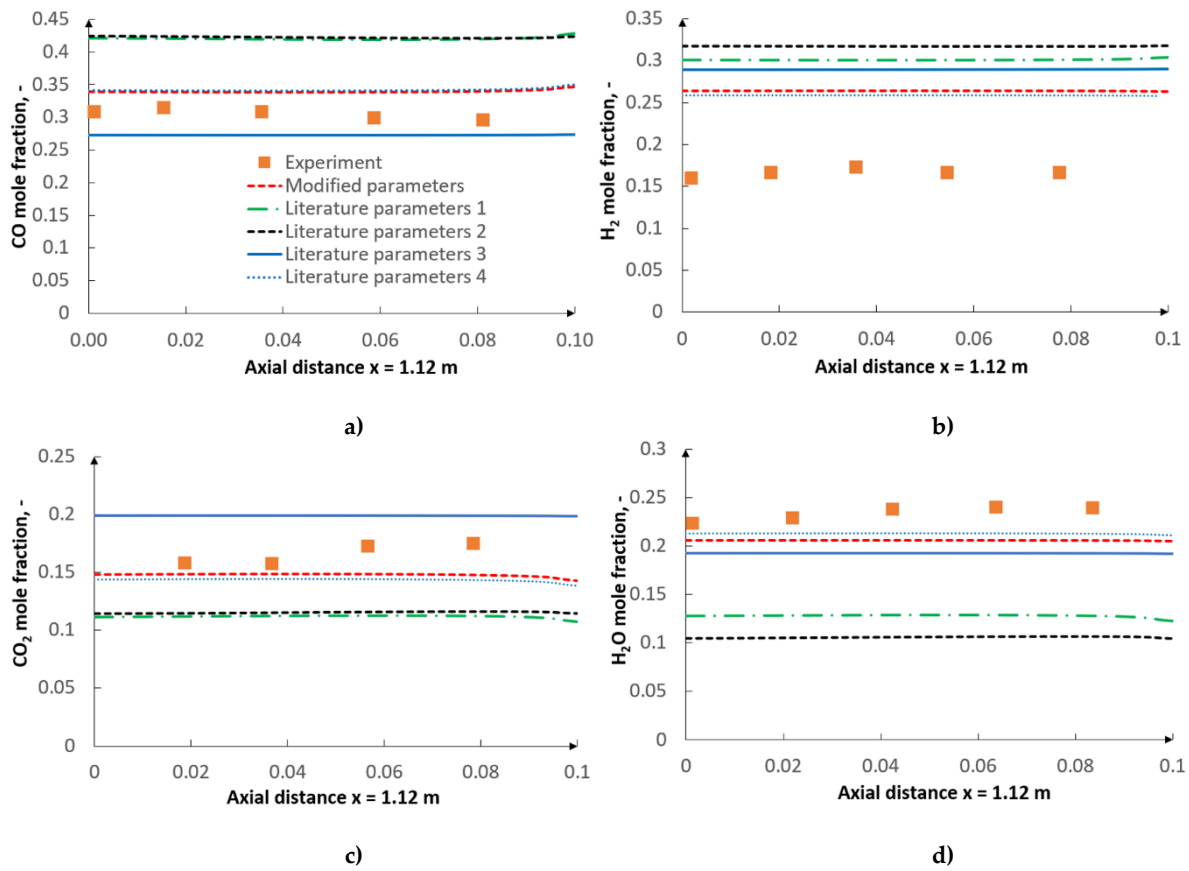
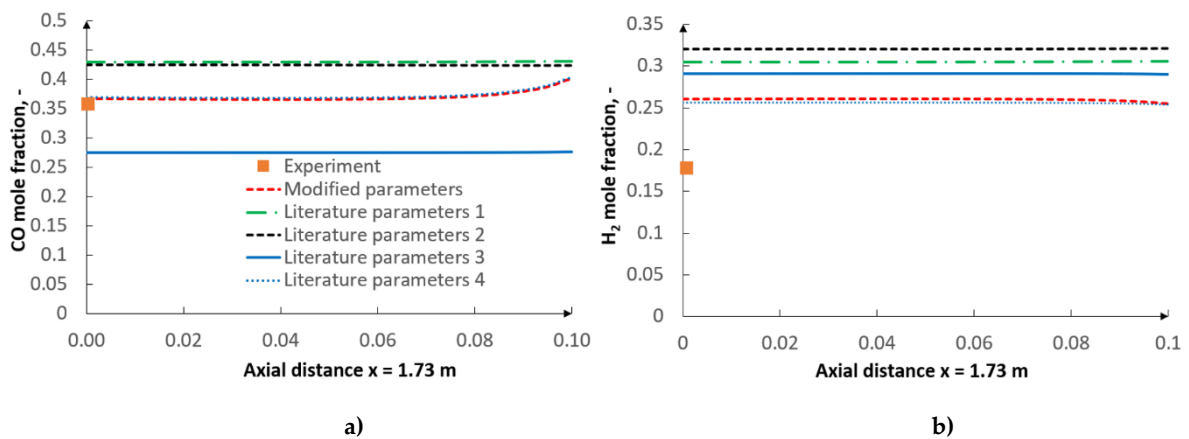


Figure 6.19. CO, H<sub>2</sub>, CO<sub>2</sub> and H<sub>2</sub>O mole fraction distribution along the radial traverse  $x=1.73\text{m}$  for five different sets of kinetic parameters [245].



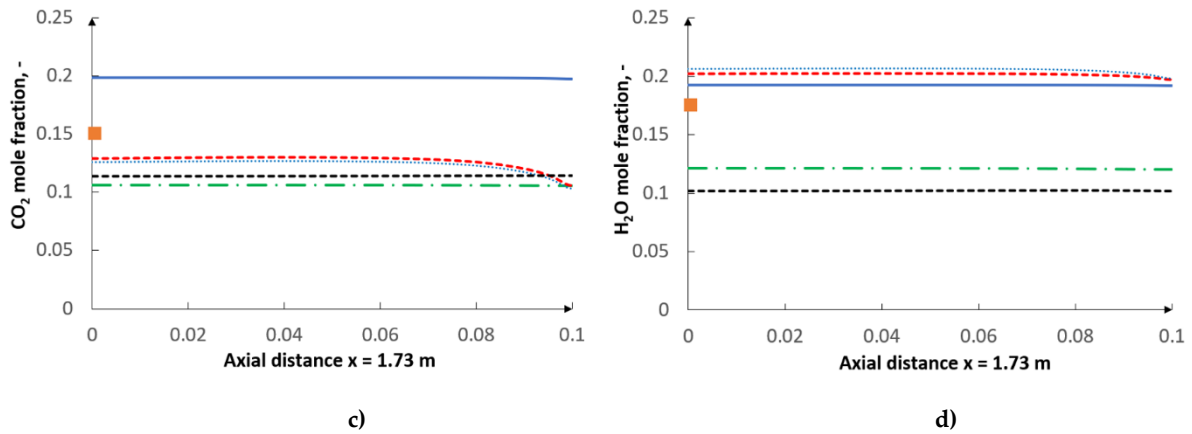


Figure 6.20.  $CO$ ,  $H_2$ ,  $CO_2$  and  $H_2O$  mole fraction distribution along the radial traverse  $x=1.73m$  for five different sets of kinetic parameters [245].

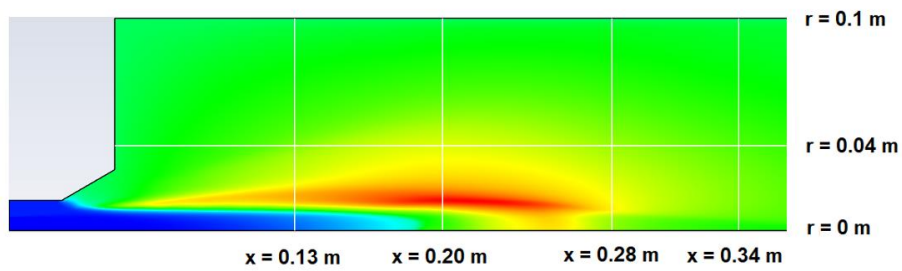


Figure 6.21. CFD results – contour plot of temperature with axial and radial distances [245].

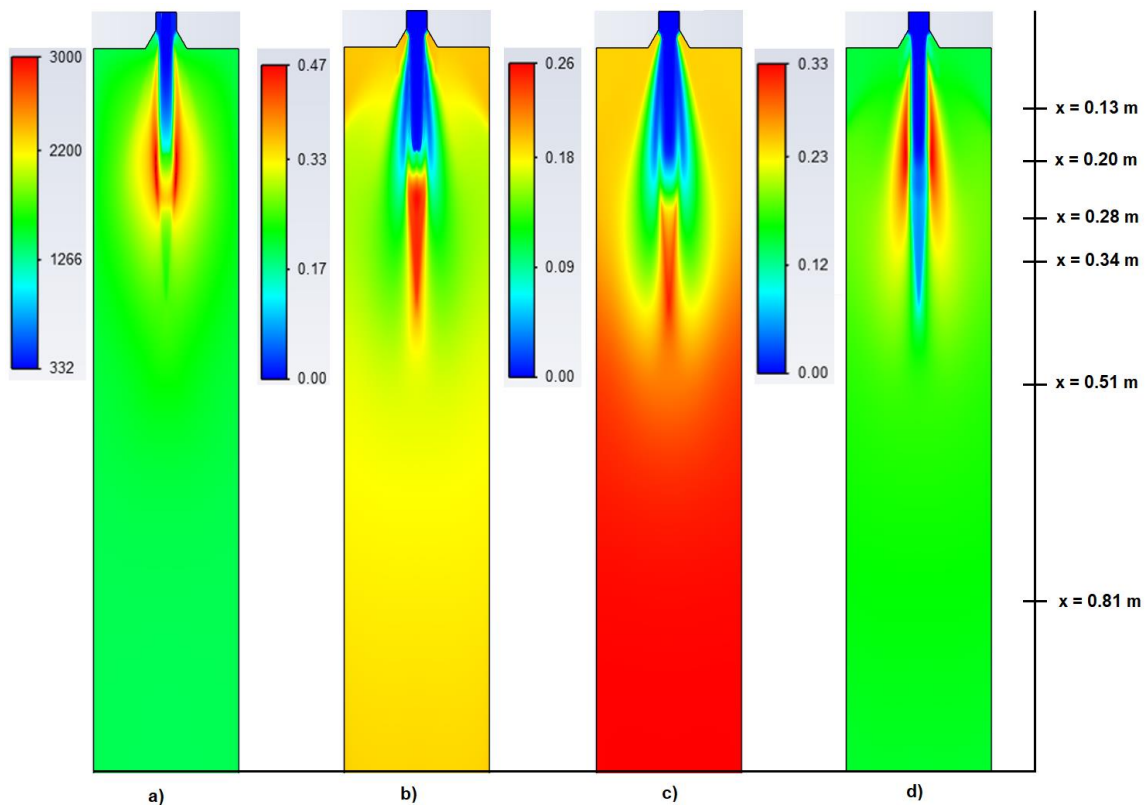


Figure 6.22. Contours for the optimized kinetic parameters: a) temperature (K), b)  $CO$  mole fraction, c)  $H_2$  mole fraction, d)  $CO_2$  mole fraction [245].

Figure 6.22 shows the contour plots of temperature, CO, H<sub>2</sub>, and CO<sub>2</sub> mole fractions, while Figure 6.23 presents the contour plots of H<sub>2</sub>O, O<sub>2</sub> mole fractions, and devolatilization reaction rate. Five regions can be noticed in the reactor: the lean zone, the recirculation zone, the flame zone, the post-flame zone, and the reforming zone. In the lean zone, equivalence ratios are lower than stoichiometric conditions, which corresponds to high O<sub>2</sub> content – Figure 6.23b. This zone is mainly composed of O<sub>2</sub> and H<sub>2</sub>O which are introduced in the primary and secondary streams. The flame zone begins downstream of the lean zone reaching very high temperatures – 3000K owing to the high O<sub>2</sub> content in the primary stream. CO and H<sub>2</sub> content are relatively low. In the post-flame zone, which follows the flame zone, the temperatures are lower than in the flame. This region is also characterized by a very rich mixture. CO and H<sub>2</sub> are mainly formed in this region because of the combined effect of the water-gas shift reaction and the gasification reactions. The next zone is dominated by reforming reactions. In this region, there are lower temperatures, extremely small gradients, and low conversion rates. CO and H<sub>2</sub> continue to increase slowly approaching the equilibrium conditions. The last region is characterized by a strong recirculation of the gas and coal particles – the recirculation zone. It is located between the lean, flame, post-flame zones and the reactor wall.

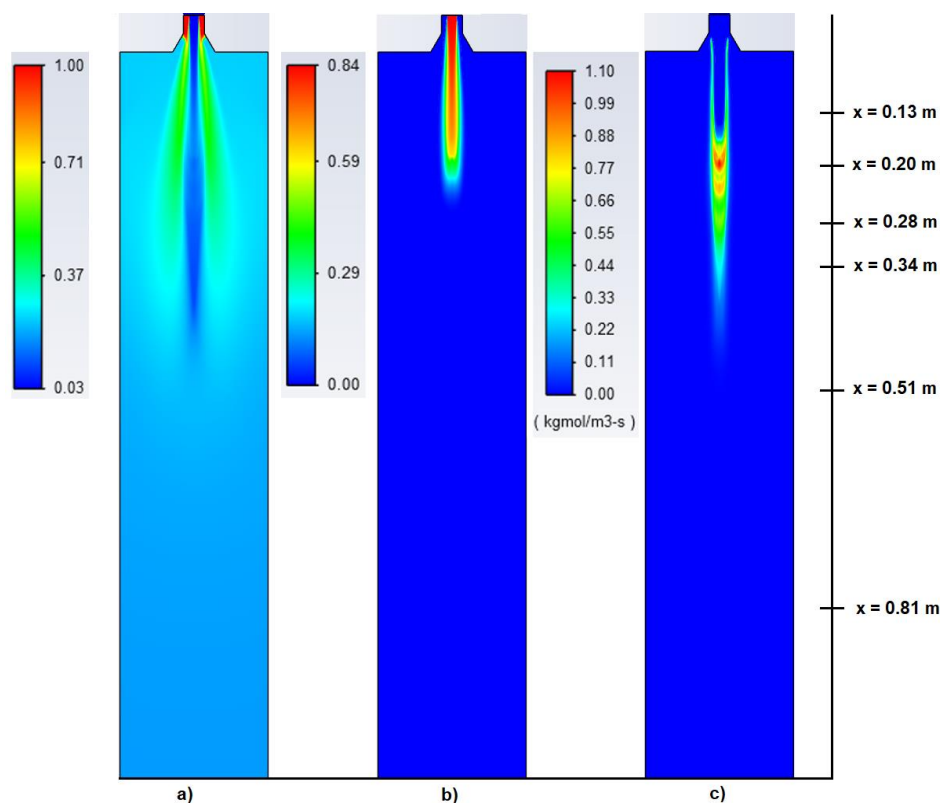


Figure 6.23. Contours for the optimized kinetic parameters: a) H<sub>2</sub>O mole fraction, b) O<sub>2</sub> mole fraction, c) devolatilization rate (kmol/m<sup>3</sup>s) [245].

### 6.5.3 CFD results – GRI-Mech vs Global reaction approach

This section considers the optimized parameters for the char conversion kinetic-diffusion model obtained through the optimization procedure for two gas-phase modeling approaches: a)

GRI-Mech with eddy dissipation concept and b) global approach with finite-rate/eddy dissipation model. Figure 6.24 depicts the in-reactor gas composition for GRI-Mech and for the global approach along the centerline, while Figure 6.25 - Figure 6.31 present the in-reactor gas composition for GRI-Mech and for global approach for the radial traverses. Judging by the results, one can also notice a non-negligible impact of the applied gas-phase modeling techniques on the in-reactor gas formation. The differences between the experimental data and the numerical results are smaller for the detailed GRI-Mech mechanism with the eddy dissipation concept. Figure 6.32 presents the contour plots of temperature, CO mole fraction, H<sub>2</sub> mole fraction, and CO<sub>2</sub> mole fraction for GRI-Mech with eddy dissipation concept. With regard to Figure 6.22 which considers the same variables but for the global approach with finite-rate/eddy dissipation model, the most substantial differences can be observed in the flame region. Although the global reaction approach and the GRI-Mech mechanism were found to be in close agreement for the plug flow reactor study and the perfectly stirred reactor study in chapter 5, the CFD results confirm that these approaches differ significantly.

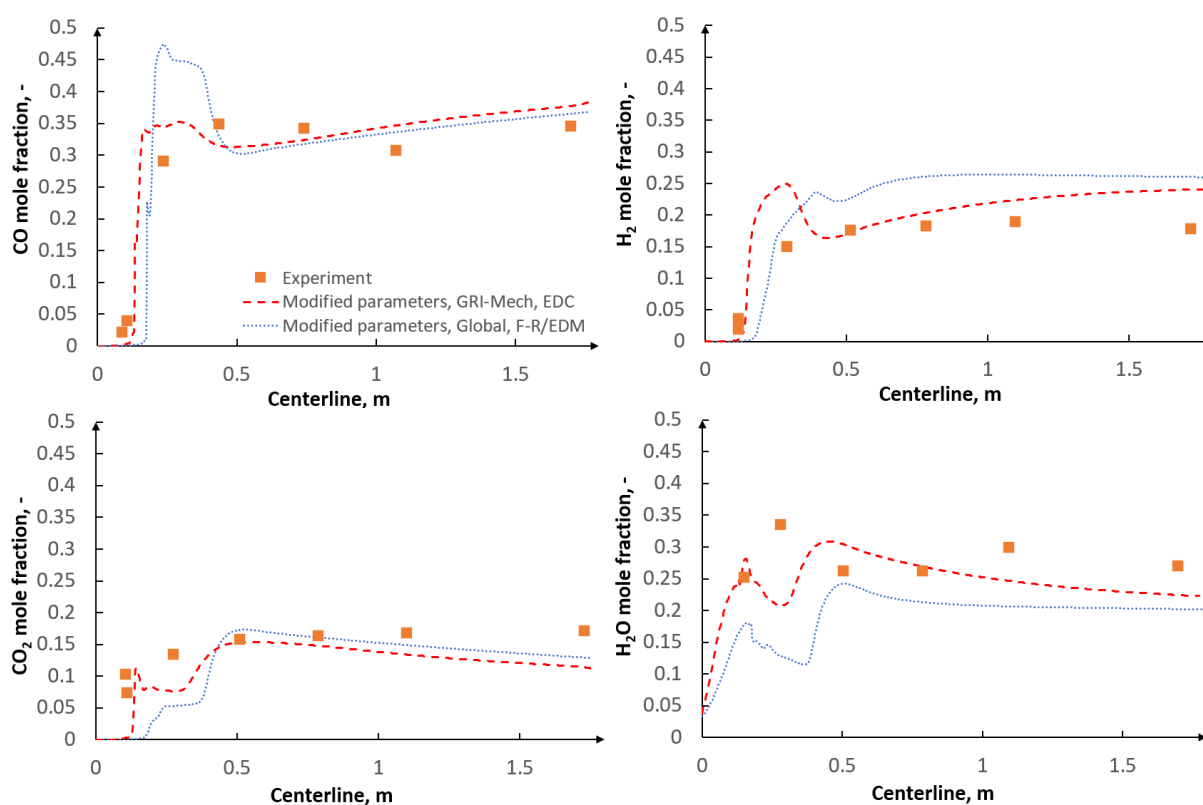


Figure 6.24. CO, H<sub>2</sub>, CO<sub>2</sub> and H<sub>2</sub>O mole fraction distribution along the centerline for modified kinetic parameters for global approach with F-R/EDM and for GRI-Mech with EDC.

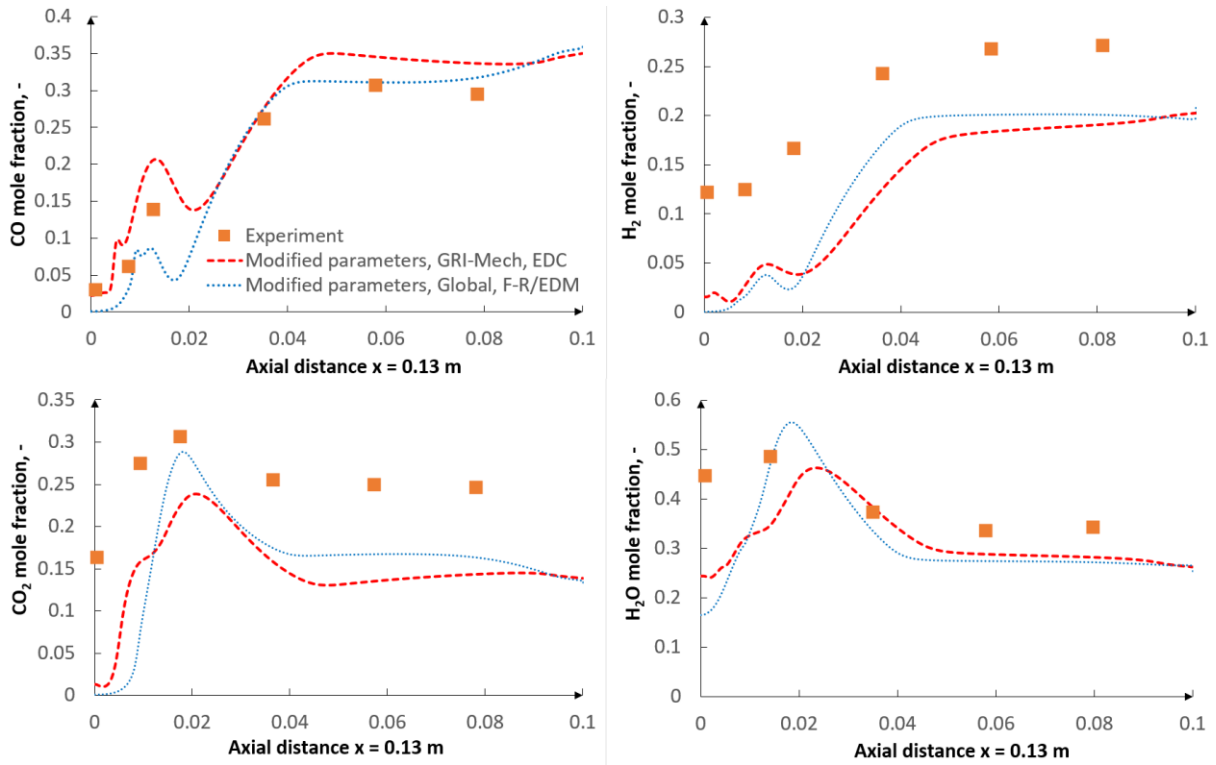


Figure 6.25. CO, H<sub>2</sub>, CO<sub>2</sub> and H<sub>2</sub>O mole fraction distribution along the radial traverse  $x=0.13$ m for modified kinetic parameters for global approach with F-R/EDM and for GRI-Mech with EDC.

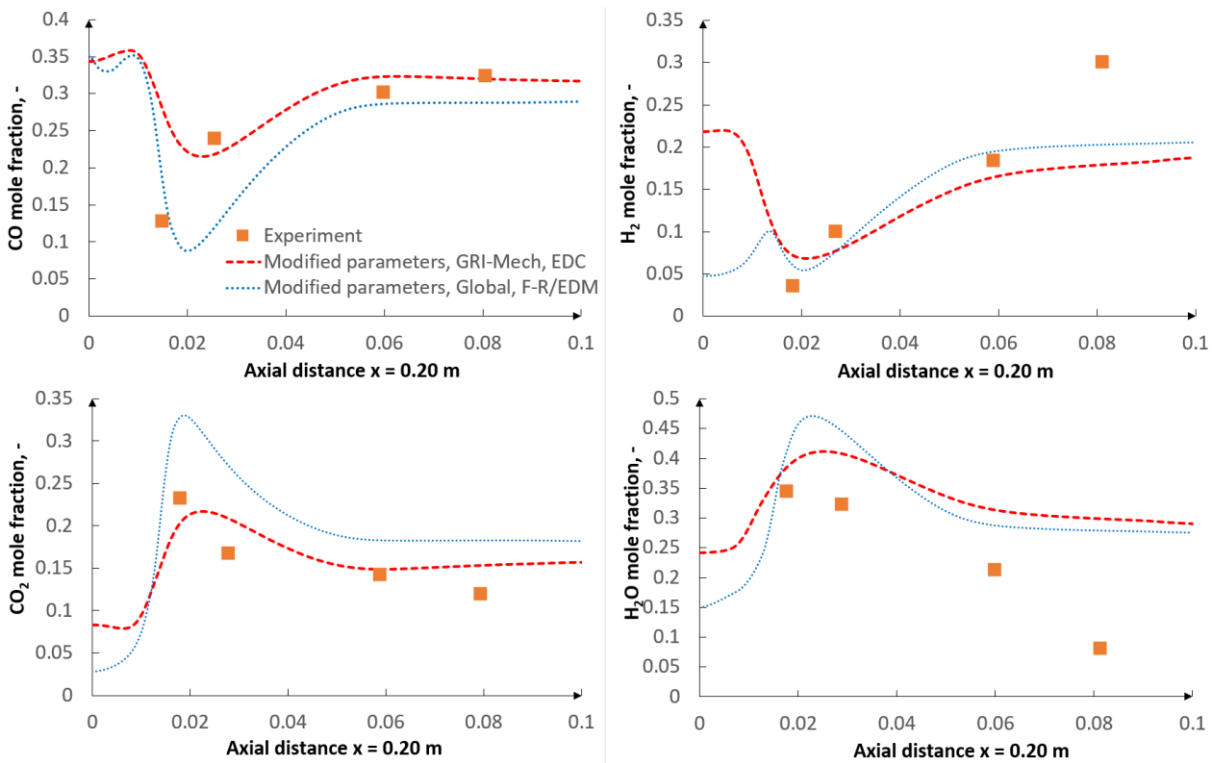


Figure 6.26. CO, H<sub>2</sub>, CO<sub>2</sub> and H<sub>2</sub>O mole fraction distribution along the radial traverse  $x=0.20$ m for modified kinetic parameters for global approach with F-R/EDM and for GRI-Mech with EDC.

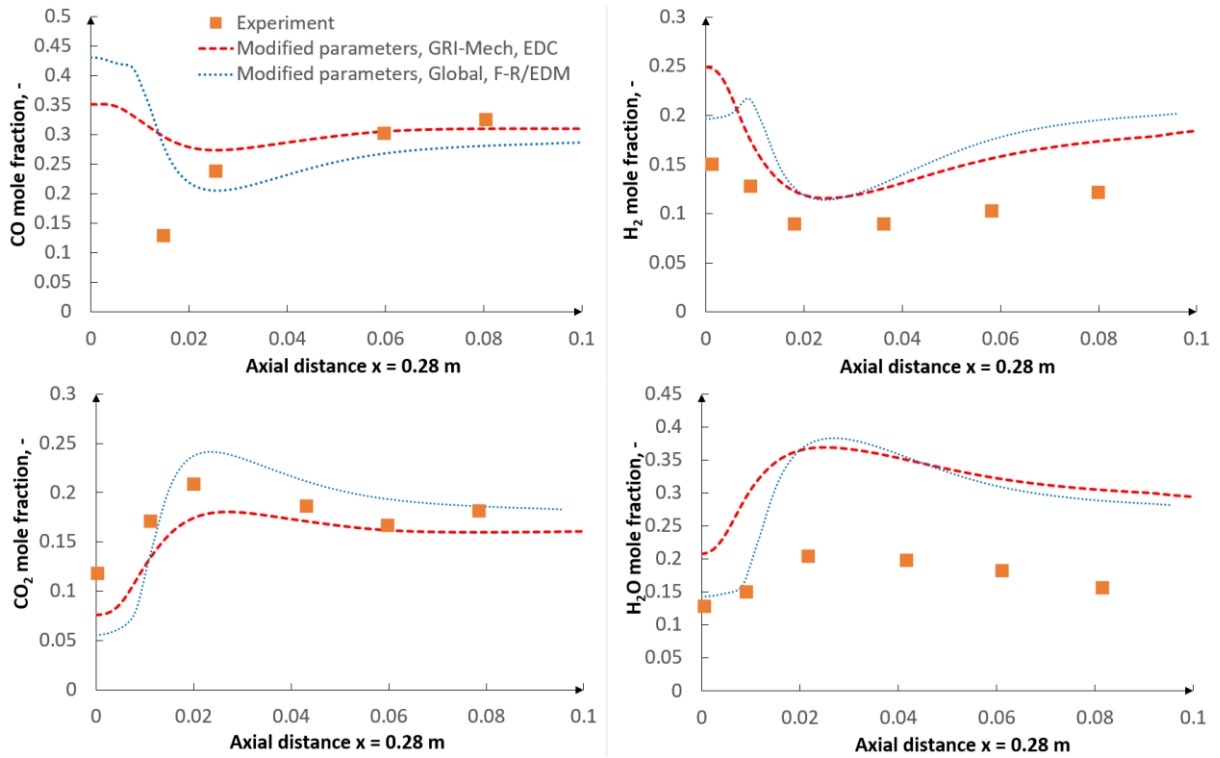


Figure 6.27. CO, H<sub>2</sub>, CO<sub>2</sub> and H<sub>2</sub>O mole fraction distribution along the radial traverse  $x=0.28$ m for modified kinetic parameters for global approach with F-R/EDM and for GRI-Mech with EDC.

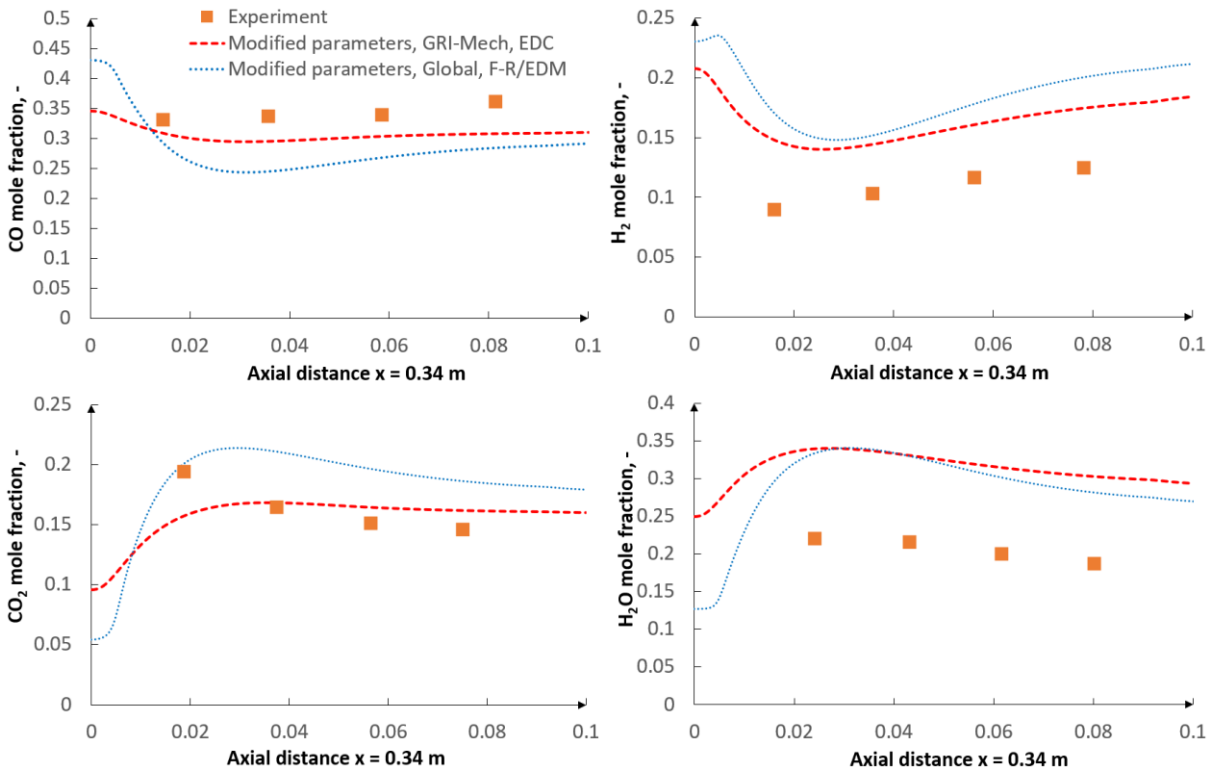


Figure 6.28. CO, H<sub>2</sub>, CO<sub>2</sub> and H<sub>2</sub>O mole fraction distribution along the radial traverse  $x=0.34$ m for modified kinetic parameters for global approach with F-R/EDM and for GRI-Mech with EDC.

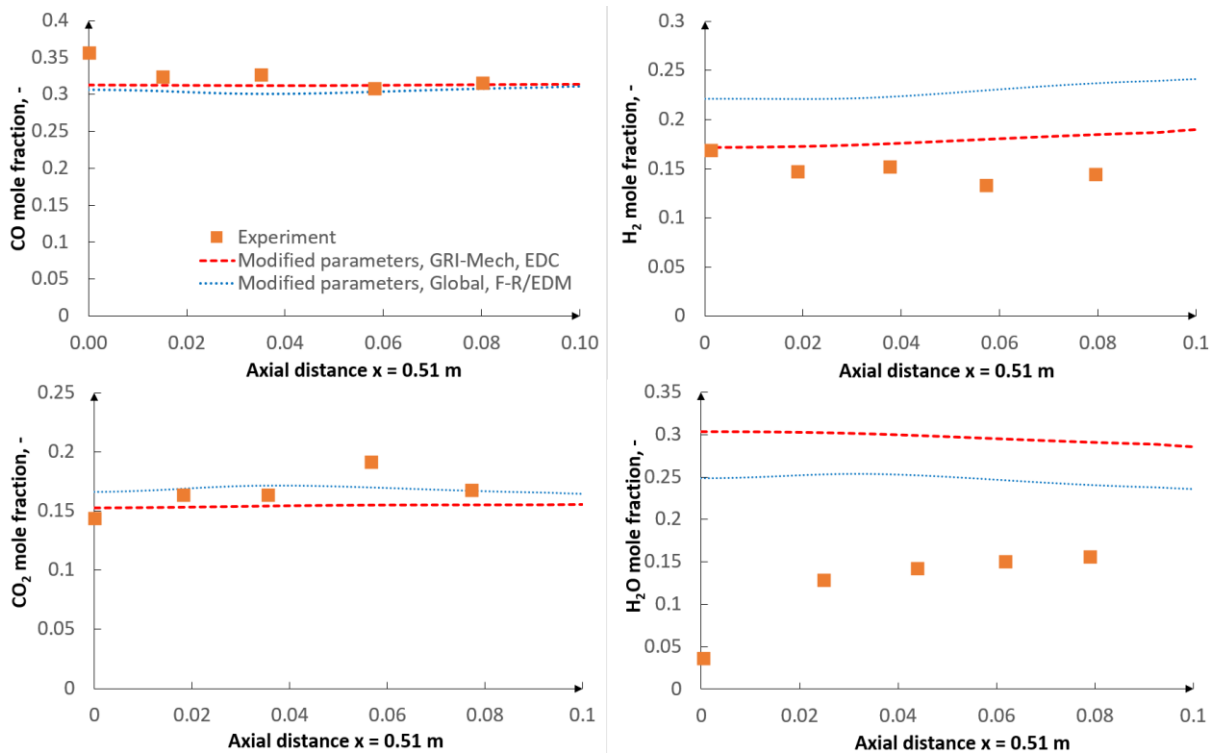


Figure 6.29. CO, H<sub>2</sub>, CO<sub>2</sub> and H<sub>2</sub>O mole fraction distribution along the radial traverse  $x=0.51$ m for modified kinetic parameters for global approach with F-R/EDM and for GRI-Mech with EDC.

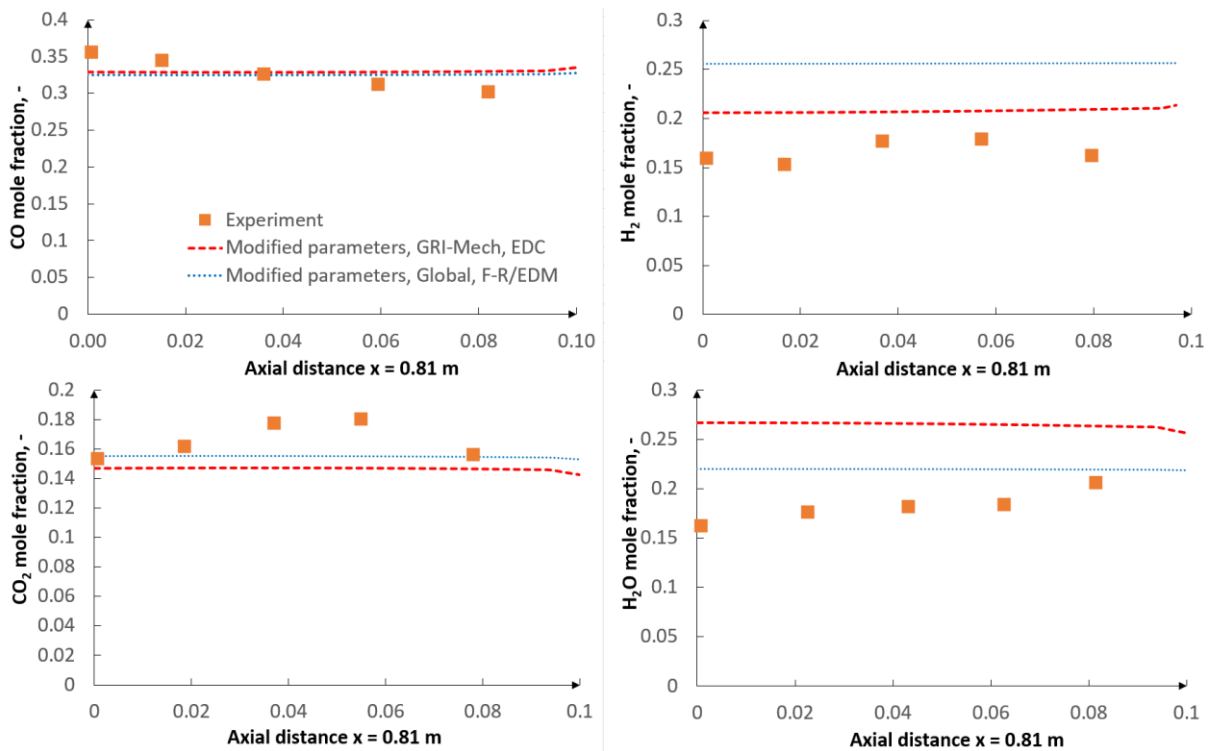


Figure 6.30. CO, H<sub>2</sub>, CO<sub>2</sub> and H<sub>2</sub>O mole fraction distribution along the radial traverse  $x=0.81$ m for modified kinetic parameters for global approach with F-R/EDM and for GRI-Mech with EDC.



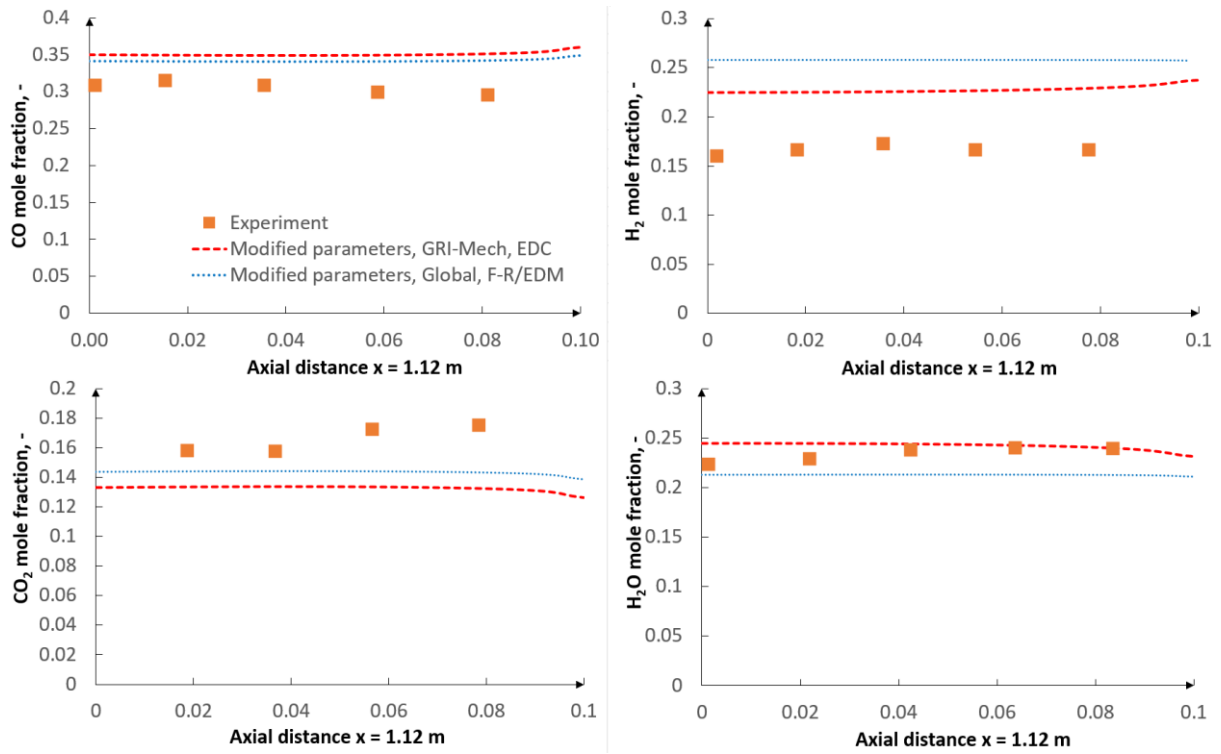


Figure 6.31. CO, H<sub>2</sub>, CO<sub>2</sub> and H<sub>2</sub>O mole fraction distribution along the radial traverse  $x=1.12$  m for modified kinetic parameters for global approach with F-R/EDM and for GRI-Mech with EDC.

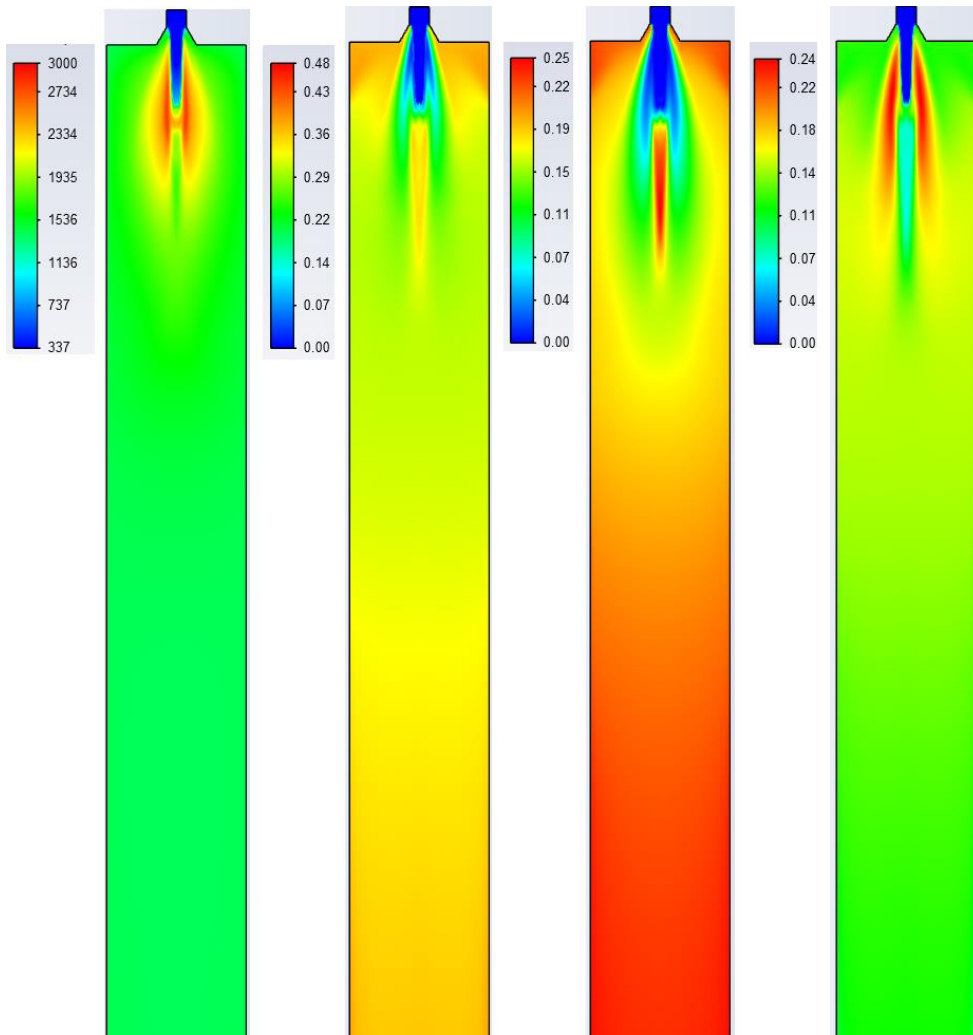


Figure 6.32. Contours for the optimized kinetic parameters for GRI-Mech with EDC: a) temperature (K), b) CO mole fraction, c)  $H_2$  mole fraction, d)  $CO_2$  mole fraction.

Table 6.5 presents the char conversion results for the optimized kinetic parameters for GRI-Mech with EDC and for the global approach with F-R/EDM. Apart from in-reactor gas composition, GRI-Mech with EDC predicts a more accurate value of the char conversion factor with respect to the experimental value.

Table 6.5. Char conversion degree for optimized char conversion parameters for GRI-Mech with EDC and for global approach with F-R/EDM.

Char conversion degree %		
	Simulation results all particle fractions 1 - 85 $\mu\text{m}$	Experiment All particle fractions 1 - 85 $\mu\text{m}$
Optimized parameters for GRI-Mech with EDC	82.8 %	82%
Optimized parameters for Global approach with F-R/EDM	77 %	

## 6.5.4 Conclusions

An optimization procedure for the empirical char conversion kinetic-diffusion model, based on the detailed CBK/E and CBK/G models, was presented. The numerical model was validated against the experimental data from the BYU gasifier. The BYU reactor reference measurements are suitable for this purpose since in-reactor measurement data are available which is vital when one considers the credible and effective assessment of the predictive capabilities of the CFD model. The following main conclusions can be drawn:

- The use of the optimization procedure resulted in a better agreement between the model results and the experimental data in terms of the gas composition and char conversion factor.
- The applied kinetic parameters of the char-oxidation and char-gasification reactions proved to have a significant impact in the gasification process simulations. The major effect could be observed on the final gas composition and the char conversion factor, but also on the gas composition in the flame zone.
- Due to the versatile character of the method, the presented optimization procedure can be applied in other areas of interest, provided that both complex and simple models are available.

## 7. General conclusions and future work

### 7.1 Conclusions

A multiscale model of entrained flow coal gasification has been developed. Validation of the proposed model has been performed on a variety of the gasifiers operating conditions including oxygen-blown to air-blown, atmospheric pressure to pressurized, lab-scale to pilot-scale, axially injected to tangentially injected, gasification to pyrolysis. Overall, three entrained flow gasifiers, one drop tube pyrolysis reactor, and two ideal reactors (a plug flow reactor, a perfectly stirred reactor) were investigated. The main aim of the thesis which was to increase the accuracy of CFD simulations by applying optimization methods and efficient modeling

approaches has been satisfied. The optimized devolatilization and char conversion models managed to increase the level of accuracy with respect to the experimental data. As regards the gas phase, the investigated reaction mechanisms and turbulence-chemistry interaction approaches turned out to have a substantial impact on the gasification process. The investigation made it possible to determine the most accurate modeling approaches.

## 7.2 Future work

Future research will regard above all the optimization procedure of kinetic parameters for intrinsic char conversion global models. The second research will concern the tabulated devolatilization (TDM) model and its effect on entrained flow coal gasification. The proposed optimization technique in the current dissertation will be compared with the TDM model in both coal gasification and coal pyrolysis for a wide range of operating conditions. Future research will also regard other solid fuels such as biomass.

## References

- [1] Hurt R, Sun J-K, Lunden M. A Kinetic Model of Carbon Burnout in Pulverized Coal Combustion. *Combust Flame* 1998;113:181–97. [https://doi.org/10.1016/S0010-2180\(97\)00240-X](https://doi.org/10.1016/S0010-2180(97)00240-X).
- [2] Hurt R H, Lunden M M, Brehob E G, Maloney D J. Statistical kinetics for pulverized coal combustion. *Symp Combust* 1996;26:3169–77.
- [3] Hurt RH, Calo JM. Semi-global intrinsic kinetics for char combustion modeling††Entry 2 has also been referred to as “Langmuir kinetics.” The present paper adopts common chemical engineering usage, in which the designation “Langmuir” is applied to the equilibrium adsorption. *Combust Flame* 2001;125:1138–49. [https://doi.org/10.1016/S0010-2180\(01\)00234-6](https://doi.org/10.1016/S0010-2180(01)00234-6).
- [4] Lang T, Hurt RH. Char Combustion Reactivities for a Suite of Diverse Solid Fuels and Char-Forming Organic Model Compounds. *Proc Combust Inst* 2002;29:423–31. [https://doi.org/10.1016/S1540-7489\(02\)80056-6](https://doi.org/10.1016/S1540-7489(02)80056-6).
- [5] Grant DM, Pugmire RJ, Fletcher TH, Kerstein AR. Chemical Model of Coal Devolatilization Using Percolation Lattice Statistics. *Energy and Fuels* 1989;3:175–86. <https://doi.org/10.1021/ef00014a011>.
- [6] Fletcher TH, Kerstein AR, Pugmire RJ, Solum MS, Grant DM. Chemical Percolation Model for Devolatilization. 3. Direct Use of <sup>13</sup>C NMR Data To Predict Effects of Coal Type. *Energy and Fuels* 1992;6:414–31. <https://doi.org/10.1021/ef00034a011>.
- [7] Fletcher TH, Kerstein AR, Pugmire RJ, Grant DM. Chemical percolation model for devolatilization. 2. Temperature and heating rate effects on product yields. *Energy & Fuels* 1990;4:54–60. <https://doi.org/10.1021/ef00019a010>.
- [8] Solomon PR, Hamblen DG, Carangelo RM, Serio MA, Deshpande G V. General Model of Coal Devolatilization. *ACS Div Fuel Chem Prepr* 1987;32:83–98. <https://doi.org/10.1021/ef00010a006>.
- [9] Smith G, Golden D, Frenklach M, Moriarty N, Eiteneer B, Goldenberg M, et al. GRI-Mech 3.0 2000. <http://combustion.berkeley.edu/gri-mech/version30/text30.html> (accessed October 14, 2018).
- [10] Ranzi E, Cavallotti C, Cuoci A, Frassoldati A, Pelucchi M, Faravelli T. New reaction classes in the kinetic modeling of low temperature oxidation of n-alkanes. *Combust Flame* 2015;162:1679–91. <https://doi.org/10.1016/j.combustflame.2014.11.030>.
- [11] Niksa S, Liu GS, Hurt RH. Coal conversion submodels for design applications at elevated pressures. Part I. Devolatilization and char oxidation. *Prog Energy Combust Sci* 2003;29:425–77. [https://doi.org/10.1016/S0360-1285\(03\)00033-9](https://doi.org/10.1016/S0360-1285(03)00033-9).
- [12] Niksa S, Liu GS. Coal conversion submodels for design applications at elevated pressures. Part II. Char

- gasification. *Prog Energy Combust Sci* 2004;30:679–717. <https://doi.org/10.1016/j.pecs.2004.08.001>.
- [13] Bell DA, Towler BF, Fan M. *Coal gasification and Its Applications*. 2011. <https://doi.org/10.1016/b978-0-8155-2049-8.10015-4>.
- [14] Today in Energy - U.S. Energy Information Administration (EIA) n.d. <https://www.eia.gov/todayinenergy/detail.php?id=26912> (accessed October 8, 2020).
- [15] World coal consumption, 1971-2018 – Charts – Data & Statistics - IEA n.d. <https://www.iea.org/data-and-statistics/charts/world-coal-consumption-1978-2019> (accessed October 8, 2020).
- [16] World Coal Statistics - Worldometer n.d. <https://www.worldometers.info/coal/> (accessed October 8, 2020).
- [17] Emissions – Global Energy & CO2 Status Report 2019 – Analysis - IEA n.d. <https://www.iea.org/reports/global-energy-co2-status-report-2019/emissions> (accessed October 8, 2020).
- [18] • World energy consumption by energy source 2040 | Statista n.d. <https://www.statista.com/statistics/222066/projected-global-energy-consumption-by-source/> (accessed October 8, 2020).
- [19] • Projected CO2 emissions worldwide 2050 | Statista n.d. <https://www.statista.com/statistics/263980/forecast-of-global-carbon-dioxide-emissions/> (accessed October 8, 2020).
- [20] Ultra-Supercritical & Advanced Ultra-Supercritical Technology | SteamH | GE Power n.d. <https://www.ge.com/power/steam/steam-power-plants/advanced-ultra-supercritical-usc-ausc> (accessed October 8, 2020).
- [21] What is CCS? – The Carbon Capture & Storage Association (CCSA) n.d. <http://www.ccsassociation.org/what-is-ccs/> (accessed October 8, 2020).
- [22] Integrated Gasification Combined Cycle Plant - an overview | ScienceDirect Topics n.d. <https://www.sciencedirect.com/topics/engineering/integrated-gasification-combined-cycle-plant> (accessed October 8, 2020).
- [23] Higman C, Burgt M. *Gasification*. 2nd. ed. 2008. <https://doi.org/10.1016/B978-0-7506-8528-3.X0001-6>.
- [24] Alonso MJG, Borrego AG, Alvarez D, Mene R. Pyrolysis behaviour of pulverised coals at different temperatures 1999;78:1501–13.
- [25] Rezaiyan J, Cheremisinoff NP. *Gasification technologies: A primer for engineers and scientists*. 2005.
- [26] Nikrityuk PA, B M. *Gasification Processes: modelling and simulation*. 2014.
- [27] Nikrityuk PA. *Thermochemical Processing of Biomass into Fuels , Chemicals and Power Integrative Computational Materials Modeling Hydrogen and Syngas Production and Purification Computational Thermo-Fluid*. 2014.
- [28] Benyon PJ. *COMPUTATIONAL MODELLING OF ENTRAINED FLOW* By 2002.
- [29] Luque R, Campelo JM, Clark JH. *Handbook of Biofuels Production: Processes and Technologies* 2010:1–659.
- [30] 5.2. Commercial Gasifiers | netl.doe.gov n.d. <https://www.netl.doe.gov/research/Coal/energy-systems/gasification/gasifipedia/types-gasifiers> (accessed October 8, 2020).
- [31] Mularski J, Pawlak-Kruczek H, Modlinski N. A review of recent studies of the CFD modelling of coal gasification in entrained flow gasifiers, covering devolatilization, gas-phase reactions, surface reactions, models and kinetics. *Fuel* 2020;271:1–36. <https://doi.org/10.1016/j.fuel.2020.117620>.
- [32] Briesemeister L, Geißler A, Halama S, Herrmann S, Kleinhans U, Steibel M, et al. Coal Pyrolysis. *Ullmann’s Encycl Ind Chem* 2016:1–44. [https://doi.org/doi:10.1002/14356007.a07\\_245.pub2](https://doi.org/doi:10.1002/14356007.a07_245.pub2).
- [33] Gavalas G. *Coal Science and Technology 4: Coal Pyrolysis*. vol. 4. 1982. <https://doi.org/10.1016/B978-0-444-81476-0.50001-6>.

- [34] Schlosberg R. Chemistry of Coal Conversion. 1985. <https://doi.org/10.1007/978-1-4899-3632-5>.
- [35] Smith LK, Smoot LD, Fletcher TH, Pugmire RJ. The structure and reaction processes of coal. vol. 91. Springer Science+Buisness Medial, LLC; 1994.
- [36] Solomon PR, Serio MA, Suuberg EM. Coal pyrolysis: Experiments, kinetic rates and mechanisms. *Prog Energy Combust Sci* 1992;18:133–220. [https://doi.org/10.1016/0360-1285\(92\)90021-R](https://doi.org/10.1016/0360-1285(92)90021-R).
- [37] Badzioch S, Hawksley P. Kinetics of thermal decomposition of pulverized coal particles. *Ind Eng Chem Process Des Dev* 1970;9:521–30. <https://doi.org/10.1021/i260036a005>.
- [38] Anthony DB, Howard JB, Hottel HC, Meissner HP. Rapid devolatilization of pulverized coal. *Symp Combust* 1975;15:1303–17. [https://doi.org/10.1016/S0082-0784\(75\)80392-4](https://doi.org/10.1016/S0082-0784(75)80392-4).
- [39] Kobayashi H, Howard JB, Sarofim AF. Coal devolatilization at high temperatures. *Symp Combust* 1977;16:411–25. [https://doi.org/10.1016/S0082-0784\(77\)80341-X](https://doi.org/10.1016/S0082-0784(77)80341-X).
- [40] Solomon PR, Colket MB. Coal devolatilization. *Symp Combust* 1979;17:131–43. [https://doi.org/10.1016/S0082-0784\(79\)80016-8](https://doi.org/10.1016/S0082-0784(79)80016-8).
- [41] Serio MA, Hamblen DG, Markham JR, Solomon PR. Kinetics of Volatile Product Evolution in Coal Pyrolysis: Experiment and Theory. *Energy and Fuels* 1987;1:138–52. <https://doi.org/10.1021/ef00002a002>.
- [42] Miura K, Maki T. Simplified method to estimate f(E) in distributed activation energy model for analyzing coal pyrolysis reaction. *J Chem Eng Japan* 1998;31:228–35. <https://doi.org/10.1252/jcej.31.228>.
- [43] Niksa L. Global Rates of Devolatilization for Various Coal Types 1993;307:293–307. [https://doi.org/10.1016/0010-2180\(93\)90075-E](https://doi.org/10.1016/0010-2180(93)90075-E).
- [44] Please CP, McGuinness MJ, McElwain DLS. Approximations to the distributed activation energy model for the pyrolysis of coal. *Combust Flame* 2003;133:107–17. [https://doi.org/10.1016/S0010-2180\(02\)00554-0](https://doi.org/10.1016/S0010-2180(02)00554-0).
- [45] Suuberg. Approximate Solution Technique for Nonisothermal, Gaussian Distributed Activation Energy Models 1983;245:243–5.
- [46] Yamamoto K, Murota T, Okazaki T, Taniguchi M. Large eddy simulation of a pulverized coal jet flame ignited by a preheated gas flow. *Proc Combust Inst* 2011;33:1771–8. <https://doi.org/10.1016/j.proci.2010.05.113>.
- [47] Biagini E, Tognotti L. A generalized correlation for coal devolatilization kinetics at high temperature. *Fuel Process Technol* 2014;126:513–20. <https://doi.org/10.1016/j.fuproc.2014.06.008>.
- [48] Schroeder BB, Smith ST, Smith PJ, Fletcher TH, Packard A, Frenklach M, et al. Scale-Bridging Model Development for Coal Particle Devolatilization 2016.
- [49] Paea S, McGuinness M. Higher order approximations to coal pyrolysis distribution. *J Sustain Min* 2018;17:76–86. <https://doi.org/10.1016/j.jsm.2018.03.002>.
- [50] Tremel A, Spliethoff H. Gasification kinetics during entrained flow gasification - Part I; Devolatilisation and char deactivation. *Fuel* 2013;103:663–71. <https://doi.org/10.1016/j.fuel.2012.09.014>.
- [51] Güneş M, Güneş S. A direct search method for determination of DAEM kinetic parameters from nonisothermal TGA data (note). *Appl Math Comput* 2002;130:619–28. [https://doi.org/10.1016/S0096-3003\(01\)00124-2](https://doi.org/10.1016/S0096-3003(01)00124-2).
- [52] Scott SA, Dennis JS, Davidson JF, Hayhurst AN. An algorithm for determining the kinetics of devolatilisation of complex solid fuels from thermogravimetric experiments. *Chem Eng Sci* 2006;61:2339–48. <https://doi.org/10.1016/j.ces.2005.11.002>.
- [53] Anthony DB, Howard JB. Coal devolatilization and hydrogasification. *AIChE J* 1976;22:625–56. <https://doi.org/10.1002/aic.690220403>.
- [54] Cai J, Wu W, Liu R. An overview of distributed activation energy model and its application in the

- pyrolysis of lignocellulosic biomass. *Renew Sustain Energy Rev* 2014;36:236–46. <https://doi.org/10.1016/j.rser.2014.04.052>.
- [55] Niksa S. FLASHCHAIN Theory for Rapid Coal Devolatilisation Kinetics. 2. Impact of Operation Conditions. *Energy & Fuels* 1991;5:665–73.
- [56] Niksa S, Kerstein AR. FLASHCHAIN Theory for Rapid Coal Devolatilization Kinetics. 1. Formulation. *Energy & Fuels* 1991;5:647–65.
- [57] Niksa S. FLASHCHAIN Theory for Rapid Coal Devolatilization Kinetics. 3. Modeling the Behavior of Various Coals. *Energy and Fuels* 1991;5:673–83. <https://doi.org/10.1021/ef00029a008>.
- [58] Li T, Chaudhari K, Vanessendelft D, Turton R, Nicoletti P, Shahnam M, et al. Computational fluid dynamic simulations of a pilot-scale transport coal gasifier: Evaluation of reaction kinetics. *Energy and Fuels* 2013;27:7896–904. <https://doi.org/10.1021/ef401887r>.
- [59] Genetti D, Fletcher TH. Modeling nitrogen release during devolatilization on the basis of chemical structure of coal. *Energy and Fuels* 1999;13:1082–91. <https://doi.org/10.1021/ef990056i>.
- [60] Fletcher TH, Hardesty DR. Compilation of Sandia Coal Devolatilization Data Milestone Report 1992:362.
- [61] Goshayeshi B, Sutherland JC. A comparison of various models in predicting ignition delay in single-particle coal combustion. *Combust Flame* 2014;161:1900–10. <https://doi.org/10.1016/j.combustflame.2014.01.010>.
- [62] Jupudi RS, Zamansky V, Fletcher TH. Prediction of light gas composition in coal devolatilization. *Energy and Fuels* 2009;23:3063–7. <https://doi.org/10.1021/ef9001346>.
- [63] Li S, Yang H, Fletcher TH, Dong M. Model for the Evolution of Pore Structure in a Lignite Particle during Pyrolysis. *Energy and Fuels* 2015;29:5322–33. <https://doi.org/10.1021/acs.energyfuels.5b00726>.
- [64] Sheng C, Azevedo JLT. Modeling the evolution of particle morphology during coal devolatilization. *Proc Combust Inst* 2000;28:2225–32. [https://doi.org/10.1016/S0082-0784\(00\)80632-3](https://doi.org/10.1016/S0082-0784(00)80632-3).
- [65] Tian Y, Xie K, Zhu S, Fletcher TH. Simulation of Coal Pyrolysis in Plasma Jet by CPD Model. *Energy & Fuels* 2001;15:1354–8. <https://doi.org/10.1021/ef0002142>.
- [66] Veras CAG, Carvalho JA, Ferreira MA. The chemical percolation devolatilization model applied to the devolatilization of coal in high intensity acoustic fields. *J Braz Chem Soc* 2002;13:358–67. <https://doi.org/10.1590/S0103-50532002000300011>.
- [67] Wang Z, Wan K, Xia J, He Y, Liu Y, Liu J. Pyrolysis Characteristics of Coal, Biomass, and Coal-Biomass Blends under High Heating Rate Conditions: Effects of Particle Diameter, Fuel Type, and Mixing Conditions. *Energy and Fuels* 2015;29:5036–46. <https://doi.org/10.1021/acs.energyfuels.5b00646>.
- [68] B. Yan, Y. Cheng, P. Xu, C. Cao YC. Generalized Model of Heat Transfer and Volatiles Evolution Inside Particles for Coal Devolatilization. *Rom J Morphol Embryol* 2015;56:1495–502. <https://doi.org/10.1002/aic>.
- [69] Yang H, Li S, Fletcher TH, Dong M. Simulation of the swelling of high-volatile bituminous coal during pyrolysis. *Energy and Fuels* 2014;28:7216–26. <https://doi.org/10.1021/ef5016846>.
- [70] Yang H, Li S, Fletcher TH, Dong M. Simulation of the swelling of high-volatile bituminous coal during pyrolysis. Part 2: Influence of the maximum particle temperature. *Energy and Fuels* 2015;29:3953–62. <https://doi.org/10.1021/acs.energyfuels.5b00609>.
- [71] Yang H, Li S, Fletcher TH, Dong M, Zhou W. Simulation of the evolution of pressure in a lignite particle during pyrolysis. *Energy and Fuels* 2014;28:3511–8. <https://doi.org/10.1021/ef500584q>.
- [72] Fletcher TH. Review of 30 Years of Research Using the Chemical Percolation Devolatilization Model. *Energy & Fuels* 2019;33:12123–53. <https://doi.org/10.1021/acs.energyfuels.9b02826>.
- [73] Ubhayakar SK, Stickler DB, Von Rosenberg CW, Gannon RE. Rapid devolatilization of pulverized coal in hot combustion gases. *Symp Combust* 1977;16:427–36. <https://doi.org/10.1016/S0082->

0784(77)80342-1.

- [74] Richards AP, Fletcher TH. A comparison of simple global kinetic models for coal devolatilization with the CPD model. *Fuel* 2016;185:171–80. <https://doi.org/10.1016/j.fuel.2016.07.095>.
- [75] Silaen A, Wang T. Effect of turbulence and devolatilization models on coal gasification simulation in an entrained-flow gasifier. *Int J Heat Mass Transf* 2010;53:2074–91. <https://doi.org/10.1016/j.ijheatmasstransfer.2009.12.047>.
- [76] BAUM MM, STREET PJ. Predicting the Combustion Behaviour of Coal Particles. *Combust Sci Technol* 1971;3:231–43. <https://doi.org/10.1080/00102207108952290>.
- [77] Vascellari M, Arora R, Hasse C. Simulation of entrained flow gasification with advanced coal conversion submodels. Part 1: Pyrolysis. *Fuel* 2013;113:654–69. <https://doi.org/10.1016/j.fuel.2013.11.004>.
- [78] Czajka KM, Modliński N, Kisiela-Czajka AM, Naidoo R, Peta S, Nyangwa B. Volatile matter release from coal at different heating rates –experimental study and kinetic modelling. *J Anal Appl Pyrolysis* 2019;139:282–90. <https://doi.org/10.1016/j.jaap.2019.03.001>.
- [79] Fletcher DF, Haynes BS, Christo FC, Joseph SD. A CFD based combustion model of an entrained flow biomass gasifier. *Appl Math Model* 2000;24:165–82. [https://doi.org/10.1016/S0307-904X\(99\)00025-6](https://doi.org/10.1016/S0307-904X(99)00025-6).
- [80] Watanabe H, Otaka M. Numerical simulation of coal gasification in entrained flow coal gasifier. *Fuel* 2006;85:1935–43. <https://doi.org/10.1016/j.fuel.2006.02.002>.
- [81] Shi S-P, Zitney SE, Shahnam M, Syamlal M, Rogers WA. Modelling coal gasification with CFD and discrete phase method. *J Energy Inst* 2006;79:217–21. <https://doi.org/10.1179/174602206X148865>.
- [82] Lu X, Wang T. Investigation of radiation models in entrained-flow coal gasification simulation. *Int J Heat Mass Transf* 2013;67:377–92. <https://doi.org/10.1016/j.ijheatmasstransfer.2013.08.011>.
- [83] Hla SS, Roberts DG, Harris DJ. A numerical model for understanding the behaviour of coals in an entrained-flow gasifier. *Fuel Process Technol* 2015;134:424–40. <https://doi.org/10.1016/j.fuproc.2014.12.053>.
- [84] Sun Z, Dai Z, Zhou Z, Guo Q, Yu G. Numerical simulation of industrial opposed multiburner coal-water slurry entrained flow gasifier. *Ind Eng Chem Res* 2012;51:2560–9. <https://doi.org/10.1021/ie201542q>.
- [85] Slezak A, Kuhlman JM, Shadle LJ, Spenik J, Shi S. CFD simulation of entrained-flow coal gasification: Coal particle density/sizefraction effects. *Powder Technol* 2010;203:98–108. <https://doi.org/10.1016/j.powtec.2010.03.029>.
- [86] Kumar M, Zhang C, Monaghan RFD, Singer SL, Ghoniem AF, Asme. CFD Simulation of Entrained Flow Gasification with Improved Devolatilization and Char Consumption Submodels. *Imece2009 Proc Asme Int Mech Eng Congr Expo Vol 3* 2010:383–95. <https://doi.org/10.1115/IMECE2009-12982>.
- [87] Kumar M, Ghoniem AF. Multiphysics Simulations of Entrained Flow Gasification . Part II : Constructing and Validating the Overall Model. *Energy & Fuels* 2012;26:464–79. <https://doi.org/10.1021/ef2008858>.
- [88] Abani N, Ghoniem AF. Large eddy simulations of coal gasification in an entrained flow gasifier. *Fuel* 2013;104:664–80. <https://doi.org/10.1016/j.fuel.2012.06.006>.
- [89] Vicente W, Ochoa S, Aguillón J, Barrios E. An Eulerian model for the simulation of an entrained flow coal gasifier. *Appl Therm Eng* 2003;23:1993–2008. [https://doi.org/10.1016/S1359-4311\(03\)00149-2](https://doi.org/10.1016/S1359-4311(03)00149-2).
- [90] Lu X, Wang T. Investigation of Low Rank Coal Gasification in a 2014;2014:1–12.
- [91] Lu X, Wang T. Water-gas shift modeling in coal gasification in an entrained-flow gasifier - Part 2: Gasification application. *Fuel* 2013;108:620–8. <https://doi.org/10.1016/j.fuel.2013.02.024>.
- [92] Silaen A, Wang T. COMPARISON OF INSTANTANEOUS, EQUILIBRIUM, AND FINITE-RATE GASIFICATION MODELS IN AN ENTRAINED-FLOW COAL GASIFIER. *Proc 26th Int Pittsburgh Coal Conf* 2009:1–11.



- [93] Ma J, Zitney SE. Computational fluid dynamic modeling of entrained-flow gasifiers with improved physical and chemical submodels. *Energy and Fuels* 2012;26:7195–219. <https://doi.org/10.1021/ef301346z>.
- [94] Vascellari M, Arora R, Hasse C. Simulation of entrained flow gasification with advanced coal conversion submodels. Part 2: Char conversion. *Fuel* 2014;118:369–84. <https://doi.org/10.1016/j.fuel.2013.11.004>.
- [95] Richter A, Vascellari M, Nikrityuk PA, Hasse C. Detailed analysis of reacting particles in an entrained-flow gasifier. *Fuel Process Technol* 2016;144:95–108. <https://doi.org/10.1016/j.fuproc.2015.12.014>.
- [96] Labbafan A, Ghassemi H. Numerical modeling of an E-Gas entrained flow gasifier to characterize a high-ash coal gasification. *Energy Convers Manag* 2016;112:337–49. <https://doi.org/10.1016/j.enconman.2016.01.040>.
- [97] Vascellari M, Cau G. Influence of turbulence-chemical interaction on CFD pulverized coal MILD combustion modeling. *Fuel* 2012;101:90–101. <https://doi.org/10.1016/j.fuel.2011.07.042>.
- [98] Park SS, Jeong HJ, Hwang J. 3-D CFD modeling for parametric study in a 300-MWe one-stage oxygen-blown entrained-bed coal gasifier. *Energies* 2015;8:4216–36. <https://doi.org/10.3390/en8054216>.
- [99] Vascellari M, Roberts DG, Hla SS, Harris DJ, Hasse C. From laboratory-scale experiments to industrial-scale CFD simulations of entrained flow coal gasification. *Fuel* 2015;152:58–73. <https://doi.org/10.1016/j.fuel.2015.01.038>.
- [100] Steibel M, Halama S, Geißler A, Spliethoff H. Gasification kinetics of a bituminous coal at elevated pressures: Entrained flow experiments and numerical simulations. *Fuel* 2017;196:210–6. <https://doi.org/10.1016/j.fuel.2017.01.098>.
- [101] Halama S, Spliethoff H. Numerical simulation of entrained flow gasification: Reaction kinetics and char structure evolution. *Fuel Process Technol* 2015;138:314–24. <https://doi.org/10.1016/j.fuproc.2015.05.012>.
- [102] Chen C, Horio M, Kojima T. Numerical simulation of entrained flow coal gasifiers. Part II: effects of operating conditions on gasifier performance. *Chem Eng Sci* 2000;55:3861–74. [https://doi.org/10.1016/S0009-2509\(00\)00030-0](https://doi.org/10.1016/S0009-2509(00)00030-0).
- [103] Chen C, Horio M, Kojima T. Use of numerical modeling in the design and scale-up of entrained flow coal gasifiers. *Fuel* 2001;80:1513–23. [https://doi.org/10.1016/S0016-2361\(01\)00013-8](https://doi.org/10.1016/S0016-2361(01)00013-8).
- [104] Chen C, Horio M, Kojima T. Numerical simulation of entrained flow coal gasifiers. Part I: modeling of coal gasification in an entrained flow gasifier. *Fuel* 2000;55:3861–74.
- [105] Jones WP, Lindstedt RP. Global reaction schemes for hydrocarbon combustion. *Combust Flame* 1988;73:233–49. [https://doi.org/10.1016/0010-2180\(88\)90021-1](https://doi.org/10.1016/0010-2180(88)90021-1).
- [106] Dryer FL, Westbrook CK. Simplified Reaction Mechanisms for the Oxidation of Hydrocarbon Fuels in Flames. *Combust Sci Technol* 1981;27:31–43. <https://doi.org/10.1080/00102208108946970>.
- [107] Nakod P. CFD Modeling and Validation of Oxy-Fired and Air-Fired Entrained Flow Gasifiers 2013;2:28–40.
- [108] Luan YT, Chyou YP, Wang T. Numerical analysis of gasification performance via finite-rate model in a cross-type two-stage gasifier. *Int J Heat Mass Transf* 2013;57:558–66. <https://doi.org/10.1016/j.ijheatmasstransfer.2012.10.026>.
- [109] Jeong HJ, Seo DK, Hwang J. CFD modeling for coal size effect on coal gasification in a two-stage commercial entrained-bed gasifier with an improved char gasification model. *Appl Energy* 2014;123:29–36. <https://doi.org/10.1016/j.apenergy.2014.02.026>.
- [110] Rakhshi A, Wiltowski T. A framework for devolatilization breakdown in entrained flow gasification modeling. *Fuel* 2017;187:173–9. <https://doi.org/10.1016/j.fuel.2016.09.036>.
- [111] Chyou Y, Huang C, Luan Y, Wang T. Numerical Simulation of Gasification Process in a Cross-type Two-stage Gasifier. *Int Pittsburgh Coal Conf* 2010. <https://doi.org/10.3109/17435390.2010.537791>.

- [112] Bockelie MJ, Denison MK, Chen Z, Linjewile T, Senior CL, Sarofim AF. CFD Modeling For Entrained Flow Gasifiers In Vision 21 Systems 2001:1–42.
- [113] Bockelie MJ, Denison MK, Chen Z, Senior CL, Linjewile T, Sarofim a F. CFD Modeling For Entrained Flow Gasifiers In Vision 21 Systems. Gasif Technol Conf 2002:1–42.
- [114] Wang L, Jia YJ, Kumar S, Li R, Mahar RB, Ali M, et al. Numerical analysis on the influential factors of coal gasification performance in two-stage entrained flow gasifier. *Appl Therm Eng* 2017;112:1601–11. <https://doi.org/10.1016/j.applthermaleng.2016.10.122>.
- [115] Jeong HJ, Hwang IS, Park SS, Hwang J. Investigation on co-gasification of coal and biomass in Shell gasifier by using a validated gasification model. *Fuel* 2017;196:371–7. <https://doi.org/10.1016/j.fuel.2017.01.103>.
- [116] Choi YC, Li XY, Park TJ, Kim JH, Lee JG. Numerical study on the coal gasification characteristics in an entrained flow coal gasifier. *Fuel* 2001;80:2193–201. [https://doi.org/10.1016/S0016-2361\(01\)00101-6](https://doi.org/10.1016/S0016-2361(01)00101-6).
- [117] X.Liu, W.Zhang, T.Park. Modelling coal gasification in an entrained flow gasifier. *Combust Theory Model* 2001;5:595–608.
- [118] Tremel A, Spliethoff H. Gasification kinetics during entrained flow gasification - Part II: Intrinsic char reaction rate and surface area development. *Fuel* 2013;107:653–61. <https://doi.org/10.1016/j.fuel.2012.10.053>.
- [119] Tremel A, Spliethoff H. Gasification kinetics during entrained flow gasification - Part III: Modelling and optimisation of entrained flow gasifiers. *Fuel* 2013;107:170–82. <https://doi.org/10.1016/j.fuel.2013.01.062>.
- [120] Khan J, Wang T. Implementation of a Demoisturization and Devolatilization Model in Multi-Phase Simulation of a Hybrid Entrained-Flow and Fluidized Bed Mild Gasifier. *Int J Clean Coal Energy* 2013;02:35–53. <https://doi.org/10.4236/ijcce.2013.23005>.
- [121] Wu Y, Zhang J, Smith PJ, Zhang H, Reid C, Lv J, et al. Three-dimensional simulation for an entrained flow coal slurry gasifier. *Energy and Fuels* 2010;24:1156–63. <https://doi.org/10.1021/ef901085b>.
- [122] Wu Y, Smith PJ, Zhang J, Thornock JN, Yue G. Effects of turbulent mixing and controlling mechanisms in an entrained flow coal gasifier. *Energy and Fuels* 2010;24:1170–5. <https://doi.org/10.1021/ef9011214>.
- [123] Xu J, Qiao L. Mathematical modeling of coal gasification processes in a well-stirred reactor: Effects of devolatilization and moisture content. *Energy and Fuels* 2012;26:5759–68. <https://doi.org/10.1021/ef3008745>.
- [124] Kobayashi H. Devolatilization of pulverized coal at high temperatures 1976.
- [125] Ajilkumar A, Sundararajan T, Shet USP. Numerical modeling of a steam-assisted tubular coal gasifier. *Int J Therm Sci* 2009;48:308–21. <https://doi.org/10.1016/j.ijthermalsci.2008.08.006>.
- [126] Liu H, Kojima T. Theoretical Study of Coal Gasification in a 50 ton/day HYCOL Entrained Flow Gasifier. I. Effects of Coal Properties and Implications. *Energy and Fuels* 2004;18:908–12. <https://doi.org/10.1021/ef030162r>.
- [127] Liu H, Kojima T. Theoretical Study of Coal Gasification in a 50 ton/day HYCOL Entrained Flow Gasifier. II. Effects of Operating Conditions and Comparison with Pilot-Scale Experiments. *Energy and Fuels* 2004;18:913–7.
- [128] MHI Gasifier | netl.doe.gov n.d. <https://netl.doe.gov/research/coal/energy-systems/gasification/gasifipedia/mhi-gasifier> (accessed October 16, 2020).
- [129] CB&I E-GAS™ Gasifiers | netl.doe.gov n.d. <https://netl.doe.gov/research/coal/energy-systems/gasification/gasifipedia/egas> (accessed October 16, 2020).
- [130] Lee H, Choi S, Paek M. A simple process modelling for a dry-feeding entrained bed coal gasifier. *Proc Inst Mech Eng Part A J Power Energy* 2011;225:74–84. <https://doi.org/10.1177/2041296710394249>.
- [131] Liu, G, Rezaei L. Modelling of a pressurised entrained flow coal gasifier: the effect of reaction kinetics and char structure. *Fuel* 2000;79:1767–79. [https://doi.org/10.1016/S0016-2361\(00\)00037-5](https://doi.org/10.1016/S0016-2361(00)00037-5).

- [132] Abaimov NA, Ryzhkov AF. Development of a Model of Entrained Flow Coal Gasification and Study of Aerodynamic Mechanisms of Action on Gasifier Operation 2015;62:767–72. <https://doi.org/10.1134/S0040601515110014>.
- [133] Authier O, Thunin E, Plion P, Schönnenbeck C, Leysens G, Brillhac JF, et al. Kinetic study of pulverized coal devolatilization for boiler CFD modeling. *Fuel* 2014;122:254–60. <https://doi.org/10.1016/j.fuel.2014.01.026>.
- [134] Authier O, Thunin E, Plion P, Porcheron L. Global kinetic modeling of coal devolatilization in a thermogravimetric balance and drop-tube furnace. *Energy and Fuels* 2015;29:1461–8. <https://doi.org/10.1021/ef502600t>.
- [135] Chen CJ, Hung CI, Chen WH. Numerical investigation on performance of coal gasification under various injection patterns in an entrained flow gasifier. *Appl Energy* 2012;100:218–28. <https://doi.org/10.1016/j.apenergy.2012.05.013>.
- [136] Westbrook CK, Dryer FL. Chemical kinetic modeling of hydrocarbon combustion. *Prog Energy Combust Sci* 1984;10:1–57. [https://doi.org/10.1016/0360-1285\(84\)90118-7](https://doi.org/10.1016/0360-1285(84)90118-7).
- [137] Dryer FL, Glassman I. High-temperature oxidation of CO and CH<sub>4</sub>. *Symp Combust* 1973;14:987–1003. [https://doi.org/https://doi.org/10.1016/S0082-0784\(73\)80090-6](https://doi.org/https://doi.org/10.1016/S0082-0784(73)80090-6).
- [138] Andersen J, Rasmussen CL, Giselsson T, Glarborg P. Global combustion mechanisms for use in CFD modeling under oxy-fuel conditions. *Energy and Fuels* 2009;23:1379–89. <https://doi.org/10.1021/ef8003619>.
- [139] Hautman DJ, Dryer FL, Schug KP, Glassman I. A multiple-step overall kinetic mechanism for the oxidation of hydrocarbons. *Combust Sci Technol* 1981;25:219–35. <https://doi.org/10.1080/00102208108547504>.
- [140] Rehm M, Seifert P, Meyer B. Theoretical and numerical investigation on the EDC-model for turbulence-chemistry interaction at gasification conditions. *Comput Chem Eng* 2009;33:402–7. <https://doi.org/10.1016/j.compchemeng.2008.11.006>.
- [141] Smith R J B, Loganathan M, Shantha MS. A Review of the Water Gas Shift Reaction Kinetics. *Int J Chem React Eng* 2010;8. <https://doi.org/10.2202/1542-6580.2238>.
- [142] Lu X, Wang T. Water-gas shift modeling in coal gasification in an entrained-flow gasifier. Part 1: Development of methodology and model calibration. *Fuel* 2013;108:629–38. <https://doi.org/10.1016/j.fuel.2013.02.023>.
- [143] Sato T, Kurosawa S, Smith RL, Adschiri T, Arai K. Water gas shift reaction kinetics under noncatalytic conditions in supercritical water. *J Supercrit Fluids* 2004;29:113–9. [https://doi.org/10.1016/S0896-8446\(03\)00049-4](https://doi.org/10.1016/S0896-8446(03)00049-4).
- [144] Bustamante F, Enick RM, Cugini A V., Killmeyer RP, Howard BH, Rothenberger KS, et al. High-Temperature Kinetics of the Homogeneous Reverse Water-Gas Shift Reaction. *AIChE J* 2004;50:1028–41. <https://doi.org/10.1002/aic.10099>.
- [145] Bustamante F, Enick RM, Killmeyer RP, Howard BH, Rothenberger KS, Cugini A V., et al. Uncatalyzed and wall-catalyzed forward water-gas shift reaction kinetics. *AIChE J* 2005;51:1440–54. <https://doi.org/10.1002/aic.10396>.
- [146] Veynante D, Vervisch L. Turbulent combustion modeling 2002;28.
- [147] Stöllinger M, Naud B, Roekaerts D, Beishuizen N, Heinz S. PDF modeling and simulations of pulverized coal combustion – Part 1 : Theory and modeling 2013;160:384–95. <https://doi.org/10.1016/j.combustflame.2012.10.010>.
- [148] Stöllinger M, Naud B, Roekaerts D, Beishuizen N, Heinz S. PDF modeling and simulations of pulverized coal combustion – Part 2 : Application 2013;160:396–410. <https://doi.org/10.1016/j.combustflame.2012.10.011>.
- [149] Vascellari M, Xu H, Hasse C. Flamelet modeling of coal particle ignition 2013;34:2445–52. <https://doi.org/10.1016/j.proci.2012.06.152>.

- [150] Chen L, Yong SZ, Ghoniem AF. Oxy-fuel combustion of pulverized coal: Characterization, fundamentals, stabilization and CFD modeling. *Prog Energy Combust Sci* 2012;38:156–214. <https://doi.org/10.1016/j.pecs.2011.09.003>.
- [151] Magnussen BF, Hjertager BH. On mathematical modeling of turbulent combustion with special emphasis on soot formation and combustion. *Symp Combust* 1977;16:719–29. [https://doi.org/10.1016/S0082-0784\(77\)80366-4](https://doi.org/10.1016/S0082-0784(77)80366-4).
- [152] Spalding DB. Development of the eddy-break-up model of turbulent combustion. *Symp Combust* 1977;16:1657–63. [https://doi.org/10.1016/S0082-0784\(77\)80444-X](https://doi.org/10.1016/S0082-0784(77)80444-X).
- [153] André Bakker. CFD Class 2002. <http://www.bakker.org/dartmouth06/engs150/> (accessed October 12, 2018).
- [154] Ali M, Jahromi Y, Atashkari K, Kalteh M. Performance Evaluation of a Two-Stage Entrained-Flow Coal Gasifier Using Numerical Simulation. *Chem Eng Technol* 2020;43:1316–26. <https://doi.org/10.1002/ceat.201900093>.
- [155] Magnussen BF. On the Structure of Turbulence and a Generalized Eddy Dissipation Concept for Chemical Reaction in Turbulent Flow. Nineteenth AIAA Meet 1981.
- [156] Lewandowski MT, Ertesvåg IS. Analysis of the Eddy Dissipation Concept formulation for MILD combustion modelling. *Fuel* 2018;224:687–700. <https://doi.org/10.1016/j.fuel.2018.03.110>.
- [157] Siminski VJ, Wright FJ, Edelman R, Economos C, Fortune O. Research on methods of improving the combustion characteristics of liquid hydrocarbon fuels. Report 1972;Volume I:242.
- [158] Chui EH, Majeski AJ, Lu DY, Hughes R, Gao H, McCalden DJ, et al. Simulation of entrained flow coal gasification. *Energy Procedia* 2009;1:503–9. <https://doi.org/10.1016/j.egypro.2009.01.067>.
- [159] Wen CY, Chaung TZ. Entrainment Coal Gasification Modeling. *Ind Eng Chem Process Des Dev* 1979;18:684–95. <https://doi.org/10.1021/i260072a020>.
- [160] Saraf CPPS and DN. High-Temperature Water-Gas Shift Reactors 1977;16:313–9.
- [161] ANSYS FLUENT 12.0 Theory Guide - Contents n.d. <http://www.afs.enea.it/project/neptunius/docs/fluent/html/th/node1.htm> (accessed May 12, 2018).
- [162] K.Hou RH. The kinetics of methane steam reforming over a Ni/a-Al<sub>2</sub>O catalyst 2010;88:2010.
- [163] Zahradnik RL, Grace RJ. Chemistry and Physics of Entrained Coal Gasification. *Am Chem Soc Div Fuel Chem Prepr* 1973;18:203–27. <https://doi.org/10.1021/ba-1974-0131.ch009>.
- [164] Petersen I, Werther J. Experimental investigation and modeling of gasification of sewage sludge in the circulating fluidized bed. *Chem Eng Process Process Intensif* 2005;44:717–36. <https://doi.org/10.1016/j.cep.2004.09.001>.
- [165] Turns SR. An introduction to combustion: concepts and applications. McGraw-Hill; 1996.
- [166] Virk PS, Chambers LE, Woebecke HN. Thermal Hydrogasification of Aromatic-Compounds. *Adv Chem Ser* 1974:237–58.
- [167] Lasa-Benito M, Marin O, Meggio F, Pinna LA, Jess A. Mechanisms and kinetics of thermal reactions of aromatic hydrocarbons from pyrolysis of solid fuels. vol. 75. 1996. [https://doi.org/10.1016/0016-2361\(96\)00136-6](https://doi.org/10.1016/0016-2361(96)00136-6).
- [168] Smith IW. The combustion rates of coal chars: A review. *Symp Combust* 1982;19:1045–65. [https://doi.org/10.1016/S0082-0784\(82\)80281-6](https://doi.org/10.1016/S0082-0784(82)80281-6).
- [169] Edge P, Gharebaghi M, Irons R, Porter R, Porter RTJ, Pourkashanian M, et al. Combustion modelling opportunities and challenges for oxy-coal carbon capture technology. *Chem Eng Res Des* 2011;89:1470–93. <https://doi.org/10.1016/j.cherd.2010.11.010>.
- [170] Field MA. Rate of combustion of size-graded fractions of char from a low-rank coal between 1 200°K and 2 000°K. *Combust Flame* 1969;13:237–52. [https://doi.org/10.1016/0010-2180\(69\)90002-9](https://doi.org/10.1016/0010-2180(69)90002-9).
- [171] Bell D, Towler BF, Fan M. Gasification Fundamentals. 2011. <https://doi.org/10.1016/B978-0-8155->

2049-8.10003-8.

- [172] Laurendeau N. Heterogeneous kinetics of coal char gasification and combustion. *Prog Energy Combust Sci* 1978;4:221–70. [https://doi.org/10.1016/0360-1285\(78\)90008-4](https://doi.org/10.1016/0360-1285(78)90008-4).
- [173] R.Aris. On shape factors for irregular particles-I. *J Mol Struct THEOCHEM* 1992;258:139–58. [https://doi.org/10.1016/0166-1280\(92\)85036-K](https://doi.org/10.1016/0166-1280(92)85036-K).
- [174] Kleinhans U, Halama S, Spliethoff H. Char particle burning behavior: Experimental investigation of char structure evolution during pulverized fuel conversion. *Fuel Process Technol* 2018. <https://doi.org/10.1016/j.fuproc.2017.10.022>.
- [175] Halama S, Spliethoff H. Reaction Kinetics of Pressurized Entrained Flow Coal Gasification: Computational Fluid Dynamics Simulation of a 5MW Siemens Test Gasifier. *J Energy Resour Technol* 2016;138. <https://doi.org/10.1115/1.4032620>.
- [176] S.K. Bhatia D. P. A Randon Pore Model for Fluid-Solid Reactions: 1. Isothermal, Kinetic Control 1980;26:379–86.
- [177] Liu H, Luo C, Kato S, Uemiya S, Kaneko M, Kojima T. Kinetics of CO<sub>2</sub>/Char gasification at elevated temperatures. Part I: Experimental results. *Fuel Process Technol* 2006;87:775–81. <https://doi.org/10.1016/j.fuproc.2006.02.006>.
- [178] Lee JG, Kim JH, Lee HJ, Park TJ, Kim SD. Characteristics of entrained flow coal gasification in a drop tube reactor. *Fuel* 1996;75:1035–42. [https://doi.org/10.1016/0016-2361\(96\)00084-1](https://doi.org/10.1016/0016-2361(96)00084-1).
- [179] Halama DS, Spliethoff PH, München TU. Computational Modeling ( CFD ) of Entrained Flow Gasification Kinetics with focus on the Structural Evolution of Char Particles 2014:19–22.
- [180] Hodge EM. The coal char-CO<sub>2</sub> reaction at high temperature and high pressure 2008:375.
- [181] Hodge EM, Roberts DG, Harris DJ, Stubington JF. The significance of char morphology to the analysis of high-temperature char-CO<sub>2</sub> reaction rates. *Energy and Fuels* 2010;24:100–7. <https://doi.org/10.1021/ef900503x>.
- [182] Jiménez S, Ballester J. Study of the evolution of particle size distributions and its effects on the oxidation of pulverized coal. *Combust Flame* 2007;151:482–94. <https://doi.org/10.1016/j.combustflame.2007.08.001>.
- [183] Kajitani S, Hara S, Matsuda H. Gasification rate analysis of coal char with a pressurized drop tube furnace. *Fuel* 2002;81:2–6.
- [184] Benfell KE, of Newcastle (N.S.W.). Dept. of Geology U. Assessment of Char Morphology in High Pressure Pyrolysis and Combustion. University of Newcastle; 2001.
- [185] Cetin E, Gupta R, Moghtaderi B. Effect of pyrolysis pressure and heating rate on radiata pine char structure and apparent gasification reactivity. *Fuel* 2005;84:1328–34. <https://doi.org/10.1016/j.fuel.2004.07.016>.
- [186] Barrio M, Gøbel B, Rimes H, Henriksen U, Hustad JE, Sørensen LH. Steam Gasification of Wood Char and the Effect of Hydrogen Inhibition on the Chemical Kinetics. *Prog Thermochem Biomass Convers* 2008:32–46. <https://doi.org/10.1002/9780470694954.ch2>.
- [187] Weeda, Abcouwer, Kapteijn M. STEAM GASIFICATION KINETICS AND BURN-OFF BEHAVIOUR FOR A BITUMINOUS COAL DERIVED CHAR IN THE PRESENCE OF H<sub>2</sub>. *Science (80- )* 1993;36:235–42.
- [188] Mühlen HJ, van Heek KH, Jüntgen H. Kinetic studies of steam gasification of char in the presence of H<sub>2</sub>, CO<sub>2</sub> and CO. *Fuel* 1985;64:944–9. [https://doi.org/10.1016/0016-2361\(85\)90149-8](https://doi.org/10.1016/0016-2361(85)90149-8).
- [189] Huang Z, Zhang J, Zhao Y, Zhang H, Yue G, Suda T, et al. Kinetic studies of char gasification by steam and CO<sub>2</sub> in the presence of H<sub>2</sub> and CO. *Fuel Process Technol* 2010;91:843–7. <https://doi.org/10.1016/j.fuproc.2009.12.020>.
- [190] Everson RC, Neomagus HWJP, Kasaini H, Njapha D. Reaction kinetics of pulverized coal-chars derived from inertinite-rich coal discards: Gasification with carbon dioxide and steam. *Fuel* 2006;85:1076–82.

<https://doi.org/10.1016/j.fuel.2005.10.016>.

- [191] Roberts DG, Harris DJ. Char gasification in mixtures of CO<sub>2</sub> and H<sub>2</sub>O: Competition and inhibition. *Fuel* 2007;86:2672–8. <https://doi.org/10.1016/j.fuel.2007.03.019>.
- [192] Szekely J, Evans J, Sohn HY. Gas-solid reactions. *Spectrochim Acta - Part A Mol Biomol Spectrosc* 1976;62:1131–9. <https://doi.org/10.1016/j.saa.2005.03.030>.
- [193] Cai HY, Güell AJ, Chatzakis IN, Lim JY, Dugwell DR, Kandiyoti R. Combustion reactivity and morphological change in coal chars: Effect of pyrolysis temperature, heating rate and pressure. *Fuel* 1996;75:15–24. [https://doi.org/10.1016/0016-2361\(94\)00192-8](https://doi.org/10.1016/0016-2361(94)00192-8).
- [194] Salatino P, Senneca O, Masi S. Assessment of thermodeactivation during gasification of a bituminous coal char. *Energy and Fuels* 1999;13:1154–9. <https://doi.org/10.1021/ef9900334>.
- [195] Schulze S, Richter A, Vascellari M, Gupta A, Meyer B, Nikrityuk PA. Novel intrinsic-based submodel for char particle gasification in entrained-flow gasifiers: Model development, validation and illustration. *Appl Energy* 2016;164:805–14. <https://doi.org/10.1016/j.apenergy.2015.12.018>.
- [196] Roberts DG, Harris DJ. A Kinetic Analysis of Coal Char Gasification Reactions at High Pressures. *Energy & Fuels* 2006;20:2314–20. <https://doi.org/10.1021/ef060270o>.
- [197] Von Zedtwitz P, Steinfeld A. Steam-gasification of coal in a fluidized-bed/packed-bed reactor exposed to concentrated thermal radiation - Modeling and experimental validation. *Ind Eng Chem Res* 2005;44:3852–61. <https://doi.org/10.1021/ie050138w>.
- [198] Lussier MG, Zhang Z, Miller DJ. CHARACTERIZING RATE INHIBITION IN H<sub>2</sub>O/H<sub>2</sub> GASIFICATION VIA MEASUREMENT OF ADSORBED HYDROGEN CONCENTRATION 1800:206–40.
- [199] Trommer D, Steinfeld A. Kinetic modeling for the combined pyrolysis and steam gasification of petroleum coke and experimental determination of the rate constants by dynamic thermogravimetry in the 500-1520 K range. *Energy and Fuels* 2006;20:1250–8. <https://doi.org/10.1021/ef050290a>.
- [200] Keller F, Küster F, Meyer B. Determination of coal gasification kinetics from integral drop tube furnace experiments with steam and CO<sub>2</sub>. *Fuel* 2018;218:425–38. <https://doi.org/10.1016/j.fuel.2017.11.120>.
- [201] Umemoto S, Kajitani S, Hara S. Modeling of coal char gasification in coexistence of CO<sub>2</sub> and H<sub>2</sub>O considering sharing of active sites. *Fuel* 2013;103:14–21. <https://doi.org/10.1016/j.fuel.2011.11.030>.
- [202] Niksa S. PC Coal Lab Version 5.0 User Guide and Tutorial 2011.
- [203] Zhang M, Yu J, Xu X. A new flame sheet model to reflect the influence of the oxidation of CO on the combustion of a carbon particle. *Combust Flame* 2005;143:150–8. <https://doi.org/10.1016/j.combustflame.2005.05.010>.
- [204] Yu J, Zhang MC. Experimental and modeling study on char combustion. *Energy and Fuels* 2009;23:2874–85. <https://doi.org/10.1021/ef900018b>.
- [205] Zhang J, Zhang M, Yu J. Extended application of the moving flame front model for combustion of a carbon particle with a finite-rate homogenous reaction. *Energy and Fuels* 2010;24:871–9. <https://doi.org/10.1021/ef900994k>.
- [206] Schulze S, Kestel M, Nikrityuk PA, Safronov D. From Detailed Description of Chemical Reacting Carbon Particles to Subgrid Models for CFD. *Oil Gas Sci Technol – Rev d'IFP Energies Nouv* 2013;68:1007–26. <https://doi.org/10.2516/ogst/2012069>.
- [207] Mayers MA. The rate of reduction of carbon dioxide by graphite. *J Am Chem Soc* 1934;56:70–76. <https://doi.org/10.1021/ja01316a021>.
- [208] Mayers MA. The Rate of Oxidation of Graphite by Steam. *J Am Chem Soc* 1934;56:1879–81. <https://doi.org/10.1021/ja01324a015>.
- [209] Govind R, Shah J. Modeling and Simulation of An Entrained Flow Coal Gasifier. *Combustion* 1984;30:79–92. <https://doi.org/10.1002/aic.690300113>.

- [210] Brown BW, Smoot LD, Smith PJ, Hedman PO. Measurement and prediction of entrained-flow gasification processes. *AIChE J* 1988;34:435–46. <https://doi.org/10.1002/aic.690340311>.
- [211] D.G.Roberts, D.J.Harris. Char gasification with O<sub>2</sub>, CO<sub>2</sub> and H<sub>2</sub>O: Effects of Pressure on Intrinsic Reaction Kinetics 2000:2271.
- [212] Smith PJ, Thomas H. F, Smoot LD. Model for pulverized coal-fired reactors. *Symp Combust* 1981;18:1285–93. [https://doi.org/10.1016/S0082-0784\(81\)80132-4](https://doi.org/10.1016/S0082-0784(81)80132-4).
- [213] Bösenhofer M. On the modeling of multi-phase reactive flows: Thermo-chemical conversion in the raceway zone of blast furnaces. Doctoral thesis 2020.
- [214] Poinso T, Veynante D. *Theoretical and Numerical Combustion*. Edwards; 2005.
- [215] Ansys Fluent User guide n.d. [https://www.sharcnet.ca/Software/Ansys/18.2.2/en-us/help/ai\\_sinfo/flu\\_intro.html](https://www.sharcnet.ca/Software/Ansys/18.2.2/en-us/help/ai_sinfo/flu_intro.html) (accessed March 9, 2019).
- [216] Crowe C, Sharma MP, Stosk DE. The Particle-source-in Cell (PSI-CELL) Model for Gas-droplet Flows. *J Fluids Eng* 1977;99:392–332. <https://doi.org/doi:10.1115/1.3448756>.
- [217] Kim S-E, Choudhury D, Patel B. Computations of Complex Turbulent Flows Using the Commercial Code ANSYS FLUENT. *Proc ICASE/LaRC/AFOSR Symp Model Complex Turbul Flows* 1997.
- [218] Shih T-H, Liou WW, Shabbir A, Yang Z, Zhu J. A new k- $\epsilon$  eddy viscosity model for high reynolds number turbulent flows. *Comput Fluids* 1995;24:227–38. [https://doi.org/10.1016/0045-7930\(94\)00032-T](https://doi.org/10.1016/0045-7930(94)00032-T).
- [219] Kumar M, Ghoniem AF. Multiphysics simulations of entrained flow gasification. Part I: Validating the Nonreacting Flow Solver and the Particle Turbulent Dispersion Model. *Energy and Fuels* 2012;26:464–79. <https://doi.org/10.1021/ef2008858>.
- [220] Kumar M. *Multiscale CFD Simulations of Entrained Flow Gasification* 2011:227.
- [221] Ranz, W. E. and Marshall WR. *Che Eng Pro*48, 141.pdf. *Chem Eng Prog* 1952;48:141–6.
- [222] Cheng P. Two-dimensional radiating gas flow by a moment method. *AIAA J* 1964;2:1662–4. <https://doi.org/10.2514/3.2645>.
- [223] Chui EH, G.D R. COMPUTATION OF RADIANT HEAT TRANSFER ON A NONORTHOGONAL MESH USING THE FINITE-VOLUME METHOD. *Numer Heat Transf Part B* 1993;23:269–88.
- [224] Mularski J, Modliński N. Entrained flow coal gasification process simulation with the emphasis on empirical devolatilization models optimization procedure. *Appl Therm Eng* 2020;175:1–14. <https://doi.org/10.1016/j.applthermaleng.2020.115401>.
- [225] Holstein A, Bassilakis R, Wójtowicz MA, Serio MA. Kinetics of methane and tar evolution during coal pyrolysis. *Proc Combust Inst* 2005;30 II:2177–85. <https://doi.org/10.1016/j.proci.2004.08.231>.
- [226] de Jong W, Di Nola G, Venneker BCH, Spliethoff H, Wójtowicz MA. TG-FTIR pyrolysis of coal and secondary biomass fuels: Determination of pyrolysis kinetic parameters for main species and NOxprecursors. *Fuel* 2007;86:2367–76. <https://doi.org/10.1016/j.fuel.2007.01.032>.
- [227] Várhegyi G. Aims and methods in non-isothermal reaction kinetics. *J Anal Appl Pyrolysis* 2007;79:278–88. <https://doi.org/10.1016/j.jaap.2007.01.007>.
- [228] Scaccia S. TG-FTIR and kinetics of devolatilization of Sulcis coal. *J Anal Appl Pyrolysis* 2013;104:95–102. <https://doi.org/10.1016/j.jaap.2013.09.002>.
- [229] Czajka K, Kisiela A, Moroń W, Ferens W, Rybak W. Pyrolysis of solid fuels: Thermochemical behaviour, kinetics and compensation effect. *Fuel Process Technol* 2016;142:42–53. <https://doi.org/10.1016/j.fuproc.2015.09.027>.
- [230] Saddawi A, Jones JM, Williams A, Wójtowicz MA. Kinetics of the Thermal Decomposition of Biomass. *Energy & Fuels* 2010;24:1274–82. <https://doi.org/10.1021/ef900933k>.
- [231] BRADLEY D. Flame Propagation in a Tube: The Legacy of Henri Guenoche. *Combust Sci Technol* 2000;158:15–33. <https://doi.org/10.1080/00102200008947325>.

- [232] Zhang Z, Lu B, Zhao Z, Zhang L, Chen Y, Li S, et al. CFD modeling on char surface reaction behavior of pulverized coal MILD-oxy combustion: Effects of oxygen and steam. *Fuel Process Technol* 2020;204:106405. <https://doi.org/10.1016/j.fuproc.2020.106405>.
- [233] Lu M, Xiong Z, Li J, Li X, Fang K, Li T. Catalytic steam reforming of toluene as model tar compound using Ni/coal fly ash catalyst. *Asia-Pacific J Chem Eng* 2020;1–13. <https://doi.org/10.1002/apj.2529>.
- [234] Dukowicz JK. A particle–fluid numerical model for liquid sprays. *J Comput Phys* 1980;35:229–53. [https://doi.org/10.1016/0021-9991\(80\)90087-X](https://doi.org/10.1016/0021-9991(80)90087-X).
- [235] van Krevelen DW. *Coal: Typology, Chemistry, Physics, Constitution*. Elsevier Publishing Company; 1961.
- [236] Genetti D. Development and application of a correlation of <sup>13</sup>C NMR chemical structural analyses of coal based on elemental composition and volatile matter content. *Energy and Fuels* 1999;13:60–8. <https://doi.org/10.1021/ef980074k>.
- [237] Vascellari M, Arora R, Pollack M, Hasse C. Simulation of entrained flow gasification with advanced coal conversion submodels. Part 1: Pyrolysis - Appendix. *Fuel* 2013;113:654–69. <https://doi.org/10.1016/j.fuel.2013.06.014>.
- [238] Perrone D, Castiglione T, Klimanek A, Morrone P, Amelio M. Numerical simulations on Oxy-MILD combustion of pulverized coal in an industrial boiler. *Fuel Process Technol* 2018;181:361–74. <https://doi.org/10.1016/j.fuproc.2018.09.001>.
- [239] Patankar S., Spalding D. A calculation procedure for heat, mass and momentum transfer in three-dimensional parabolic flows. *Int J Heat Mass Transf* 1972;15:1787–806. [https://doi.org/10.1016/0017-9310\(72\)90054-3](https://doi.org/10.1016/0017-9310(72)90054-3).
- [240] Weber R. Extracting mathematically exact kinetic parameters from experimental data on combustion and pyrolysis of solid fuels. *J Energy Inst* 2008;81:226–33. <https://doi.org/10.1179/014426008X370997>.
- [241] Mularski J, Modliński N. Impact of Chemistry–Turbulence Interaction Modeling Approach on the CFD Simulations of Entrained Flow Coal Gasification. *Energies* 2020;13:6467. <https://doi.org/10.3390/en13236467>.
- [242] Wang L, Liu Z, Chen S, C.Zheng. Comparison of different global combustion mechanisms under hot and diluted oxidation conditions. *Combust Sci Technol* 2012;184:259–76. <https://doi.org/10.1080/00102202.2011.635612>.
- [243] Modlinski N, Hardy T. Development of high-temperature corrosion risk monitoring system in pulverized coal boilers based on reducing conditions identification and CFD simulations. *Appl Energy* 2017;204:1124–37. <https://doi.org/10.1016/j.apenergy.2017.04.084>.
- [244] Ranzi E, Frassoldati A, Stagni A, Pelucchi M, Cuoci A, Faravelli T. CRECK Modeling 2020. <http://creckmodeling.chem.polimi.it/menu-kinetics/menu-kinetics-detailed-mechanisms/107-category-kinetic-mechanisms/399-mechanisms-1911-c1-c3-ht> (accessed November 28, 2020).
- [245] Mularski J, Modlinski N. Entrained-flow Coal Gasification Process Simulation with the Emphasis on Empirical Char Conversion Models Optimization Procedure. *Energies* 2021;14:1–20. <https://doi.org/10.3390/en14061729>.
- [246] Liu G su, Tate AG, Bryant GW, Wall TF. Mathematical modeling of coal char reactivity with CO<sub>2</sub> at high pressures and temperatures. *Fuel* 2000;79:1145–54. [https://doi.org/10.1016/S0016-2361\(99\)00274-4](https://doi.org/10.1016/S0016-2361(99)00274-4).
- [247] Goetz GJ, Nsakala N y., Patel RL, Lao TC. *Combustion and Gasification Characteristics of Chars From Four Commercially Significant Coals of Different Rank*. Electr Power Res Institute, Adv Power Syst Div EPRI AP 1982.